

Advances in Science, Technology & Innovation
IEREK Interdisciplinary Series for Sustainable Development

Abdul Hai Alami *Editor*

PV Technology and Manufacturing

Advances in Science, Technology & Innovation

IEREK Interdisciplinary Series for Sustainable Development

Editorial Board

Anna Laura Pisello, Department of Engineering, University of Perugia, Italy

Dean Hawkes, University of Cambridge, Cambridge, UK

Hocine Bougdah, University for the Creative Arts, Farnham, UK

Federica Rosso, Sapienza University of Rome, Rome, Italy

Hassan Abdalla, University of East London, London, UK

Sofia-Natalia Boemi, Aristotle University of Thessaloniki, Greece

Nabil Mohareb, Faculty of Architecture—Design and Built Environment,
Beirut Arab University, Beirut, Lebanon

Saleh Mesbah Elkaffas, Arab Academy for Science, Technology and Maritime Transport,
Cairo, Egypt

Emmanuel Bozonnet, University of La Rochelle, La Rochelle, France

Gloria Pignatta, University of Perugia, Italy

Yasser Mahgoub, Qatar University, Qatar

Luciano De Bonis, University of Molise, Italy

Stella Kostopoulou, Regional and Tourism Development, University of Thessaloniki,
Thessaloniki, Greece

Biswajeet Pradhan, Faculty of Engineering and IT, University of Technology Sydney,
Sydney, Australia

Md. Abdul Mannan, Universiti Malaysia Sarawak, Malaysia

Chaham Alalouch, Sultan Qaboos University, Muscat, Oman

Iman O. Gawad, Helwan University, Helwan, Egypt

Anand Nayyar , Graduate School, Duy Tan University, Da Nang, Vietnam

Series Editor

Mourad Amer, International Experts for Research Enrichment and Knowledge Exchange
(IEREK), Cairo, Egypt

Advances in Science, Technology & Innovation (ASTI) is a series of peer-reviewed books based on important emerging research that redefines the current disciplinary boundaries in science, technology and innovation (STI) in order to develop integrated concepts for sustainable development. It not only discusses the progress made towards securing more resources, allocating smarter solutions, and rebalancing the relationship between nature and people, but also provides in-depth insights from comprehensive research that addresses the **17 sustainable development goals (SDGs)** as set out by the UN for 2030.

The series draws on the best research papers from various IEREK and other international conferences to promote the creation and development of viable solutions for a **sustainable future and a positive societal** transformation with the help of integrated and innovative science-based approaches. Including interdisciplinary contributions, it presents innovative approaches and highlights how they can best support both economic and sustainable development, through better use of data, more effective institutions, and global, local and individual action, for the welfare of all societies.

The series particularly features conceptual and empirical contributions from various interrelated fields of science, technology and innovation, with an emphasis on digital transformation, that focus on providing practical solutions to **ensure food, water and energy security to achieve the SDGs**. It also presents new case studies offering concrete examples of how to resolve sustainable urbanization and environmental issues in different regions of the world.

The series is intended for professionals in research and teaching, consultancies and industry, and government and international organizations. Published in collaboration with IEREK, the Springer ASTI series will acquaint readers with essential new studies in STI for sustainable development.


ASTI series has now been accepted for Scopus (September 2020). All content published in this series will start appearing on the Scopus site in early 2021.

Abdul Hai Alami
Editor

PV Technology and Manufacturing

 Springer

Editor

Abdul Hai Alami 
Sustainable and Renewable Energy
Engineering Department
University of Sharjah
Sharjah, United Arab Emirates

ISSN 2522-8714 ISSN 2522-8722 (electronic)
Advances in Science, Technology & Innovation
IEREK Interdisciplinary Series for Sustainable Development
ISBN 978-3-031-31348-6 ISBN 978-3-031-31349-3 (eBook)
<https://doi.org/10.1007/978-3-031-31349-3>

© The Editor(s) (if applicable) and The Author(s), under exclusive license to Springer Nature
Switzerland AG 2023

This work is subject to copyright. All rights are solely and exclusively licensed by the Publisher, whether the whole or part of the material is concerned, specifically the rights of translation, reprinting, reuse of illustrations, recitation, broadcasting, reproduction on microfilms or in any other physical way, and transmission or information storage and retrieval, electronic adaptation, computer software, or by similar or dissimilar methodology now known or hereafter developed.

The use of general descriptive names, registered names, trademarks, service marks, etc. in this publication does not imply, even in the absence of a specific statement, that such names are exempt from the relevant protective laws and regulations and therefore free for general use.

The publisher, the authors, and the editors are safe to assume that the advice and information in this book are believed to be true and accurate at the date of publication. Neither the publisher nor the authors or the editors give a warranty, expressed or implied, with respect to the material contained herein or for any errors or omissions that may have been made. The publisher remains neutral with regard to jurisdictional claims in published maps and institutional affiliations.

This Springer imprint is published by the registered company Springer Nature Switzerland AG
The registered company address is: Gewerbestrasse 11, 6330 Cham, Switzerland

To Seif and Suleiman: the dual nature of my life.

Also, to my wonderful authors and their families: Shamma, Haya, M. Ayoub, Adnan, Ayman and Ranem. This would not have been possible without you.

Foreword

As one of the pioneers of the field of Bioelectronics and an active contributor to the field by providing natural, “green” materials as candidates of sustainable technologies, for the benefit of both our society and our host planet Earth; as a co-organizer of multiple Materials Research Society symposia on the topic of sustainability in electronics; and finally, as a co-editor of the Green Electronics joint special edition of Wiley’s Advanced Materials Technologies and Advanced Sustainable Systems, I am coming more often than not to the critical question posed by the scientific community: “*How about a reliable and sustainable energy source to power the (bio)electronics?*”. The book of Abdul Hai Alami, *PV Technology and Manufacturing* helps the reader answer the above question and is in essence a pivotal contribution to the field of photovoltaics that makes the reader take part to a fabulous journey, passing all the way from the past, through the present and to the future of photovoltaic technologies. The chapters are fluent, independent of one another, yet they progress like an interthread, a fact that gives the reader both pleasure to read new pieces of information and time to digest the scientific material in the same time. The first-, second- and third-generation solar cells, as well as their practical designs, are thoroughly presented, together with their industrial fabrication techniques. The book finishes with a perspective chapter dedicated to recent advances of large-scale photovoltaics production and makes a very balanced approach to both science and engineering all throughout its chapters. By doing so it appeals to a broad audience, particularly physicists, synthetic chemists, materials and electrical engineers, to name a few. Abdul Hai Alami is a young and energetic member of photovoltaic research community dedicated to both research and teaching, and it is the latter of his passions that when translated from the teaching board to the text of the manuscript makes the book highly attractive to students of all ages and study programs. I am personally looking forward to add this book to my personal collection of books on photovoltaic technologies.

Mihai Irimia-Vladu
Assistant Professor
Institute of Physical Chemistry and Linz Institute
for Organic Solar Cells (LIOS)
Johannes Kepler University Linz
Linz, Austria
e-mail: Mihai.irimia-vladu@jku.at

Preface

The development of photovoltaic technologies in terms of power output and efficiency has seen significant advances in the past decade. The technoeconomic forces that affected the PV market have acted in two distinct directions. First, the “old” technologies of making solar cells from silicon materials have been significantly revamped. This editor remembers a time when the price of ten PV silicon wafer was around \$100 in 2006. After 2012, the hundred wafers are obtainable for that price. This has reflected positively on the growth of installed capacity of photovoltaic panels and encouraged more countries to embark on ambitious projects to power their populace with this technology.

The second direction was the exploration of novel technologies that refrained from processing silicon altogether. The monopoly of giant manufacturers of silicon, especially in China, has meant that global manufacturing centers faced serious supply chain bottle necks. This precluded any large-scale purchase of quality raw materials, reflecting negatively on their product final price. Nowadays there is no hope for a small silicon wafer manufacturer to exist and compete. Thus, a different set of technologies has to either be developed from scratch or be adapted and nurtured from an existing ancestor. Such introspection of the manufacturing market has given rise to all thin-film technologies (second generation) and later third-generation photovoltaics. Now smaller laboratories and companies can experiment with new materials with new combinations and permutations to deliver a competitive price/kWh ratio at an acceptable efficiency.

The bottom line of this melting pot of technological developments is excelling in manufacturing a PV cell that can survive its tolling environment long enough to pass the scrutiny of an economic feasibility study. This is, by large, the determining factor on whether a PV power plant gets funded or not.

This book undertakes the task of introducing all available PV manufacturing technologies, analyzing them and objectively discussing their pros and cons. It starts with the conventional silicon-based manufacturing technologies with a comprehensive analysis that takes the reader from “sand to wafer”. Thin-film technologies are also discussed and comprehensively covered. There are also three separate chapters dedicated to third-generation technologies, namely dye-sensitized solar cells (DSSC), organic photovoltaics (OPV) and perovskite solar cells (PSC).

The book mainly focuses on the manufacturing technologies, and with experimentally talented authors, the book offers a unique glance at what they are developing in the laboratory through a simple do-it-yourself projects for DSSC and PSC. The projects are conducted in academic laboratories and hence are meant to introduce the keen reader to the processes and materials needed, not to break any efficiency records. There is also a YouTube channel: (<https://www.youtube.com/channel/UCjfc9g4bBtDfe3dKO1AOCUw>) that has been created to post any new DIY projects that get filmed, so the reader can bookmark it for future reference.

This is the eighth year that the editor has taught the PV Technology and Manufacturing course at the University of Sharjah. The course is not a regular theoretical course that simply explains the physics of PV as this is done in a different course offered by the university. Rather, it focuses on manufacturing processes development as well as the materials required.

There are two dedicated chapters that present, in detail, the manufacturing processes that a PV manufacturer is expected to require as well as the characterization techniques used for both materials and cell evaluation. If the reader is inspired to experiment with materials chemical, physical, optical and mechanical properties to make their own cell, then the book has served its purpose.

Abdul Hai Alami, Ph.D.
Professor and Chair
Sustainable and Renewable Energy Engineering Department
University of Sharjah
Sharjah, United Arab Emirates

Contents

Introduction to Photovoltaic Cell Manufacturing	1
Abdul Hai Alami, Shamma Alasad, Haya Aljaghoub, Mohamad Ayoub, Adnan Alashkar, Ayman Mdallal, and Ranem Hasan	
First-Generation Photovoltaics: History and Conventional Manufacturing	7
Abdul Hai Alami, Shamma Alasad, Haya Aljaghoub, Mohamad Ayoub, Adnan Alashkar, Ayman Mdallal, and Ranem Hasan	
Silicon Feedstock and Ultra-Refinement	21
Abdul Hai Alami, Shamma Alasad, Haya Aljaghoub, Mohamad Ayoub, Adnan Alashkar, Ayman Mdallal, and Ranem Hasan	
Solar Grade Silicon Feedstock Properties	33
Abdul Hai Alami, Shamma Alasad, Haya Aljaghoub, Mohamad Ayoub, Adnan Alashkar, Ayman Mdallal, and Ranem Hasan	
Manufacturing of Silicon Solar Cells and Modules	45
Abdul Hai Alami, Shamma Alasad, Haya Aljaghoub, Mohamad Ayoub, Adnan Alashkar, Ayman Mdallal, and Ranem Hasan	
Second-Generation Photovoltaics: Thin-Film Technologies	65
Abdul Hai Alami, Shamma Alasad, Haya Aljaghoub, Mohamad Ayoub, Adnan Alashkar, Ayman Mdallal, and Ranem Hasan	
Third-Generation Photovoltaics: Dye-Sensitized Solar Cells (DSSC)	77
Abdul Hai Alami, Shamma Alasad, Haya Aljaghoub, Mohamad Ayoub, Adnan Alashkar, Ayman Mdallal, and Ranem Hasan	
Third-Generation Photovoltaics: Organic Photovoltaics (OPV)	93
Abdul Hai Alami, Shamma Alasad, Haya Aljaghoub, Mohamad Ayoub, Adnan Alashkar, Ayman Mdallal, and Ranem Hasan	
Third-generation Photovoltaics: Perovskite Solar Cells (PSC)	105
Abdul Hai Alami, Shamma Alasad, Haya Aljaghoub, Mohamad Ayoub, Adnan Alashkar, Ayman Mdallal, and Ranem Hasan	
Recent Advances in Solar Cells	115
Abdul Hai Alami, Shamma Alasad, Haya Aljaghoub, Mohamad Ayoub, Adnan Alashkar, Ayman Mdallal, and Ranem Hasan	
Characterization Techniques for Photovoltaics Manufacturing	139
Abdul Hai Alami, Shamma Alasad, Haya Aljaghoub, Mohamad Ayoub, Adnan Alashkar, Ayman Mdallal, and Ranem Hasan	
Third-Generation Photovoltaic Cell Manufacturing Processes	155
Abdul Hai Alami, Shamma Alasad, Haya Aljaghoub, Mohamad Ayoub, Adnan Alashkar, Ayman Mdallal, and Ranem Hasan	

List of Figures

Introduction to Photovoltaic Cell Manufacturing

Fig. 1	Energy conversion steps to obtain electrical energy (Alami 2020)	2
Fig. 2	Various energy conversion losses for a wind energy system (Alami 2020).	2
Fig. 3	Average monthly solar PV module prices by technology and manufacturing country sold in Europe, 2010 to 2020 (top) and average yearly module prices by market in 2013 and 2019 (bottom) (International Renewable Energy Agency 2019).	3
Fig. 4	Annual PV panels production by country (Jäger-Waldau 2018)	3
Fig. 5	Best research PV cell efficiency (https://www.nrel.gov/pv/cell-efficiency.html).	4
Fig. 6	Growth rate [%/yr] as a function of CE _e D [kWh _e /Wp] (top axis) and electricity payback time (E _e PBT) [yrs] assuming an 11.5% capacity factor (bottom axis) for a number of fractional reinvestment rates [%] (diagonal lines). Red lines indicate negative net electricity yield, and green lines indicate positive net electricity yield. The trajectories of CE _e D (or E _e PBT) and annual growth rates for PV technologies are depicted on a biannual basis between 2000 and 2010. The size of the circles represents the amount of installed capacity [GW] of each technology on a logarithmic basis (Dale and Benson 2013)	5
Fig. 7	A depiction of various photovoltaic technologies (Alami 2020)	5
Fig. 8	Roll-to-roll (R2R) production of solar cells using solution-based processing	6

First-Generation Photovoltaics: History and Conventional Manufacturing

Fig. 1	Schematic of the progress of phase 3 of Mohammed Bin Rashid Al Maktoum Solar Park (DEWA 2019).	8
Fig. 2	Solar PV module shipments by country of origin (IEA 2019), 2012–2019, IEA, Solar PV module shipments by country of origin, 2012–2019, IEA, Paris https://www.iea.org/data-and-statistics/charts/solar-pv-module-shipments-by-country-of-origin-2012-2019	8
Fig. 3	Energy use per capita in 2013 (Bank 2013)	10
Fig. 4	Human development index versus per capita electricity use (Dale 2014)	10
Fig. 5	Module production by PV technology (Mehta 2010)	11
Fig. 6	Structure of a p–n junction solar cell	11
Fig. 7	Early photovoltaic devices through history: a E. Becquerel photoelectrochemical cell circa 1839, b Adams and Day investigation of photoelectric effects in selenium circa 1876 (Adams and Day 1877), c Fritts thin-layered selenium-based photovoltaic device circa 1883 (Fritts 1883) and d Grondahl–Geiger copper-cuprous oxide photovoltaic cell circa 1927 (Grondahl 1933)	12

Fig. 8	Life cycle of a product	14
Fig. 9	Phase 1 of a product's life cycle—material extraction/processing	14
Fig. 10	Phase 2 of a product's life cycle—manufacturing	15
Fig. 11	Phase 3 of a product's lifetime—transportation (Ship—Wikipedia 2022)— (globe- Wikipedia 2022)	15
Fig. 12	Phase 4 of a product's lifetime—usage	15
Fig. 13	Phase 5 of a product's lifetime—end of life	16
Fig. 14	Silicon solar PV modules degradation with time (How Long Do Solar Panels Last 2022)	16
Fig. 15	China Solar Resource (Solar resource maps and GIS data for 200+ countries Solargis 2022), obtained from the Global Solar Atlas 2.0, a free, web-based application developed and operated by the company Solargis s.r.o. on behalf of the World Bank Group, utilizing Solargis data, with funding provided by the Energy Sector Management Assistance Program (ESMAP)	17

Silicon Feedstock and Ultra-Refinement

Fig. 1	Carbothermic process of metallurgical silicon refinement	22
Fig. 2	From sand to high-purity silicon	23
Fig. 3	CVD setup for obtaining highly pure solar grade and semiconductor grade silicon	23
Fig. 4	Siemens process for polysilicon purification and refinement a the Siemens chamber or bell and b polysilicon rods ready to be broken into silicon chunks (Polysilicon Production 2023)	24
Fig. 5	A schematic of the process of silicon purification and refinement via a fluidized bed reactor	25
Fig. 6	Process of obtaining monocrystalline silicon through the Czochralski- Silicon method. The photo is a Cz grown ingot displayed in the Science Museum of London (Silizium und für die Waferherstellung 2023)	26
Fig. 7	Several stages incorporated in the float zone method for obtaining monocrystalline silicon	27
Fig. 8	a A close-up of the float zone process and b a picture of the induction coil around the cast silicon ingot (Si-crystal floatingzone 2023)	27
Fig. 9	Directional solidification	28
Fig. 10	a Production of multi-crystalline silicon through the string ribbon method and b similarity of soap bubble adhesion to the filaments (Soap-Bubble Shapes 2023)	28
Fig. 11	Ribbon growth method for obtaining multi-crystalline silicon, where V_R is the speed of the moving substrate	29
Fig. 12	Process comparison of a bulk silicon wafer production and b ribbon or sheet grown silicon	29
Fig. 13	Main steps for bulk silicon and string ribbon processes	29
Fig. 14	Main steps of producing wafers from bulk silicon production	30
Fig. 15	a Using an inner saw reduces the broken edges and provides better control over the cut and b diamond-coated steel wires allow lower waste from the slicing operation	31
Fig. 16	Adding different features to the wafer to distinguish doping status and exposed crystallographic planes	31
Fig. 17	Schematic of a wafer lapping machine and its similarities with electric shaver razor (DOTSOG in this case)	31
Fig. 18	Crystallographic plane families that are exposed according to silicon wafer etching	31

Solar Grade Silicon Feedstock Properties

Fig. 1	Interaction between a photon and a material is a function of the energy bandgap of the material. If the bandgap is (a) less than or equal to the photon energy, then an electron/hole pair will generate, however, if the bandgap is (b) larger than the energy of the photon, no interaction is expected	34
Fig. 2	Basketball analogy with bandgap and photon energies: a energy bandgap less than or equal photon energy, indicating a full interaction that yields an electron/hole pair and b energy bandgap is more than the photon energy and no interaction	34
Fig. 3	Bandgap of metals, semiconductors, and insulators (https://upload.wikimedia.org/wikipedia/commons/thumb/0/0b/Band_gap_comparison.svg/2000px-Band_gap_comparison.svg.png)	34
Fig. 4	Absorptivity test setup	35
Fig. 5	Bandgap calculation using Tauc formula in graphical form (a) is taken with a xenon light source and a UV-range spectrometer, where a TiO ₂ peak is seen and the bandgap is shown inset as the tangent to the graph extended to intersect the x-axis to directly read the bandgap value in eV, while in (b) a halogen light source is used to determine the absorptivity of a material powder in the Vis regime, with a bandgap plot inset showing the application of the Tauc formula	35
Fig. 6	Shockley–Queisser limit for the maximum possible efficiency of a solar cell (https://en.wikipedia.org/wiki/Shockley%E2%80%93Queisser_limit#/media/File:ShockleyQueisserFullCurve.svg)	36
Fig. 7	Simple periodic table (https://commons.wikimedia.org/w/index.php?curid=98955505)	37
Fig. 8	Charge carriers versus electron/hole pairs	38
Fig. 9	Operation of a solar cell	39
Fig. 10	P-N junction under dark conditions.	40
Fig. 11	<i>I</i> – <i>V</i> curves of a photovoltaic cell in dark and under illumination conditions	40
Fig. 12	Silicon solar cell equivalent circuit	40
Fig. 13	Light <i>J</i> – <i>V</i> curve of a typical solar cell	41
Fig. 14	Semi-log dark <i>J</i> – <i>V</i> curve.	41
Fig. 15	Ideality factor versus voltage	42
Fig. 16	Unavoidable recombination: a radiative recombination and b Auger recombination	42
Fig. 17	Avoidable recombination as in trap state recombination around defects or grain boundaries	43

Manufacturing of Silicon Solar Cells and Modules

Fig. 1	Global market share of PV technologies (https://commons.wikimedia.org/wiki/File:Global_Market_Share_by_PV_Technology_from_1990_to_2013.svg)	46
Fig. 2	Solar cell technologies contribution in 2006 (Miles et al. 2007)	46
Fig. 3	High concentration of carriers (<i>n</i> ⁺) compared to ideally doped <i>n</i> -type regions	47
Fig. 4	Permutations of contacts placed on wafers	48
Fig. 5	a PERL versus b commercial solar cells (Green et al. 2001) (with permission 5364101367492)	49
Fig. 6	Heavily doped (<i>n</i> ⁺) emitter layer underneath contact finger	50

Fig. 7	Adding a passivating layer on top of emitter to ensure surface passivation	51
Fig. 8	Adding a heavily doped n^{++} layer right underneath the contact to enhance electron diffusion.	51
Fig. 9	Topology of a heterojunction solar cells	51
Fig. 10	Topology of the back-surface field (BSF)	52
Fig. 11	Spectacles a without anti-reflection coating (ARC) and b with ARC (https://www.allaboutvision.com/lenses/anti-reflective.htm)	52
Fig. 12	Texturing effects on incident solar radiation causing multiple reflections within the material	53
Fig. 13	Sequential manufacturing processes of a silicon solar cell	54
Fig. 14	General sequence of silicon wafer-to-module processing	54
Fig. 15	Using KOH to texturize a silicon wafer results in random-sized pyramids (https://scialert.net/fulltext/?doi=jas.2017.374.383)	55
Fig. 16	Inverted pyramids produced by Hydrofluoric (HF) acidic etching of silicon (Gao et al. 2018).	55
Fig. 17	Pyramids used by plasma (RIE) at different processing times (Addonizio et al. 2019) (with permission 5364110390101).	56
Fig. 18	Quartz tube furnace.	56
Fig. 19	Belt furnace	57
Fig. 20	A depiction of the CVD process.	57
Fig. 21	a CVD and b enhanced CVD processes	58
Fig. 22	PECVD process	58
Fig. 23	Direct-plasma batch reactor for the simultaneous PECVD deposition of SiN onto many Si wafers (Aberle 2001) (with permission 5364110735212).	58
Fig. 24	Deposition of SiN in a a direct-plasma reactor and b a remote-plasma reactor using microwave excitation (Aberle 2001) (with permission 5364110735212).	59
Fig. 25	Depiction of the sputtering process.	59
Fig. 26	Silk screen with contact finger pattern pre-inscribed.	60
Fig. 27	Steps of the screen-printing process	60
Fig. 28	Fully Assembled PV Module a Top view, b cross-section view.	62
Fig. 29	Flash test of assembled PV panel (Findlay 2022).	62

Second-Generation Photovoltaics: Thin-Film Technologies

Fig. 1	Photovoltaic electric generation capacity by panel material in the United States of America (EIA: U.S Energy Information Administration 2017)	67
Fig. 2	Thin-film (CdTe, CIGS, and a-Si) percentage among other types of cells (50 GW Solar Production: A 2014)	67
Fig. 3	Topaz Solar Farm in Arizona, USA in 2015 (Topaz Solar Farm 2015)	68
Fig. 4	Structure of cadmium-telluride (CdTe) solar cell.	68
Fig. 5	CIGS cell structure	69
Fig. 6	CIGS scanning electron microscope image of the cell with superposed cell components (Kazmerski 2022).	70
Fig. 7	Chemical vapor deposition of CIGS solar cells on glass substrate	71
Fig. 8	Electroplating process for CIGS solar cells.	71
Fig. 9	Tandem amorphous-crystalline solar cell a structure and b generalized absorption regimes	73
Fig. 10	Schematic of the p-i-n structure of amorphous silicon	74

Fig. 11	Range of film structures (schematic), obtained with different PECVD parameters, for films deposited on glass substrates; the dashed lines indicate the transitions between amorphous and mixed-phase material, as well as between mixed-phase material and highly crystalline material. The x-axis is log the dilution ratio, R , calculated as $\log [H]/[SiH_4]$ (Han et al. Aug. 2017)	75
---------	---	----

Third-Generation Photovoltaics: Dye-Sensitized Solar Cells (DSSC)

Fig. 1	Cost-efficiency graph, where costs are modules per peak W (CleanEnergyWIKI 2022)	78
Fig. 2	a General structure of a solid-state silicon photovoltaic technologies and b photo-electrochemical third-generation technologies	79
Fig. 3	Titanium dioxide (TiO_2) absorbance in the UV range.	79
Fig. 4	Simplified DSSC cell structure	80
Fig. 5	Dye-sensitized solar cells principle of operation	80
Fig. 6	Dye-sensitized solar cell's typical energy diagram	81
Fig. 7	A typical DSSC construction with voltage reference points highlighted in yellow.	82
Fig. 8	Four-probe test to determine the sheet resistance of glass with TCO	83
Fig. 9	a Chemical structure of ruthenium-based synthetic sensitizers and b absorbance in the UV-Vis region for the N3 and black dyes (nm) (Nazeeruddin et al. 2004). (With permission 5,364,120,164,714)	85
Fig. 10	Electron transfer process in DSSC	87
Fig. 11	DSSC module connectivity, Z-type (above) and W-type (below)	88
Fig. 12	Cleaning process for TCO substrates	89
Fig. 13	TiO_2 paste preparation, deposition, post-treatment (annealing)	89
Fig. 14	Dye deposition on TiO_2 substrates	90
Fig. 15	Cell finalization and electrolyte injection	90
Fig. 16	Dye-sensitized solar cell testing setup.	91
Fig. 17	Dye-sensitized solar cell J-V curve	91

Third-Generation Photovoltaics: Organic Photovoltaics (OPV)

Fig. 1	Ground state molecule with aligned π^* orbitals	94
Fig. 2	Energy states and π^* orbitals' shift with added energy—ground and state 1	94
Fig. 3	Energy states and π^* orbitals' shift with added energy—state 2 and state 3	95
Fig. 4	HOMO and LUMO levels	95
Fig. 5	Single layer OSC structure	96
Fig. 6	Bilayer OSC structure.	96
Fig. 7	a Bulk-hetero junction OSC, b Aligned bulk-hetero junction OSC, while c is a depiction of BHJ and d is that of aligned BHJ	97
Fig. 8	P3HT chemical structure (Brinkmann et al. 2010) (http://gisaxs.com/index.php/Material:P3HT).	97
Fig. 9	PCBM chemical structure (“Phenyl-C61-butyric acid methyl ester” 2021)	97
Fig. 10	PEDOT:PSS chemical structure (Brinkmann et al. 2010) (https://en.wikipedia.org/wiki/PEDOT:PSS#/media/File:Polythiophenes_Pedotpss.png)	98
Fig. 11	a Microscopic image of inkjet-printed silver grid on PEN substrate and b its line profile. c Microscopic image of Inktec TEC-PA-010 ink screen printed and d its line profile (Galagan and Andriesse 2012)	99

Fig. 12	Comparison between the current density versus voltage for grids and ITO-based devices (Galagan and Andriessse 2012)	100
Fig. 13	Spin coating process	100
Fig. 14	a Reflectance and transmittance b Absorbance for P3HT:PCBM blend at different spin coating frequencies and annealed at 160 °C for 5 min (Shaban et al. 2021)	101
Fig. 15	a Effect of annealing on absorbance and b J-V characteristic curves (Galagan and Andriessse 2012)	101
Fig. 16	a Depiction of the slot-die deposition process and b layer thickness versus position in coating direction (Galagan and Andriessse 2012)	102
Fig. 17	Performance of two organic cells of different areas (Galagan and Andriessse 2012)	103

Third-generation Photovoltaics: Perovskite Solar Cells (PSC)

Fig. 1	Depiction of the perovskite crystal structure	106
Fig. 2	a Perovskite solar cell structure and b solid-state dye-sensitized solar cell charge transfer mechanism	106
Fig. 3	Perovskite solar cell structural evolution from a discrete construction, b homogeneous construction and c blended construction	107
Fig. 4	a UV–Vis setup and b typical perovskite absorbance against wavelength	107
Fig. 5	Tauc transformation plot	108
Fig. 6	Perovskite solar cell—energy bands	108
Fig. 7	Perovskite solar cell PCE change with relative humidity and time for $\text{CH}_3\text{NH}_3\text{Pb}(\text{I}_1 - x\text{Br}_x)_3$ ($x = 0, 0.06, 0.20, 0.29$) (Park 2015)	108
Fig. 8	Change in PSC efficiency between 2008 and 2020 (Dai et al. 2021)	108
Fig. 9	Summary of the steps for PSC manufacturing processes.	109
Fig. 10	Etching of FTO substrate	109
Fig. 11	FTO substrates preparation	110
Fig. 12	Spin coating process shows the spin coating machine with disposable aluminum foil to reduce device contamination resulting from solution splash	110
Fig. 13	Flow of perovskite deposition process	111
Fig. 14	J-V a HTL deposition, b thermal evaporation step, c perovskite cell assembly and d characterization within a solar simulator	111
Fig. 15	Perovskite solar cell J-V curve	112

Recent Advances in Solar Cells

Fig. 1	Series-connected tandem solar cell (Tandem Cells 2022)	116
Fig. 2	Typical tandem process flow (Leijtens et al. 2018).	116
Fig. 3	Architectures of various perovskite/Si tandem cells (Chen et al. 2020).	117
Fig. 4	Various perovskite film formation techniques (Chen et al. 2020)	117
Fig. 5	Flow process and steps for the recycling of perovskite solar modules (Chen et al. 2021).	118
Fig. 6	Bifacial solar panels' working principle (Deline et al. 2019)	120
Fig. 7	Comparison of power generation curves for monofacial and bifacial modules (Kopecek and Libal 2018)	120
Fig. 8	Architecture of the different types of bifacial solar cells: a PERC, b PERT and c HJT (Stein et al. 2021)	121
Fig. 9	Modeled costs and minimum sustainable prices for Al-BSF, PERC, PERT, SHJ and IBC cell technologies (Woodhouse et al. 2019)	122

Fig. 10	Amount of aluminum per cell required for monofacial (blue) and bifacial (yellow) PERC (Photovoltaic Equipment International Technology Roadmap for Photovoltaic (ITRPV) 2019 Results 2019).....	123
Fig. 11	Worldwide market shares for bifacial technology (Photovoltaic Equipment International Technology Roadmap for Photovoltaic (ITRPV) 2019 Results 2019).....	123
Fig. 12	Schematic diagram of the energy fluxes for OSC greenhouse with shades (Ravishankar et al. 2020).....	124
Fig. 13	Depiction of an OSC-integrated greenhouse indicating spectral use of sunlight (Ravishankar et al. 2021).....	124
Fig. 14	Variation of the AVT and J_{ph} with respect to the Ag layer thickness for the ST-OSC (Çetinkaya et al. 2021).....	125
Fig. 15	Structure of FTO/ZnO/P3HT:PCBM/MoO ₃ /Ag/MoO ₃ (-/40/130/10/6/30 nm) ST-OSC (Çetinkaya et al. 2021).....	126
Fig. 16	Structure of (ITO/SnO ₂ NP _s /perovskite/Spiro-OMe-TAD/MoO ₃ /Ag/WO ₃) ST-PSC (Liang et al. 2020).....	126
Fig. 17	Timeline for the implementation of agrivoltaics between 2010 and 2021 (Trommsdorff 2021).....	127
Fig. 18	Potential for producing power in India, according to the National Institute of Solar Energy (NISE) (Mahto et al. 2021).....	128
Fig. 19	Solar energy potential in Africa (Edmond 2022).....	129
Fig. 20	Location of University of Djilali Bounaama in North Algeria (Trommsdorff 2021).....	130
Fig. 21	Architecture of a flexible solar cell with two electrodes and an active layer (Elsevier, Open Access) (Li et al. 2021).....	131
Fig. 22	Documented records of the reported efficiencies of different active layers applied in flexible solar cells (Elsevier, Open Access) (Li et al. 2021).....	132
Fig. 23	Depiction of the most utilized substrate material for flexible solar cells organized in a chronological order (Elsevier, Open Access) (Li et al. 2021).....	132

Characterization Techniques for Photovoltaics Manufacturing

Fig. 1	a X-ray diffractor apparatus and b X-ray beam generator and detector (based on reflected radiation).....	140
Fig. 2	XRD perovskite film (CH ₃ NH ₃ PbI ₃).....	141
Fig. 3	SEM result for a perovskite film.....	141
Fig. 4	SEM result of perovskite film (large grain size).....	142
Fig. 5	Analyzed SEM result.....	143
Fig. 6	Atomic force microscope.....	143
Fig. 7	AFM result of passive film on stainless-steel substrate for thickness measurement (Wang et al. 2019).....	143
Fig. 8	AFM result.....	144
Fig. 9	Plotted AFM result.....	144
Fig. 10	Absorbance profile for a perovskite thin-film coated on a glass substrate.....	145
Fig. 11	Absorption coefficient profile versus energy blue and Tauc plot pink.....	146
Fig. 12	STC light spectrum (AM1.5G).....	146
Fig. 13	J-V curve for a perovskite solar cell.....	146
Fig. 14	External quantum efficiency (https://www.pveducation.org/pvcdrom/solar-cell-operation/quantum-efficiency).....	147
Fig. 15	Quantum efficiency apparatus.....	148

Fig. 16	Comparison between steady-state and time-resolved photoluminescence spectroscopy (Dave et al. 2021)	148
Fig. 17	Simplified fluorescence spectroscopy process	149
Fig. 18	TRPL decay of perovskite solar cells	149
Fig. 19	Scattering modes taking place when light interacts with a molecule	150
Fig. 20	Jablonski diagram for the origin of the scattered light (https://www.edinst.com/us/blog/what-is-raman-spectroscopy/).	151
Fig. 21	Raman spectrometer	151
Fig. 22	Raman spectra of CuO thin films	151
Fig. 23	Typical EIS Nyquist plot	152
Fig. 24	Impedance (Nyquist) spectra for DSSC with Calotropis dye (Alami et al. 2021)	153

Third-Generation Photovoltaic Cell Manufacturing Processes

Fig. 1	Schematic representation of a semiconductor device patterning process (Newport 2022).	156
Fig. 2	Depiction of the screen-printing process steps.	157
Fig. 3	Example of the screen-printing process (Hussain et al. 2022) (with permission 5273590576001)	157
Fig. 4	CdTe–CdCl ₂ phase diagram (Saraie et al. 1978).	158
Fig. 5	Screen printing with subsequent sintering process (Burgelman 1998)	158
Fig. 6	Screen printed metal-grid embedded DSSC (Ramasamy et al. 2007) (With permission 5274140611103)	159
Fig. 7	Spin coater exterior.	160
Fig. 8	Vacuum-assisted substrate holder—side and top view	160
Fig. 9	Spin coater vacuum system-nitrogen tank—compressor	161
Fig. 10	Chuck substrate holder	161
Fig. 11	Spin coater cover	161
Fig. 12	Spin coater interface	162
Fig. 13	Spin coating process steps a deposition, b spin up, c spin off, and d evaporation (Yilbas et al. 2019) (with permission: 5260980863854).	162
Fig. 14	Slot-die coater.	164
Fig. 15	Slot-die coating head (https://www.ossila.com/pages/slot-die-coating-theory)	164
Fig. 16	Various manifold designs (https://www.ossila.com/pages/slot-die-coating-theory)	165
Fig. 17	Meniscus guide shim (https://www.ossila.com/products/slot-die-head?_pos=1&_sid=bc1331a13&_ss=r&variant=41159008878755).	165
Fig. 18	Syringe pump (https://www.ossila.com/products/syringe-pump)	166
Fig. 19	Rotary pump with a gear and lobe design (Bajpai 2018) (with permission 5262570110935).	166
Fig. 20	Coating bead (Romero et al. 2006) (with permission 5262941365999).	167
Fig. 21	Illustration of coating window with meniscus (https://www.ossila.com/pages/slot-die-coating-theory)	167
Fig. 22	Viscocapillary model stable coating window (Higgins 2011)	168
Fig. 23	Slot-die coating process (Patidar et al. 2020) (with permission 5263681213473).	168
Fig. 24	Thermal evaporator.	169
Fig. 25	Thermal evaporator glass chamber with protective mesh around it a open and b closeup	169
Fig. 26	a Boat/ resistive heaters, b location in thermal evaporator	170

Fig. 27	Substrate holder	170
Fig. 28	Thermal evaporation coating process (with permission 5273140799497)	171
Fig. 29	Doctor blade coating process	171
Fig. 30	Curtain coating process	172
Fig. 31	Pad printing process	172
Fig. 32	Spray coating process	173
Fig. 33	Dip coating process.	173



Introduction to Photovoltaic Cell Manufacturing

Abdul Hai Alami[✉], Shamma Alasad[✉], Haya Aljaghoub[✉],
Mohamad Ayoub[✉], Adnan Alashkar[✉], Ayman Mdallal[✉],
and Ranem Hasan[✉]

Abstract

Solar photovoltaics are synonyms to renewable energy resources. It is rare to find a poster or a presentation about renewable energy without a photovoltaic panel in the background. This introduction is a concise presentation on the importance of manufacturing technologies on the price, development and prefabrication of the solar panels. It is important to realize how critical the effect of manufacturing technologies is on the performance and cost of panels, which will be gradually introduced throughout this book.

1 Introduction to Solar Photovoltaics Manufacturing

Energy conversion is a fascinating concept. It is especially true when it takes place spontaneously, or with minimal external coercion. For example, the massive exothermic energy that results from fossil fuel combustion is initiated by a small amount of energy input (in the form of a spark). This

energy is then converted into pressurized steam, the release of which into turbines converts the thermal energy into kinetic energy and subsequently electric energy. This spontaneity is a strong reason why fossil fuels have dominated as long as they did and are currently the most reliable form of energy.

In a more intuitive manner, energy from the sun can also be converted into thermal energy once a proper receiver is introduced. The interaction of electromagnetic energy from the sun on a human body causes the absorbed fraction of this radiation to be converted into sensible heat. The rest is either reflected or transmitted, depending on the radiation wavelength and receiving surface condition and dimensions. Heat, however, is not a coveted form of energy, and direct electricity from the sun would be a better option.

Since the whole world is electrically plugged, the energy most sought-after is indeed electrical. Giving someone a fistful of thermal or kinetic energy would be a cruel joke when all they require is enough electricity to recharge a dying smart phone. Almost all energy conversion operations will eventually lead to electrical energy as evident from Fig. 1.

Unfortunately, with each energy conversion step there exist losses. Hence, the concept of efficiency was coined to quantify these losses and entice engineers to reduce them. Efficiency is defined as the ratio of input/output, and many energy conversion steps will drop the overall efficiency of a system by quite a lot. Remember that the overall system efficiency is the multiple of the individual efficiencies of each conversion process that occurs in series. Figure 2 shows an example of losses for a wind energy system, from generation to storage. These losses will accumulate and the energy retrieved from the battery would be a small fraction of the energy originally available in the wind.

The above discussion emphasizes the appeal of having a material or a device that is capable of converting solar radiation directly into electricity. Solar photovoltaic (PV) wafers and materials are devices that can do just that.

A. H. Alami (✉) · H. Aljaghoub · M. Ayoub · A. Mdallal ·
R. Hasan
University of Sharjah, Sharjah, United Arab Emirates
e-mail: aalalami@sharjah.ac.ae

H. Aljaghoub
e-mail: haljaghoub@sharjah.ac.ae

M. Ayoub
e-mail: mohamad.ayoub@sharjah.ac.ae

A. Mdallal
e-mail: ayman.mdallal@sharjah.ac.ae

S. Alasad · A. Alashkar
American University of Sharjah, Sharjah, United Arab Emirates
e-mail: g00070854@aus.edu

A. Alashkar
e-mail: b00028197@alumni.aus.edu

Fig. 1 Energy conversion steps to obtain electrical energy (Alami 2020)

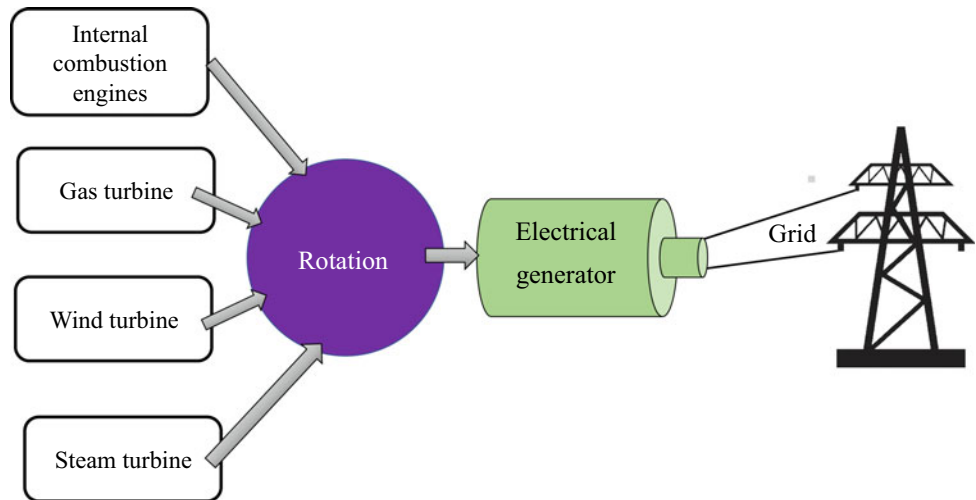
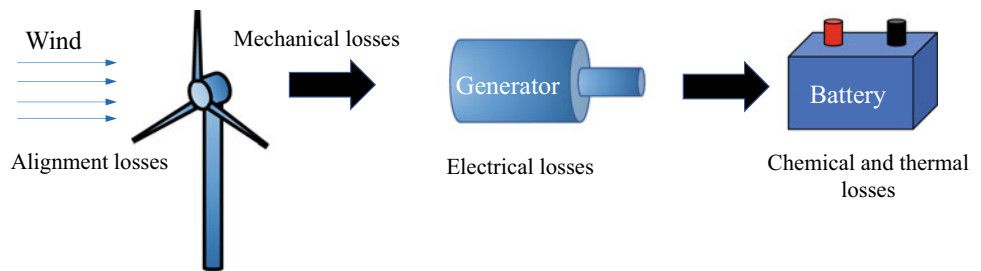


Fig. 2 Various energy conversion losses for a wind energy system (Alami 2020)



The story of PV technology is quite old: Around three hundred years old, ever since A. E. Becquerel published his work on the electrical effect derived from solar radiation in 1839 as will be discussed in subsequent chapters.

The development of solar PV technology can also be chronicled in different ways. One can focus on the leaps made in enhancing their figure of merit (FOM), which is the cost to generate a unit of electrical energy (dollar per kilowatt-hour, or \$/kWh). Figure 3 shows the rapid drop of module prices, which is a direct reflection of the total cost of any installed system (International Renewable Energy Agency 2019) and is a driving force in reducing the \$/kWh in all major PV installations.

From Fig. 3, China stands out as one of the main players in the PV market, since it has achieved the steepest cost reduction slope. It is very interesting to note that China is a late comer to the PV manufacturing market. Being almost non-existent before 2007, China currently controls more than one-third the world production of PV modules according to Fig. 4. The price of PV panels has fallen by around 80% as China dominated the production of silicon-based PV after 2007 (Fialka 2016). Having the only net-positive economy in a world hit by the 2007/2008 crises, China did not simply purchase mature technology from USA and Europe, but they also carefully examined the pertinent manufacturing processes and proceeded to apply crucial

changes to the utilization and consumption of silicon material and the energy needed to make solar cells. Adapting manufacturing processes that are amenable to mass production of solar wafers with high quality and at a competitive cost is hence the main key to push the PV industry into the future.

Another interesting and important resource to understand trends in PV manufacturing is the efficiency chart that is kept by the National Renewable Energy Lab (NREL). This chart chronicles the efficiency of solar cells with time. All technologies are represented in this graph, and thus, it provides a roadmap of available technologies from 1976 till present. This chart is found on <https://www.nrel.gov/pv/cell-efficiency.html> and the current iteration of it is shown in Fig. 5.

The choice of manufacturing processes for various PV technologies is a key factor for determining the energy payback time (EPBT) of the produced panels. So far, current PV technologies are not net-positive energy devices, meaning that the energy required to produce them, starting from raw materials such as silica, is more than they will produce in their operational lifetime (Dale and Benson 2013). Expanding the installation of PV panels is understandably desirable to conform to governmental mandates of switching to renewable energy sources by a specific timeline. This guarantees that the generated electricity produces no

Fig. 3 Average monthly solar PV module prices by technology and manufacturing country sold in Europe, 2010 to 2020 (top) and average yearly module prices by market in 2013 and 2019 (bottom) (International Renewable Energy Agency 2019)

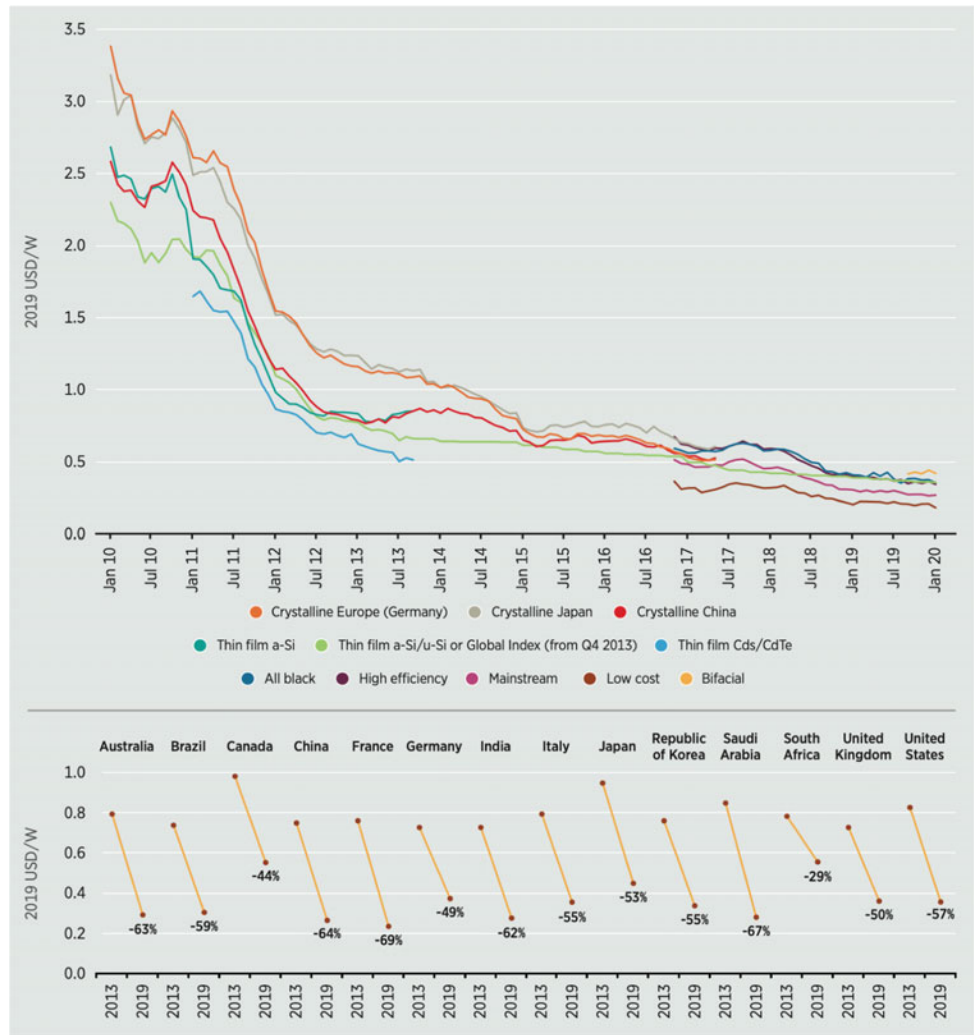
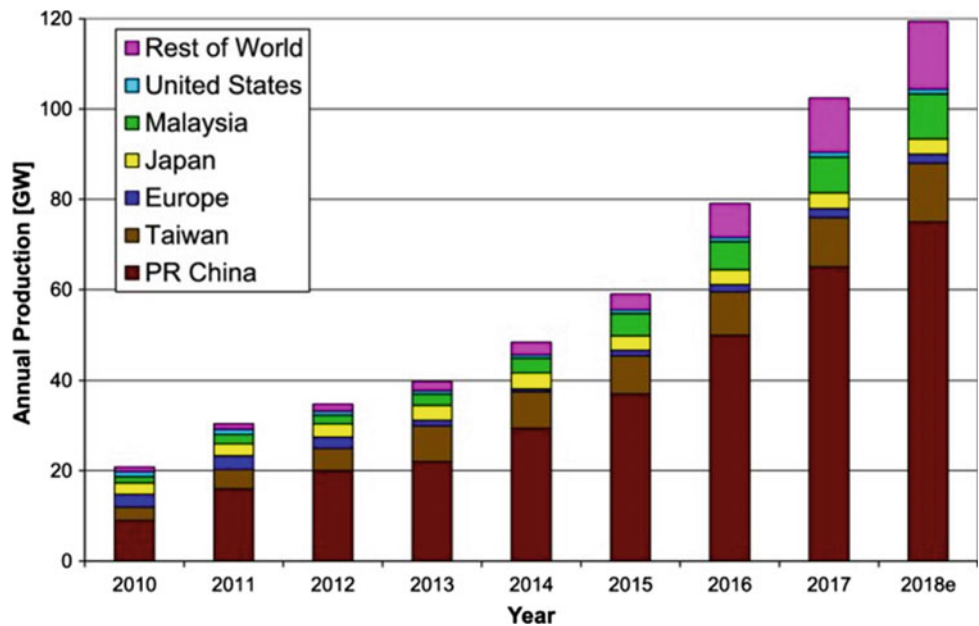


Fig. 4 Annual PV panels production by country (Jäger-Waldau 2018)



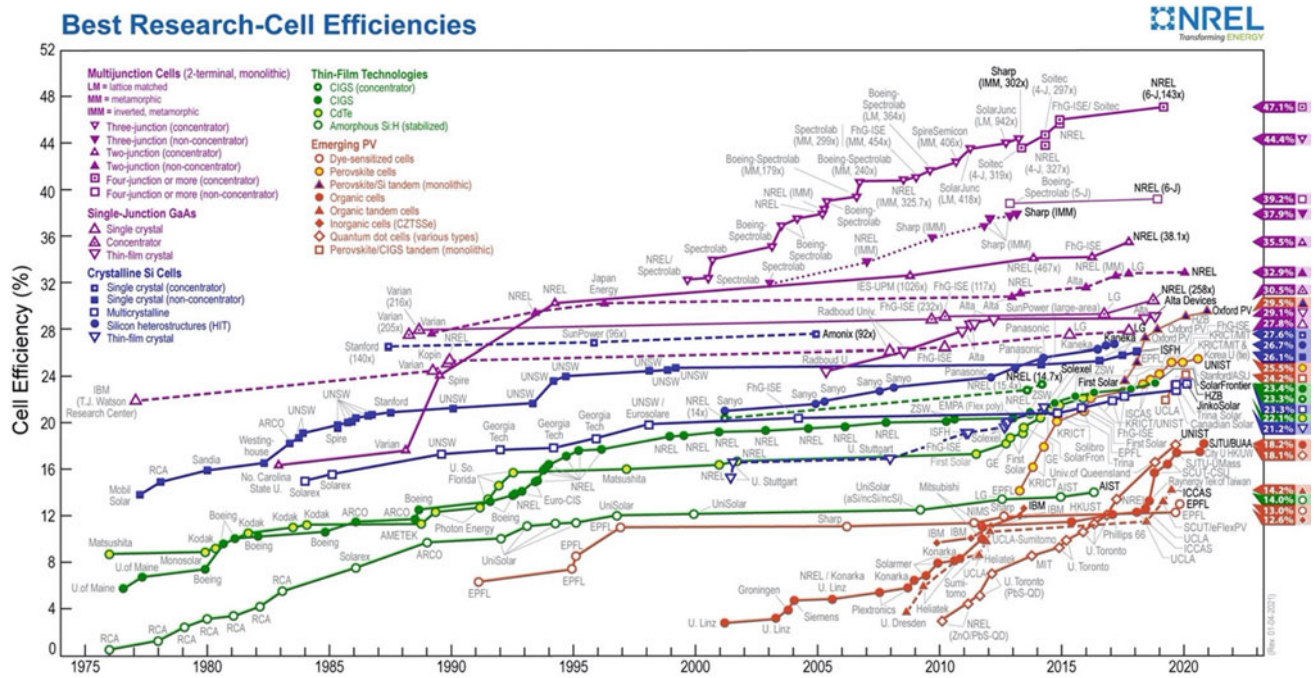


Fig. 5 Best research PV cell efficiency (<https://www.nrel.gov/pv/cell-efficiency.html>)

pollutants and allows the diversifying of available energy mix. But unless the EPBT becomes more reasonable by either lowering the cumulative energy demand (CED) or enhancing the capacity factor of available technologies, the probability of having PV technologies as net-positive remains a 50–50 chance. It is interesting to note from Fig. 6 that the only technology that allows a tangible EPBT are ribbon technologies as their production is less energy intensive than other technologies. But by re-examining Fig. 5, the efficiency of such thin-film technologies is still inferior to that of other mature technologies, and the number of required modules to produce a similar level of energy has to indeed be larger. Thus, any contribution in making the PV manufacturing processes more productive at lower prices and lower energy requirements is full of future opportunities for material scientists and engineers.

In this textbook, the manufacturing processes and technologies will be introduced and discussed for the three generations of PV modules. In general, and seen in Fig. 5, the technologies are divided into first, second, and third generations. First generation covers the conventional silicon-based modules that have classically dominated the market since late seventies of the twentieth century. The available silicon purification and processing technologies paved the way for adopting silicon as the material of choice for PV, since it is well-known that PV processing technologies were directly inherited from the silicon-based transistor technologies that produced microprocessors. Historically, monocrystalline silicon solar cells preceded the

cheaper and easier to produce polycrystalline ones, as seen in Fig. 7, only because monocrystalline silicon was used in the microprocessor industry.

Thin-film PV technologies are the second-generation cells made from thin-film materials, to reduce cost and material waste. Thin-film manufacturing processes are independent of the large-scale installations required to produce silicon cost-effectively. Processes such as chemical vapor deposition (CVD), sputtering, thermal evaporation, and others can be housed in a relatively small facility and used to produce high-quality thin films. Cadmium telluride (CdTe) cells and copper–indium–gallium–diselenide cells (CIGS) as well as gallium arsenide (GaAs) solar cells have been the most notable of these thin-film technologies, along with a resurrection of silicon wafers in the form of the large bandgap amorphous silicon films. Those can be used in tandem with their crystalline counterparts or are heat-treated to create crystalline films using manufacturing techniques that will be discussed later in this book.

Finally, the third-generation solar cells came as a complete departure from conventional silicon material and processing. They comprise three main technologies that can be manufactured using smaller scale equipment and setups to assemble and produce the cells, compared with the first two generations. The down side is that the produced cells still lack the reliability, stability, and power output of silicon solar cells. This being said, the promise they carry in terms of lower energy demand to produce as well as easier recyclability compared to silicon panels makes them serious

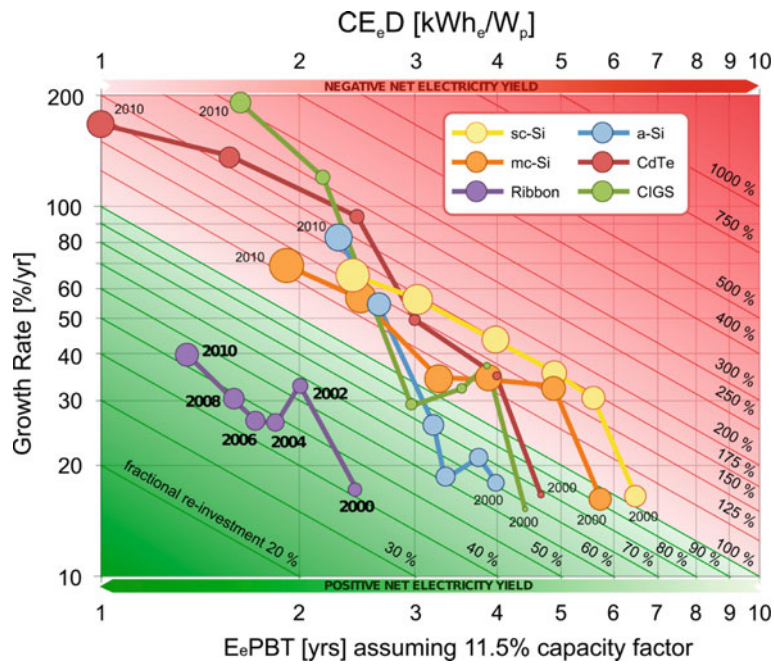
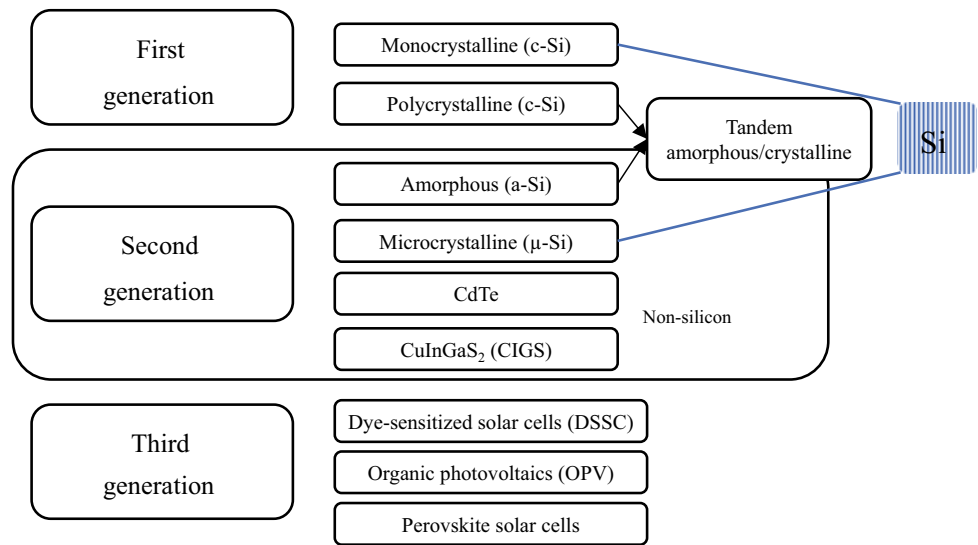


Fig. 6 Growth rate [%/yr] as a function of CE_{eD} [kWh_e/W_p] (top axis) and electricity payback time (E_ePBT) [yrs] assuming an 11.5% capacity factor (bottom axis) for a number of fractional reinvestment rates [%] (diagonal lines). Red lines indicate negative net electricity yield, and green lines indicate positive net electricity yield. The

trajectories of CE_{eD} (or E_ePBT) and annual growth rates for PV technologies are depicted on a biannual basis between 2000 and 2010. The size of the circles represents the amount of installed capacity [GW] of each technology on a logarithmic basis (Dale and Benson 2013)

Fig. 7 A depiction of various photovoltaic technologies (Alami 2020)



future contenders in the PV market. The three technologies are (i) dye-sensitized solar cells, (ii) organic cells, and (iii) perovskite cells; each has a separate chapter devoted to their development and construction. The aim from pursuing such technologies is that one day they can be adapted into roll-to-roll (R2R) technologies, which use solution-processes to deposit and combine precursors and electrodes, respectively, into a single device in a rapid and continuous manner.

The active inks and materials are similar to old printing inks for newspapers in old printing presses, but instead of producing ink-heavy newspapers, thin-film solar cells can be produced as fast (see Fig. 8), which would make up for their lower efficiency and stability issues. This concept is not far from being the norm in PV manufacturing, but there are several obstacles along the way that require creative solutions and combinations of materials and substrates.

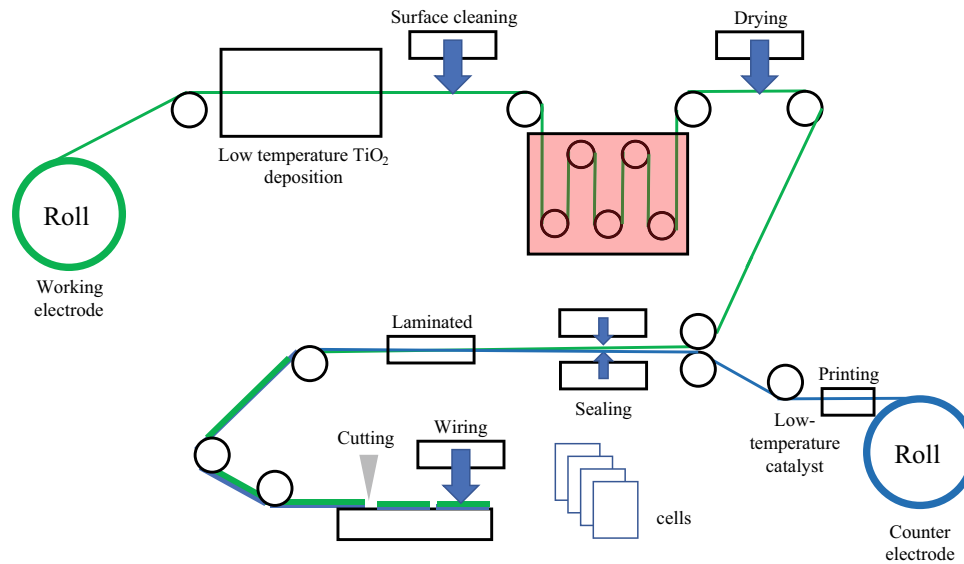


Fig. 8 Roll-to-roll (R2R) production of solar cells using solution-based processing

References

- Alami AH (2020) Introduction to mechanical energy storage. In: Alami AH (ed) Mechanical energy storage for renewable and sustainable energy resources. Springer International Publishing, Cham, pp 1–12. https://doi.org/10.1007/978-3-030-33788-9_1
- Best Research-Cell Efficiency Chart. [Online]. Available: <https://www.nrel.gov/pv/cell-efficiency.html>
- Dale M, Benson SM (2013) Energy balance of the global photovoltaic (PV) industry—is the PV industry a net electricity producer? *Environ Sci Technol* 47(7):3482–3489. <https://doi.org/10.1021/es3038824>
- Fialka J (2016) Why China is dominating the solar industry. *Scientific American*. <https://www.scientificamerican.com/article/why-china-is-dominating-the-solar-industry/>
- International Renewable Energy Agency (2020) Renewable power generation costs in 2019
- Jäger-Waldau A (2018) Snapshot of photovoltaics—February 2018. *EPJ Photovoltaics* 9:6. <https://doi.org/10.1051/EPJPV/2018004>



First-Generation Photovoltaics: History and Conventional Manufacturing

Abdul Hai Alami[✉], Shamma Alasad[✉], Haya Aljaghoub[✉],
Mohamad Ayoub[✉], Adnan Alashkar[✉], Ayman Mdallal[✉],
and Ranem Hasan[✉]

Abstract

The conversion of solar energy into electricity has been sought since the 1800s. The augmentation of the once electrochemical system as a solid state device went hand-in-hand with the development of semiconductors. These semiconductors are made from ultra-fine silicon material that were doped with modifiers to make them behave as either positively or negatively charged materials. In this chapter, a brief history of PV manufacturing is presented, highlighting the proliferation of PV technology in the energy market over the years. A life cycle analysis (LCA) that will help in arriving at better PV device structure with recyclability and energy consciousness in mind.

1 Introduction

The development of photovoltaic solar cell technologies has been influenced by two strongly correlated factors: technological availability and economy. It is well known that advances in silicon-based photovoltaics were ushered by the

experience already available from the development of semiconductors used in printed circuit boards for computers and microcontrollers. The silicon feedstock was excavated, refined, processed and then refined even more to achieve a “nine nines” or 9N purity required for semiconductor purity. The N being the total number of nines in the purity quote (99.999999%). Semiconductor silicon requires a purity of at least nine nines and purities between five and seven nines are acceptable in the photovoltaic industry. Since device performance is a strong function of materials that make it up, lowering the energy required to convert feedstock into wafers while still maintaining pertinent costs at minimum is important. This can only be achieved by mass-scale production that guarantees maximum quality and lowest prices by the economy of scale.

An example of the declining prices per kilowatt-hour (kWh) is the installations at Mohammed Bin Rashid Solar Park (MBRSP) that belongs to Dubai Electricity and Water Authority (DEWA) in Dubai, United Arab Emirates (DEWA 2019). Phase one was announced in 2013 and was planned to generate 13 MW of electricity using silicon photovoltaic panels. The progress continued with phases two and three in 2017, phase four in 2018 and phase 5 in 2021. A 1GW of installed power is currently installed for the latter phase. The goal is to provide around 5GW of power from photovoltaic panels by 2030, in line with the UAE strategic energy initiatives. The project achieved record savings in carbon emissions as well as prices per kWh. The lowest levelized cost of electricity (LCOE) of 2.4 US cents per kWh for the 250 MW photovoltaic solar panels technology was announced for the fourth phase and has reached less than 1 US cent for the fifth phase. A more detailed information on this massive project can be obtained from the DEWA website (dewa.gov.ae). Some of the milestones and data of Phase 3 are shown in Fig. 1.

A quite telling graph about the market share and price of a Watt of electricity produced by silicon photovoltaic modules is shown in Fig. 2. China has entered the

A. H. Alami (✉) · H. Aljaghoub · M. Ayoub · A. Mdallal ·
R. Hasan
University of Sharjah, Sharjah, United Arab Emirates
e-mail: aalalami@sharjah.ac.ae

H. Aljaghoub
e-mail: haljaghoub@sharjah.ac.ae

M. Ayoub
e-mail: mohamad.ayoub@sharjah.ac.ae

A. Mdallal
e-mail: ayman.mdallal@sharjah.ac.ae

S. Alasad · A. Alashkar
American University of Sharjah, Sharjah, United Arab Emirates
e-mail: g00070854@aus.edu

A. Alashkar
e-mail: b00028197@alumni.aus.edu

Fig. 1 Schematic of the progress of phase 3 of Mohammed Bin Rashid Al Maktoum Solar Park (DEWA 2019)

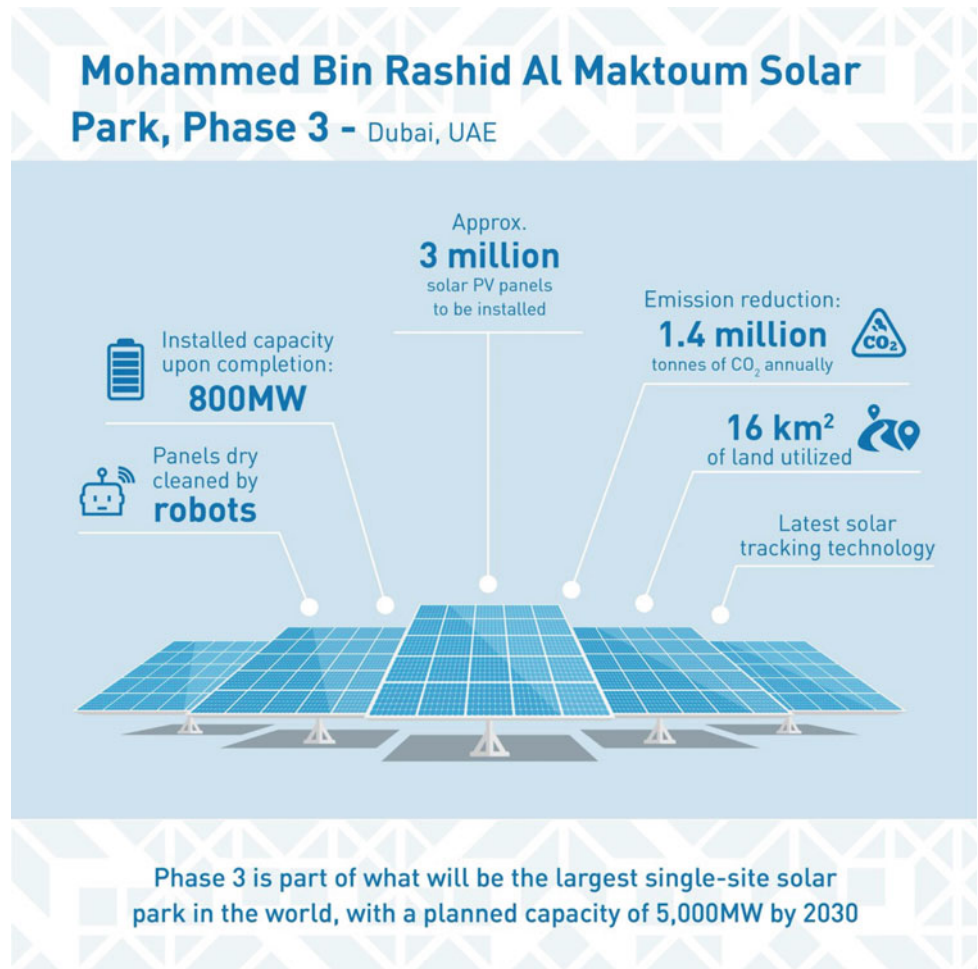
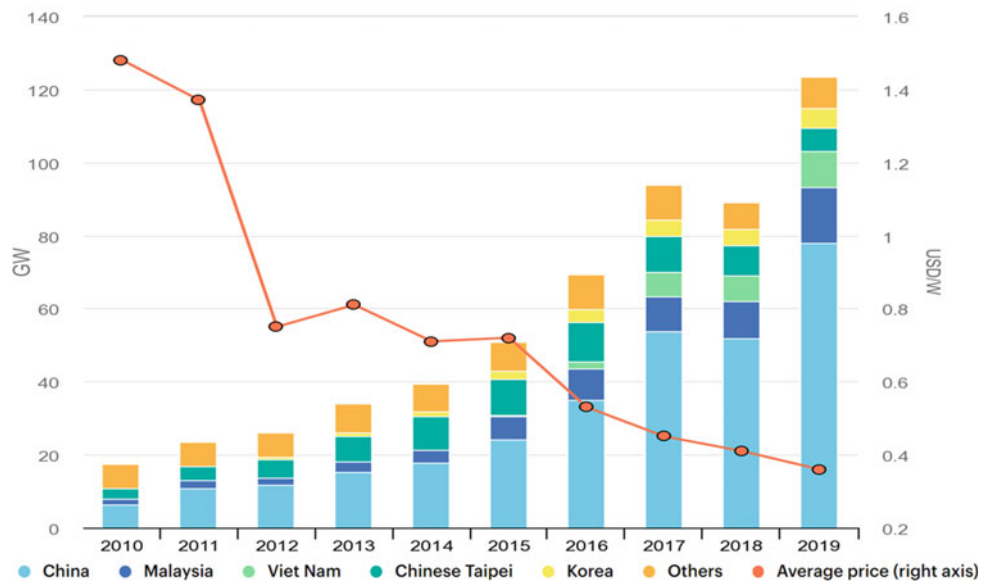


Fig. 2 Solar PV module shipments by country of origin (IEA 2019), 2012–2019, IEA, Solar PV module shipments by country of origin, 2012–2019, IEA, Paris <https://www.iea.org/data-and-statistics/charts/solar-pv-module-shipments-by-country-of-origin-2012-2019>



production market around 2008, and by 2010, the price per kW has decreased in a scale similar to the increase of their market share, that is in excess of 71% by 2019.

A useful analogy between silicon made for solar cells and microchips can be constructed in light of Moore's law. It is an expert prediction made by Intel co-founder Gordon Moore in 1966 which states that the number of transistors that can be placed on a chip will double every two years. This has held true for decades for microchips. And since there is a similarity between the manufacturing technologies in microprocessors and photovoltaics, an equivalent of Moore's law in terms of price/energy can be inferred from data like the one shown in Fig. 2, but this will be left for the mathematicians to quantify.

The concept of innovating a technology or a set of technologies to allow the world to remain connected to electrical power is strongly related to the development of photovoltaic technologies. This is a matter of survival for humanity and not a mere luxury. Photovoltaic technologies permit the direct conversion of solar radiation into electricity with no phase transformations of a working fluid, moving parts, extreme thermal gradients, or noise. Figure 3 depicts the global energy use per capita in 2013 (Bank 2013). Although the information would seem dated, it is data from after 2007 which was a significant year for technological development when the smart phone was introduced. Years after 2007 have witnessed a surge in demand for electricity to charge and recharge smart phones along with their accessories (e.g., wireless routers, smart watches, battery banks). Although the biggest consumers are First World countries such as Europe, Australia and North America, a strong trend is emerging in the Middle East. The Middle East owns large reserves of fossil fuels, and it is understandable that they require extensive energy to power air conditioning most of the year and thus justifying their large electricity requirement. There is also the growing population with multiple smart devices for a COVID19-enforced educational paradigm shift. For Middle Eastern countries, however, there are also ample opportunities presented by being located in the Sun Belt where unimpeded solar irradiance falls 330 days per year over acres of uninhabitable open desert lands (Alami 2020). This is a good reason for locating MBRSP where it is and why it is most likely to succeed.

Solar harvesting opportunities are further highlighted when considering the impact of having reliable connection to electricity on the human development index (HDI). Figure 4 shows this very correlation, where the upper left corner is the most sought after quadrant, indicating intrinsic human development at minimal energy consumption requirements. It can be seen that most developing countries have achieved neutrality in consumption but at the expense of having acceptable HDI. Developed countries occupy central

locations of this map (see the USA and Germany), while Middle Eastern countries have a relatively high HDI but are among largest consumers of energy. With the focus of countries like the UAE on renewable energy in general and photovoltaic technologies in particular, it is promising to observe them capitalizing solar energy utilization to move toward the second quadrant of the curve, since they are as rich in sun as they are in oil and gas. Also, spreading awareness among younger generations is made easier once these generations witness arrays of PV panels spread over tens of kilometers in the desert, powering their gadgets for education and entertainment.

2 PV Technologies Introduction and Proliferation

Photovoltaic technologies have provided a new effective alternative for energy conversion to replace traditional means. Utilizing solar photovoltaic energy to directly produce electricity can augment other sources of renewable energy, such as wind, solar-thermal or hydro-energy. The discovery of solar PV technology as we know it in the early 1950s and its evolution from the semiconductor industry led to the huge success of implementing and commercializing this technology.

This growth of silicon solar PV cell technologies, exploiting nearly 85% of the PV market, can be seen in Fig. 5 (Mehta 2010). The reasons behind the increase of silicon-based technologies in prominence are its wide abundance, non-toxicity, high conversion efficiency, enhanced energy payback time, and durability. Furthermore, the continuous reduction of material and manufacturing costs have made crystalline silicon occupy the top position in PV market. Thin-film technologies represented by copper-indium-gallium-di-selenide (CIGS), cadmium telluride (CdTe) and amorphous silicon (a-Si) can also be seen in Fig. 5, although their collective contribution is around 13%. These thin-film technologies were pursued to achieve lower manufacturing costs of modules but at the cost of sacrificing cell efficiency. Efficiency is lost with light absorption deficits due to significantly lower cell thicknesses associated with less material used. The reduction in cost and material waste, however, has been significant.

For silicon-based technologies, the solar cell construction involves a compatible physical, optical and electrical interaction of two oppositely doped silicon wafers. Figure 6 shows a general structure of a simple silicon solar cell. In reality, the cell construction is usually more complex, with numerous layers added to enhance light absorption or reduce recombination of charged species. The solar cell acts in a similar fashion but as the reverse to a P/N junction diode that

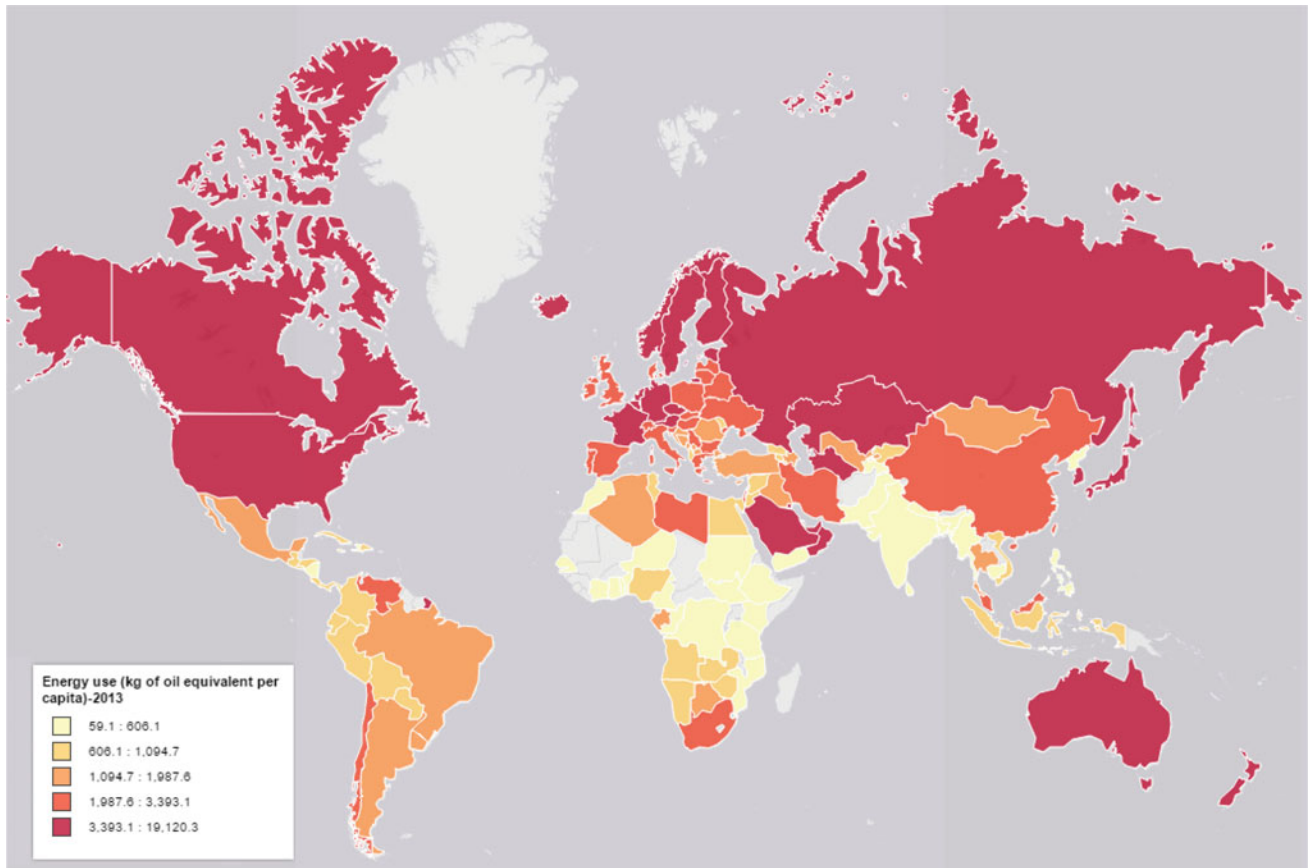
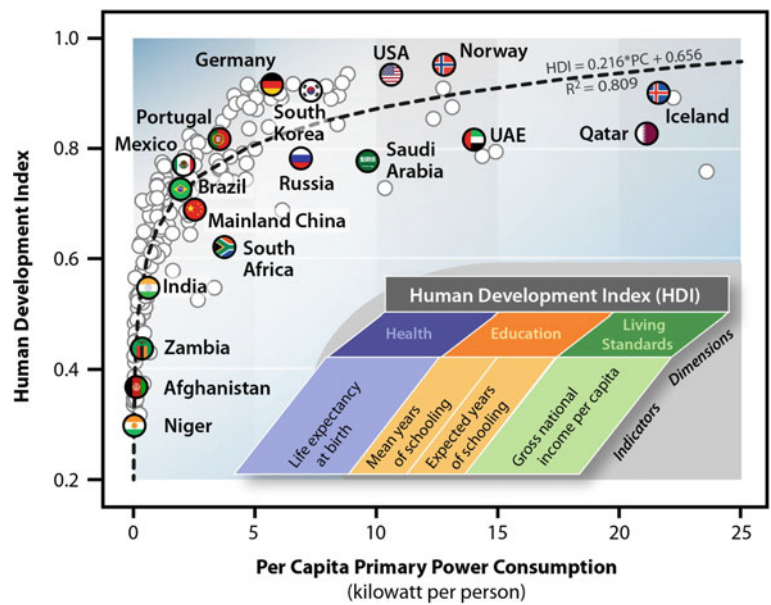


Fig. 3 Energy use per capita in 2013 (Bank 2013)

Fig. 4 Human development index versus per capita electricity use (Dale 2014)



includes embedded metal materials on the electrode front side to avoid penetration of direct solar irradiation. The physical size and shape of a solar cell should allow for

a maximum surface area facing illumination while keeping losses due to contact resistance and recombination to a minimum.

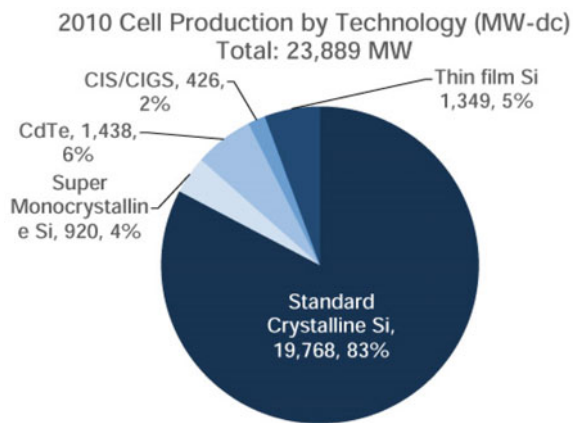


Fig. 5 Module production by PV technology (Mehta 2010)

To maintain the development with respect to manufacturing simplicity and commercial competitiveness, the PV industry relies on two essential parameters: (i) maximizing the energy conversion efficiency and (ii) minimizing costs associated with cell and module manufacturing. Whenever these two characteristics breakeven, energy production from PV would be equivalent to common electricity generation methods with all advantages mentioned before (Bohra 2014).

3 History of Manufacturing Technology

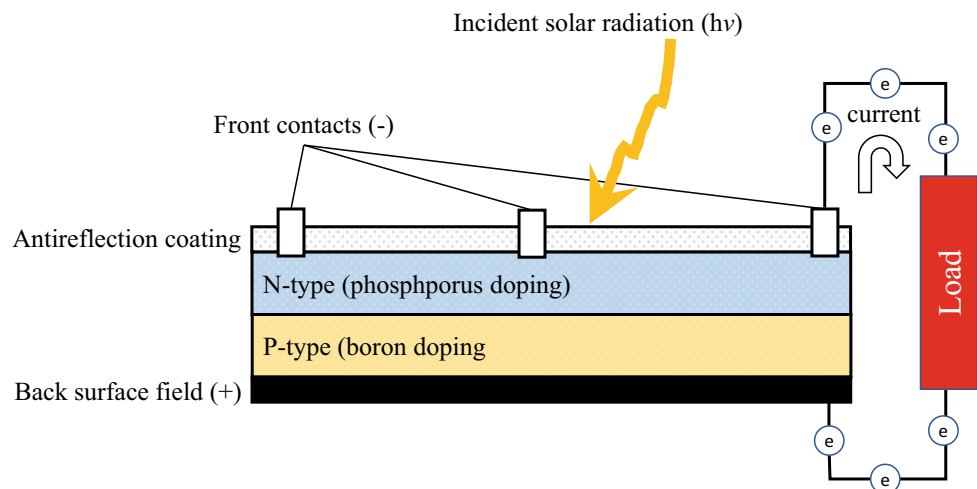
Photovoltaics history goes back to the nineteenth century, since the first operative electrochemical PV device was made by Edmond Becquerel in 1839 (Becquerel 1839). He covered electrodes with light-sensitive materials (e.g., silver chloride and silver bromide) and also used platinum as shown in Fig. 7a. The next significant device idea was made by Adams and Day by investigating the selenium effect on

harnessing solar energy in 1876 (Adams and Day 1877), shown in Fig. 7b. They manufactured the device in a glass tube by inserting a selenium cylinder with platinum electrodes pushed at each end of this cylinder. Electric current was generated once the selenium material interacted with light (Adams and Day 1877). Following this, Fritts in 1883 manufactured a layered device by melting Se on a metal substrate and placing a silver or gold leaf on top as a contact with an area of approximately 30 cm^2 . The current generated can either be stored in storage batteries or transmitted for usage as shown in Fig. 7c. It is worth noting that Fritts was the first to manufacture a solid state PV and paved the way for future development of solar cells. In the twentieth century, Grondhal has built and tested another solid state device from a combination of cuprous oxide, copper and lead in 1927 (Grondahl 1933). As seen in Fig. 7d, the junction was made by sputtering the metals in order to control the size of the resulting grid.

The emergence of modern photovoltaics began in 1954, when scientists coincidentally observed that *P/N* junction diodes produced a voltage while the light was turned on. As a result, a 6% silicon *P/N* junction solar cell was reported. Another group recorded a solar cell with the same efficiency based on thin-film heterojunction using $\text{Cu}_2\text{S}/\text{CdS}$ in the same year. One year later, 6% GaAs solar cell was obtained (Jordan et al. 2020).

Photovoltaics found strong utilization in space applications as well. The tension in most space missions peaked until the photovoltaic modules have unfolded and started providing power busbars with electricity. As early as the sixties, Si PV cells were used by the US space program for powering satellites, Li-doped Si was utilized for radiation effects and radiation-tolerant devices. In the 1980s, the potential of PV implementation in industry began to grow, as the manufacturing facilities for using Si wafer *P/N* junction were growing to produce PV modules in USA, Japan and

Fig. 6 Structure of a p-n junction solar cell



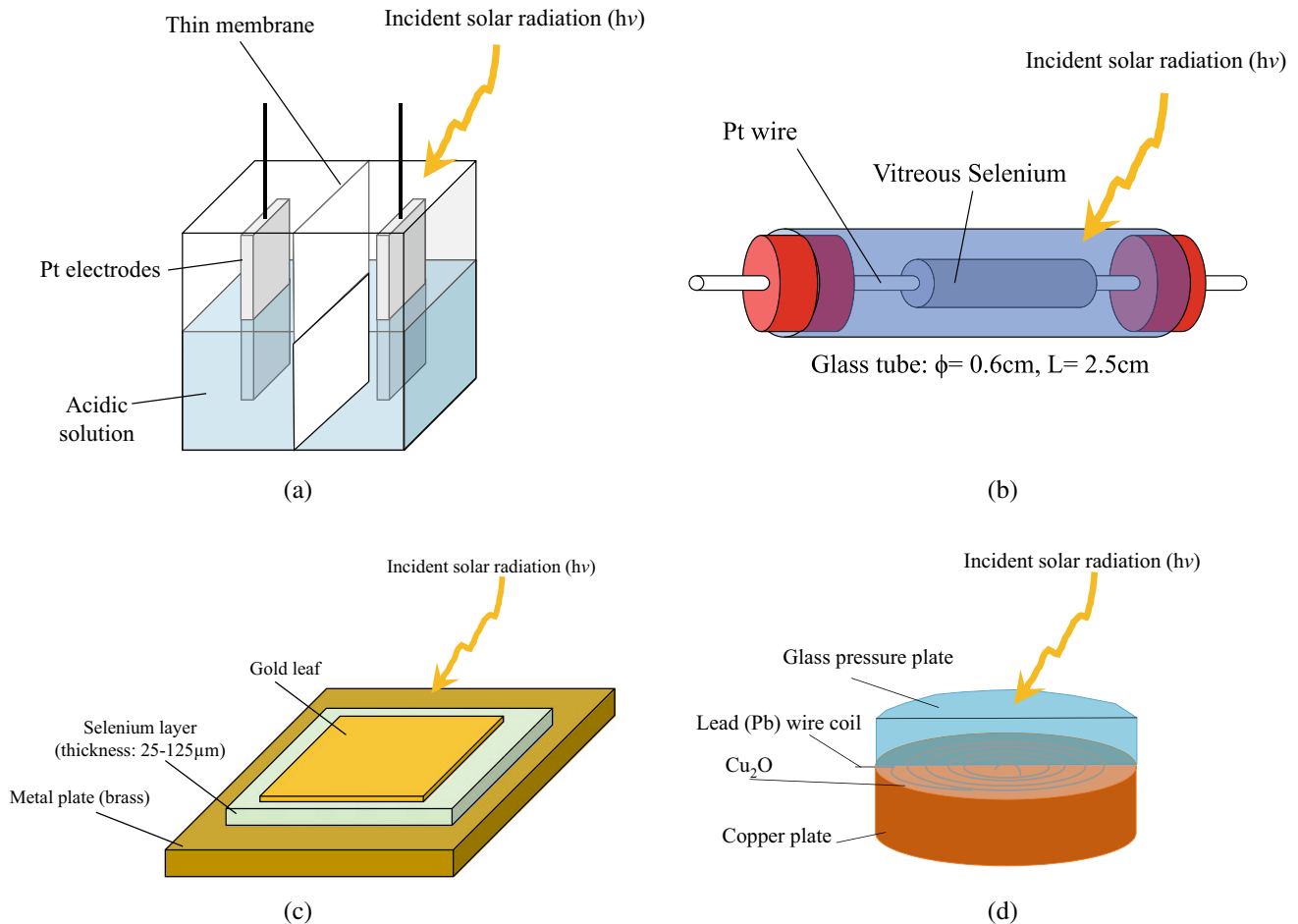


Fig. 7 Early photovoltaic devices through history: **a** E. Becquerel photoelectrochemical cell circa 1839, **b** Adams and Day investigation of photoelectric effects in selenium circa 1876 (Adams and Day 1877),

c Fritts thin-layered selenium-based photovoltaic device circa 1883 (Fritts 1883) and **d** Grondahl-Geiger copper-cuprous oxide photovoltaic cell circa 1927 (Grondahl 1933)

Europe. New technologies started to extend from governments, universities and laboratories into mainstream production and applications.

4 Harmonizing Materials and Manufacturing Processes

Different semiconductor materials candidates are used in PV fabrication. Silicon is most widely as its optical and electrical (semiconductor) properties give it a unique niche. The material is abundant, its bandgap (a concept that will be thoroughly explained later) is fit to the peak incident solar radiation, and energy conversion and solar cell manufacturing processes are mature. On the other hand, starting up a manufacturing facility that refines silicon into a high purity version amenable to doping is a costly process from a financial and energy point of view. An extremely large number of wafers have to be produced (refined, doped,

wired, assembled and encapsulated) to achieve a profitable working model. In terms of dollar-per-Watt, first-generation solar cells are considered the most successful and thus are more widely used compared to all other generations combined.

Silicon technologies are divided into three groups: (i) monocrystalline silicon (m-Si or mono-Si), (ii) polycrystalline silicon (poly-Si or multi-Si), and (iii) thin-film amorphous silicon (a-Si). The latter belongs to thin-film (2nd generation) technologies rather than first generation. Monocrystalline silicon color is usually black or gray and fabricated from pure monocrystalline silicon; hence, they exhibit higher efficiencies and costs. Ingots of multi-crystalline silicon are used for manufacturing polycrystalline PV cells. This type offers less costs but less effective. Amorphous silicon has to be grown on a substrate that hosts thin uncrystallized silicon materials attached to it, allowing cells to be comparably thin. Amorphous silicon cells are reddish-brown or black hues.

Power conversion efficiencies (PCE) obtained from these silicon solar cells vary and depend on the cell construction, size and possible contamination or defects. Monocrystalline solar cells have efficiencies in the range of 16 and 24%. Polycrystalline cells have efficiencies between 14 and 18%. The power per unit area differs between 75 and 155 W_p/m^2 for these two cells. For amorphous cells, the efficiency changes from 4 to 10%, with 40 to 65 W_p/m^2 . The development of various types of PV cells other than the conventional silicon-based PV cells are being under continuous improvement to enhance the power efficiency, in addition to reduction of the manufacturing, operation, and maintenance costs of the solar cells.

As will be explained in the next chapter, various technologies are deployed in industry to produce pure electronic grade silicon. To achieve high purity, silica is reduced with coke (petroleum coke) at high temperature for production of 98% pure metallurgical grade silicon. For further purification, the energy-intensive Siemens technique is extensively employed, which requires production and distillation of trichlorosilane (TCS). Hydrogenation of TCS using hydrochloric acid (HCl) catalyst process occurs at high temperature (1150°C) and presented for activation of polysilicon growth on the silicon rods surface that are located inside Siemens reactors. The rods are then broken into polysilicon pieces. Fluidized bed reactor (FBR) is a technology that produces polysilicon granules, this process utilizes a cone-shaped vessel to fluidize small seed particles of crystalline silicon, with a fluidizing gas (hydrogen) flowing upward to suspend it. A purified layer of crystalline silicon accumulates when the required decomposition temperature of silane is attained, and its size allows silicon granules to fall and be collected at the bottom of the cone. Despite of utilizing reactant gases and consuming energy; this technology is considered efficient. Melting the polysilicon has another advantage which allows FBR granules to be fed simultaneously in Czochralski pullers to carry on three daughter ingots instead of loading polysilicon chunks in a single batch process. Technical issues that involve heating fluidized beds have restricted the ability of supplying FBR materials.

Development of wire-saw technology allows for more wafers per unit volume by producing thick wafers of 180 μm . Although wafer-sawing Kerf production could be recycled, preventing the waste is more beneficial. Emerging technologies like edge-defined film-fed growth (EFG) and string ribbon silicon technology can produce 100-mm-wide and 300- μm -thick wafers substituting the wire-saw technique. Solar cells manufacturing using Kerfless wafers, or ultra-thin silicon ribbons, are also under development. While investments in these technologies have added to the cost, enhanced energy conversion efficiencies and improvements in the process have counterbalanced the initial investment.

Ultra-thin silicon (ut-Si) technology is another technique that was considered which involved the absorbing silicon layer with a thickness of 5–50 μm . The few approaches deployed were heteroepitaxial growth that was followed by lift-off, coating amorphous silicon followed by thermal recrystallization, using stress-induced lift-off to peel ut-Si sheets from silicon ingot. Preserving high-performance and cost-effective production with mechanical handling of wafers is a challenge associated with ut-Si wafers.

While these technologies are effective for silicon-based technologies, the large initial investment prohibits competition from even entering the market. This is a main reason why thin-film technologies were pursued, where instead of starting from silica, different precursors, deposition techniques and process parameters can be tuned to arrive at the sought cell structure. As will be discussed later in the book, such technologies allowed researchers to test new materials and processes to arrive at efficient cells without having to make a risky investment. Processes, such as chemical vapor deposition (CVD), spin-coating, slot-die deposition, screen-printing, have emerged to handle second and third generations of photovoltaics and attempt to reach its performance level and stability. Granted, that the road is still long, but the various permutations of materials, precursors (solid, gas or liquid) as well as processing techniques hold the promise to arrive at efficient solar cells with low energy and economic expenditure and can last as long as conventional silicon cells.

5 Life Cycle Analysis of Photovoltaic Technologies

Life cycle analysis (LCA) can be defined as a standardized method or a framework that is used to evaluate the various footprints that certain products or technologies bear on the environment. The goal behind an LCA is usually to optimize the processes behind products to adhere to environmental regulations set a by governments and meet the market demand with the lowest environmental impact possible. LCA analyzes a material, product/service, a company, or as far as a whole industry and defines a functional unit. A functional unit is a quantity that describes the function of the overall product/system to be analyzed and is considered as a reference basis for all the calculations moving forward in an LCA (Arzoumanidis et al. 2020).

An LCA ultimately comes down to the life cycle of a product or a service. It assesses raw material extraction/processing, manufacturing, transportation, usage and end-of-life phases. A product's life cycle is shown in Fig. 8. The first phase, which is raw material extraction and processing, is inevitably accompanied with undesired effects and byproducts that adversely impact the environment.

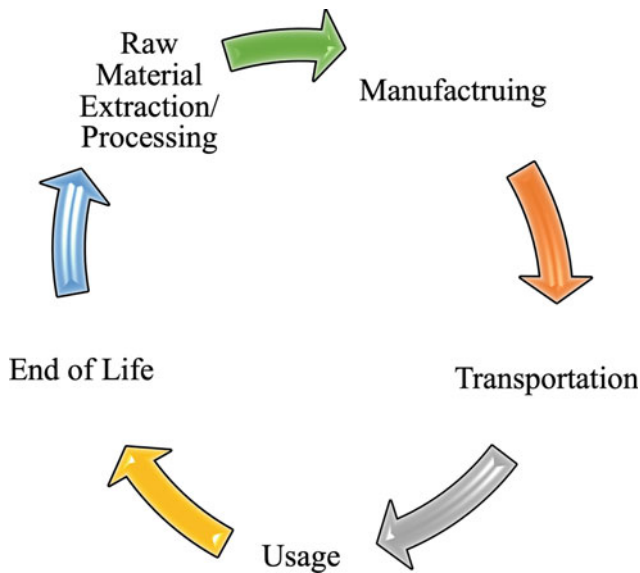
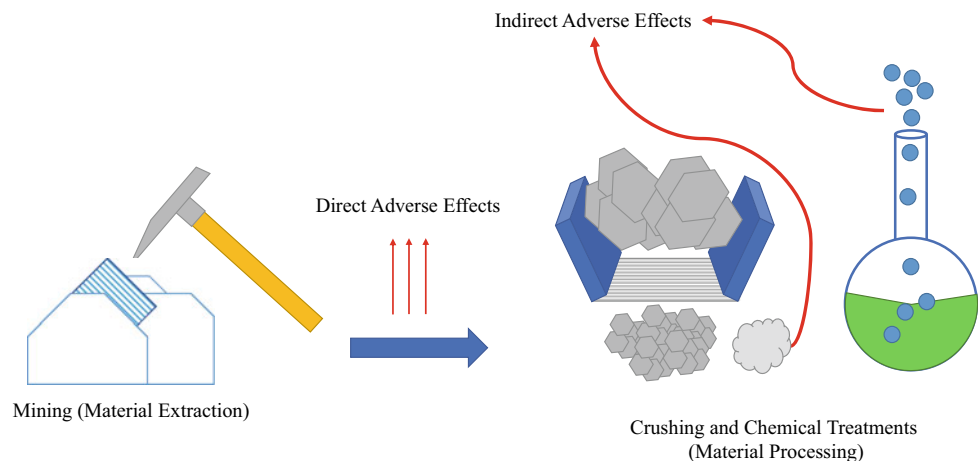


Fig. 8 Life cycle of a product

Direct environmental effects reside within the scope of extraction methods (i.e., mining) and indirectly through processes like crushing, sorting and milling (Teplická and Straka 2020), such as shown in Fig. 9. In first-generation silicon photovoltaics, the raw material extraction and processing is represented by obtaining silica (SiO_2), reducing it to metallurgical silicon, and through Siemens or fluidized bed processes to obtain high-purity silicon, more on that in the following sections.

The second phase, which is the manufacturing process in an LCA, is energy intensive and relates to the end product by subdividing it into the contributing components. In the case of conventional silicon photovoltaics, this stage is carried out via Czochralski or float-zone processes, through which a lot of energy and large quantities of emissions are produced in the silicon melting preparation step, such as shown in Fig. 10.

Fig. 9 Phase 1 of a product's life cycle—material extraction/processing



In the third stage, which is transportation, an LCA takes into account the distance covered and the fuel consumed in the process of transporting base materials to a factory, or an end product to a consumer. Options including air or ocean freight are considered of utmost importance, as this will have an extreme effect on the fuel consumed and the emissions produced during the process, such as shown in Fig. 11.

In the fourth phase, which is usage, components replacement, maintenance, servicing as well as emissions are considered. These factors affect parameters such as the cost of the product or a system and its environmental impact that is manifested in the natural resources usage and the carbon footprint throughout its whole lifetime. For example, in photovoltaic systems, inverters are bound to be replaced halfway through the lifetime of the photovoltaic modules (cost), such as shown in Fig. 12, and water consumption for cleaning is essential to maintain the modules and prolong their time-of-service (environmental impact).

In the fifth and final stage of an LCA, the end-of-life options of a product are explored to reach an optimum choice. End-of-life options manifested in landfill, combustion, recycling or reusing, such as shown in Fig. 13, can have a huge impact on the carbon footprint reduction, given that a lot of subcomponents in products require energy intensive manufacturing processes and recycling them would skip a step with adverse effects in the large scheme of the product.

There are different variations of an LCA, which are cradle-to-gate, cradle-to-grave and cradle-to-cradle, where the LCA ends at a specific stage in each of them. Cradle-to-gate LCA studies a product from the material extraction phase up to the delivery to the consumer. Moreover, a cradle-to-grave assessment takes into account the phases of an LCA up to the end-of-life of a product. Whereas a cradle-to-cradle LCA studies the whole life cycle of a product.

Fig. 10 Phase 2 of a product’s life cycle—manufacturing

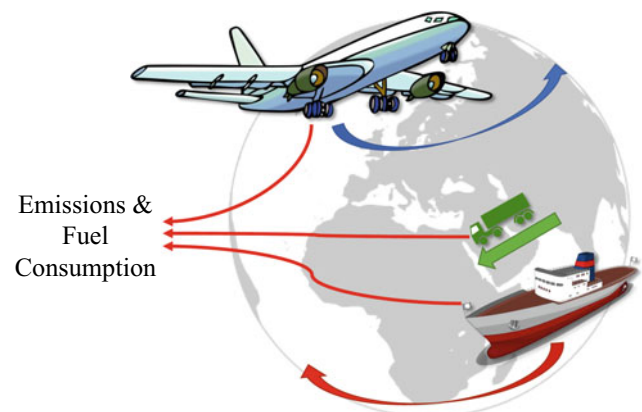
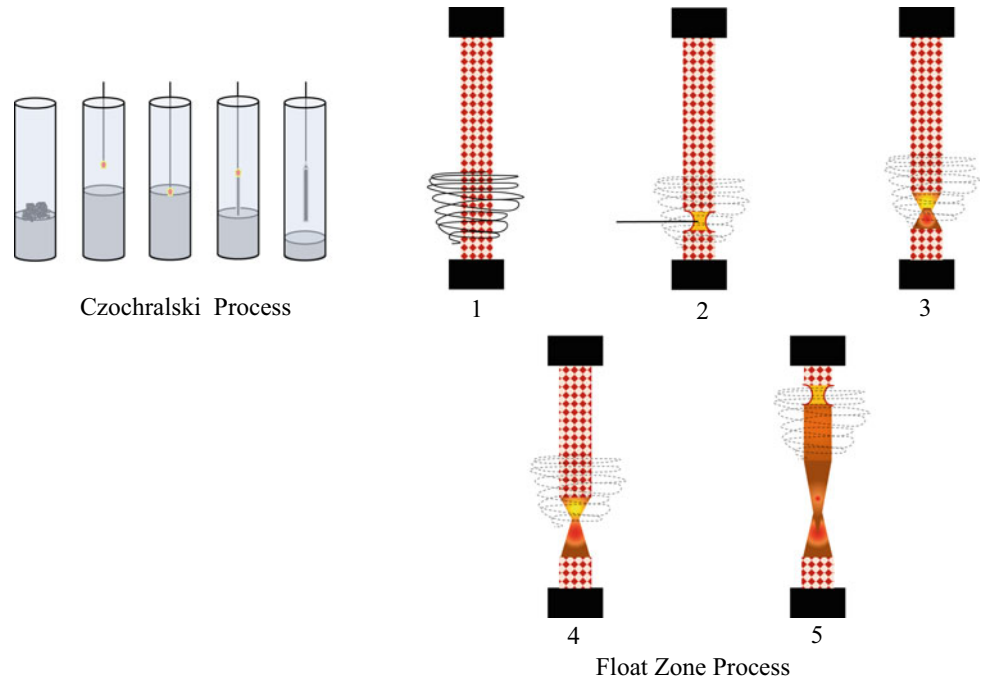


Fig. 11 Phase 3 of a product’s lifetime—transportation (Ship—Wikipedia 2022)—(globe- Wikipedia 2022)

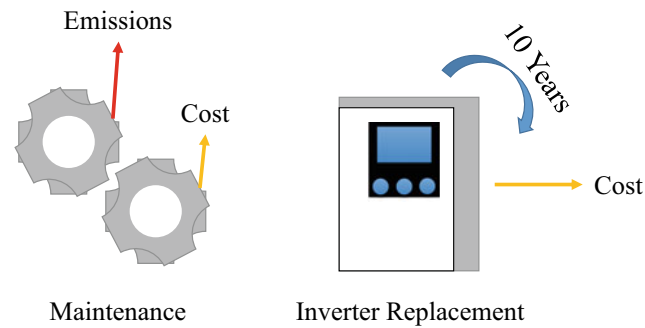


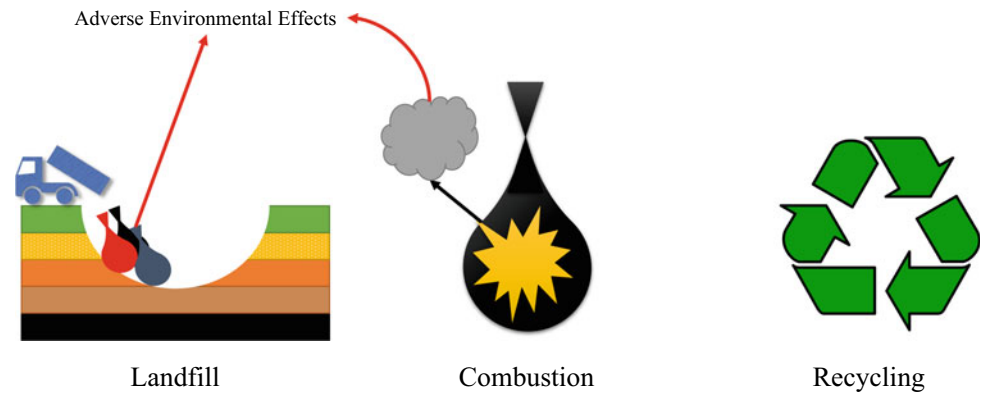
Fig. 12 Phase 4 of a product’s lifetime—usage

5.1 PV Systems Components and Technologies-To-Be-Analyzed

Although solar photovoltaic modules are considered the crowning jewel of solar power harnessing systems, there are other components that play vital roles to ensure smooth operations and outputs. Solar modules need to be mounted on sturdy structures. Charge controllers must be used in stand-alone systems to control the output to loads as well as energy storage subsystems. Moreover, given that the output of solar photovoltaic modules is direct current (DC), inverters must be utilized in grid connected systems. This variety of components, that are known as the balance of the system (BOS), widens the scope of an LCA and elevates the study to cover more aspects when it comes to these systems (Muteri et al. 2020). In a given LCA, the study is overseen by ISO (The Revision of ISO Standards 14040–3—ISO 14040 2005) and EU-specific (European Commission 2011) standards and guidelines. LCAs are carried out based on standardized inventory data, mainly Ecoinvent (2022) as well as IEA PVPS 2015 (Frischknecht et al. 2015), which refer to silicon PV production dating back to 2005 and 2001, respectively.

Mounting structures are used to filter out factors like wind, soil disruptions and any external factor that can physically affect the orientation of solar photovoltaic modules. They can be used to accurately set the tilt angle of solar

Fig. 13 Phase 5 of a product's lifetime—end of life



modules for an optimized harnessing condition (An Overview to Solar Panel Mounting Structures—Energy Company in Pakistan 2022).

Charge controllers are used in solar systems with a very important purpose, which is to prevent batteries from overcharging/discharging and to protect the loads from current surges. Storage systems, mainly batteries, rarely recover from overcharging/discharging incidents (High Efficiency Plants and Building Integrated Renewable Energy Systems 2019), so a charge controller can severely affect batteries' lifetime and hence the conclusion of an LCA.

Storage systems are used to overcome the uncertainty that accompanies solar technologies and to ensure that the loads are fed with power regardless of whether solar irradiation is available at the time or not.

Silicon PV module design, glass-backsheet (G-BS) or glass-glass (G-G) heavily affects the LCA of a given system. It is projected that within 2030, a 30% share of the silicon solar PV market will be attributed to the G-G module design (Fischer et al. 2021). Moreover, the G-G design protects the solar PV module from water vapor and shows a reduction in the cells' mechanical stress as well as a lower degradation rate (Zhang et al. 2015), which is a crucial parameter in the lifetime energy calculation of a solar PV module, such as shown in Eq. 1 and Fig. 14, where T is the lifetime in years, DR is the mean annual degradation rate, I is the global tilted average annual solar irradiation $\text{kWh}/(\text{m}^2\text{year})$, A is the surface area, η is the solar PV module efficiency and PR_i is the initial performance ratio (Müller et al. 2021). A G-G design has the leisure of omitting the aluminum frame, which reduces the cost of solar PV modules extensively and lowers the ozone depletion potential.

$$E_{\text{total}} = \sum_{t=1}^T (1 - DR)^t \times I \times A \times \eta \times PR_i \quad (1)$$

Solar power harnessing technologies is a vast topic, and it contains all three generations of solar photovoltaics which are first-generation crystalline silicon, second-generation thin films and third-generation dye-sensitized solar cells

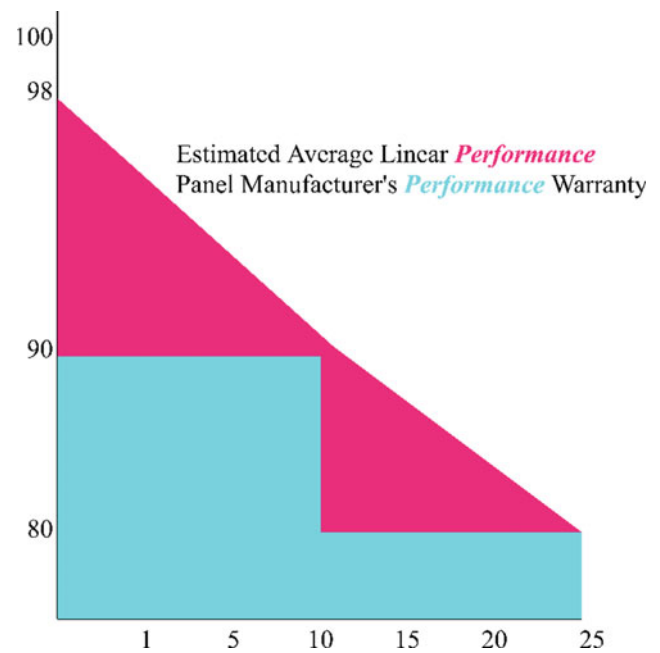


Fig. 14 Silicon solar PV modules degradation with time (How Long Do Solar Panels Last 2022)

(DSSC), organic (OPV) and perovskite solar cells (PSC). Each of these technologies set a unique direction from processing, manufacturing and usage conditions. More importantly, these technologies vary in efficiencies, which directly affects the energy consumption per unit manufacturing, as well as emissions and most importantly cost (Muteri et al. 2020).

5.2 Energy Impact and Emissions of Silicon Solar PV Technologies

Life cycle analysis on solar PV systems can be traced back to the 1970s, in which cradle-to-gate analysis took place. These studies considered the energy payback time (EPBT), which is calculated using Eq. 2, as well as environmental

impacts on the manufacturing and processing of these technologies. To present an accurate energy and environmental impact analysis regarding PV technologies, it is important that the information is obtained over a sufficient period of time on a specific geographical location that has implemented these technologies, one of which is the country of China. Given the large area that China covers, the solar resource incident on it varies with the location (949- 2118 kWh/m² yearly) that a solar PV system is placed in, just as shown in Fig. 15. However, according to Fu et al. (Fu et al. 2015), only few studies have considered other implications on the biological toxicity and acidification. In their work, they assessed the life cycle environmental effects on photovoltaics' operations in China. Silicon extraction, ingot growing and processing as well as module fabrication were considered; however, the BOS was excluded given that its effect is not related to the environment. According to Wild-Scholten (2013), the BOS only adds about 3 months of additional EPBT and almost negligible greenhouse emission gasses.

$$EBPT = \frac{\text{Total Primary Energy Demand [MJ]}}{\text{Annual Power Generation} \left[\frac{\text{MJ}}{\text{Year}} \right]} \quad (2)$$

They concluded in their study that the primary energy demand was associated with non-renewable energy sources to produce solar grade silicon cell such as coal firing, which contributes to about 48.5% of the total energy demand. Moreover, crude oil and natural gas were used intensely in the assembly stage of the silicon solar modules, accounting for 25% of the total energy demand. Cell processing and silicon ingots' casting accounted for 19% and 5%, respectively. EPBT according to their study varied between 2 and 6 years when the solar PV systems were installed in first and fifth class areas, respectively. Table 1 provides an overview of the LCA of PV modules focusing mainly on single crystalline silicon (Sc-Si), multi-crystalline silicon (Mc-Si) and passivated emitter and rear cells (PERCs).

According to a study conducted by Fu et al. (2015), the environmental impact of solar PV systems is as crucial to consider as the energy consumption per lifetime. There are

Fig. 15 China Solar Resource (Solar resource maps and GIS data for 200+ countries | Solargis 2022), obtained from the Global Solar Atlas 2.0, a free, web-based application developed and operated by the company Solargis s.r.o. on behalf of the World Bank Group, utilizing Solargis data, with funding provided by the Energy Sector Management Assistance Program (ESMAP)

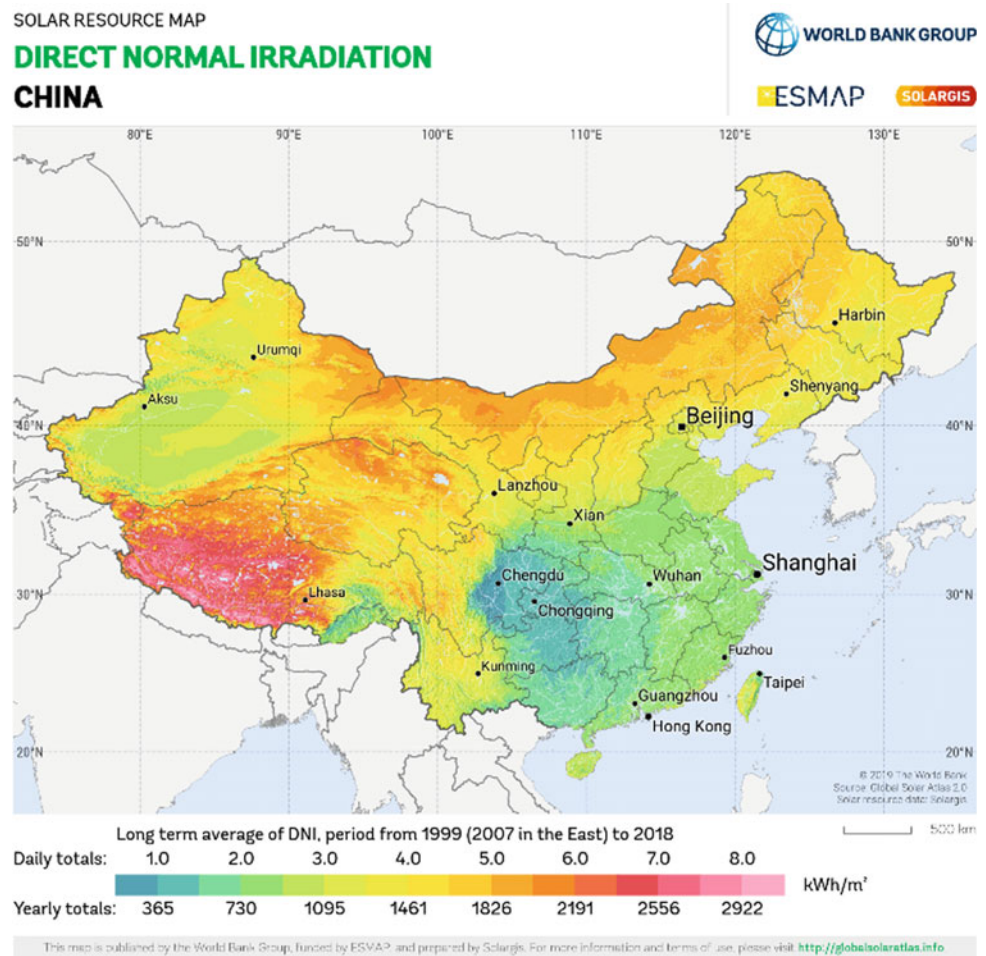


Table 1 A summary of LCA of PV modules

Location	Technology	Module efficiency (%)	Lifetime (year)	GWP of electricity (g CO ₂ /kwh)	References
Europe	Sc, mc, ribbon Si	14	30	45	Alsema and Wild (2005)
Europe, China	Sc and various PV technology	14.8	30	33–81.2	Wild-Scholten (2013)
Europe, China	Sc, mc, ribbon Si	14	30	37.3 (EU), 72.2 (CN)	Yue et al. (2014)
Korea	Sc- and mc-Si	15.96	30	41.9	Kim et al. (2014)
Europe	Sc- and SHJ-Si	19.5	30	25	Louwen et al. (2015)
Europe, USA, China	Sc-, mc-Si, CdTe, CIGS	17	30	28–83	Leccisi et al. (2016)
China	Sc-Si	15.7	25	5.6–12.1	Chen et al. (2016)
China	mc-Si	12.7	25	56.15	Hong et al. (2016)
Europe, China	Sc- and mc-Si	16.4	30	28.5–59.4	Stamford and Azapagic (2018)
Singapore	Mc-Si	16.4	30	29.2	Luo et al. (2018)
China	Sc-Si, PERC cells	18.2	25	20.9	Lunardi et al. (2018)
China, Europe	Sc-Si, PERC half cells	20.1	30	16.5–45.3	Müller et al. (2021)
China, Europe	Sc-Si, PERC full cells	19.8	30	12.9–29.9	Müller et al. (2021)

different aspects to consider while studying the environmental impacts, which are the acidification potential, eutrophication potential, global warming potential, human toxicity potential, ozone layer depletion potential and photochemical ozone creation potential. The acidification potential, which is referenced to the equivalent kg SO₂ production per kWh, was approximated to be 4.27×10^{-4} . The eutrophication potential, which is the equivalent production of kg PO₄³⁻/kWh, was estimated to be 4.23×10^{-5} . The global warming potential was estimated to be 5.09×10^{-2} kgCO₂/kWh. The human toxicity potential, the ozone layer depletion potential and the photochemical ozone creation potential were 1.76×10^{-2} kgDCB(equivalent)/kWh, 3.02×10^{-9} kgR11(equivalent)/kWh and 2.69×10^{-5} kg-ethene (equivalent)/kWh. 73.4% of the acidification potential, 45.6% of the eutrophication potential and 50% of the global warming potential were attributed to the high electricity consumption in the phase of solar grade silicon production, given that Chinese electricity is mainly produced by coal-fired power plants. The human toxicity potential is 74.4% due to the heavy metals' emissions to air, which is attributed to steam and electricity consumption in the whole lifetime of solar PV modules' production. The ozone depletion potential is 67.8% due to the production of the aluminum frames that are used in the assembly phase of a solar PV module, where an electricity-intense process takes place. The photochemical ozone creation potential had a main contributor, which is sulfur dioxide standing at 56.1%, also due to electricity usage during the production of solar

modules. To put things into perspective, almost all adverse effects are caused mainly by the electricity usage during the processing of metallurgical silicon into solar grade silicon, and the manufacturing of the solar cells, as well as their assembly, which make up the first two stages of an LCA. The authors covered different aspects of emissions and determined the processes that demand the most energy as well as their sources for a solar power system in China.

References

- Adams WG, Day RE (1877) The action of light on selenium. In: Proceedings of the royal society, London, vol A25
- Airplane clipart—Wikipedia, https://ar.wikipedia.org/wiki/%D9%85%D9%84%D9%81:Airplane_clipart.svg (Accessed 07 Aug 2022)
- Alami AH (2020) Thermal storage. Mechanical energy storage for renewable and sustainable energy resources. Cham, Springer International Publishing, pp 27–34. https://doi.org/10.1007/978-3-030-33788-9_4
- Alsema E, de Wild MJ (2005) Environmental impact of crystalline silicon photovoltaic module production. MRS Proc 895:0895-G03–05. <https://doi.org/10.1557/PROC-0895-G03-05>
- An Overview to Solar Panel Mounting Structures—Energy Company in Pakistan. <https://www.reonenergy.com/an-overview-to-solar-panel-mounting-structures/> (Accessed 07 Aug 2022)
- Arzoumanidis I, D'Eusario M, Raggi A, Petti L (2020) Functional unit definition criteria in life cycle assessment and social life cycle assessment: a discussion. In: Perspectives on social LCA, Traverso M, Petti L, Zamagni A (eds) Cham, Springer International Publishing, pp 1–10. https://doi.org/10.1007/978-3-030-01508-4_1

- Bank TW (2013) Energy use per capita. https://commons.wikimedia.org/wiki/File:World_Map_-_Energy_Use_2013.png
- Becquerel AE (1839) Recherches sur les effets de la radiation chimique de la lumiere solaire au moyen des courants electriques. Comptes Rendus de L'Academie des Sciences 9
- Bohra MH (2014) Process development for single-crystal silicon solar cells
- Chen W, Hong J, Yuan X, Liu J (2016) Environmental impact assessment of monocrystalline silicon solar photovoltaic cell production: a case study in China. *J Clean Prod* 112:1025–1032 <https://doi.org/10.1016/j.jclepro.2015.08.024>
- Dale B (2014) Growing poor slowly: why we must have renewable energy. <https://www.ourenergypolicy.org/growing-poor-slowly-why-we-must-have-renewable-energy/>
- DEWA (2019) Mohammed bin Rashid Al Maktoum Solar Park—a leading project that promotes sustainability in the UAE. <https://www.dewa.gov.ae/en/about-us/media-publications/latest-news/2019/03/mohammed-bin-rashid-al-maktoum-solar-park>
- Ecoinvent—ecoinvent. <https://ecoinvent.org/> (Accessed 07 Aug 2022)
- European Commission—Joint Research Centre—Institute for Environment and Sustainability, International Reference Life Cycle Data System (ILCD) Handbook-Recommendations for Life Cycle Impact Assessment in the European Context. Publications Office of the European Union, Luxemburg (2011)
- Ficheiro: LKW mit Aufleger aus Zusatzzeichen 1048–14.svg—Wikipédia, a enciclopédia livre. https://pt.wikipedia.org/wiki/Ficheiro:LKW_mit_Aufleger_aus_Zusatzzeichen_1048-14.svg (Accessed 07 Aug 2022)
- Fischer M, Woodhouse M, Herritsch S, Trube J (2021) International technology roadmap for photovoltaic (ITRPV). *VDMA EV* <https://itrpv.vdma.org/en/ueber-uns>
- Frischknecht R et al (2015) Life cycle inventories and life cycle assessments of photovoltaic systems. <https://doi.org/10.2172/1561526>
- Fritts CE (1883) On a new form of selenium photocell. *Am J Sci* 26
- Fu Y, Liu X, Yuan Z (2015) Life-cycle assessment of multi-crystalline photovoltaic (PV) systems in China. *J Clean Prod* 86:180–190 <https://doi.org/10.1016/j.jclepro.2014.07.057>
- Globe—Wikipedia. https://en.m.wikipedia.org/wiki/File:Blank_globe.svg (Accessed 07 Aug 2022)
- Grondahl LO (1933) The copper-cuprous-oxide rectifier and photoelectric cell. *Rev Modern Phys* 5
- High efficiency plants and building integrated renewable energy systems. In: *Handbook of energy efficiency in buildings*, Elsevier, pp 441–595 (2019). <https://doi.org/10.1016/B978-0-12-812817-6.00040-1>
- Hong J, Chen W, Qi C, Ye L, Xu C (2016) Life cycle assessment of multicrystalline silicon photovoltaic cell production in China. *Sol Energy* 133:283–293 <https://doi.org/10.1016/j.solener.2016.04.013>
- How Long Do Solar Panels Last? <https://www.paradisepvenergy.com/blog/solar-panel-degradation-and-the-lifespan-of-solar-panels> (Accessed 07 Aug 2022)
- IEA, Solar PV module shipments by country of origin. Report. <https://www.iea.org/data-and-statistics/charts/solar-pv-module-shipments-by-country-of-origin-2012-2019>
- Jordan DC, Marion B, Deline C, Barnes T, Bolinger M (2020) PV field reliability status—analysis of 100 000 solar systems. *Prog Photovoltaics Res Appl* 28(8):739–754 <https://doi.org/10.1002/pip.3262>
- Kim B, Lee J, Kim K, Hur T (2014) Evaluation of the environmental performance of sc-Si and mc-Si PV systems in Korea. *Sol Energy* 99:100–114 <https://doi.org/10.1016/j.solener.2013.10.038>
- Leccisi E, Raugi M, Fthenakis V (2016) The energy and environmental performance of ground-mounted photovoltaic systems—a timely update. *Energies (Basel)* 9(8):622 <https://doi.org/10.3390/en9080622>
- Louwen A, Sark van WGJHM, Schropp REI, Turkenburg WC, Faaij APC (2015) Life-cycle greenhouse gas emissions and energy payback time of current and prospective silicon heterojunction solar cell designs. *Prog Photovoltaics Res Appl* 23(10):1406–1428 <https://doi.org/10.1002/pip.2540>
- Lunardi MM, Alvarez-Gaitan JP, Chang NL, Corkish R (2018) Life cycle assessment on PERC solar modules. *Sol Energy Mater Sol Cells* 187:154–159 <https://doi.org/10.1016/j.solmat.2018.08.004>
- Luo W (2018) A comparative life-cycle assessment of photovoltaic electricity generation in Singapore by multicrystalline silicon technologies. *Sol Energy Mater Sol Cells* 174:157–162 <https://doi.org/10.1016/j.solmat.2017.08.040>
- Mariska de Wild-Scholten MJ (2013) Energy payback time and carbon footprint of commercial photovoltaic systems. *Solar Energy Mater Solar Cells* 119:296–305. <https://doi.org/10.1016/j.solmat.2013.08.037>
- Mehta S (2011) PV news annual data collection results: 2010 cell, module production explodes past 20 GW. *Greentechmedia.com*. <https://www.greentechmedia.com/articles/print/pv-news-annual-data-collection-results-cell-and-module-production-explode-p>
- Müller A, Friedrich L, Reichel C, Herceg S, Mittag M, Neuhaus DH (2021) A comparative life cycle assessment of silicon PV modules: impact of module design, manufacturing location and inventory. *Solar Energy Mater Solar Cells* 230(April):111277 <https://doi.org/10.1016/j.solmat.2021.111277>
- Muteri V (2020) Review on life cycle assessment of solar photovoltaic panels. *Energies (Basel)* 13(1):252 <https://doi.org/10.3390/en13010252>
- Ship—Wikipedia. <https://en.wikipedia.org/wiki/Ship> (Accessed 07 Aug 2022)
- Solar resource maps and GIS data for 200+ countries | Solargis. <https://solargis.com/maps-and-gis-data/download/china> (Accessed 07 Aug 2022)
- Stamford L, Azapagic A (2018) Environmental impacts of photovoltaics: the effects of technological improvements and transfer of manufacturing from Europe to China. *Energy Technol* 6(6):1148–1160 <https://doi.org/10.1002/ente.201800037>
- Teplická K, Straka M (2020) Sustainability of extraction of raw material by a combination of mobile and stationary mining machines and optimization of machine life cycle. *Sustainability* 12(24):10454 <https://doi.org/10.3390/su122410454>
- The Revision of ISO Standards 14040–3—ISO 14040: Environmental management—Life cycle assessment—Principles and framework—ISO 14044: Environmental management—Life cycle assessment—Requirements and guidelines\textbar SpringerLink
- Yue D, You F, Darling SB (2014) Domestic and overseas manufacturing scenarios of silicon-based photovoltaics: life cycle energy and environmental comparative analysis. *Sol Energy* 105:669–678 <https://doi.org/10.1016/j.solener.2014.04.008>
- Zhang Y (2015) Long-term reliability of silicon wafer-based traditional backsheet modules and double glass modules. *RSC Adv* 5 (81):65768–65774 <https://doi.org/10.1039/C5RA11224A>



Silicon Feedstock and Ultra-Refinement

Abdul Hai Alami^{ID}, Shamma Alasad^{ID}, Haya Aljaghoub^{ID},
Mohamad Ayoub^{ID}, Adnan Alashkar^{ID}, Ayman Mdallal^{ID},
and Ranem Hasan^{ID}

Abstract

This chapter focuses on obtaining and refining silicon under the stringent requirements of the photovoltaic manufacturing industry. Starting with the carbothermal process; a well-established manufacturing process of silicon, other processes such as chemical vapor deposition for further silicon refinement are also introduced and their history discussed. Doping processes are also important so these are also discussed in detail.

1 The Carbothermal Refinement Process

Silicon is one of the most abundant elements in the Earth's crust, as it exists in the silica or the silicon oxide (SiO₂) form. Silicon is an essential element in many industries, mainly the microprocessor and solar photovoltaic cells and modules. Pure silicon has to be extracted (reduced) from its oxide form then ultra-refined in order to be useful in aforementioned industries. In addition to the production of solar grade silicon, metallurgical grade silicon is obtained by

acquiring the hyper-pure (more than 99.9999999% pure) silicon form. The hyper-pure form is obtained by devising processing technologies for removing oxygen atoms that are connected to the silicon grain. This allows arriving at what is known as “metallic silicon” that is around 96% pure. Further refinement of the silicon allows doping it with selected elements to control its electric and electronic behavior. This allows for the production of the semiconductor grade silicon and other devices that have become indispensable for everyday life. Silicon refinement for acquiring metallurgical grade silicon is carried out by a carbothermic process. This process involves placing the SiO₂ material in a compatible quartz crucible and subjecting it to energy to break the Si/O bonds. Supplying energy in the form of heat helps in breaking the Si-O₂ bonds, but the amount of heat has to be in the range of 159.8 J/g (melting point of silica), which is substantial and challenging to provide. Thus, an innovative method similar to the one used to extract aluminum from bauxite (aluminum oxide ore) that allows for breaking the Si/O bond is utilized. As will be explained later, the carbothermal process breaks the SiO₂ bonds, and hence a reduction reaction takes place, whereas the carbon atoms replace silicon in bonding with the O₂ atoms resulting in elemental Si as shown in Fig. 1. A crucible containing the SiO₂ is placed within an arc furnace, with retractable graphite electrodes acting as both an electricity conductor and also as a source of pure carbon for the reaction. Once the electric circuit is closed, the graphite electrodes (positive terminal) are lowered enough toward the raw materials of silicon oxide and carbon, and an arc is generated. This arc provides the energy as well as the carbon required for the reaction to proceed. This is the reason behind the name “arc furnace”. The furnace is also utilized to initially heat the carbon (around 1500–2000 °C), then to supply the required amount of energy through the electric arc to break the SiO₂ bonds.

The following chemical reaction represents the carbothermal process:

A. H. Alami (✉) · H. Aljaghoub · M. Ayoub · A. Mdallal · R. Hasan

University of Sharjah, Sharjah, United Arab Emirates
e-mail: aalalami@sharjah.ac.ae

H. Aljaghoub
e-mail: haljaghoub@sharjah.ac.ae

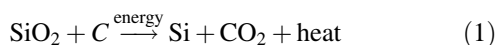
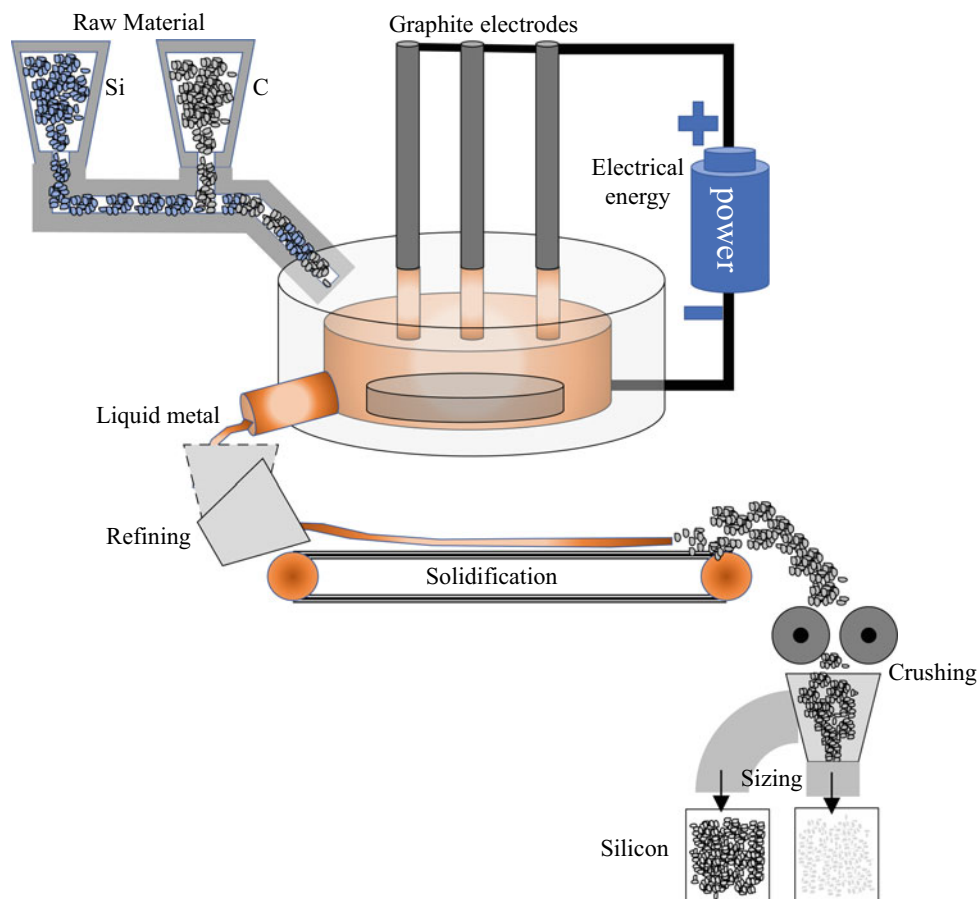
M. Ayoub
e-mail: mohamad.ayoub@sharjah.ac.ae

A. Mdallal
e-mail: ayman.mdallal@sharjah.ac.ae

S. Alasad · A. Alashkar
American University of Sharjah, Sharjah, United Arab Emirates
e-mail: g00070854@aus.edu

A. Alashkar
e-mail: b00028197@alumni.aus.edu

Fig. 1 Carbothermic process of metallurgical silicon refinement



It is evident that elemental silicon is obtained after breaking the SiO_2 bond, carbon dioxide results as well as heat. This heat can and should be recovered by attaching a regenerative cycle to the setup shown in Figure 1. Silicon issues from the crucible in liquid form, however upon pouring and crushing it, chunks of metallic Si are obtained with a purity level of $\sim 96\%$.

2 Silicon Ultra-Refinement

Further refinement to the silicon leads to the production of solar grade silicon (SOG-Si). As a result, the level of purity of the Si should increase from 96% to 99.99999% (5–7 nines succeeding the decimal point). To achieve such purity, specialized processes under pristine environmental control have to be used. This strict environmental control is applied to personnel as well, and thus, it is quite common to see people in full hazmat suits handling silicon and making it ultra-pure.

In general, there are two routes for carrying out the silicon purification and ultra-refinement: (i) chemical metallurgical

purification of trichlorosilane in Siemens reactor or silane in fluidized bed reactor and (ii) electrochemical refinement, involving the dissolution of quartz in fluoride and three-layer electro-refining Si. In both cases, chunks of metallic silicon are digested chemically into a gas then deposited on a substrate that is made of a single crystal silicon material called the “seed crystal”. This approach benefits from the strong cohesive forces between similar materials. The silicon processing is shown in Fig. 2.

The chemical route utilizes trichlorosilane (SiHCl_3) gas to carry the silicon material and decomposes it (deposits it) on the seed crystal. The gas results from the chemical reaction between the silicon chunks and hydrochloric acid in the presence of hydrogen. Silane gas (SiH_4) can also be used, but it is less reactive than when chlorine is added from the reaction with HCl. Silane, dichlorosilane, or trichlorosilane are then used to deposit silicon in either the Siemens process or the fluidized bed reactor. These two processes are well developed and have historically been used to produce ultrapure silicon mainly for microchips and microprocessors for the PC industry. The processes fall under the umbrella of chemical vapor deposition (CVD), a process class that is essential for solar cell making. It is a chemical process that produces high-quality and high-performance solid materials.

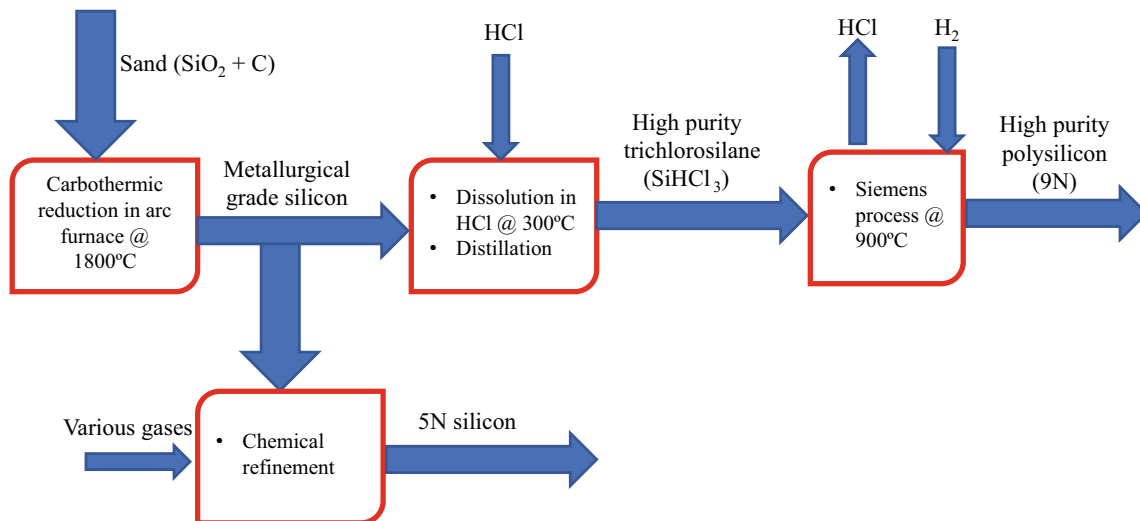


Fig. 2 From sand to high-purity silicon

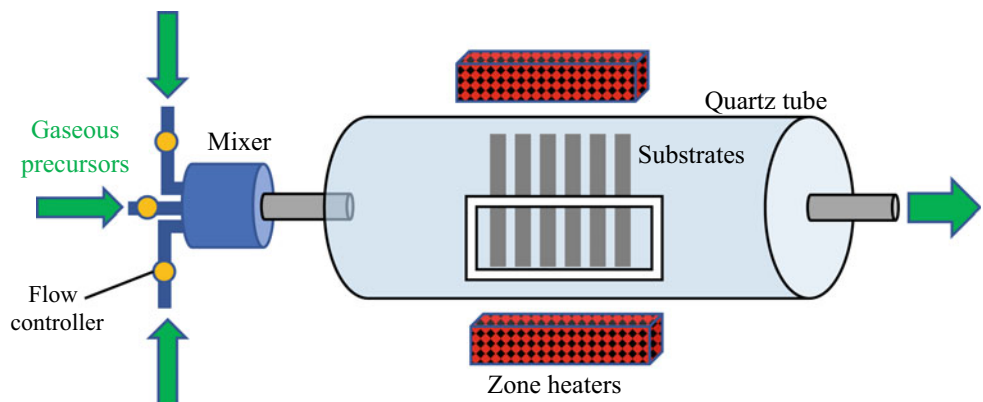
The inputs of the CVD process are gasses, including carrier gasses that will carry the silicon to the substrates. The silicon chunks will first be dissolved with hydrochloric acid (HCl) and carried by hydrogen to the heated substrates. The substrates are added and heated into the tubes that are made up of quartz as shown in Fig. 3 Quartz is a very hard material that is at the same time transparent and heat resistant; hence, it is recommended to utilize it as the designated material of the tube.

Hydrochloric acid dissolves the silicon, which allows the formation of either dichlorosilane (SiH_2Cl_2) or trichlorosilane (SiHCl_3) gases. Hydrogen carries the SiHCl_3 gas through the tube to the substrates. The gasses then come into contact with the heated substrates that are placed within the tube, and the gasses decompose and cover the substrates with silicon. Afterward, a stream of hydrogen is inserted through the tube in order to bond with the chloride. This in return produces HCl gas, which can be collected, recycled, and reused. In general, the CVD process can incorporate any number of gasses which pass through the tube, and the

gasses interact with each other and with the silicon. The silicon is then transported by a carrier gas to the substrates. The substrates are originally made of pure silicon that act as the seed particle which initiates the process of acquiring refined silicon. The carried silicon and gasses are then decomposed onto the silicon substrates. Extra hydrogen flows through the tube to react with chloride and leave the pure silicon on the substrates. The interaction between the hydrogen and the chloride results in the production of HCl gas. The seed particle, made up of pure silicon, can either be manufactured by hand or through a special process.

On an environmental consciousness note, the amount of CO_2 produced and energy utilized in the arc furnace to break the SiO_2 bond is high. Moreover, the production of highly refined silicon does not only require large amounts of energy, but also excessive amounts of HCl acid. Thus, every 4 tons of acid produces 1 ton of silicon. Hence, it is evident that the extensive usage of water, energy, and acids hinders the production of solar cells. The real problem lies in the difference between the amount of energy utilized into

Fig. 3 CVD setup for obtaining highly pure solar grade and semiconductor grade silicon



building the solar cells and the energy produced by the cells. It was found that the amount of energy produced by the module over its lifetime of approximately 25 years will not cover the amount of energy that went into building them. For this reason, it is necessary to search for more efficient ways, that are both environmentally friendly and not energy intensive, to produce PV modules. The current processes to produce PV modules are energy intensive, wasteful, produce excessive amounts of CO₂ emissions and involve the utilization of chemicals and acids.

2.1 Siemens Process

One of the oldest techniques for silicon making, it is basically a CVD technique. It starts with metallurgical silicon with 96% purity as input material from the arc furnace and ends with ultrapure silicon. By injecting hydrochloric (HCl) acid to dissolve the silicon, trichlorosilane (SiHCl₃) gas is generated.

Throughout this process, seed silicon rods made up of highly pure silicon are added as substrates. Hydrogen is added to interact with the chloride in the SiHCl₃ gas and isolate the silicon, resulting in the formation of HCl gas. Silicon accumulates on top of the silicon seed rods. Once the process is over, the deposited Si is removed and collected. Figure 4 demonstrates the Siemens process to purify silicon. The following chemical reactions represent the process of first dissolving silicon with HCl, then acquiring the SiHCl₃ gas and excess hydrogen. The chemical reaction also shows that the SiHCl₃ and hydrogen gasses produce pure silicon and excess HCl gas.

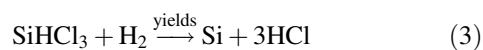
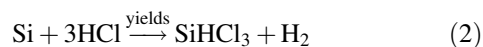
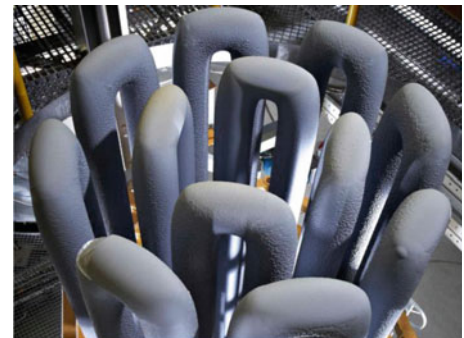
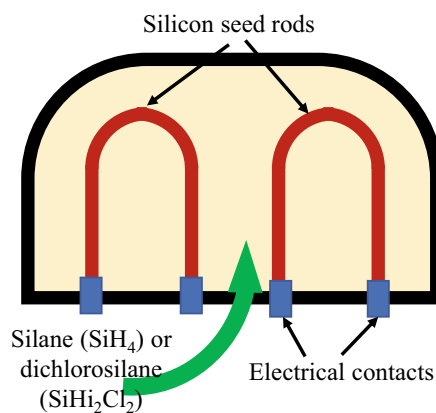


Fig. 4 Siemens process for polysilicon purification and refinement **a** the Siemens chamber or bell and **b** polysilicon rods ready to be broken into silicon chunks (Polysilicon Production 2023)



2.2 Fluidized Bed Reactor Process

In addition to the Siemens process, chemical metallurgical silicon refinement can also be carried out by the fluidized bed reactor (FBR). The FBR is an old process that does not utilize large quantities of hydrogen or HCl gasses to react with silane gas that is injected from the bottom of the reactor. The FBR process was found to compensate for the drawbacks of the Siemens process. The Siemens process is a non-continuous process that disturbs the continuity of the process to collect and obtain pure silicon. In contrast, the FBR process is a continuous process that does not need to stop to collect the produced silicon. To obtain pure silicon, silane (SiH₄) gas with silicon particles and hydrogen can be readily injected through the reactor, as shown in Fig. 5.

Unlike the Siemens process, the FBR process does not initially require dissolving the silicon with HCl to obtain the SiHCl₃ gas, instead silane gas with silicon particles can be directly inserted into the reactor. As soon as the gas enters, it decomposes on tiny little seeds, made of pure silicon. Once enough silicon is collected on the seeds, bigger granules form and sink to the bottom of the reactor, where they are regularly removed from the process. Consequently, the silicon is obtained without the need to discontinue the process at any occurrence. Compared to the conventional rod reactor (Siemens process), the FBR consumes as little as 10% of the electricity for a matched output. The reduction in the electricity utilization is attributed to the heat loss bypass due to the heated gas/cold silicon seed surface interface reaction. Moreover, the FBR process suits the rapidly expanding photovoltaic industry by producing less-expensive polysilicon.

3 Monocrystalline Silicon Production

The Siemens and the FBR processes assist in acquiring high-purity chunks of silicon grains with irregular shapes. These shapes, however, are not suitable to be readily utilized

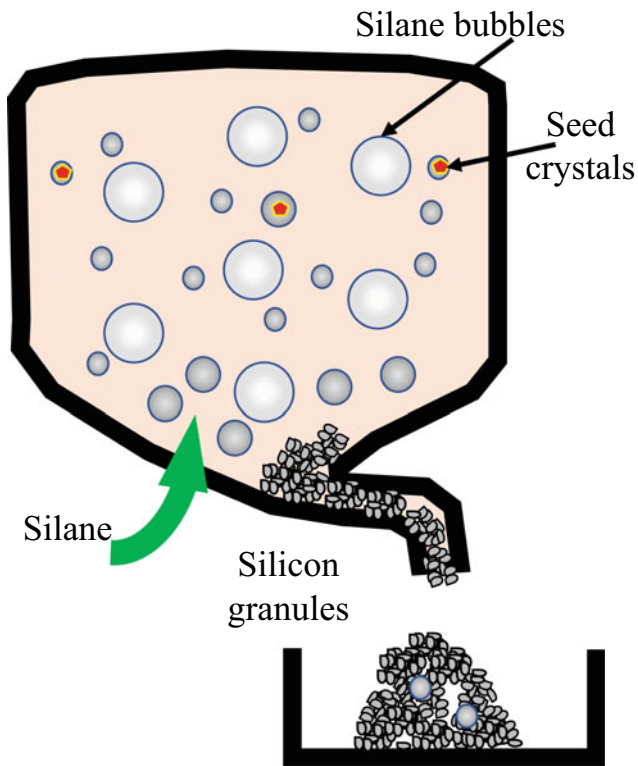


Fig. 5 A schematic of the process of silicon purification and refinement via a fluidized bed reactor

in making solar cells. The silicon grains need to be melted and solidified again to facilitate the process of making silicon wafers. The purity of chunks of silicon grains can be shaped into monocrystalline or multi-crystalline silicon wafers through specific processes. Two processes are used for the production of ultrapure ingots of monocrystalline silicon. These processes are (i) the Czochralski (Cz) process and (ii) the float zone (Fz) process.

3.1 The Czochralski Process

Jan Czochralski, a Polish scientist, invented the self-titled technique “The Czochralski Process” in 1916, while studying the different rates at which metals crystallize. This process is used to produce a single crystal “monocrystal” of semiconductors, metals, and salts. This process is used to this day due to its simplicity to control the crystallization rates of semiconductors, such as silicon (What does Czochralski Process Mean? 2023). The Cz-Si is the Czochralski-Silicon process that started producing monocrystalline silicon which is still more expensive than the polycrystalline silicon, as it requires directional solidification and patient workers to produce them. The process is carried out by first melting the high-purity,

semiconductor-grade silicon chunks in a crucible at 1425 °C, usually made of quartz, into homogenous molten silicon. By adding precise amounts of dopant impurity atoms, such as boron and phosphorus, the produced silicon can be altered to become p or n-type, respectively, with varied electronic properties. Then, a seed crystal mounted on a rod that is precisely oriented is dipped into the molten silicon. As the silicon starts to crystallize around the seed crystal, the rod is controllably pulled out while being rotated to collect more silicon through its ascension. The temperature gradients, rod pulling rate, and rotation speed are precisely controlled to extract a large single-crystal cylindrical ingot of silicon. To prevent issues such as immature crystallization and the formation of grain boundaries, the process is undertaken in an inert atmosphere of argon, or in an inert chamber made out of quartz. Figure 6 shows the process of the Czochralski-Silicon method to acquire monocrystalline silicon, and the picture shown in the figure is taken in the Science Museum in London (a highly recommended visit if you are in London: <https://www.sciencemuseum.org.uk/>).

The Cz-Si process results in oxygen-rich silicon wafers. Oxygen impurities ultimately lower the minority carrier lifetime (a concept which will be discussed later) and reduce the voltage, current, and efficiency of solar cells. There are various sources of oxygen impurities, such as the atmosphere and the seed crystal. Additionally, oxygen impurities are active at higher temperatures, which results in temperature-sensitive wafers, and hinders the quality of any following processes. To address this issue, an alternative method, the float zone method, was introduced.

3.2 Float Zone Process

The float zone (Fz-Si) is an alternative to the Cz method for single crystal making. The process produces high-purity silicon wafers with extremely low concentrations of oxygen and carbon impurities. Nevertheless, the float zone method has high concentrations of nitrogen impurities that are intentionally added to aid in controlling the microdefects. Most importantly, nitrogen impurities are added to enhance the mechanical strength of the silicon wafers. The float zone method is similar to the Cz-Si procedure; however, it does not pull the seed crystal, instead it involves casting the molten silicon and then applying a strong magnetic field to induce heat within the ingot. The induction coil is mobile and moves either up or down the ingot while being wrapped around it. The magnetic effects induce heat and is applied to the cast silicon regions, or zones, which results in multiple float, or molten, zones. As the induction coil moves up, the float zones carry the impurities and move up simultaneously, leaving behind a big grain of monocrystalline range. With

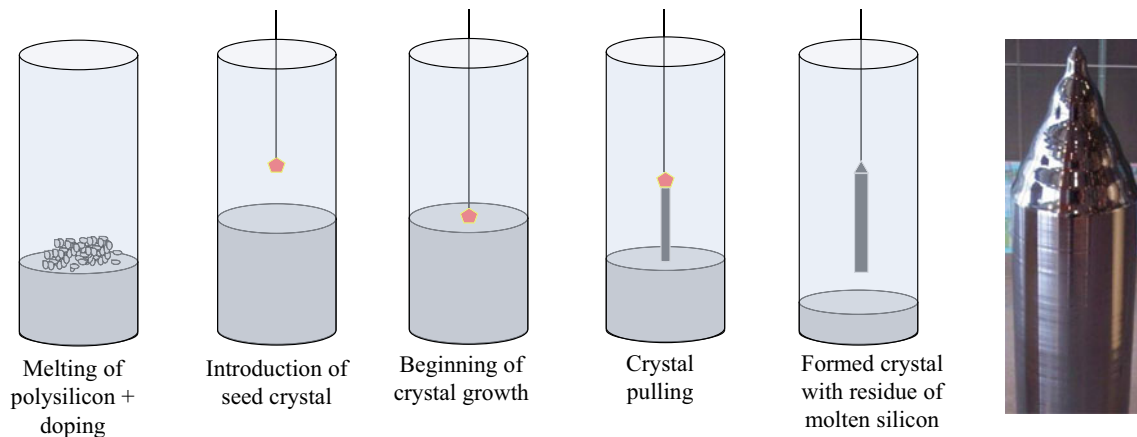


Fig. 6 Process of obtaining monocrystalline silicon through the Czochralski-Silicon method. The photo is a Cz grown ingot displayed in the Science Museum of London (Silizium und für die Waferherstellung 2023)

the continuation of the upward coil motion, the monocrystalline range enlarges simultaneously. At the end of the process, all the excess parts of the casted silicon, including the molten zones and impurities, are cut, leaving behind a monocrystalline silicon wafer with extremely low impurities. In the float zone method, the surface tension of the silicon limits the sizes of the monocrystalline wafers. Most sizes of monocrystalline wafers do not exceed 20 cm. Additionally, the shape of the monocrystalline is heavily influenced by the float zone and the coil size. For instance, as the float zone or the coil size increases, most of the cast silicon starts to melt, consequently, the monocrystalline shape cannot be formed. Figure 7 details the several stages associated with the float zone method for producing monocrystalline silicon. Figure 8 shows a close-up of the process as well as a picture of the coil in action.

Both the Cz and the Fz processes have their own merits and drawbacks. The quality and the budget available for each process are important selection parameters. A summary of the pros and cons of each is given in Table 1.

The Cz-Si process and the float zone method both produce monocrystalline silicon crystals. Monocrystalline silicon is manufactured and produced due to its high efficiency; however, it is rather expensive. On the other hand, multi-crystalline silicon is more cost-effective to produce; however, most of the produced multi-crystalline silicon have low efficiencies and highly visible grains and grain boundaries.

4 Multi-crystalline Silicon (MS-Si) Production Processes

Multi-crystalline silicon is produced by two processes, either (i) directional solidification or (ii) ribbon growth.

Directional solidification

This process controls the direction of heat loss from the silicon melt in a crucible. It is carried out by initially placing highly pure silicon into a silicon nitrate (Si_3N_4)-coated crucible, made of quartz. Two filaments, containing a seed crystal made up of pure silicon, are dipped into the crucible. The filaments are pulled back to obtain the accumulated silicon around the exterior walls of the filaments. After obtaining the multi-crystalline silicon, the silicon block is cut by a metallic wire, then diced and sliced into thin wafers. Upon acquiring the thin silicon wafers, the wafers are properly washed and prepared. Total growth times range between 20 and 30 hours producing large half-ton ingots. Figure 9 presents the process of directional solidification for producing multi-crystalline silicon.

4.1 String Ribbon Process

In this process, there is no double crucible setup as in the directional solidification technique. A seed crystal with wire filaments are dipped into a molten silicon crucible made of quartz as shown in Fig. 10a. In a process that depends on cohesive forces and surface tension, a thin sheet of silicon is formed akin to the formation of a soap bubble on a special frame (see Fig. 10b). This method saves post-processing steps as the wafer is produced to the required dimensions, but it is slow and requires complex control, intense labor involvement, and training.

4.2 Ribbon Growth Technique

In contrast to directional solidification, ribbon growth reduces the waste induced from post-processing steps, such

Fig. 7 Several stages incorporated in the float zone method for obtaining monocrystalline silicon

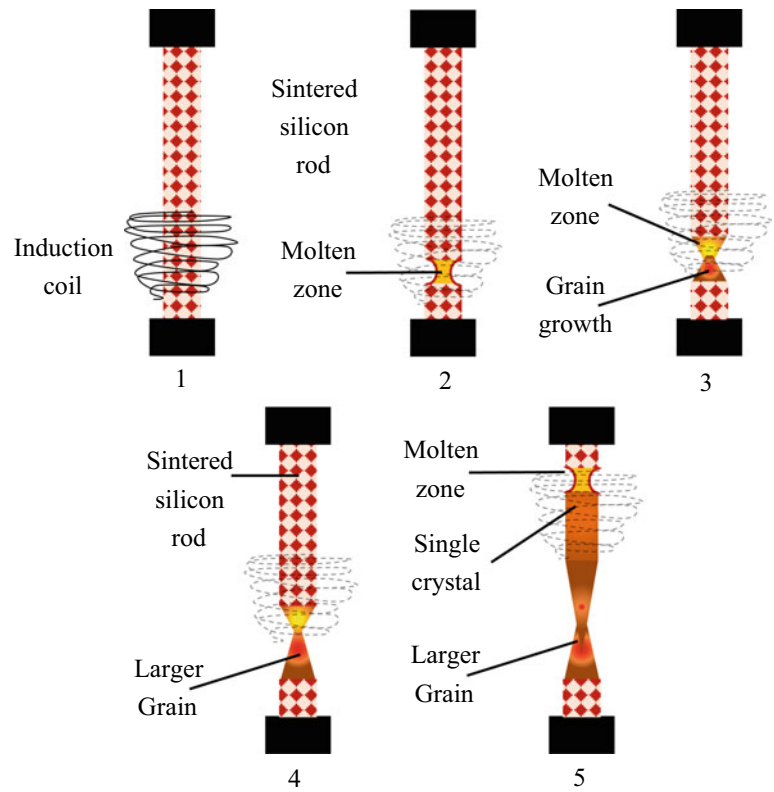


Fig. 8 a A close-up of the float zone process and **b** a picture of the induction coil around the cast silicon ingot (Si-crystal floatingzone 2023)

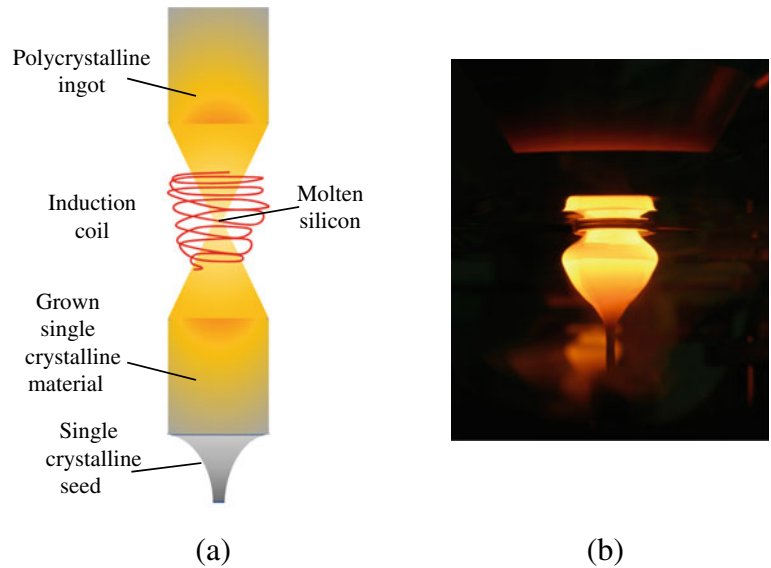


Table 1 Comparison between Cz and float zone

	Cz technique	Float zone technique
Advantages	<ul style="list-style-type: none"> • Allows big crystal diameters (~46 cm) • Lower production cost 	<ul style="list-style-type: none"> • Low-impurity concentration • Dopant concentration in the final crystal is homogenous
Disadvantages	<ul style="list-style-type: none"> • Higher impurities (oxygen and carbon) from quartz and graphite crucibles • Low homogeneity of axial and radial dopant concentrations due to oscillations 	<ul style="list-style-type: none"> • More expensive than Cz • Crystal diameter limited to ~20 cm

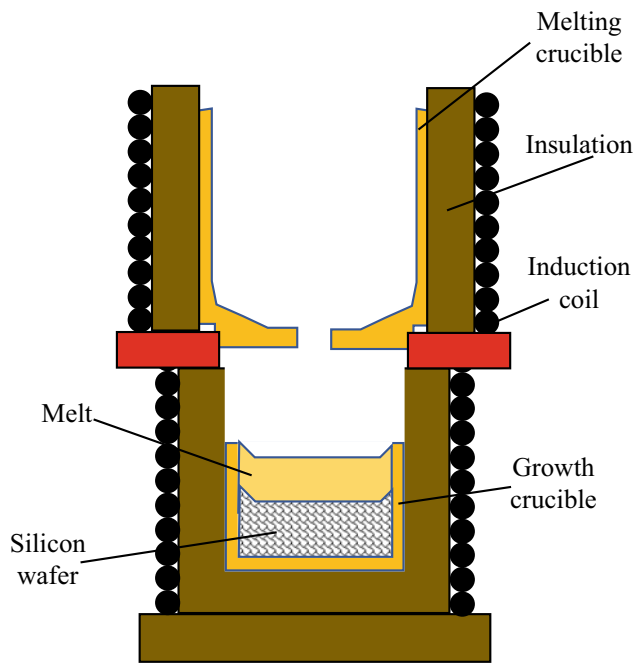
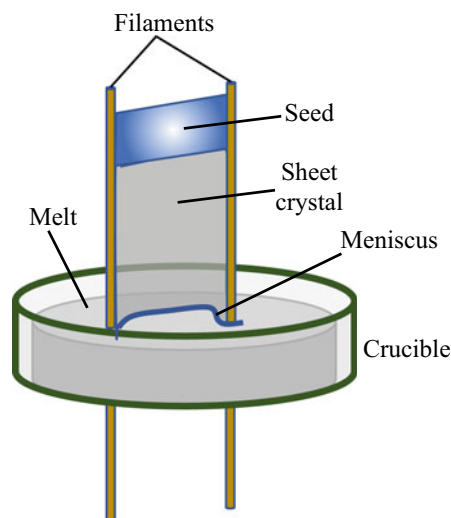


Fig. 9 Directional solidification

as slicing and dicing, just like string ribbon process. Ribbon growth is another alternative to produce multi-crystalline silicon wafers from molten silicon in less than an hour. In this method, the molten silicon is poured into a dye. A substrate is placed underneath the dye to shape the thickness of the multi-crystalline silicon wafer. Hence, the thickness of the produced multi-crystalline silicon depends on the speed of the moving substrate. Ribbon growth produces thin multi-crystalline wafers without the need of slicing or dicing the wafers; this in return reduces waste. Nevertheless, other post-processing steps, such as cleaning and polishing, are

Fig. 10 a Production of multi-crystalline silicon through the string ribbon method and **b** similarity of soap bubble adhesion to the filaments (Soap-Bubble Shapes 2023)



a



b

still necessary. The produced multi-crystalline wafers are made of doped silicon; thus, they tend to be extremely fragile. For this reason, the wafers need to be contained within an insulating, anti-reflective material, such as glass, this in return seals the wafers from water, humidity, or other impurities. Figure 11 shows the production of multi-crystalline silicon wafers by utilizing the ribbon growth method. The process is similar to road marking technique, where hot thermoplastic paint is applied through a machine with a shaping dye that holds the hot paint, while a dye opening applies a homogenous thickness of paint that depends on the size and speed of the dye.

4.3 Comparison Between Bulk Process and Ribbon Growth

In general, bulk processes produce a lot of waste of virtually nonrecyclable material. As can be seen from Fig. 12, bulk silicon processing requires 1–2 days to start producing wafers that utilize 30–50% of the starting ultrapure silicon. The rest must go through the refinement process one more time. On the other hand, ribbon or string grown silicon requires less than an hour for the first wafer to appear. But the process is slow and requires intensive trained labor intervention. Figure 13 lists the main steps for each process (bulk and ribbon), with less steps for the latter.

5 Silicon Post-processing

Post-processing of the produced ingots from the CZ or the float zone methods is both time consuming and extremely wasteful. Post-processing of the ingots is carried out to

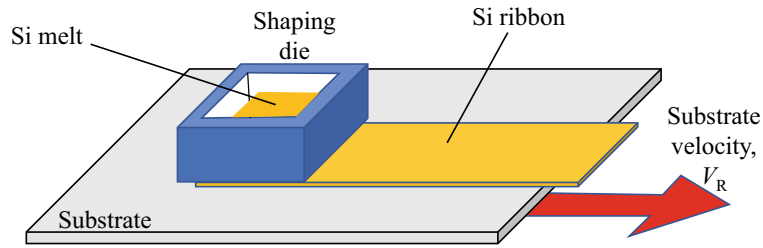


Fig. 11 Ribbon growth method for obtaining multi-crystalline silicon, where V_R is the speed of the moving substrate

Fig. 12 Process comparison of **a** bulk silicon wafer production and **b** ribbon or sheet grown silicon

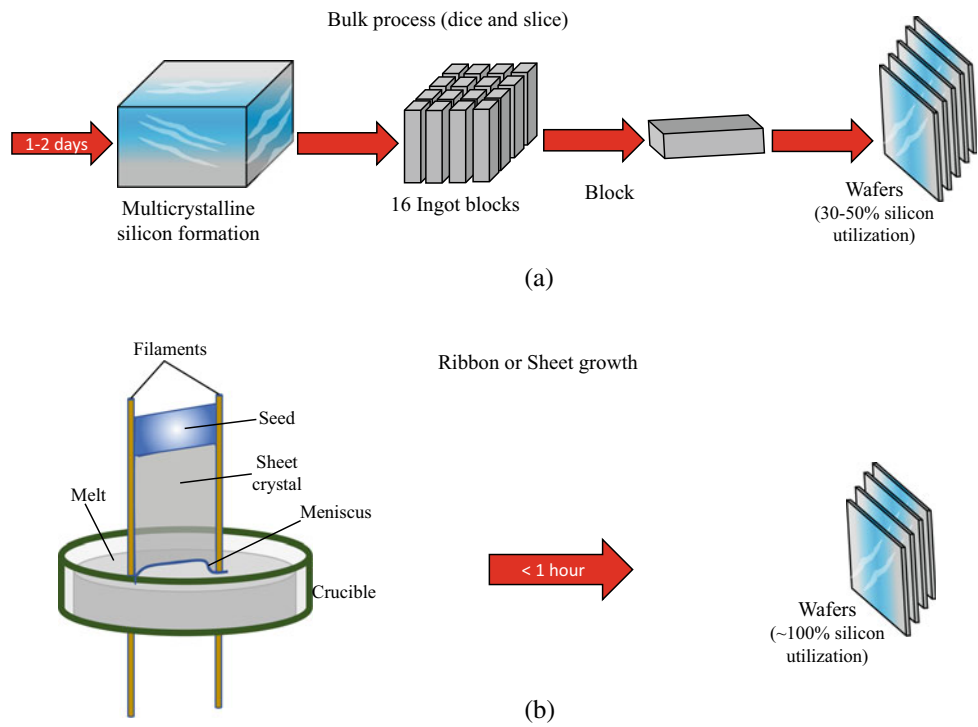
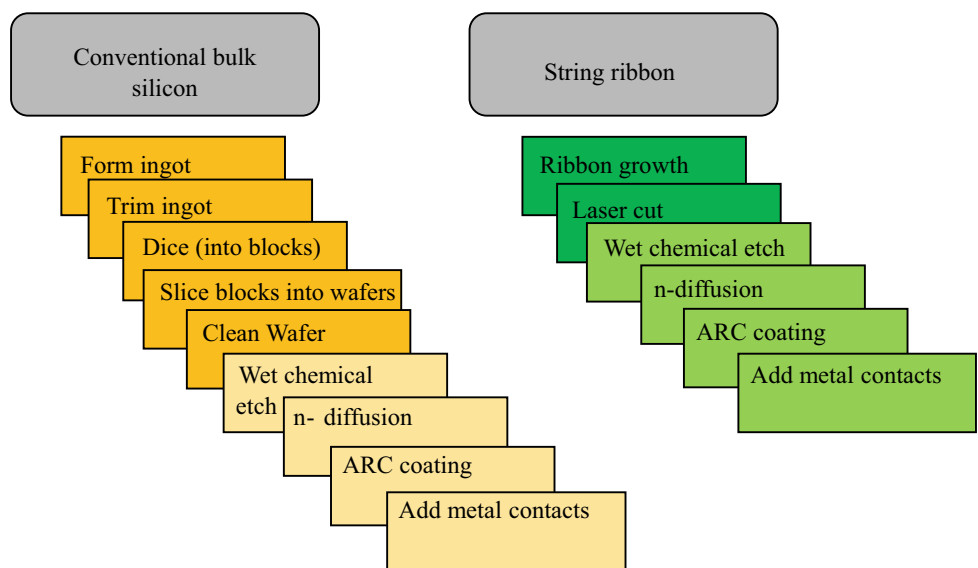


Fig. 13 Main steps for bulk silicon and string ribbon processes



convert mono-crystalline silicon into thin either mono or multi-crystalline wafers. Figure 14 shows the steps required to arrive at the wafer, which starts either with a Cz monocrystalline ingot, or as a MS-Si from a silicon melt in a quartz crucible. The silicon is allowed to solidify (into MS-Si), is diced into blocks (16 is a conventional number); then it is sliced with either a saw or diamond-tipped metallic wire (just like country bread is cut into slices) for wafers to be produced.

The silicon from Cz comes in the form of cylinders. These cylinders are diced either by an inner diameter sawing or a wire saw. As can be seen in Fig. 15a, the wafer is sliced using an inner diameter sawing technique, in which the cutting edge of the circular blade is embedded with diamond splinters. A better idea is to use a wire saw that cuts the wafer with several parallel wires. This will minimize the induced wastes from dicing, as shown in Fig. 15b. Try using unscented floss to cut a cake instead of using a knife and you will appreciate how low the waste (stuck to the knife) is. The wire is made up of steel with a diameter of 100–200 μm and a speed of 10 m/s.

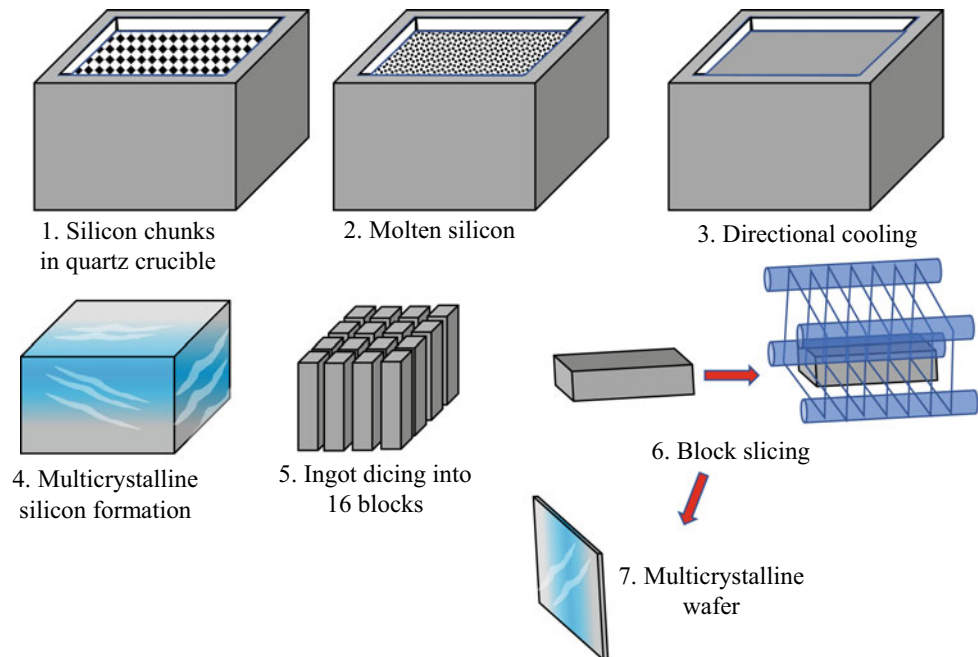
The first step is grinding, which involves decreasing the diameter of the ingots using either the CZ or FZ method with the aim of making them more workable and cutting them

into shorter cylinders. Grinding also adds certain features to the formed cylinders to distinguish the p-type from the n-type material. This is shown in Fig. 16.

Once the wafers have been diced, they are lapped on both sides in attempt to eliminate any surface debris that could have been fractured as a result of the slicing process, as well as to thin the wafer to the desired thickness. Figure 17 demonstrates a schematic view of a wafer lapping machine. After the required thickness of thin wafers has been obtained, they are etched using either KOH (a base) or HNO_3/HF (an acid) to remove any damaged surfaces.

The wafers are then polished to remove any excess acids/bases left on the wafers. Super-flat, mirrored surface with minimum surface roughness wafers are attained after polishing. Once the wafers have been polished, they go through a cleaning process with ultra-pure chemicals, which gets rid of the polishing agents and ensures that the wafers do not contain any residuals. Etching, polishing, and cleaning are categorized as finishing processes that are responsible for adding small features on the surface of the wafers to indicate the type of interaction the wafers have with the incoming solar radiation. These small features are also known as the miller indices, or exposed planes, which are shown in Fig. 18.

Fig. 14 Main steps of producing wafers from bulk silicon production



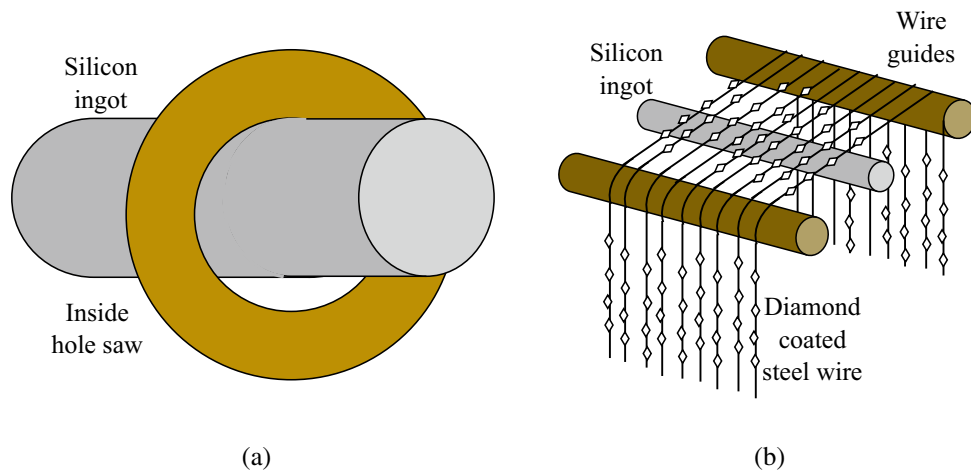


Fig. 15 a Using an inner saw reduces the broken edges and provides better control over the cut and b diamond-coated steel wires allow lower waste from the slicing operation

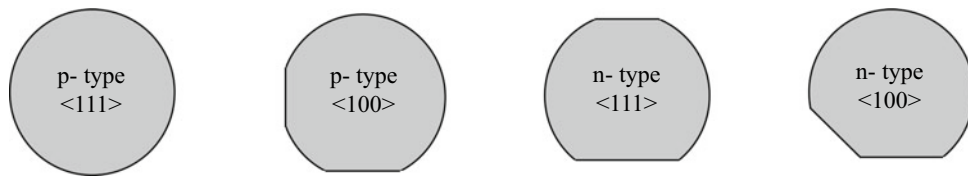


Fig. 16 Adding different features to the wafer to distinguish doping status and exposed crystallographic planes

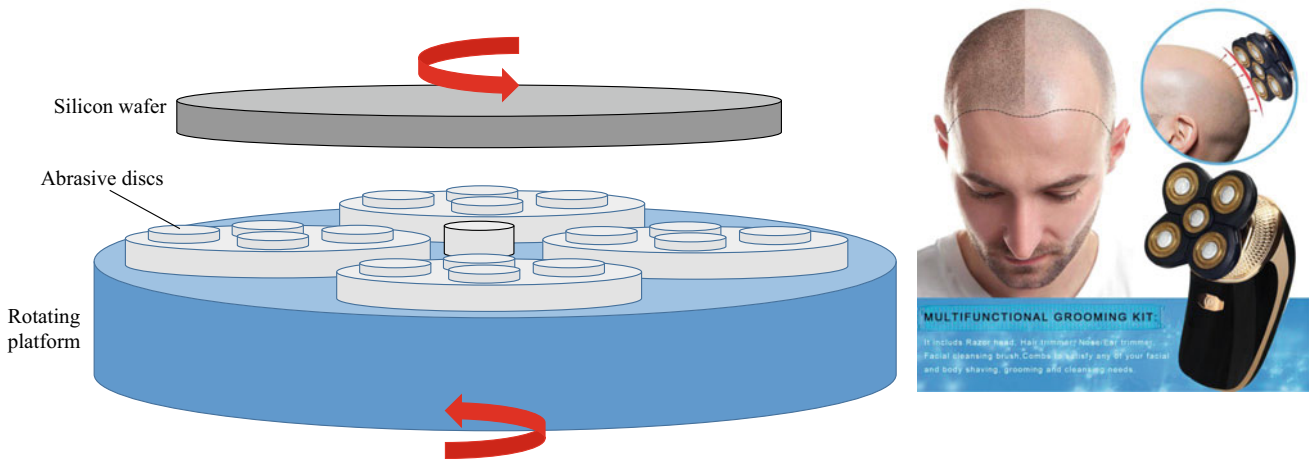


Fig. 17 Schematic of a wafer lapping machine and its similarities with electric shaver razor (DOTSOG in this case)

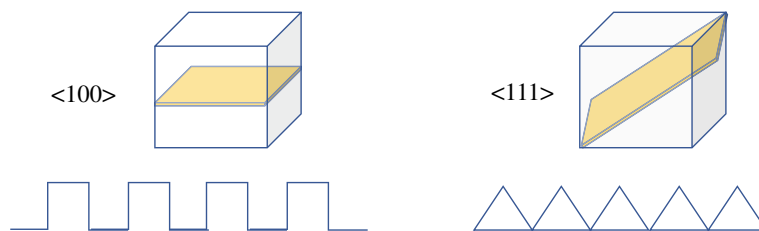


Fig. 18 Crystallographic plane families that are exposed according to silicon wafer etching

References

- Monokristalines Silizium für die Waferherstellung- Wikimedia Commons. https://commons.wikimedia.org/wiki/File:Monokristalines_Silizium_f%C3%BCr_die_Waferherstellung.jpg (Accessed 05 Mar 2023)
- Polysilicon Production: Siemens Process | Bernreuter Research. <https://www.bernreuter.com/polysilicon/production-processes/> (Accessed 15 Feb 2023)
- Si-crystal floatingzone—Wikimedia Commons. https://commons.wikimedia.org/wiki/File:Si-crystal_floatingzone.jpg (Accessed 15 Feb 2023)
- Soap-Bubble Shapes: Color, Light and Waves Science Project | Exploratorium Science Snacks—CubeForTeachers—Cube For Teachers. <https://cubeforteachers.com/post/IC7neMB4sf1qT1xjJpcGV4fuq5uO8Mdc> (Accessed 15 Feb 2023)
- What does Czochralski process mean? <https://www.definitions.net/definition/Czochralski%20process> (Accessed 05 Mar 2023)



Solar Grade Silicon Feedstock Properties

Abdul Hai Alami[✉], Shamma Alasad[✉], Haya Aljaghoub[✉],
Mohamad Ayoub[✉], Adnan Alashkar[✉], Ayman Mdallal[✉],
and Ranem Hasan[✉]

Abstract

There is more than the maturity of the semiconductor industry that makes silicon a lucrative material for photovoltaic device manufacturing. Other advantages include the suitability of silicon material to absorb solar radiation in the visible region, where most of the useful and energetic solar radiation resides. This chapter introduces the physical, optical, and chemical properties of silicon that aid it in occupying the high rank it does in energy conversion and production. This chapter also provides a concise description on performance calculations of silicon solar photovoltaic cells.

1 Introduction to Energy Bandgap

The attractive physical and optical properties of silicon made it the backbone of the photovoltaic industry (Alami et al. 2016a). The interaction of solar radiation with the material is the genesis of the photovoltaic conversion, which is a quantum–mechanical interaction exploiting the

dual nature of light. Light as observed from various experiments travels as a wave with distinctive wavelength (or frequency), and whenever it is stationary, it acts as a particle known as a photon. Photons have energy written as $h\nu$ where h is Plank's constant, and ν is the frequency (Alami et al. 2015). Once this photon strikes, a certain material one of two things can happen. The photon is either absorbed by the material, or it passes through it without any interaction. This depends on a material property called the energy bandgap (E_g), and if the material bandgap is less than or equal to the photon energy level, the photon will excite the material enough to generate an electron/hole pair as shown in Fig. 1a. Excessive interaction will cause heat to also generate within the material, with many adverse effects on the efficiency of the photovoltaic generation. On the other hand, if the material bandgap is larger than the photon energy, the photon will not interact with the material (no electron hole pair will generate) indicating no interaction between incident radiation and the material. This is shown in Fig. 1b.

The difference between the two cases of photon/material interaction can be further explained by considering an analogy describing two basketball dunks with different rim sizes. The basketball (the photon) interacts fully with the rim if the rim (bandgap) is smaller or equal to the size of the ball. The basketball would also be stuck (unwanted heat generated) if the rim is too small, as seen in Fig. 2a. On the other hand, if the ball goes through the rim without any interaction (a layup), then the basketball will fall to the other side leaving the rim undisturbed, as seen in Fig. 2b.

Metals do not have a bandgap as there exists an overlap in their energy states. The bandgap of a semiconductor is small compared to insulators, as the level of energy required to move one electron from the valence band to the conduction band is larger as electrons are not readily available. If that particular energy is supplied, the material could be destroyed by absorbing energy levels sufficient to break its molecular bonds. Therefore, only semiconductors can allow electrons

A. H. Alami (✉) · H. Aljaghoub · M. Ayoub ·
A. Mdallal · R. Hasan
University of Sharjah, Sharjah, United Arab Emirates
e-mail: aalalami@sharjah.ac.ae

H. Aljaghoub
e-mail: haljaghoub@sharjah.ac.ae

M. Ayoub
e-mail: mohamad.ayoub@sharjah.ac.ae

A. Mdallal
e-mail: ayman.mdallal@sharjah.ac.ae

S. Alasad · A. Alashkar
American University of Sharjah, Sharjah, United Arab Emirates
e-mail: g00070854@aus.edu

A. Alashkar
e-mail: b00028197@alumni.aus.edu

Fig. 1 Interaction between a photon and a material is a function of the energy bandgap of the material. If the bandgap is (a) less than or equal to the photon energy, then an electron/hole pair will generate, however, if the bandgap is (b) larger than the energy of the photon, no interaction is expected

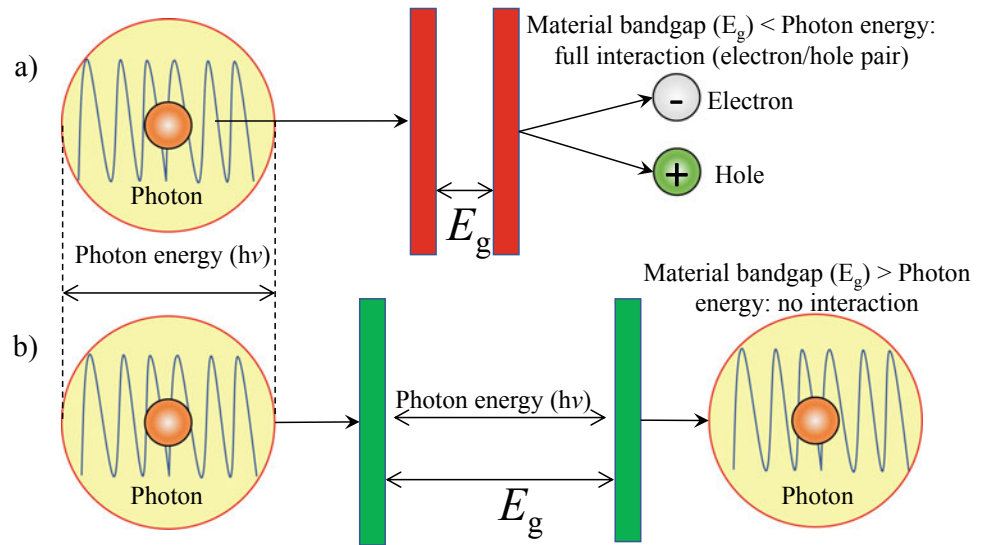


Fig. 2 Basketball analogy with bandgap and photon energies: a energy bandgap less than or equal photon energy, indicating a full interaction that yields an electron/hole pair and b energy bandgap is more than the photon energy and no interaction

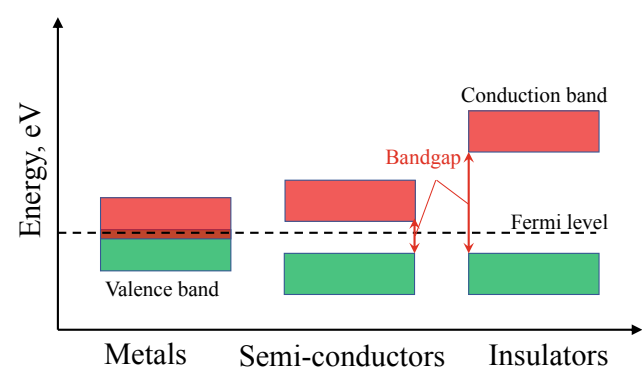
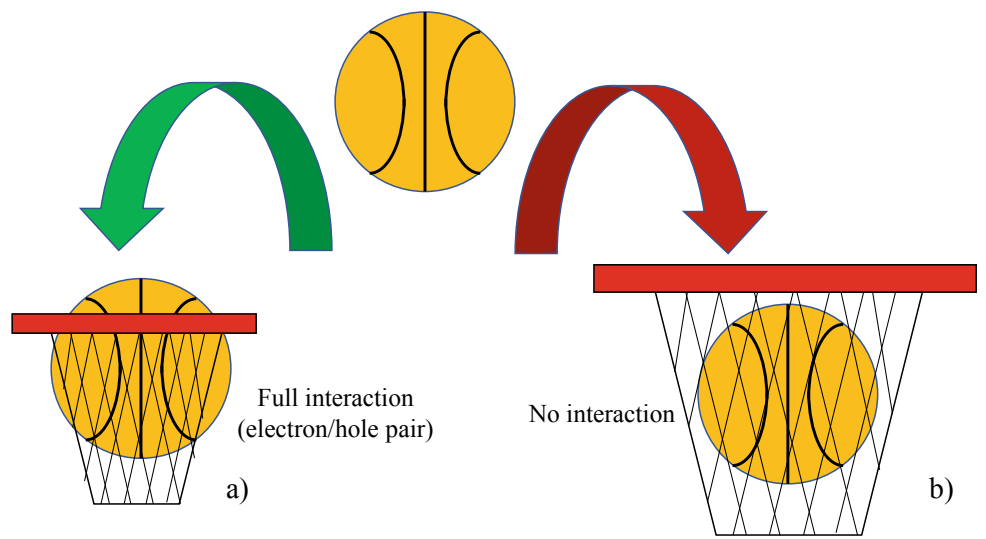


Fig. 3 Bandgap of metals, semiconductors, and insulators (https://upload.wikimedia.org/wikipedia/commons/thumb/0/0b/Band_gap_comparison.svg/2000px-Band_gap_comparison.svg.png)

to be excited and moved to higher energy states and be harvested by external loads. Figure 3 illustrates the difference in the bandgaps of metals, semiconductors, and insulators (https://upload.wikimedia.org/wikipedia/commons/thumb/0/0b/Band_gap_comparison.svg/2000px-Band_gap_comparison.svg.png). The Fermi level indicated in the figure is the energy level at which the charged species are most likely to be found. It is analogous to the resting fluid level between two reservoirs located at different elevations.

The energy bandgap of a material can be calculated from bulk and surface absorptivity tests of the material. A typical test setup is shown in Fig. 4, where a light source of known wavelength range is shone on the material sample, and the absorptivity versus wavelength is recorded.

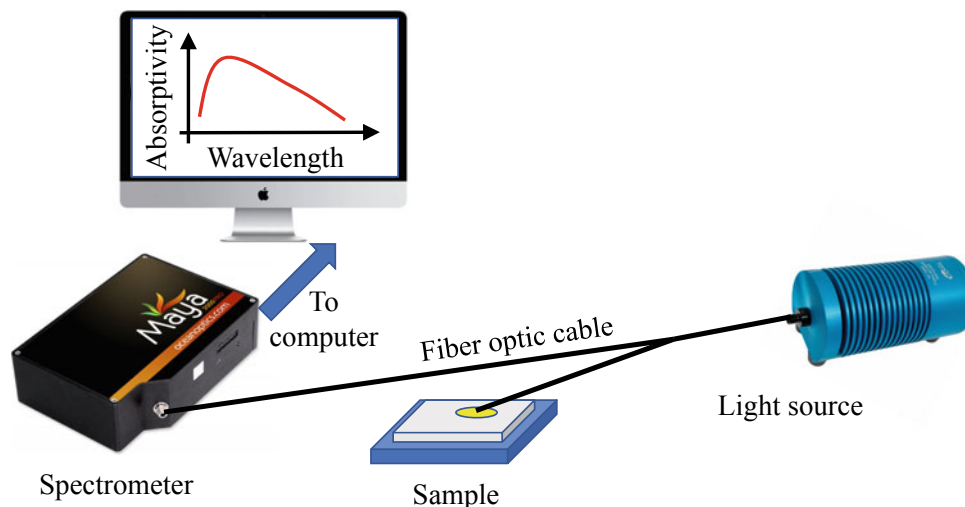


Fig. 4 Absorptivity test setup

The results can then be fed into the Tauc relationship to calculate the bandgap. The equation reads as follows:

$$\alpha \cdot h\nu = A \cdot (h\nu - E_g)^n \quad (1)$$

where α is the absorptivity from the experimental measurements, A is a constant (the edge width parameter), E_g is the optical bandgap, and n is a constant that depends on the nature of the transition. Note that α and λ are measured, where the latter can be converted into frequency by incorporating the speed of light, c as $\nu = c/\lambda$. Finally, by plotting $(\alpha \cdot h\nu)^{\frac{1}{n}}$ versus the photoenergy $h\nu$ and finding the tangent of the curve to extrapolate it to the zero point, where $h\nu = E_g$, the energy bandgap (eV) is directly read from the figure. Figure 5 shows absorptivity results taken from an experimental setup identical to that shown in Fig. 4. The

absorptivity is plotted versus wavelength and the results are fed into Eq. 1 and a plot is generated (inset), where the tangent to the resulting plot is extended to intersect with the x-axis (units being eV), enabling reading the bandgap value directly (Alami et al. 2016b).

1.1 Shockley–Queisser Limit

The Shockley–Queisser limit is a concept that is closely related to the bandgap of a material. It represents the maximum solar conversion efficiency of a single-junction solar cell versus the material energy bandgap. For silicon solar cells, the bandgap that corresponds to the visible light wavelength range ($\sim 300\text{--}800$ nm) will produce the maximum efficiency. Semiconductors such as silicon have a

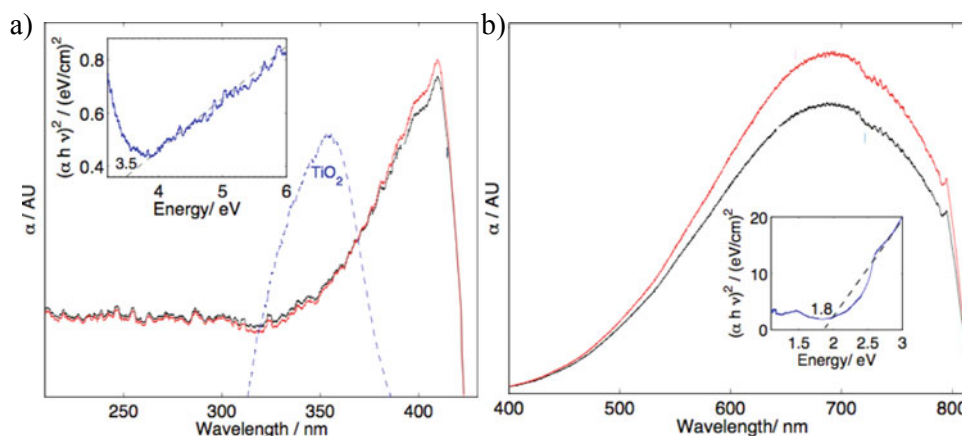


Fig. 5 Bandgap calculation using Tauc formula in graphical form (a) is taken with a xenon light source and a UV-range spectrometer, where a TiO_2 peak is seen and the bandgap is shown inset as the tangent to the graph extended to intersect the x-axis to directly read

the bandgap value in eV, while in (b) a halogen light source is used to determine the absorptivity of a material powder in the Vis regime, with a bandgap plot inset showing the application of the Tauc formula

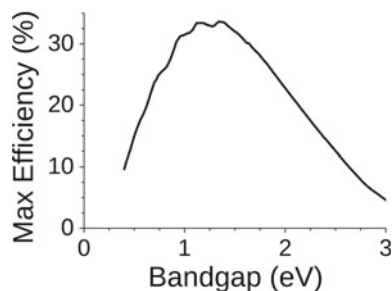


Fig. 6 Shockley–Queisser limit for the maximum possible efficiency of a solar cell (https://en.wikipedia.org/wiki/Shockley%E2%80%9393Queisser_limit#/media/File:ShockleyQueisserFullCurve.svg)

bandgap between 1 and 1.5 eV. Cadmium telluride (CdTe) also has a bandgap of 1.5 eV which makes it desirable for solar cell application. Figure 6 shows the Shockley–Queisser limit, where the maximum efficiency lays at bandgap values between 1 and 1.5 eV. Thus, any material with a bandgap in this range should theoretically possess the best performance.

As mentioned before, if the bandgap of a material is too high, a lot of photons from the solar radiation will not be absorbed as they will not interact with the material. On the other hand, a too low bandgap will cause energy to be wasted (as sensible heat) since photons energy are higher than required to excite electrons to cross the bandgap.

1.2 Bandgap and Semiconductors

It should now be clear why silicon is most common semiconductor material used for the conversion of light into electricity. Table 1 shows some materials with their corresponding bandgap. Silicon has a bandgap of 1.14 eV which corresponds to the theoretical maximum possible efficiency seen from Fig. 6. This reason is not the only one for the dependence on silicon for photovoltaic device design and

manufacture. Silicon is found abundantly in the Earth’s crust as Silicon oxide (SiO_2) as it is harder to find metallic silicon (at least 96% of silicon). Elemental silicon is produced when carbon is added to the SiO_2 with a tremendous amount of energy (temperatures approaching $2200\text{ }^\circ\text{C}$), and this can be achieved by the process of electrolysis.

2 Physical Properties of Silicon

Based on its crystal structure, silicon can be divided to two types: amorphous or crystalline which can either be single (monocrystalline) or multicrystalline (polycrystalline). In 1824, silicon was first prepared by Jöns Jacob Berzelius by passing silicon tetrachloride over heated potassium. Berzelius discovery led to the preparation and purification of amorphous silicon. In 1854, the first crystalline silicon was made coincidentally by Sainte-Claire Deville, while working on aluminum electrolysis.

A silicon atom is tetrahedrally bonded to four neighboring silicon atoms. In crystalline silicon (c-Si), the carbon atoms can form very long crystal structures that are crystalline (long-term order). Additionally, unlike other elements and compounds, silicon contracts when melting and expands when cooling (solidifying). The other property of silicon is that it gets crystallized into a diamond cubic structure that can also go into a body-centered lattice at very high pressures (15 GPa). Once the crystalline silicon is growing, the crystalline structure faces are going to be {111} and also have epitaxial films which is the layer-by-layer growth as a consequence of polysilicon deposition. The temperature of vapour deposition also affects the physical property of silicon. Under temperatures less than $500\text{ }^\circ\text{C}$, amorphous silicon is resulted. While at temperatures above $500\text{ }^\circ\text{C}$, crystallization is formed.

Amorphous silicon, on the other hand, lacks the long-term order and most of the time it’s made using

Table 1 List of bandgaps of different materials (https://en.wikipedia.org/wiki/Band_gap)

Group	Material	Symbol	Band gap (eV) @ 302 K
III–V	Aluminum nitride	AlN	6.0
IV	Diamond	C	5.5
IV	Silicon	Si	1.14
IV	Germanium	Ge	0.67
III–V	Gallium nitride	GaN	3.4
III–V	Gallium phosphide	GaP	2.26
III–V	Gallium arsenide	GaAs	1.43
IV–V	Silicon nitride	Si_3N_4	5
IV–VI	Lead(II) sulfide	PbS	0.37
IV–VI	Silicon dioxide	SiO_2	9
	Copper(I) oxide	Cu_2O	2.1

evaporation condensation by the process of chemical vapor deposition (CVD), which will be studied in detail later, where silicon is cooled in a very short period of time which will not facilitate the creation of crystals, and therefore, it will be very amorphous with less atoms being fourfold coordinated. Sometimes amorphous silicon can have a disordered nature that results in dangling bonds which designate defects. Despite its disadvantages, amorphous silicon is very easy to obtain and grow; in addition, it's thinner so less carbon material is needed compared to the crystalline silicon.

2.1 Effect of Doping on Silicon Properties

The behavior of a silicon material changes to a semiconductor by the addition of a very small amount of atoms called dopants. The incorporation of impurity elements during crystal growth or post-treatment affects the silicon semiconductor lattice when they ionize at low temperatures. This depends on the charge carriers and happens by supplying either free electrons or holes. Dopants from group VA, which occupy column 15 as shown in Fig. 7, provide electrons to the conduction band by substituting the Si atom in the lattice and are thus called n-dopants or donors. On the other hand, elements from group IIIA, are called p-dopants or acceptors as they replace a Si atom to give holes that will be starved for electrons. Having two materials oppositely charged placed next to each other will create a voltage difference and hence, charges will be allowed to move from one place to another and this is how the circuit functions simply in a solar cell. Phosphorus and boron each represent n-dopants and p-dopants, respectively, and are the two

dopants most mostly introduced into the semiconductor material for PV processing. The impurity concentration is identified as atoms of impurity per cubic centimeter of host material, which is silicon, where they vary from 10^{14} to 10^{20} atoms per cm^3 for 5×10^{22} atoms/ cm^3 of Si.

It is interesting at this point to ascertain the difference between charge carriers and the generated electron/hole pairs. As can be seen in Fig. 8, the carriers available within the material are due to the doping process. Hence, the free electrons in the n-type material result from the existence of the phosphorous atom that allows an extra electron to exist in the lattice. Similarly, the boron atom creates a "lack of electron" condition, known as a hole. These carriers exist within the material whether or not there is external energy addition in the form of incident solar radiation bringing photons about. This situation is similar to an electrical wire made of copper in the off condition. Once electrical current (i.e., electrons passing per unit time) is applied by pushing it into an electrical socket, the electrons carry other electrons from one side of the wire to the other.

3 Chemical Properties of Silicon

Silicon is known to be very stable in the tetravalent state; however, this is not the case when it gets access to oxygen, as it will tend to form oxides and silicates. Therefore, it is essential to process silicon while protecting it from oxidation as much as possible. Oxygen and the oxides it produces have negative impact on the silicon composition and later on the performance of the solar cell. Artificially isolated elemental silicon gets oxidized instantly forming a thin film of silica

Group	1	2	3	4	5	6	7	8	9	10	11	12	13	14	15	16	17	18
Period 1	1 H																	2 He
Period 2	3 Li	4 Be											5 B	6 C	7 N	8 O	9 F	10 Ne
Period 3	11 Na	12 Mg											13 Al	14 Si	15 P	16 S	17 Cl	18 Ar
Period 4	19 K	20 Ca	21 Sc	22 Ti	23 V	24 Cr	25 Mn	26 Fe	27 Co	28 Ni	29 Cu	30 Zn	31 Ga	32 Ge	33 As	34 Se	35 Br	36 Kr
Period 5	37 Rb	38 Sr	39 Y	40 Zr	41 Nb	42 Mo	43 Tc	44 Ru	45 Rh	46 Pd	47 Ag	48 Cd	49 In	50 Sn	51 Sb	52 Te	53 I	54 Xe
Period 6	55 Cs	56 Ba	* 71 Lu	72 Hf	73 Ta	74 W	75 Re	76 Os	77 Ir	78 Pt	79 Au	80 Hg	81 Tl	82 Pb	83 Bi	84 Po	85 At	86 Rn
Period 7	87 Fr	88 Ra	* 103 Lr	104 Rf	105 Db	106 Sg	107 Bh	108 Hs	109 Mt	110 Ds	111 Rg	112 Cn	113 Nh	114 Fl	115 Mc	116 Lv	117 Ts	118 Og
			* 57 La	58 Ce	59 Pr	60 Nd	61 Pm	62 Sm	63 Eu	64 Gd	65 Tb	66 Dy	67 Ho	68 Er	69 Tm	70 Yb		
			* 89 Ac	90 Th	91 Pa	92 U	93 Np	94 Pu	95 Am	96 Cm	97 Bk	98 Cf	99 Es	100 Fm	101 Md	102 No		

Fig. 7 Simple periodic table (<https://commons.wikimedia.org/w/index.php?curid=98955505>)

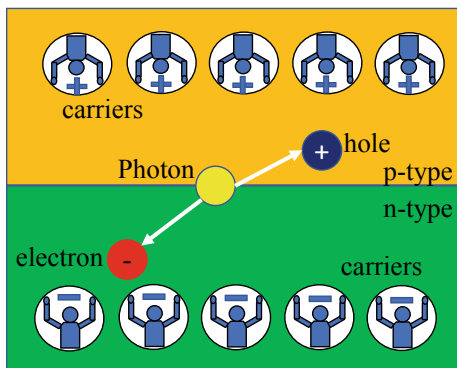


Fig. 8 Charge carriers versus electron/hole pairs

(SiO_2) of thickness less than 100 Å, thus preventing further oxidation. This can actually be etched mechanically or chemically and removed in order to get access to the elemental silicon below.

Silicon is usually added or carried by other materials to make its deposition easier. Carbon (group IVA), for example, is added to silicon to form a strong Si–C bond, for easy processing and can be used in photovoltaics and electronics applications. Silicon can also be dissolved in hydrogen producing a gas that helps in solar cell production later on. Monosilane (SiH_4) is the main gaseous chemical compound for the production of amorphous silicon using the CVD process and the silicon purification into the semiconductor grade. Therefore, silicon is easily transported and activated. This is analogous to wall painting, where paint is first added to a solvent and the paint particles get suspended. Once paint is applied on the wall and it dries, this means that the solvent has evaporated and the solid, suspended material remains stuck to the wall. In the case of silicon, chlorine (solvent) is added to allow better interaction with the chosen substrate (wall) then hydrogen is introduced to carry away the solvent and allow silicon to stay and grow. Hydrogen and chlorine produce HCl, where Cl is the halogen atom. Alkyl- and aryl-chlorosilanes are necessary to build the silicones. Trichlorosilane and tetrachlorosilane can break up to elemental silicon at high temperature, allowing facile control over the deposition process.

Chlorosilanes (e.g., dichlorosilane SiH_2Cl_2) are also used in chemical vapour deposition applications. The halogen atom is easily replaced by a hydroxyl group through hydrolysis that will react with other functional groups by exchanging the hydrogen atom. For solar cell applications, silicon with 99.99999% purity or 99.999% (7N and 5N silicon, respectively) is required. While for semiconductor applications like computers, a 9N purity is required. It is known that the higher the purity the higher the price will be.

Mono-silane gas (SiH_4) is not functional for solar cell applications as they stick to the substrates. Organic solvents or radicals such as R_n , R_p , R_q carry Si and take place of a

halogen atom as seen from the general formula of functional silanes: $X_{4-(n+p+q)}\text{SiR}_n\text{R}'_p\text{R}''_q$, where X is a halide, generally Cl, or H.

The silane gas purity is important for the resulting solar cell. Huge chemical plants are utilized to get silicon from silicon oxide or convert impure silicon to pure silicon. The hydrogen or chlorine atom is simply substituted with the organic radical.

4 Photovoltaic Primer

The mechanism of converting sunlight energy to electricity in a solar cell occurs due to the interactions between light and the semiconductor. A semiconducting material has an intermediate electrical behavior that falls between a metal and an insulator response. Given these electrical properties, semiconducting materials can generate light from electricity via radiative recombination of electron–hole pairs, amplify electrical signals, or generate electricity from harnessed light (photons).

What makes the electrical behavior of semiconductors unique and suitable for photovoltaic applications is the existence of the aforementioned bandgap. For each atom, there are discrete well-defined levels of energy that an electron can occupy. If more than two atoms are brought closely together, the interaction between them will result in a splitting of the energy levels. A semiconducting crystal can be thought of as an infinite number of atoms that are closely compacted together resulting into quasi-continuous energy bands known as the valence band, forbidden bandgap E_g , and a conduction band.

When a photon with an energy equal to the bandgap is incident on the semiconducting material, an electron from the valence band is able to absorb this energy, exciting it, and it is ballistically transferred into the conduction band, leaving behind a vacant hole. The collection of the two separated charges is the output electric current of the photovoltaic material. If the photon energy is higher than the bandgap, the electron will absorb energy far more than what is required to overcome the bandgap energy, which will result in the electron moving deep into the conduction band and losing the excess energy in the form of thermal energy. Lastly, if the photon energy is below the bandgap energy, the photon will transmit through the semiconducting material and will not be attenuated or absorbed. The photon energy is calculated using Eq. 2.

$$E = \frac{hC}{\lambda} \quad (2)$$

where h is the universal Planck's constant 6.626×10^{-34} J s, C is the speed of light 3×10^8 m s $^{-1}$, and λ is the photon wavelength in m.

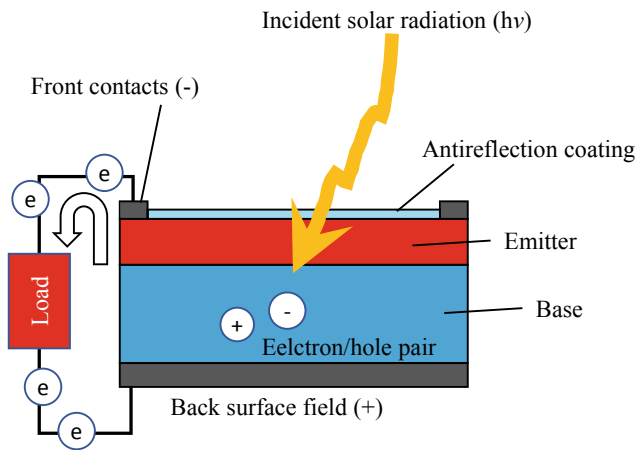


Fig. 9 Operation of a solar cell

Including light absorption and electron excitation, there are three consecutive steps that follow the electron/hole generation. These steps are (i) charge drift/diffusion, (ii) charge separation, and (iii) charge collection. Interestingly, when an electron/hole pair is generated, it happens mostly in the p-base of the semiconducting material due to the n^+ emitter being considered an electrically dead layer caused by heavy phosphorous doping (hence the plus sign, which indicates “extra” rather than “positive”). The pair must then diffuse to the space charge region in order to be separated. The electrons in the p-base diffuse as a minority carrier with a lower mobility contrary to that of holes. Once the charge carriers reach the space charge region via diffusion, they are separated and the electrons are transferred to the n^+ emitter region/front contact, and the holes are sent to the back contact of the cell. Charge separation is aided by the electric-field-caused drift current. Finally, the charges will be collected in an external load, during the charge collection step and sent back to the solar cell for them to recombine, thus initiating a loop of generation, collection, and recombination. This is schematically shown in Fig. 9.

4.1 n-Type Versus p-Type

The principle of doping means that small amounts of specific materials are added in precisely calculated amounts to the matrix material (silicon in this case). This creates a semiconducting material that deviates in behavior from its intrinsic one due to the concentration of electrons and holes within. Each silicon atom will form four bonds in order to reach a stable state, which is why silicon atoms tend to easily form bonds with impurities when they are utilized in the silicon manufacturing process, (i.e., Siemens process, phosphorous diffusion process). A p-type material needs to acquire one electron to reach a stable state. When it

combines with silicon, one electron is transferred from silicon atom to the p-type material atom, and a hole is generated. In this case, holes are the charge carriers. n-type doping combines silicon with a material that has one extra electron, which allows the negatively charged electrons to move, and the free electrons become the charge carriers. Doping grants the required mobility to minority carriers in either p- or n-type sides. This mobility in silicon is considered to be proportional to the speed at which surface recombination occurs, which means that an optimization process must take place in order to reach an economic and an operating concentration threshold. When p- and n-type semiconductor materials interact with each other through an electrical interface, a p–n junction is manifested at their point of contact. The movement of the charge carriers causes a voltage difference in the junction, the voltage will create a central region called the depletion region, and an electrical field will form with a direction going from the p- to n-type materials. The current generated in this case as a result of the voltage difference is called dark current. Figure 10 shows the p–n junction under dark conditions. No bias is when no external potential is applied and indicates that there is no current when the depletion region is generated since there will be no movement of charge carriers. Forward bias is when the positive terminal of the battery is connected to the P-type material side and negative terminal to the N-type material contact. A positive current and voltage are generated in this case. Reverse bias is when the negative terminal is connected to the P-type material, while the positive terminal to the N-type material. Negative voltage and current are generated in reverse bias, and the current is negligible compared to the forward bias current as the depletion region widens in the former and gets narrower in the latter. Figure 11 shows the difference between the I – V response of a solar cell with and without illumination. Note that the negative sign of current under illumination conditions indicates current generated out of the cell. Thus, whenever a cell is tested, the positive voltage and negative current are simple rules of thumb that the test is proceeding favorably.

4.2 Equivalent Circuits

The equivalent electrical circuit of a conventional silicon-based solar photovoltaic cell is shown in Fig. 12. It consists of a constant current source which represents the photocurrent generated from the incident photons which results in an electron/hole pair, a diode that represents the p–n junction which provides the electric field that separates the generated electron/hole pairs across the bandgap, and a series and shunt resistances that impede the electric current across the semiconducting material. The current–voltage

Fig. 10 P-N junction under dark conditions

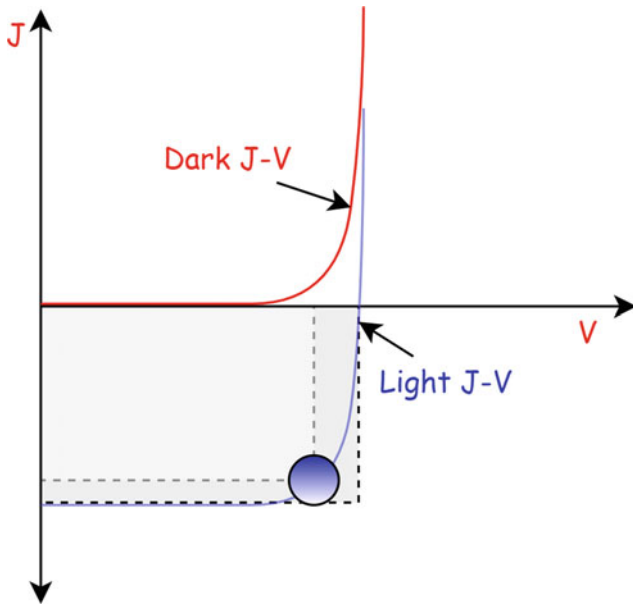
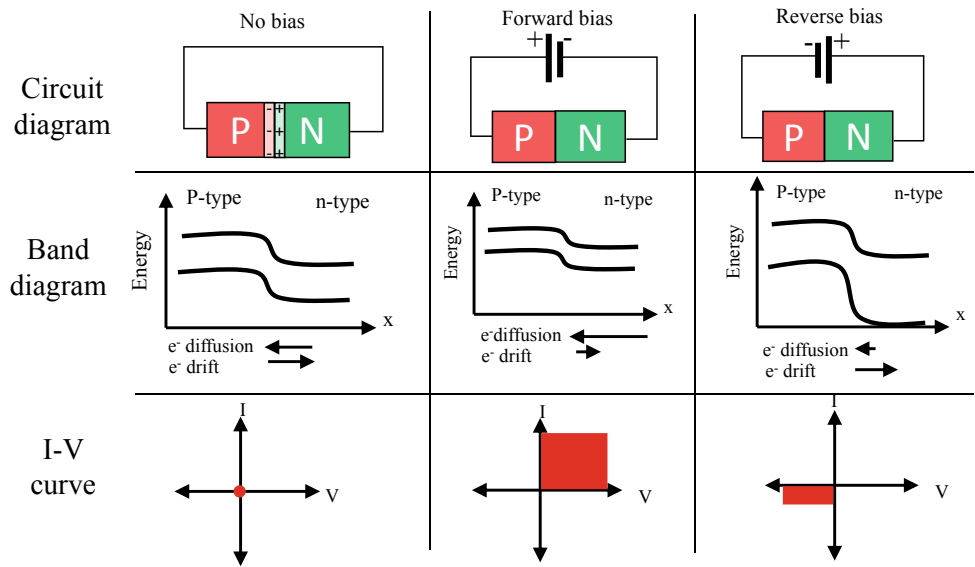


Fig. 11 *I-V* curves of a photovoltaic cell in dark and under illumination conditions

relationship in the silicon standard model is represented in Eq. 3.

$$I = I_{pv} - I_D - \frac{V + IR_S}{R_{Sh}} \tag{3}$$

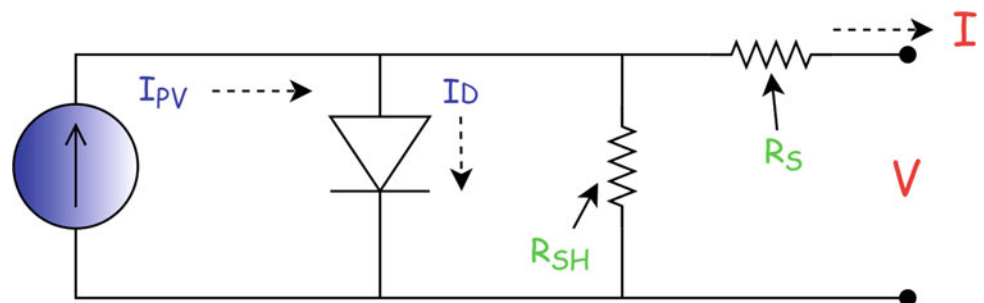
where I is the solar cell output current, I_{pv} is the photocurrent, I_D is the diode current, V is the output voltage, R_s is the series resistance, and R_{sh} is the shunt resistance, and Eq. 3 can be expanded and rewritten in the following form shown in Eq. 4, where I_s is the diode saturation current, m is the ideality factor, and V_T is the thermal voltage.

$$I = I_{pv} - I_s \left(e^{\frac{V}{mV_T}} - 1 \right) - \frac{V + IR_S}{R_{Sh}} \tag{4}$$

4.3 Performance Calculations

Figure 13 shows a standard solar cell light *J-V* curve. J stands for current density, which is a parameter that defines the current (I) over the area of a given solar cells.

Fig. 12 Silicon solar cell equivalent circuit



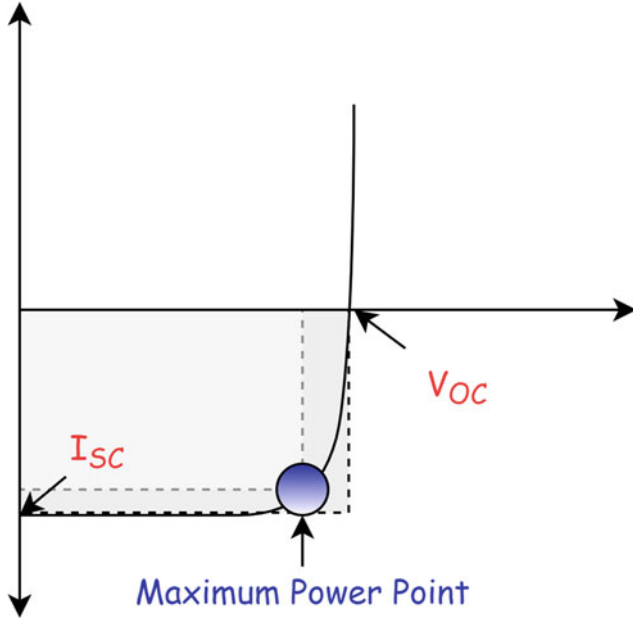


Fig. 13 Light J - V curve of a typical solar cell

Current density helps with comparing different solar cells regardless of their given area, given that increasing the area ultimately increases the area of photon collection and by that the resultant current. The short-circuit current density, which is the intersection of the J - V curve with the y-axis in Fig. 13, is the photocurrent I_{pv} in Fig. 11 divided by the cell area. The short-circuit current density is linearly proportional to the rate of the incident photon energy, which is known as solar irradiance, such as shown in Eq. 5, where E_{STC} is the irradiance under standard testing conditions with a value of 1000 W m^{-2} .

$$J_{SC_E} = J_{SC_{E_{STC}}} \left(\frac{E}{E_{STC}} \right) \quad (5)$$

In terms of voltage, an important parameter is the open-circuit voltage, that is represented by the intersection with the x-axis in Fig. 11. The open-circuit voltage is calculated using Eq. 6:

$$V_{OC} = mV_T \ln \left(\frac{I_{SC}}{I_S} \right) \quad (6)$$

The open-circuit voltage is logarithmically related to the incident solar irradiance and follows a behavior indicated by Eq. 7, where $V_{OC_{E_{STC}}}$ is the open-circuit voltage at STC conditions:

$$V_{OC} = V_{OC_{E_{STC}}} + mV_T \ln \left(\frac{E}{E_{STC}} \right) \quad (7)$$

The shunt and series resistances can be graphically obtained by taking the inverse of the slope of the tangent to

the short-circuit current and open-circuit voltage points in Fig. 13, respectively.

The ideality factor m , shown in Eq. 4, represents the deviation of a solar cell behavior from an ideal diode. The fill factor of a light J - V curve gives a representation of the electrical performance of a solar cell. It correlates the maximum power point parameters (maximum power point current density J_{MPP} and voltage V_{MPP}), as well as the short-circuit current density (J_{SC}) and the open-circuit voltage (V_{OC}), such as shown in Eq. 8.

$$FF = \frac{J_{MPP} \times V_{MPP}}{J_{SC} \times V_{OC}} \quad (8)$$

The efficiency of a solar cell compares the maximum power obtained from a light J - V curve, usually because in practical operations maximum power point tracking is used to ensure that the cells/modules operate only at the maximum power point, to the incident irradiance (E). The efficiency (η) calculation is carried out in Eq. 9:

$$\eta = \frac{P_{Max}}{E \times A} = \frac{I_{Max} \times V_{Max}}{E \times A} = \frac{J_{Max} \times V_{Max}}{E} \quad (9)$$

The ideality factor, series, and shunt resistance are usually obtained from a “dark” J - V / I - V curve rather than an illuminated one, such as was shown in Fig. 11, given that an illuminated J - V curve is obstructed by a noisy generated photocurrent. However, a simple plot between the dark current density and voltage does not reveal information about the ideality factor of the diode in the equivalent circuit, and semi-log plot is usually preferred over it, as shown in Fig. 14.

From the semi-log dark J - V curve shown in Fig. 14, the ideality factor can be extracted using Eq. 10, where $\ln(J_s)$ is the y-axis intersection of the semi-log dark J - V curve and

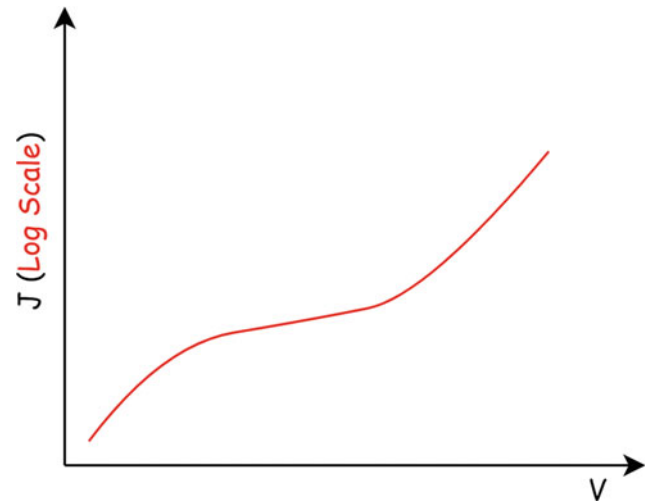


Fig. 14 Semi-log dark J - V curve

$\frac{1}{mV_T}$ is the slope. The ideality factor can be obtained graphically by taking the slope, or numerically by extracting data points and substituting them into the equation. Based on the presented equation, the ideality factor can also be taken as a function of voltage, such as shown in Fig. 15, where the ideality factor at low voltages is dominated by the shunt resistance and at high voltages by the series resistance.

$$\ln(J) = \ln(J_S) + \frac{1}{mV_T} V \quad (10)$$

5 Generation and Recombination

Photogeneration occurs during light absorption, which generates mobile electrons and holes, the carriers lose any extra kinetic energy when they harbor energies above that of the bandgap. The bandgap should be chosen properly so that the excess energy carried by the electrons deep into the conduction band of the semiconductor is not wasted in the form of thermal energy.

During recombination, which can be caused by inefficient charge separation, uneven doping or short diffusion lengths, electrons are recombined with their hand-in-hand-generated holes and the energy that was previously absorbed by the electrons is re-emitted in various forms.

There are two types of recombination: (5.1) unavoidable and (5.2) avoidable recombination.

5.1 Unavoidable Recombination

The unavoidable recombination occurs due to two reasons:

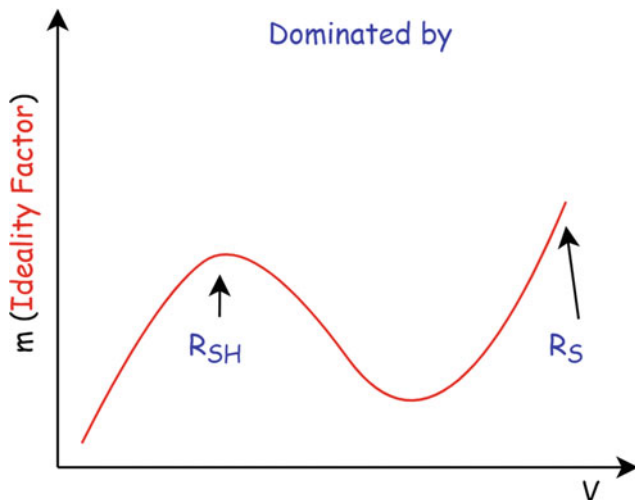


Fig. 15 Ideality factor versus voltage

- Spontaneous emission (or radiative recombination), which happens due to over excitement of electrons as shown in Fig. 16a.
- Stimulated emission (or Auger recombination), where an electron and a hole recombine, and the energy is not emitted as heat or light, instead it's given to a third carrier, an electron in the conduction band as shown in Fig. 16b.

5.2 Avoidable Recombination

The avoidable recombination involves recombination that happens due to the solar cell defects and is not emitted anywhere else. These defects can be instigated by foreign atoms, excluding the desired doping atoms, such as sulfur and iron in the form of electron traps inside the forbidden bandgap.

- Sulfur atoms create shallow traps with energies near that of the conduction band. Electrons fall easily into these traps, but they require very little energy to be transferred back into the conduction band and isn't likely to cause severe recombination effects.
- Iron atoms on the other hand are responsible for what are known as deep traps. These traps are usually located near the middle of the forbidden bandgap and electrons are not easily trapped by them. However, when they do, it requires almost half of the energy initially absorbed from the incident photon for the electron to be launched into the conduction band again, which results in almost certain recombination for any electron that falls into these traps. This is shown in Fig. 17.

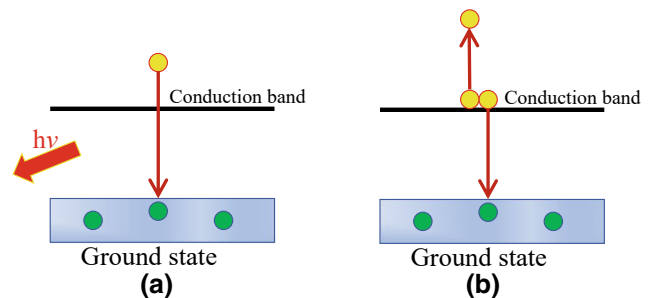
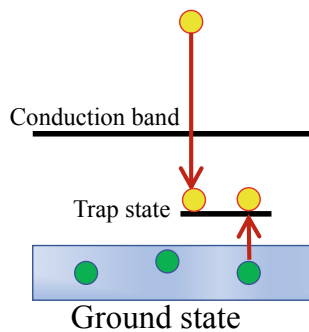


Fig. 16 Unavoidable recombination: a radiative recombination and b Auger recombination

Fig. 17 Avoidable recombination as in trap state recombination around defects or grain boundaries



References

- Alami AH, Abed J, Almheiri M, Alketbi A (2015) The Fe-Cu metastable nano-scale compound for enhanced absorption in the UV-Vis and NIR ranges. *Metall Mater Trans E* 2(4):229–235. <https://doi.org/10.1007/s40553-015-0060-y>
- Alami AH, Zhang D, Aokal C, Abed J, Abdoun IA, Alawadhi H (2016a) Influence of magnetic field on the mesoporous structure of Fe-Cu compounds in dye-sensitized photovoltaic cells. *Metall Mater Trans E* 3(1):37–45. <https://doi.org/10.1007/s40553-016-0067-z>
- Alami AH, Abed J, Almheiri M, Alketbi A, Aokal C (2016b) Fe-Cu metastable material as a mesoporous layer for dye-sensitized solar cells. *Energy Sci Eng* 4(2). <https://doi.org/10.1002/ese3.114>
- Band Gap—Wikipedia. https://en.wikipedia.org/wiki/Band_gap. Accessed 7 Aug 2022
- Bandgap Comparison. https://upload.wikimedia.org/wikipedia/commons/thumb/0/0b/Band_gap_comparison.svg/2000px-Band_gap_comparison.svg.png. Accessed 7 Aug 2022
- Shockley–Queisser Limit—Wikipedia. https://en.wikipedia.org/wiki/Shockley%E2%80%93Queisser_limit#/media/File:ShockleyQueisser_FullCurve.svg. Accessed 7 Aug 2022
- Simple Periodic Table Chart-Blocks—Wikimedia Commons” <https://commons.wikimedia.org/w/index.php?curid=98955505>. Accessed 7 Aug 2022

Alami AH, Abed J, Almheiri M, Alketbi A (2015) The Fe-Cu metastable nano-scale compound for enhanced absorption in the



Manufacturing of Silicon Solar Cells and Modules

Abdul Hai Alami[✉], Shamma Alasad[✉], Haya Aljaghoub[✉],
Mohamad Ayoub[✉], Adnan Alashkar[✉], Ayman Mdallal[✉],
and Ranem Hasan[✉]

Abstract

To get from cell making to module making requires proper preparation of pristine wafers to be physically and electrically connected in series to achieve the rated output of a PV module. This chapter highlights the “silicon wafer to PV module” journey, with all pertinent steps of optically and electrically augmenting each wafer explained in details. The steps of connecting, co-firing and testing of the modules are also given.

1 Introduction

Silicon-based solar cells (and consequently modules) still dominate the PV market (more than 85%) compared to other commercially available thin film and third-generation photovoltaics. Apart from the obvious reasons of well-established silicon manufacturing processes developed originally for microprocessors, the abundance of silicon as silicon oxide in Earth’s crust is another reason. However, not any “sand” is appropriate for wafer-building purposes. Quartz is a crystalline form of silicon oxide that can be

harvested with less chances of containing contaminants within the collected aggregate. These quartz particles, available in Unimin’s mines near Charlotte, North Carolina, can be described as ultra-pure compared to their silica counterparts available elsewhere in the world (Beiser 2018).

Terrestrial photovoltaic made from silicon starts as p-type monocrystalline Czochralski (Cz) silicon substrates. But due to the lower cost of multi-crystalline (mc) silicon, in the 1980s mc silicon wafers rose as a potential candidate to replace single-crystalline (sc) ones. On the other hand, their lower metallurgical quality due to the presence of defects in the form of grain boundaries has precluded achieving efficiencies similar to those of Cz, so that both technologies shared a rather constant and equal figure of merit (\$/W). With progress in silicon manufacturing technologies, a monocrystalline solar cell made a gradual comeback since the mid-2000s, as evident from Fig. 1. The high efficiencies of such cells as well as their aesthetic presence (since they are a darker shade of the usual blue of multi-crystalline-Si cells) made consumers and producers cause an increase in demand for monocrystalline modules.

On the other hand, the production of mc-Si has not slowed down either. As mentioned before, after 2007, the market has been presented with new opportunities in the Chinese market. The manufacturing processes’ yield and economics have yet again tipped the scale towards the multi-crystalline side. The mass production of such p-doped wafers not only enhanced their figure of merit, but also drove many wafer-making companies around the world out of business, such as Al Mulk holding who used to manufacture solar panels in the United Arab Emirates and currently the focused on installing them (UAE-based Mulk Holdings International pens JV agreement to enter US market 2021). This is clearly shown in Fig. 2 which demonstrates a clear advantage for mc-Si that has only been cemented in the years after (Miles et al. 2007).

Apart from economic aspects that are necessary for manufacturing firms to survive, there are various interrelated

A. H. Alami (✉) · H. Aljaghoub · M. Ayoub · A. Mdallal ·
R. Hasan
University of Sharjah, Sharjah, United Arab Emirates
e-mail: aalalami@sharjah.ac.ae

H. Aljaghoub
e-mail: haljaghoub@sharjah.ac.ae

M. Ayoub
e-mail: mohamad.ayoub@sharjah.ac.ae

A. Mdallal
e-mail: ayman.mdallal@sharjah.ac.ae

S. Alasad · A. Alashkar
American University of Sharjah, Sharjah, United Arab Emirates
e-mail: g00070854@aus.edu

A. Alashkar
e-mail: b00028197@alumni.aus.edu

Fig. 1 Global market share of PV technologies (https://commons.wikimedia.org/wiki/File:Global_Market_Share_by_PV_Technology_from_1990_to_2013.svg)

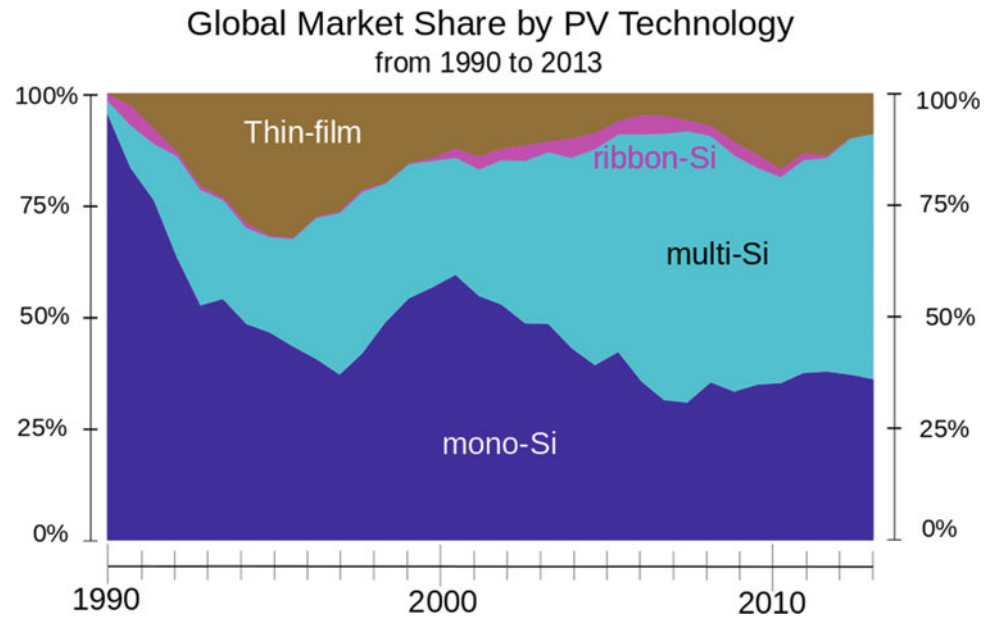
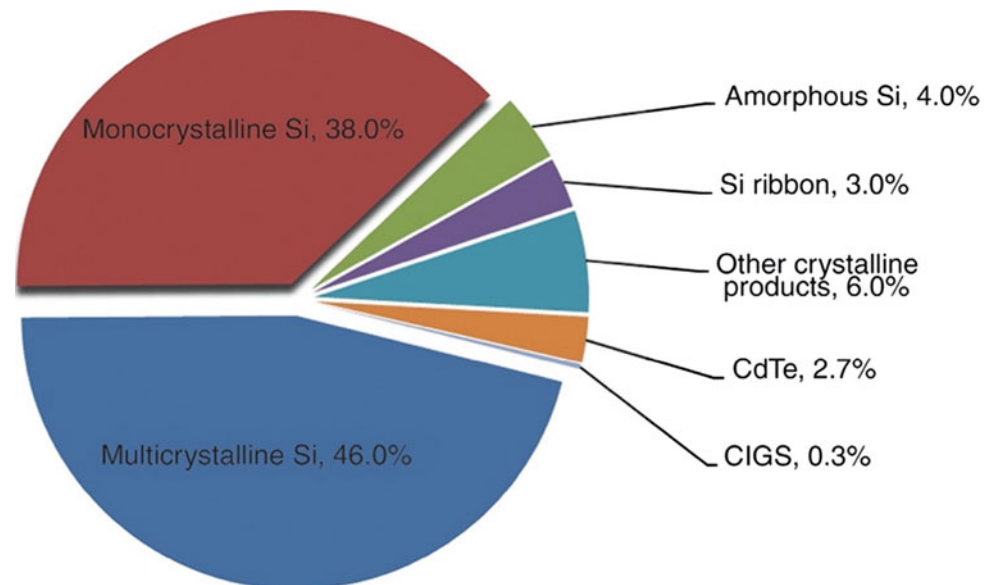


Fig. 2 Solar cell technologies contribution in 2006 (Miles et al. 2007)



parameters that are crucial to arrive at a functioning final product. The manufacturing process must integrate physical properties of the materials to their electrical performance, stability and optical performance in order to guarantee the reliability of produced solar cells. These cells will be electrically connected, encapsulated and installed, which also necessitates proper testing procedure before their dispatch to customers. The properties needed can thus be subdivided into surface and bulk properties as will be explained in the following sections.

2 Silicon Bulk Properties

The bulk properties of silicon solar cells are controlled by selecting a material that has the appropriate bandgap, selectively doping it to allow smooth movement of carriers without causing any undesirable recombination and reducing avoidable losses such as reflection or high sheet resistance as well as low carrier mobility. These main parameters are explained below.

2.1 Bandgap Selection and Tuning

Monocrystalline Si semiconductors have an indirect and a direct bandgap of $E_G = 1.17$ eV (exactly in the middle of the solar radiation) and 3 eV, respectively, at STC conditions. Two electron–hole pairs generation events are possible, however rather rare, caused by high-energy (low wavelength) UV photons. At longer wavelength than visible range (Vis: ~ 380 to 800 nm), any incident solar radiation causes the formation of excess charge carrier absorption that overshadows desired band-to-band generation and separation. In other words, care must be taken in operating silicon solar cells away from their designated wavelength range.

2.2 Carrier Concentration

The intrinsic carrier concentration links the imperfections and the disequilibrium of the crystal lattice to the potential voltage generation. At high carrier densities caused by excessive doping, the band structure is altered, which exposes more charge carriers and increases the effective intrinsic concentration. Moreover, the quality of the targeted regions (doped) is inversely related to the doping level. Although it is intuitive that having more carriers would mean better electron/hole diffusion within the material towards the contacts as seen in Fig. 3, too many carriers available is likely to slow the diffusion due to the crowding of similarly charged species that tend to generate repulsive forces. The reader is reminded at this point that the solar cell has two processes that should proceed in equilibrium, the first is the electron diffusion (through carriers) through the bulk of the material and the second is the electron motion outside of the cell and through the selected electrical load.

2.3 Recombination

The timeframe for a photogeneration event, their separation and transportation to respective side of the solar cell can be measured on a femto-second scale. Characterization and

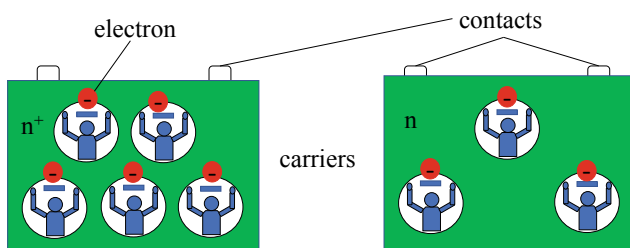


Fig. 3 High concentration of carriers (n^+) compared to ideally doped n -type regions

observation equipment capable of pursuing such processes are either economically unavailable or require extensive retrofitting to allow the observation of how electron/hole pairs are generated and how to coerce them to separate and follow the desired path to allow the cell to operate at highest quantum efficiency. Usually, recombination within the structures of Si semiconductors is governed by defects and grain boundaries are described as Shockley–Read–Hall (SRH) lifetimes and can be described by avoidable and nonavoidable recombination. The associated lifetime τ (defined with respect to the diffusion length L , which is a small portion of the solar cell overall thickness) increases for good quality materials. Remember that:

1. At higher concentrations, Auger recombination becomes more prominent (a nonavoidable recombination). Excitonic effects have also been noted to intensify Auger coefficients at high or near-high (moderate) carrier densities.
2. Band-to-band direct recombination, although a base mechanism for electron–hole pair recombination, is insignificant quantitatively. It is still nonavoidable recombination but has lower effect than Auger because it requires high-energy conversion levels.

2.4 Electron Mobility

Electrons possess mobilities that are almost triple those of holes at low or near-low (moderate) concentrations. Note that scattering caused by defects and carrier–carrier scattering are highly manifested at higher doping densities and high injected materials, respectively.

2.5 Surface Contacts

To allow electrons to reach the intended electrical load, they need to diffuse from their generated locations through available carriers to the contacts (see Fig. 3). Contacts form an interconnected network to connect the electrical circuit consisting of the solar cell and the electrical load, which are scaffolded on top of the Si solar cell surface. Even though these contacts are essential for charge carrier extraction, they cause shading as they cover 5–10% of the area exposed to incident solar radiation. Another issue is the increased series resistance as the interface between the contact and the bulk silicon material is not perfect. All the while the charge separation has to be planned to minimize recombination and slow diffusion rates which reduces the overall efficiency (through fill factor reductions) of the solar cell.

As will be explained later, a heavily doped region (n^+ , n^{++} , p^+ or p^{++}) under each of the contacts is added and would act like a conveyor belt to pump electrons or holes towards the contact in the n-region or the back-surface field, respectively. This allows the majority carriers to permeate and reach the targeted contact at a low voltage loss (but with significant resistance). The flow of minority carriers (electrons in P-regions and vice versa) is best described as the surface recombination velocity (SRV) or *S for short*. Usually, the surface recombination velocity is high ($S = 10^6 \text{ cm s}^{-1}$) and is limited only by thermal diffusion.

3 Crystalline Silicon Solar Cells

Considering the previous discussion, there are certain parameters that can be identified to augment the overall efficiency of the cell by focusing on the optimization of said parameters. Thus, the following are four cardinal rules to minimize avoidable losses:

1. Reflection events are attenuated and minimized to low levels using light trapping techniques.
2. Minimum recombination is allowed: Only Auger and radiative recombination mechanisms are accounted for.
3. Ideal contacts exhibiting no shading or series resistance losses.
4. No recombination losses while charge carriers are transported across the thickness of the cell (flat carrier profile).

Champion efficiency cells use intrinsic material to regulate and reduce the Auger recombination as well as free-carrier absorption. This cell is less than $100 \mu\text{m}$ thick, which is a trade-off between the required absorption and minimal nonavoidable expected recombination. Considering the thermodynamical limit, a 29% maximum efficiency is obtained under STC conditions.

3.1 Cell Contact Design

If contacts are placed on the top of the cell, it would intuitively satisfy rule #4 placing them as close as possible to photogeneration events. On the other hand, this will cause shading and thus the violation of rule #1, as shown in Fig. 4a.

To avoid such complications, contacts can be placed at the bottom of the cell, as in Fig. 4b which theoretically guarantees a high efficiency (23%) but might require altering doping concentration on the top because since the holes are lighter than electrons. The latter fact suggests that the best solution is to put the contact per face as in Fig. 4c which is

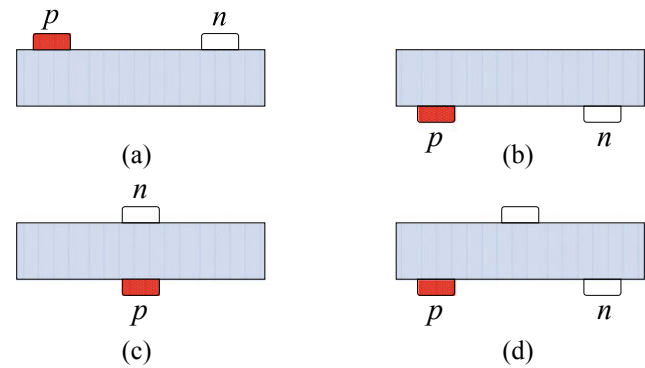


Fig. 4 Permutations of contacts placed on wafers

simpler. Minority carriers (electrons in P-substrates) in the substrate are usually extracted at the front (top) face, given that their low density hinders their collection probability. The diffusion length represents the maximum material thickness a charge carrier can cross before it is depleted (recombined). On the other hand, majority of carriers with their high diffusion length can travel all the way to the back surface for simpler collection. Several designs implemented minority carrier extraction contacts at both the front and back of cells for higher utilization of photogeneration events, as shown in Fig. 4d.

3.2 PERL and Commercial Cells

The passivated emitter rear locally diffused (or PERL for short) solar cells harbour efficiencies bordering 25% under STC, due to the implementation of novel micro-electronic techniques (Magsi 2014). The term “passivated emitter” relates to the formed high-quality oxide at the front surface of the cell that attenuates the phenomenon of charge carrier recombination in that region and improves the overall efficiency. The rear is locally diffused only at the metal contacts, to prevent recombination and retain a good electrical contact. This will be presented in detail later in this chapter.

Both laboratory-level solar cells with nearly 25% efficiency shown in Fig. 5a and commercially available ones have efficiency levels of 16% (for multi-Si) and 17% (for mono-Si) as shown in Fig. 5b. These cells display the contacting structure of one contact per face. The cell performance is shown in Table 1.

4 Conventional Solar Cell Manufacturing

The following sections will focus on most important parameters for solar cell building and how to optimize each in order to arrive at a device that functions optimally.

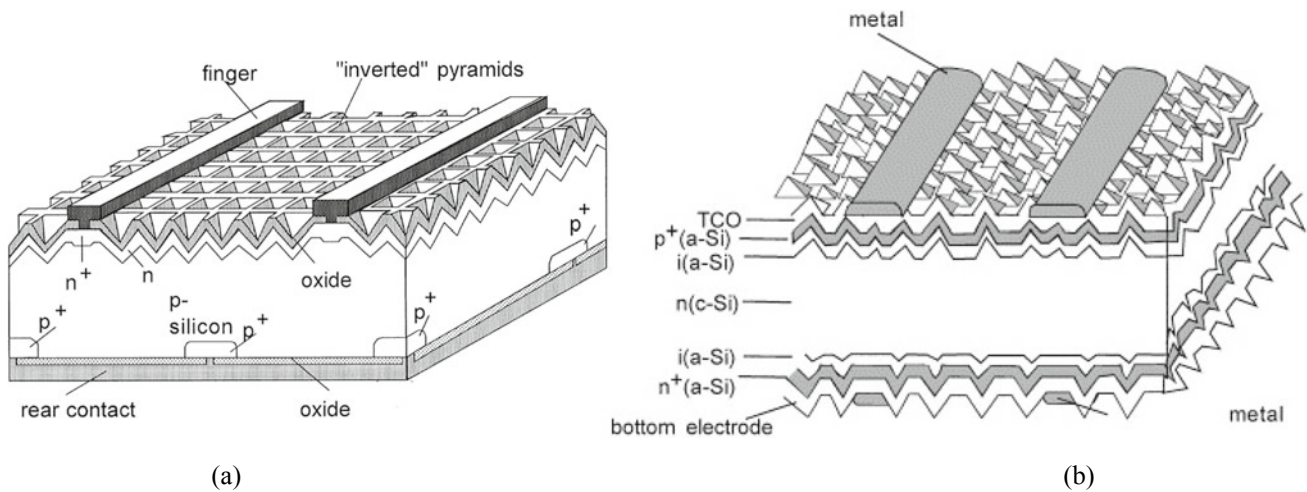


Fig. 5 a PERL versus b commercial solar cells (Green et al. 2001) (with permission 5364101367492)

Table 1 Cell performance (Bai et al. 2020)

Cell type	Ideal parameters (calculations)	Passivated emitter rear locally diffused solar cell (PERL)	Industrial solar cells' average parameters
Size, cm ²	–	4	225
Thickness, μm	80	450	250
Sheet resistance, Ωcm	Intrinsic	0.5	1
Short circuit current density, Acm ⁻²	0.0425	0.0422	0.034
Open circuit voltage, V	0.765	0.702	0.600
Fill factor, FF	0.890	0.828	0.740
Efficiency, %	28.8	24.7	15.0

4.1 Substrate Selection

Monocrystalline Cz-Si or float zone (FZ-Si) material shows the highest industrial performances with no defects in the form of grain boundaries, where there are light contamination levels of both metallic and oxygen, nitrogen and carbon (O, N, C) impurities, which leads to durable SRH lifetimes (~1 ms), however still short of the Auger limit. Magnetic Czochralski (MCz) processing of the silicon material harbours less concentrations of oxygen than sole Cz-Si and thus providing the base for higher efficiency solar cells (less O₂ = less SiO₂ = less defects = long lifetime = high efficiency). The process is, however, prohibitively expensive.

With better production economics and manufacturing technologies, commercially established photovoltaic cells are based on block/ribbon MC-Si P-substrates. Moreover, crystal defects including grain boundaries, lattice dislocations and metal impurities are more prominent than Cz or Fz because of lesser time for precipitation and gettering due to the rather rapid solidification of monocrystalline silicon. As a result, the lifetime within multi-crystalline silicon is understandably lower. This, however, can be mitigated by

applying various modifications and additions to the manufacturing process that would diminish the potent metallurgical effects. For example, using gettering techniques is known to reduce contaminant impurities resulting in less dominance of avoidable lifetime reducers. This can be achieved by adding getters. In a gettering process, a sacrificial region is formed, able to trap impurities that reduce the lifetime of charge carriers in such a way that no adverse effects are borne on the device being manufactured, or at least where they are accessible and conveniently etched off. However, due to the high concentration of impurities, this deems the getter region as “electrically dead”, which adversely affects the UV response of the manufactured device.

4.2 Doping Level and Type

Controlling the doping level can control the recombination and the series resistance. A suitable doping level is determined after an optimization process considering the structure of the cell and the governing recombination mechanism.

Boron doped (P-Substrates) hold the champion efficiency for laboratory scale cells as well as lucrative low costs for industrial applications. Such substrates harbour high Auger limiting charge carrier lifetimes; however with higher SRH recombination, higher doping levels are achieved to decrease the density of charge carriers (increase the rate of recombination), at a given voltage, while this is compensated by the reduction of the lifetime. The series resistance is also reduced at high doping levels, which is prominent in thick cells and affects the electron transport to the back surface of the cell. 10^{16} cm^{-3} doping levels are present in industrial cells. Point contact cells have achieved high efficiencies, however, with both low (PERL cells— $1 \Omega\text{cm}$) and high substrate resistivities.

4.3 Cell Thickness

In cells with high diffusion lengths with respect to the device thickness, surface recombination arises as a severe issue: if the surface recombination speed (S) is higher than diffusion length/device thickness ratio for minority carriers ($\sim 250 \text{ cm s}^{-1}$ for high performing cells), decreasing the thickness of a given cell for a given voltage increases the recombination. Although thin cells absorb less light (due to penetration depth), this can be countered by light trapping techniques. Moreover, thinner cells require more expensive feedstock material, which increases the cost and hinders the ability to industrialize thin cells. Also, technologically evolved wafering methods allow processing of very thin, large-area substrates with least breakage rates, which otherwise could lead to a large scrap fraction due to breakages during processing and transporting between processing stations. It should be mentioned here that light trapping and surface recombination are limiting factors on imposing cell thickness. With the addition of a BSF (rear passivation), the typical thickness for a solar cell has been normalized to be $200 \mu\text{m}$ which is compatible with minority carrier lifetimes.

4.4 Front Surface

A grid of metallic fingers is used at the forefront of solar cells to gather the rather segregated photogenerated charge carriers. An optimization process must be carried out between the transparency of the front surface of the cell and the series resistance as there is a trade-off between the two factors, in order to produce thick, conductive metal fingers with low series (contact) resistance. These two requirements are important, but they have an inverse relationship. Contacts carry electrons from the cell bulk to the external load, but they reduce transparency and reduce series resistance.

Thin fingers in the range of $\sim 15 \mu\text{m}$ are obtained for lab-scale solar cells using physical evaporation or photolithography processes. The choice of materials for these thin metal fingers should consider good conductivity, manufacturability as well as good compatibility (low interfacial resistance) with the bulk silicon. Material combinations such as Ti/Pd/Ag are suitable with n-type silicon producing high conductivity. Nickel possesses these characteristics but is not amenable for mass production. Nickel plating of laser-carved grooves results in $40 \mu\text{m}$ deep and $20 \mu\text{m}$ wide fingers. Laser-grooved buried grid, previously used in highest efficiency, does not suffer from coarse metallization techniques or high shading and resistance losses.

$100 \mu\text{m}$ wide lines based on screen-printed silver pastes are utilized in commercially available cells. Laser-grooved, buried grids are usually used in highest efficiency since it does not suffer from coarse metallization techniques or high shading and resistance losses, but it would complicate the manufacturing process and increase production time of a cell.

4.5 Homogenous Emitters

Under the metal lines of the contacts, the substrate benefits from heavy doping (n^+ or n^{++}) to make the contact selective and decrease recombination. Think of a conveyor belt that pulls electrons or holes to the contact. The doped region of the emitter (called emitter and has to be as thin as possible to reduce possibility of the recombination of the recently generated electron/hole pairs) covers the top surface of the solar cell offering minority carriers a gateway to be collected by the metallic contact fingers as shown in Fig. 6.

The challenge that remains for exposed surfaces that are electronically conductive is that they allow recombination to occur before the electron is transported into the external load. This highlights the importance of having passivated emitters, where the emitter (n-region) is thin and subjects minority carriers to high surface recombination velocities which results in poor collection of the generated charge carries in that region.

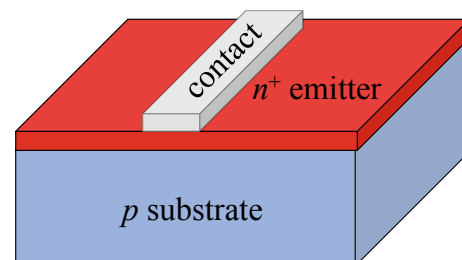


Fig. 6 Heavily doped (n^+) emitter layer underneath contact finger

Thin and highly n -doped regions surrounding the interface with the contacts (and only there) act as a pump for charge carriers while allowing the surface to be passivated as shown in Fig. 7. Lowering the doping levels in the bulk has a positive effect on the charge collection efficiency of the emitter to avoid wide-scale heavy doping and its undesirable effects. This localized higher concentration doping lowers the sheet resistance and diminishes recombination at the metallic interface by increasing the depth of the emitter. If charge carriers are said to be collected at the top surface of the solar cell, this gives away that the thickness of the emitter is less than the diffusion length of the minority carriers, which further implies a high SRV. Recombination can be further mitigated by making the interface between the emitter and the finger narrower than the finger by using laser grooving. The emitter can be made as deep as $1\ \mu\text{m}$, enhancing the contact conductance.

Further improvement involves enhancing the diffusion in different regions since requirements are so different yet can be discretized. For example, Fig. 8 depicts a strongly doped n -type emitter (n^{++}) and thick region right underneath the fingers surrounded by a thin and lightly doped (n^+) area right underneath the passivating layer.

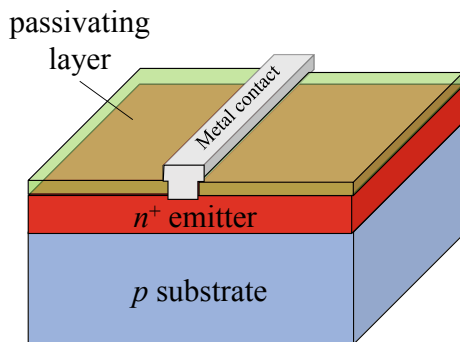


Fig. 7 Adding a passivating layer on top of emitter to ensure surface passivation

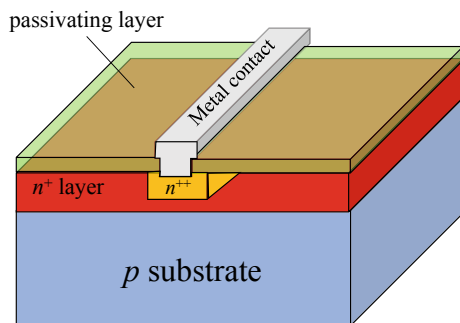


Fig. 8 Adding a heavily doped n^{++} layer right underneath the contact to enhance electron diffusion

These “selective emitters” need complicated photolithographic processing. These point emitters work best in concentrating applications (more than one sun). Small cross-section metal finger reduces series resistance.

4.6 Heterojunction Solar Cell Structure

Although it is a trait of third-generation solar cells, a transparent electrode fully covered solar cell front surface with a middle amorphous silicon layer reduces the interface recombination levels and a screen-printed grid helps with the lateral conductance. The topology of such layout is shown in Fig. 9.

Highly doped emitter decreases the contact resistance, and the layer can be buried at a shallower region so that it is not pierced during the metal finger firing and co-firing which can potentially short-circuit the junction. Moreover, metal fingers must be spaced apart to keep shading losses in order, which means that emitter and lateral conductance must also be high.

5 Industrial Cells

Commercial phosphorus-doped emitters can boast surface concentrations over $10^{19}\ \text{cm}^{-3}$ and are $0.4\ \mu\text{m}$ deep, along with $60\ \Omega\text{cm}$ sheet resistance. The highly doped region harbours a high level of getter and precipitated foreign materials (due to heavy phosphorous doping) resulting in an electrically dead layer, where the collection of short wavelength photons is improbable, with a large intrinsic current density. SiN_x suits the purpose of surface passivation which allows for screen-printed cells to incorporate selective emitters.

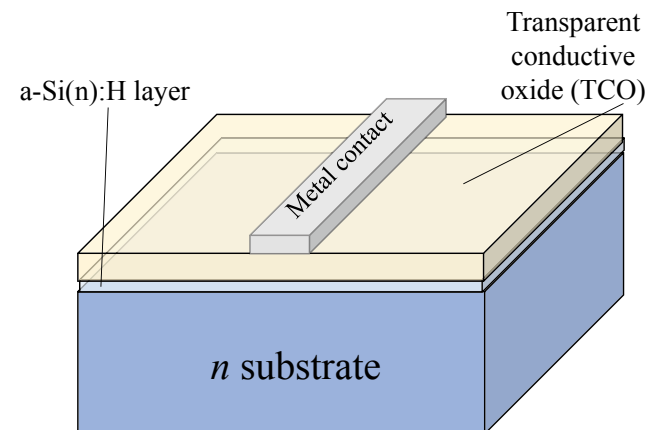


Fig. 9 Topology of a heterojunction solar cells

5.1 Back Surface Field

The back-surface field (BSF) is the hole collector. It needs not to be transparent like the emitter and thus is usually made of a thin layer of metal (preferably gold). The BSF can take advantage of a p^+ layer in order to decrease contact recombination for cells with $w < L$.

Most commercial cells can boast a screen-printed or thermally evaporated aluminium BSF with a subsequent silver (Ag) or an Ag–Al solid solution electrode. The contact can cover the whole surface and need not be in the form of a contact finger and can cover the entire back surface with a reflective layer that can assist in reflecting unabsorbed solar radiation and allow the cell a second chance to use it. An example of the back-surface field is shown in Fig. 10.

5.2 Cell Size Effects

Although larger size solar cells allow for more W/m^2 of solar irradiance absorption, working with such cells has many disadvantages from operational point of view (larger size allows more recombination events and longer distance to reach contacts which will decrease efficiency). It is known that the area of a given cell determines the device's end efficiency in lab-scale cells. And since the emitter region is contoured by masking or etching, the effective edge of the emitter is located at a respectable distance from cell's edge, which reduces recombination, as surface edges act as a hub for surface recombination that negatively affects high diffusion length devices.

Cell sizes preferred by the industry usually 12.5×12.5 cm or 15.6×15.6 cm are the norm. Apart from manufacturability issues, increasing the size of a given cell, increases the spacing between the charge carrier collection terminals, thus increasing joule losses. The electric resistance of the metal fingers is proportional to the quadratic power of its length. The mitigation of the resulting series

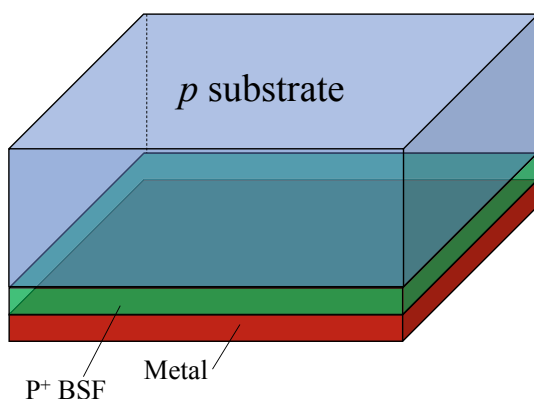


Fig. 10 Topology of the back-surface field (BSF)

resistance happens at cost of increased shading as increasing the number of terminals connected to the busbars, decreases the distance that charge carriers have to cross from the metal fingers connected to them. Another deciding factor comes from the manufacturing process of the original silicon ingot. Cz silicon is limited by the surface tension of the silicon growing around the seed crystal during production.

5.3 Cell Optics

The efficiency of a cell largely varies depending on how much incident solar radiation it can absorb. Not only due to intrinsic parameters, such as the material bandgap, but also external factors such as the surface condition of the cell. Ideally, cells must optically absorb photons from the whole spectral range of the hemisphere. For uniformity and comparison of different solar cells, a standard spectral distribution of an air mass (AM) is 1.5 and 0.1 W cm^{-2} is used. Global incident irradiation is considered at 25°C . Metal grid shading propels the level of optical losses in non-encapsulated cells. Various solutions have been both proposed and implemented to mitigate shading losses by deploying shaped fingers with a prismatic top. Industrial scale cells harbour an optical loss of the order 7% while lab-scale cells are much lower.

Next comes the losses due to direct reflection, which can amount to as much as 30% of the incident radiation for bare silicon in air due to its high refractive index. This necessitates the utilization of an anti-reflection coating (ARC) on top of the emitter. This works exactly like ARC layers on spectacles, where light will reflect off the glasses and affect communication quality if others cannot see one's eyes, as shown in Fig. 11. Adding the ARC to the emitter will prevent reflection at the outset and allow the cell the opportunity to absorb light. This reflectance can be attenuated and



Fig. 11 Spectacles **a** without anti-reflection coating (ARC) and **b** with ARC (<https://www.allaboutvision.com/lenses/anti-reflective.htm>)

can reach up to zero reflection, by utilizing a non-absorbing layer on top of the Si substrate surface with a different refractive index (nARC).

Snell law states that reflection is minimal when the thickness of the layer of a certain material is an odd multiple of quarter of the free space wavelength. Adding a thin layer of a dielectric material decreases the level of reflection due to effective interference effects which would help enhance cell output. In other cases, reflection increases up to the value of ARC, however never above it. ARC is usually at a refraction value calculated by taking the average of the refraction index of air and the targeted material (Si in this case) at 600 nm, where SiN_x is a viable material to be used at 2.4 refraction index, usually deposited by plasma enhanced chemical vapour deposition (PECVD).

5.4 Texturing of Cell Surface

Texturing exposes metallurgical planes or introduces random topological markings that scatter incident radiation within the material, as shown in Fig. 12. Chemically etched textures are utilized in both laboratory and industrial scale devices (silicon solar cells), with the addition of ARC, which reduces the optical reflection to desirable levels. Texturing can be done chemically (base or acid), mechanically or using photolithography techniques. In the case of acid etching, fine features are obtained of the inverted pyramids with a much more controllable geometry using photolithographic techniques. Thus, photons incident on the inverted pyramids (textured surface) are still normal to the cell in question.

5.5 Light Trapping

Silicon surface is only capable of weakly absorbing photons with low energy and high wavelength. Hence, unless

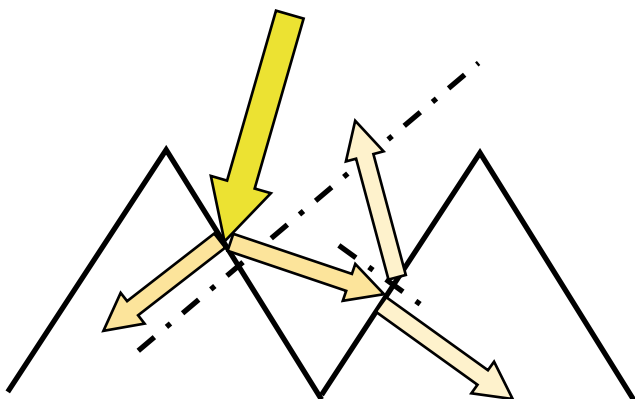


Fig. 12 Texturing effects on incident solar radiation causing multiple reflections within the material

the internal reflectance of the silicon is large, most of the photons will break out of the surface. In order to achieve high reflectance events, light trapping techniques are utilized. These events allow the cell material multiple chances at absorbing the light as it bounces back from the back-surface field or as it interacts with quantum-scale materials. Quantum dots made from special materials distributed near the surface of the cell are nano-scale material that amplify incident radiation via quantum-based interactions. These interactions are based on the dual nature of the light. Once the light hits the material quantum dots, it starts to vibrate/resonate and the light will be amplified. The BSF can turn into practical back mirrors since metals are good reflectors. Oxide structures such as Si-oxide-metal structure are able to produce large reflectance due to the optimization of the interference effects especially when it is etched, exposing the family of planes such as {111} or {001}. Light trapping improves the absorption of the wafer by increasing its effective thickness. In the case of one-side isotropic illumination in the geometrical optics regime, the maximum enhancement factor is calculated from knowing the refractive indices of silicon and air as follows:

$$F = 4 \left(\frac{n_{\text{Si}}}{n_{\text{air}}} \right)^2 \quad (1)$$

This means that each wave will resonate for fifty times within the cell thickness before escaping (remember that $n_{\text{Si}} = 3.5$ and $n_{\text{air}} = 1$). Due to high contest of absorption by free carriers at long wavelength, the improvement in the photogeneration will not be high.

6 Module Manufacturing Processes Overview

The quality of a solar photovoltaic module is a direct result of meticulous processing of individual solar cells. After the production of the wafer as per the discussion in the previous chapter, as well as the enhancement opportunities discussed above, a solar cell becomes ready to be incorporated into a module, where it is connected in series and in parallel to other cells. Figure 13 shows a general sequence of manufacturing processes to arrive at a quality solar cell.

6.1 Starting Materials and Processes

Solar-grade Cz-Si ingots are sliced into round wafers that are trimmed to a pseudo-square shape. The starting material can also consist of MC-Si square wafers with nominal

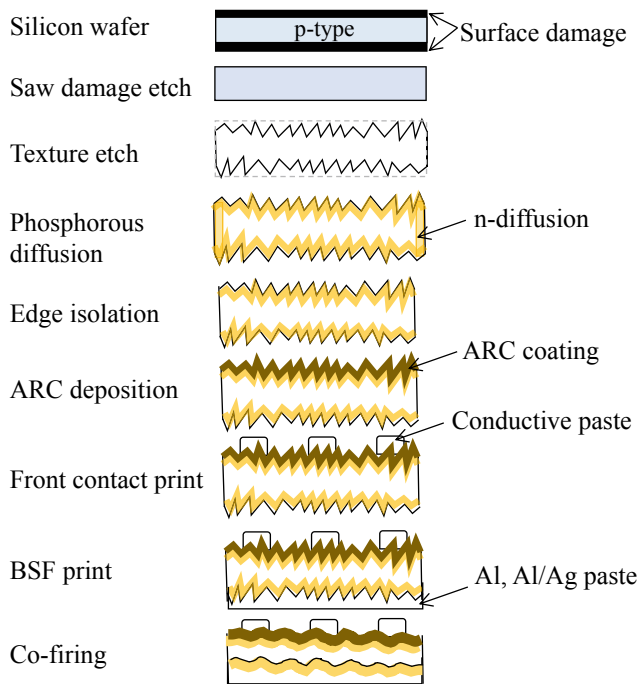


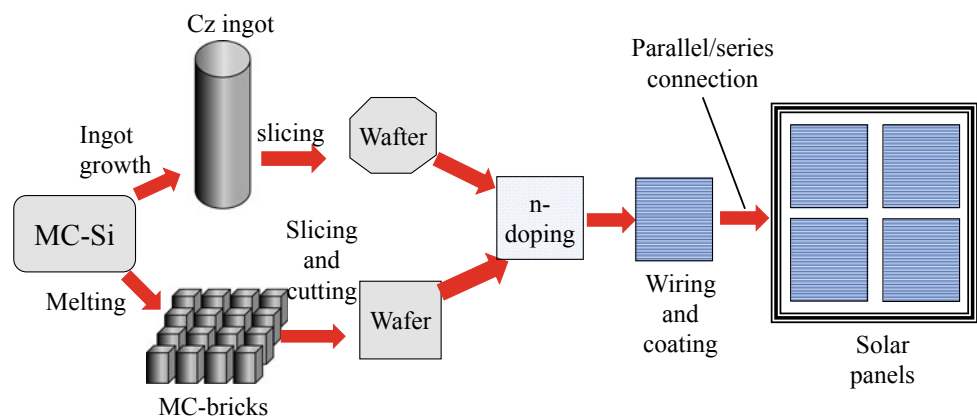
Fig. 13 Sequential manufacturing processes of a silicon solar cell

dimensions: 12.5×15.6 cm, a thickness: 180–200 μm (less is better) and standard doping of p-type (boron) to a resistivity 0.5–6 Ωcm . The diagram of Fig. 14 shows the general sequence of processes.

6.2 Saw Damage Removal

Sawing operations usually utilize abrasive materials (discs, wires, etc.) that are sure to leave the surface of wafers with an extensive damage and debris that is stuck to the outer rims of the wafer. This diminishes the quality of the surface region and renders the wafer incapable of reliably hosting further layers and/or causes the wafer to fracture during processing.

Fig. 14 General sequence of silicon wafer-to-module processing



This issue can be fixed in an acidic or alkaline bath, where 10 μm are etched off from each face. The wafers are placed in Teflon tapes that are submerged in tanks with a solution subjected to concentration and temperature regulation. Alkaline etches are advantageous to their acidic counterparts, due to their less hazardous waste. Nevertheless, acidic solutions are recommended for multi-crystalline material as they result in an isotropic structure.

6.3 Texturing

Texturing is used for cleaning and also to introduce a surface structure that allows light trapping. This can be done with chemical (acid/base), physical (plasma or laser) or mechanical etching.

6.3.1 Chemical Texturing

Potassium hydroxide (KOH) etching is applied for monocrystalline material as they form microscopic pyramids. However, pyramid size must be optimized as it affects the optical properties. For instance, sufficiently small pyramids tend to cause high reflection, whereas large ones tend to obstruct contact formation. This is shown in Fig. 15 (Al-Husseini and Lahlouh 2017), where the random-sized pyramids preclude omnidirectional reflections, promoting light reflection into the materials.

The shape and size of the pyramids as well as texturing coverage and adequate pyramid size depend on many factors including temperature, solution mixing and wafer residence time in the chemical bath. Practical bath parameters call for 5% KOH concentration at 80 $^{\circ}\text{C}$ for 15 min. Alcohol is usually added to enhance the wettability of the silicon surface, in turn enhancing the homogeneity of the solution. Anisotropic texture consisting of alkaline solutions is applied to multi-crystalline wafers; however, it yields extremely poor results. A drawback of alkaline etching is the existence of steps between grains, that can interrupt the subsequent screen-printing of metal contacts.

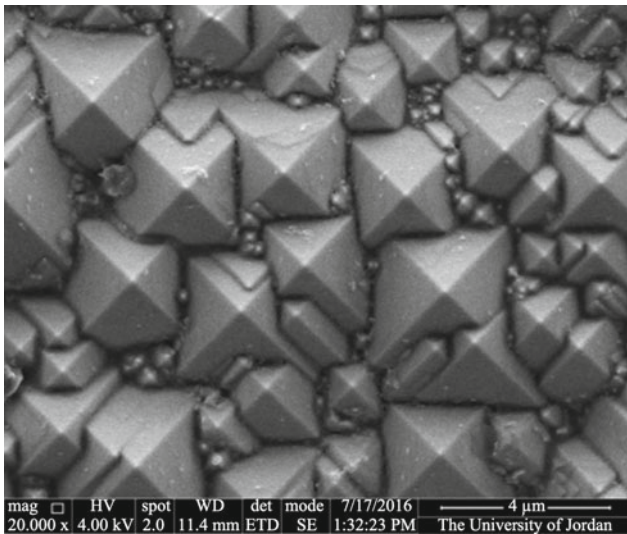


Fig. 15 Using KOH to texturize a silicon wafer results in random-sized pyramids (<https://scialert.net/fulltext/?doi=jas.2017.374.383>)

An acid can also be used, which results in an inverted pyramid structure that is preferred to ones resulting from alkaline texturing. But these pyramids require subsequent photolithographic patterning, that is a major disadvantage due to the compatibility complications with industry and process automation.

Nitric and hydrofluoric acids along with suitable additives present a more convenient method of etching, known as isotropic etching, which gives results similar to the one shown in Fig. 16.

This treatment results in uniformly distributed etch pits of 1–10 μm diameter. This can cause homogeneous reflectance over the surface of the wafer and the lack of steps between grains. The acidic chemical attack produces a porous silicon

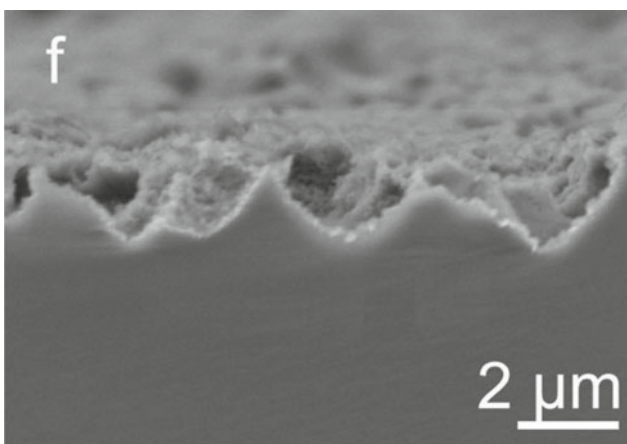


Fig. 16 Inverted pyramids produced by Hydrofluoric (HF) acidic etching of silicon (Gao et al. 2018)

layer before the etching process comes to halt. This is typically done in an alkaline solution. The acidic texturing results in a gain of short-circuit current of the order of 5–7%, but the acidic bath suffers from quick depletion of solution and exothermic effects, on top of environmental and health issues that accompany acid handling. This calls for a process redesign, involving automated wet benches that are able to manage the temperature of the etching solution and an automated process to refill the chemicals.

6.3.2 Plasma Texturing

Reactive ion etching (RIE) is a dry isotropic etching process that results in dense, porous and inclined and dimensionally limited pits usually less than 1 μm . The process is a texturization of silicon in a halogen plasma. The incorporation of these pits increases short-circuit current in the range of 10% compared with anisotropic textures as shown in Fig. 17 (Addonizio et al. 2019).

In order to create better regular features, RIE can be combined with a masking layer. However, the chemicals have the potential to elevate the severity global warming which is a disadvantage for industrial commercialization. Another disadvantage is the low process output data.

6.3.3 Mechanical Texturing

This process uses abrasive claws to mechanically introduce V-grooves about 50 μm deep on the Si wafers. The process is conducted through a traditional dicing saw, with a subsequent base etching to polish the surface and rid it of residue materials and saw damage. The average reflectivity is in the variety of 6–8%; in addition, the efficiency gains of 5% (relative) are obtained following encapsulation. Metal fingers (contacts) are screen printed in line with the etched grooves, on the unaltered regions.

Table 2 compares reflectivity gains at different wafer processing stages using texturing techniques discussed above (Macdonald et al. 2004).

6.4 Phosphorus Diffusion

Phosphorous diffusion refers to adding the *n*-type layer to the conventionally *p*-doped starting wafer. Solid-state diffusion can only take place at high temperature and a controlled atmosphere of the intended dopant. Two processes are available: either a batch process in a quartz furnace or a continuous process in a belt furnace.

6.4.1 Quartz Furnace

A quartz furnace with wafers placed in quartz boats offers material compatibility and thus low contamination that can result due to handling in noncompatible or metallic boats or furnace. An atmosphere rich with phosphorus can be

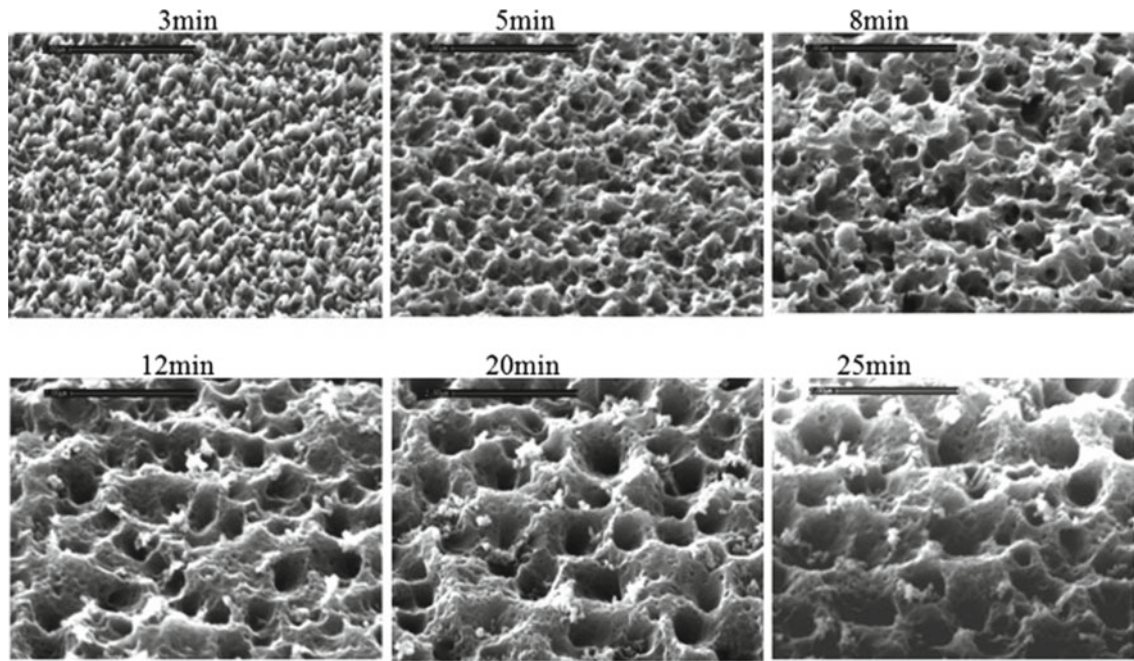
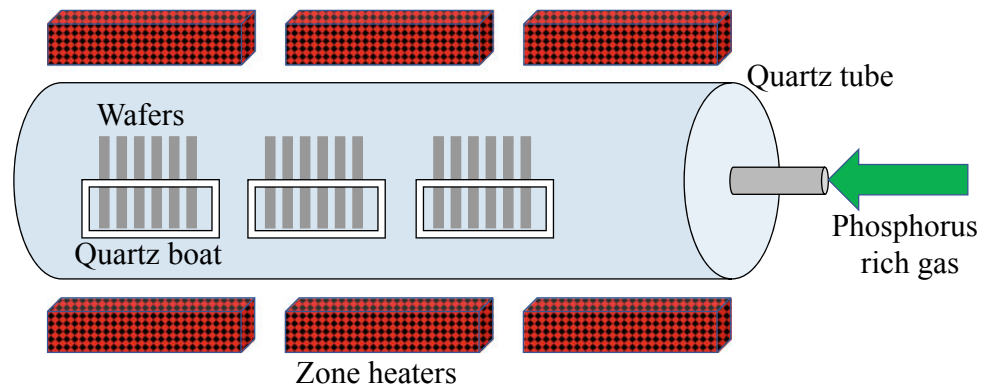


Fig. 17 Pyramids used by plasma (RIE) at different processing times (Addonizio et al. 2019) (with permission 5364110390101)

Table 2 Reflectivity of MS-Si with different texturing techniques (Macdonald et al. 2004) (with permission 5364160034473)

Reflectivity (%)	Alkaline texturing	Acidic texturing	Plasma texturing
Bare	34.4	27.6	11.0
With SiN ARC	9.0	8.0	3.9
With ARC and encapsulation	12.9	9.2	7.6

Fig. 18 Quartz tube furnace



supplied by bubbling N_2 through liquid $POCl_3$ (which has to be handled with care) before injecting it into the furnace, as shown in Fig. 18.

Tubes are generally exposed and function at atmospheric pressure, but operating at low pressures improves the uniformity and throughput. The furnace temperature ramping and heat treatment protocol are easily adjusted and controlled. Durations between 20 and 30 min at temperatures above $800^\circ C$ are typical to the treatment. Advantages of

quartz furnace include the sovereignty of Si atoms with low to almost no foreign metallic impurities high throughput is achievable since simultaneous substrates can be used in a single batch. Commercial furnaces can consist of stacks of four tubes to further enhance process throughput.

6.4.2 Belt Furnace

This furnace is a continuous process type, with phosphorus source supplied to one or both wafer faces. The temperature

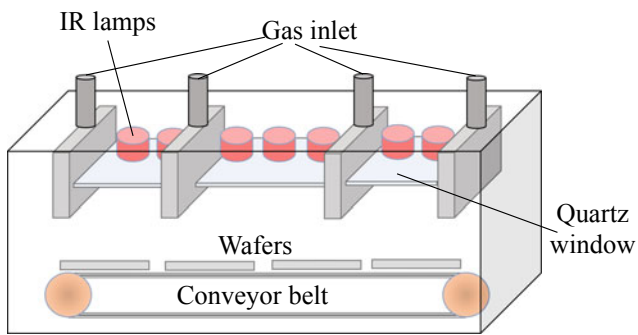


Fig. 19 Belt furnace

control (fast heat ramp up or down) can be achieved through infrared (IR) heated zones. Dopant sources can deposit using many methods such as screen printing, spinning-on, spraying-on, by CVD or by vapourization. The temperature cycle experienced by the wafer will be an exact replica of the furnace heater temperature profile along the conveyor belt, with the time frame control via speed controls. A depiction of a belt furnace is shown in Fig. 19.

Some disadvantages of the belt furnace are ambient air intrusion as well as the belt material being a potential source of metallic impurities. The main obvious advantage of such a process is the amenable automation and the capability to apply various temperature profiles for rapid heating and cooling.

7 Cell Optical Enhancements

After a desired single-faced phosphorous diffusion, a parasitic junction formed on the surface and also at the edges which causes a multitude of problems (leading to low shunt resistance) and should be removed. This layer of amorphous phosphosilicate glass usually undergoes an etching process in dilute HF as it will delay the succeeding processing steps.

Usually, titania (TiO_2) is employed to create the anti-reflection coat as it possesses an optimum refractive index for encapsulated cells. This can be done via many

processes, such as atmospheric pressure chemical vapour deposition (APCVD), spin coating or screen printing. Nowadays, hydrogenated silicon nitride (SiN:H) films are the most advantageous choice, as they associate anti-reflection with bulk and surface passivation, it also is a distant cousin of silicon, which enhances material and precursor compatibility. SiN:H can be deposited using chemical deposition CVD (fast, high-quality solid material) and plasma-enhanced CVD (PECVD), which requires low-pressure and low temperature ($<500\text{ }^\circ\text{C}$) processing.

7.1 Chemical Vapour Deposition (CVD)

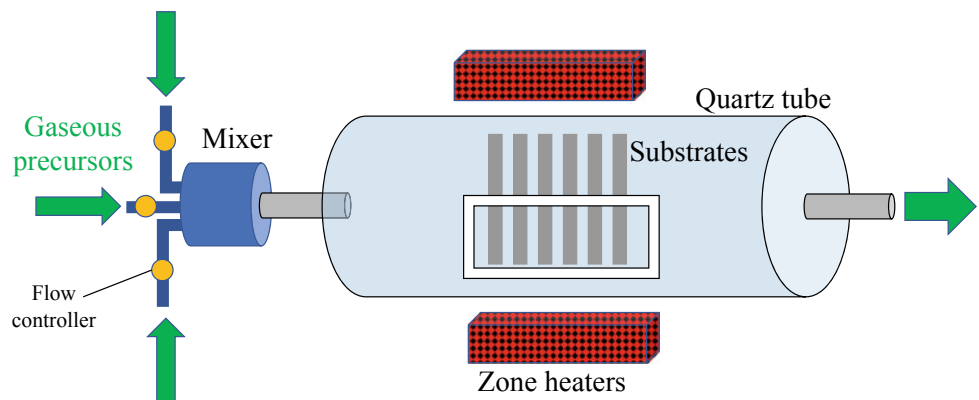
Chemical vapour deposition process is used to produce good quality solid substrates. The substrate is placed in the path of one or more volatile precursors, which react and decompose on the substrate surface as shown in Fig. 20.

In general, CVD is a reliable process, but there could be a lot of wasted materials as the mixed gaseous precursors rely on process parameters (flow rate, substrate temperature, concentration, etc.) to achieve the required deposition on the substrate. This is depicted in Fig. 21a as the conventional CVD process proceeds with limited control over the rate and quantity of which the gas molecules are interacting with the substrates. In Fig. 21b, a CVD-enhancing process such as plasma, radio waves or thermal wire has been added to impose lateral forces on the molecules, hence forcing them to deposit on the surface.

The plasma-enhanced chemical vapour deposition (PECVD) is favoured to other low-pressure CVD as it occurs at low temperatures ($T < 500\text{ }^\circ\text{C}$). The process induces hydrogenation, that is very beneficial for silicon.

For the ARC layer deposition, amorphous silicon nitride films are created by PECVD. A successive thermal step is required to activate hydrogenation; industrially, the previously mentioned firing step is sufficient. The process is depicted in Fig. 22. One issue arises which is the elaborate

Fig. 20 A depiction of the CVD process



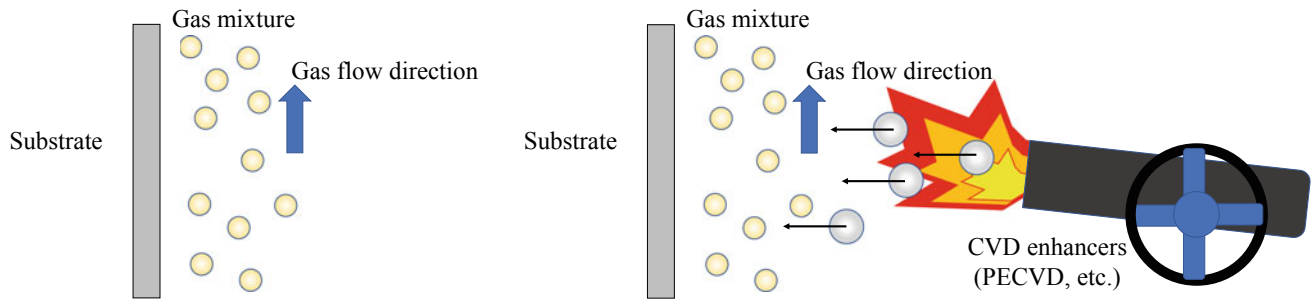


Fig. 21 a CVD and b enhanced CVD processes

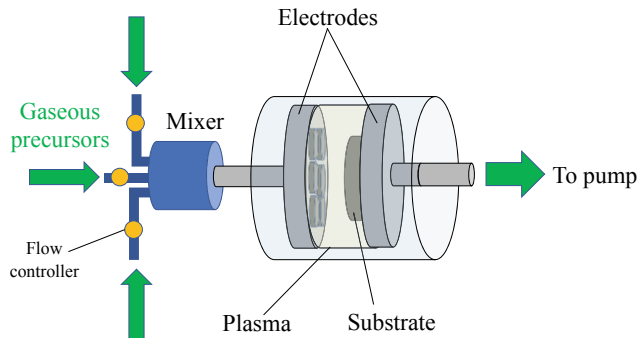


Fig. 22 PECVD process

control over process parameters, such as applied voltage across electrodes, as well as the distance between them. These parameters affect the thickness and quality of the deposited films.

The three important surface properties (ARC, bulk and surface passivation) are interconnected and cannot be altered independently; hence, optimization of all the processing parameters such as temperature, power and frequency of plasma excitation, and gas flow rate is a must. To decouple the plasma from the CVD process, two operational routes are available: (Sect. 7.2) direct PECVD (high frequency:

13.56 MHz, low frequency: 10–599 kHz) and (Sect. 7.3) Remote PECVD.

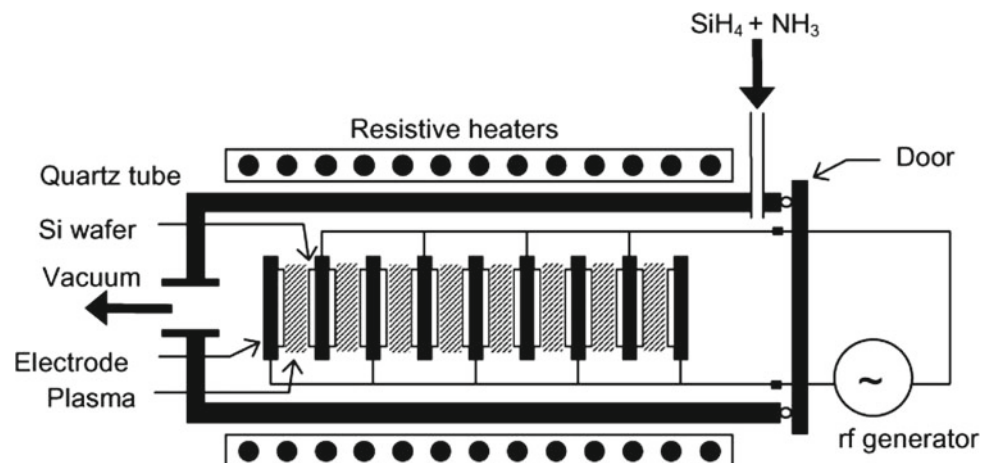
7.2 Direct PECVD

In this method, the wafers are situated in the plasma caused by the excitation of the processing gases by the electromagnetic field. Hence, the bulk is efficiently passivated, but surface passivation is not achieved properly as a result of the severe effects of long exposure of the wafers to the aggressive plasma. Furthermore, the surface passivation worsens as the wafers are exposed to UV light. The process is shown in Fig. 23 (Aberle 2001).

7.3 Remote PECVD

Wafers are situated away from where the plasma forms as shown in Fig. 24. The setup has an advantage similar to batch-type direct PECVD as wafers are fed continuously and there is no direct contact between the substrates and the plasma; thus, surface damage is avoided but surface passivation is enhanced, whereas bulk passivation reduced.

Fig. 23 Direct-plasma batch reactor for the simultaneous PECVD deposition of SiN onto many Si wafers (Aberle 2001) (with permission 5364110735212)



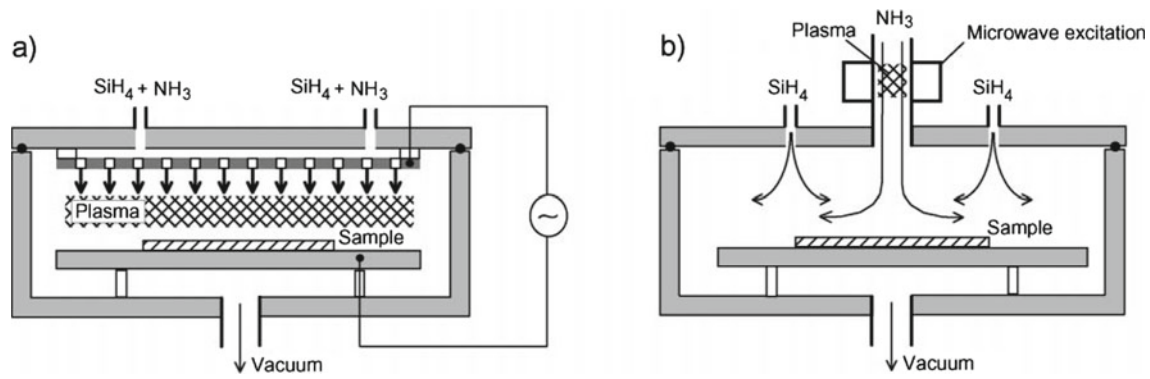


Fig. 24 Deposition of SiN in **a** a direct-plasma reactor and **b** a remote-plasma reactor using microwave excitation (Aberle 2001) (with permission 5364110735212)

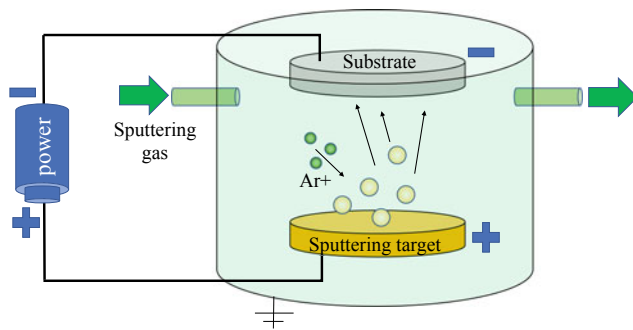


Fig. 25 Depiction of the sputtering process

7.4 Sputtering Techniques

Sputtering process takes place when atoms are ejected from a solid target material due to bombardment of the target by energetic particles. If vacuum is generated and maintained, these atoms flow from the positive (high voltage) target to the negative (low voltage) desired substrate and land on its surface. The reader should pay attention that the “target” refers to the source material that will be deposited on the substrate, which is not called a target although it appears to be one. The process is shown in Fig. 25.

8 Front Contact Print and Dry

The process of adding contact fingers to the solar cell is a delicate task. The resulting metallization allows effective electron harvesting but should not impede reception of solar radiation. There are general requirements for the front metallization material, and they include:

1. low electric resistance (related to contacts).
2. low bulk resistivity.

3. suitable contact dimensions (width and height aspect ratio).
4. surface stickiness and adhesion.
5. compatibility with subsequent encapsulating or ARC materials.
6. solderability.

The ideal contact metal is selected based on its resistivity, price and availability, making silver a very valuable option. Copper possesses similar characteristics as silver, but it does not qualify for conventional processes such as screen printing. This is mainly due to the diffusivity of copper during heat treatments which will contaminate the silicon wafer. In addition, screen printing is the de facto process of adding front contacts on silicon wafers.

8.1 Screen Printing

Screen printing does not live up to the advantages presented by vacuum physical evaporation for first three requirements mentioned above. Screen printing is utilized to adhere a paste composing of silver powder to the front face of the wafer in a mesh pattern that is used to deposit the fingers and associated busbars. The presence of solvents in the paste gives it a viscous liquid nature; the solvents can be easily evaporated in a furnace at around 250 °C and the dried paste is ready for further processing.

Automatic screen printers are available and allow nonstop operation with high throughput. The automatic screen printers can hold wafers from packs, shelf-like or a belt line. Those wafers are then situated with adequate accuracy under the screen, and once printed, they are delivered to the belt line. A sample silk screen showing contact finger pattern is shown in Fig. 26.

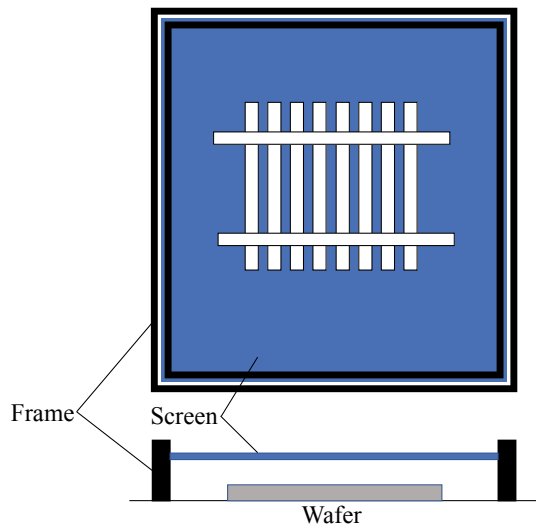
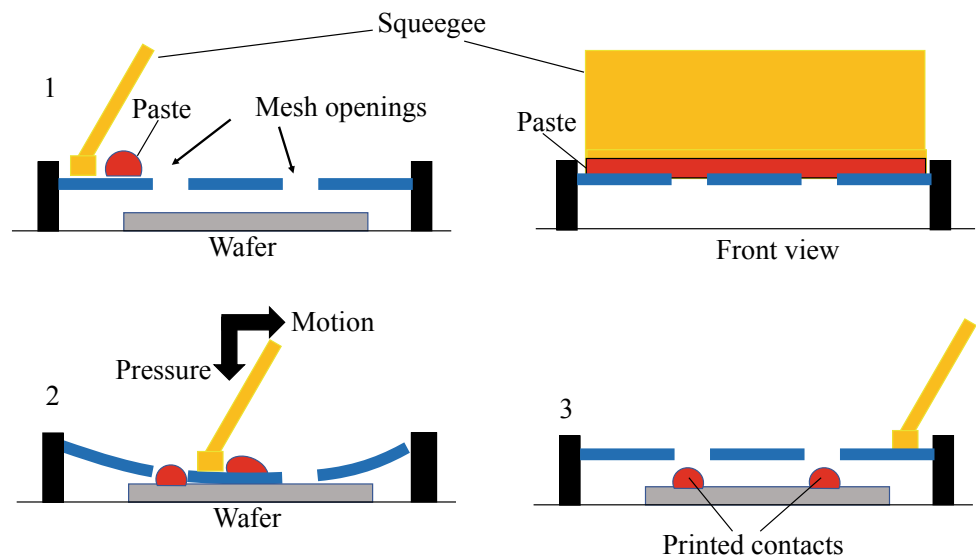


Fig. 26 Silk screen with contact finger pattern pre-inscribed

8.1.1 Screen Printing Process

The front contact of a solar cell requires a fine and thick layer. In order to achieve that through screen printing, wires must be quite thin and compact. Moreover, the reticule's opening has to be sufficiently greater in diameter than the largest grain available in the paste. A schematic of the process is shown in Fig. 27. At the start of the process, the screen and wafer are separated by a distance referred to as the snap-off. Subsequent to dispensing the paste, pressure is applied on the squeegee that is manufactured from metal or rubber. Once pressure is applied, the screen and wafer are in contact. The squeegee is then swept across the screen spreading the paste during the process. This continues until an opening is present where the paste would fill it and adheres to the wafer. The paste will stay in the opening even after the squeegee passes and the screen is returned.

Fig. 27 Steps of the screen-printing process



8.1.2 Paste Properties

The paste carries active material to wafer surface. There are some general components for the paste as follows:

1. Organic solvents: carrying the active materials and providing required paste viscosity.
2. Binders: usually organic, allow agglomeration of active material particle.
3. Conducting material: 10 μm fine silver or aluminium powder (or both). This material is the contact material and makes up around 80% of the paste weight.
4. Glass frit: scratches the surface for more intimate contact laying. Make up to 10% of the weight and consists of powder of metal oxides with low melting point and high reactivity.

8.1.3 Process Parameters

The amount of paste determines the thickness of the screen material, emulsion, open area of fabric and printed line width. For instance, it is essential for the paste to have a low viscosity to fill all the volume permitted by the fabric and emulsion without any voids. Nevertheless, the fluid must also not seep off the surface when the printing process is completed. The snap-off distance, pressure applied on the screen and the velocity of the squeegee are the vital factors that control the printing process.

9 Back Surface Field Deposition

The back-surface field (BSF) layer can be simply achieved by doping the back region of a p-type wafer with the use of screen printing an aluminium paste. The BSF layer is formed as a result of the dissolution and the epitaxial recrystallization of silicon in aluminium during cooling subsequent to

the firing step. However, soldering onto Al contacts is impossible, so it is recommended to use silver and aluminium paste to print busbars.

10 Drying and Co-Firing

The series resistance is decreased by obtaining a good conductor. This is achieved by burning off the organic components of the paste, and by sintering the metallic grains together. The metallic grains ought to form an indistinguishable interface with the preceding silicon layer. The back paste must penetrate the BSF to reach the base during firing. The thermal profiles and composition of the pastes must go under a well-controlled optimization process to adhere to the requirements and standards.

11 Testing and Sorting

Efficiency (I-V) tests are conducted under simulated STC conditions using a solar simulator with certified standard output of irradiance intensity and spectrum, with the aid of a temperature control mechanism, where a flash lamp is capable of providing the required illumination as shown in Fig. 29. The test machine or sun simulator exposes modules to a burst of bright (1000 W/m^2) light with a duration in microseconds from a xenon lamp.

Devices are categorized according to their performance, and devices that do not fall into any level of efficiency or performance bin are disposed of.

The manufacturer typically arranges the cells in different classes depending on the current achieved at a constant voltage close to the maximum power point. Subsequently, the modulus will be manufactured to match the cells of the same class in order to eliminate mismatch losses. Solar cells within a module must have a maximum of a 5% current variation for a single bin (category), to ensure a stable operation of the assembled modules.

12 Module Making

The final step after individual cell testing is their assembly in a module. The cells are electrically connected in series to increase the output voltage, relative to sole solar cells. The cells are encapsulated and furnished with various ancillary and performance-enhancing components such as bypass diodes, connections, a junction box, cabling, front glass and finally glass or a polymer (Tedlar in particular) on the rear surface of the module. The utilization of these components offers physical sturdiness for the module and protection of contacts from weather elements (e.g.

humidity, dust and elevated temperature) that cause losses and deteriorate the performance over time (Ayang et al. 2018).

Silicon solar cells are electrically connected together by a ribbon, which is a thin copper tape deposited with a tin alloy. The cells are typically immersed in a clear encapsulant that serves as a binder between the different layers of the PV panel. Ethylene-vinyl acetate (EVA) is most commonly used for encapsulation purposes due to its manufacturability and electric insulation. It is transparent and supplied in rolls that are cut into the required shapes and sizes. The deposition takes place via a vacuum thermal treatment, transforming the polymer layers into a translucent gel that coalesces on the cells by heating it at temperatures up to $150 \text{ }^\circ\text{C}$ (Şahin and Okumuş 2016; Ecoprogetti 2014). The EVA is placed on a frame of aluminium or stainless steel and protected with clear glass on the front side to finalize the lamination process (Şahin and Okumuş 2016).

The frame is the final piece that is installed in a PV module assembly. It is typically made of anodized aluminium and serves to guarantee the robustness of individual panels as well as the functional and reliable linkage to other photovoltaic modules.

A line of sealant is deposited around the panel walls and along the frame to isolate the side of the panels from rain and dust accumulation. Silicon is the most commonly employed material for this intent, though a specific sealing tape is occasionally utilized. A fully assembled PV module is shown in Fig. 28.

There are also frameless modules and special plastic solutions provided for unique applications. These solutions often include the deployment of rear-side glued supports and modules with glass-glass technology for transparent rooftop installations (Ecoprogetti 2014; Swart 2018).

As explained previously, the current generated through the photovoltaic reactions is collected by the metallic top contacts that enable electron flow and collection. Busbars are directly connected to outer leads. Whereas fingers in narrower metallization zones collect current for transfer to the busbars (<https://www.pveducation.org/pvcdrom/top-contact-design>).

A junction box is placed on the back of the PV module and provides lead wires as an outer connection to provide connection to other PV modules, charge controllers, batteries or inverters. It covers the shadow protection diodes, to prevent the generation of hotspots due to mismatched individual cells' output currents, as well as the cables that incorporate the panels in the field (Ecoprogetti 2014).

Bypass diodes are connected in parallel within the PV module, as opposed to blocking diodes that are connected in series (<https://www.sunwize.com/tech-notes/pv-module-bypass-diodes-what-are-they-and-what-do-they-do/>), and deliver an alternate current during shading or deficiency of

Fig. 28 Fully Assembled PV Module **a** Top view, **b** cross-section view

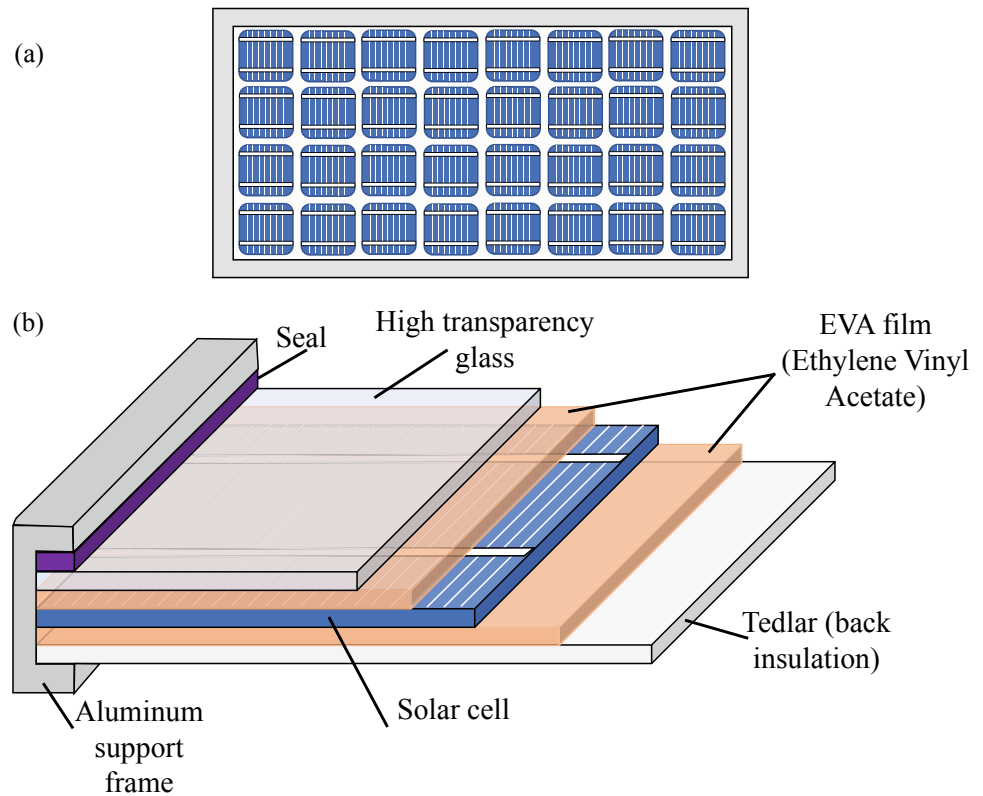


Fig. 29 Flash test of assembled PV panel (Findlay 2022)

cell or panel. In general, diodes are devices that allow the flow of current in a specific direction. The installation of the diodes can either be in the module junction box or incorporated directly into the module.

The assembled modules, similar to their unit cells, are exposed to a flash test to obtain their I-V characteristics which indicate their overall performance as seen in Fig. 29. Modules are also subjected to light-soaking (exposition to illumination for a long period of time) to verify their resistance to light-induced deterioration.

References

- Aberle AG (2001) Overview on SiN surface passivation of crystalline silicon solar cells. *Sol Energy Mater Sol Cells* 65(1):239–248. [https://doi.org/10.1016/S0927-0248\(00\)00099-4](https://doi.org/10.1016/S0927-0248(00)00099-4)
- Addonizio ML, Antonaia A, Fusco L (2019) Plasma etched c-Si wafer with proper pyramid-like nanostructures for photovoltaic applications. *Appl Surf Sci* 467–468:143–150. <https://doi.org/10.1016/j.apsusc.2018.10.078>
- Al-Husseini AM, Lahlouh B (2017) Silicon pyramid structure as a reflectivity reduction mechanism. *J Appl Sci* 17(8):374–383. <https://doi.org/10.3923/jas.2017.374.383>
- Anti-Reflective Coating for Eyeglasses—Worth The Money? <https://www.allaboutvision.com/lenses/anti-reflective.htm>. Accessed 8 Aug 2022
- Ayang A, Wamkeue R, Ouhrouche M, Saad M (2018) Faults diagnosis and monitoring of a single diode photovoltaic module based on estimated parameters. In: 2018 IEEE electrical power and energy conference, EPEC 2018. <https://doi.org/10.1109/EPEC.2018.8598308>
- Bai Q, Yang H, Cheng X, Wang H (2020) Recombination parameters of the diffusion region and depletion region for crystalline silicon solar cells under different injection levels. *Appl Sci* 10(14):4887. <https://doi.org/10.3390/app10144887>
- Beiser V (2018) The ultra-pure, super-secret sand that makes your phone possible. In: *Wired magazine*
- Ecoprogetti (2014) What is the raw material that composes a photovoltaic module? <https://ecoprogetti.com/the-structure-of-photovoltaic-module/>
- Findlay S (2022) Flash testing high capacity solar. <https://www.winaico.com.au/blog/flash-testing-high-capacity-solar>
- Gao K et al (2018) Fabrication of black silicon by Ni assisted chemical etching. *Mater Res Express* 5(1). <https://doi.org/10.1088/2053-1591/aaa1fb>

- Global Market Share by PV Technology from 1990 to 2013. https://commons.wikimedia.org/wiki/File:Global_Market_Share_by_PV_Technology_from_1990_to_2013.svg. Accessed 9 Aug 2022
- Green MA, Zhao J, Wang A, Wenham SR (2001) Progress and outlook for high-efficiency crystalline silicon solar cells. *Sol Energy Mater Sol Cells* 65(1):9–16. [https://doi.org/10.1016/S0927-0248\(00\)00072-6](https://doi.org/10.1016/S0927-0248(00)00072-6)
- Honsberg C, Bowden S, Top contact design. <https://www.pveducation.org/pvcdrom/top-contact-design>
- Macdonald DH et al (2004) Texturing industrial multicrystalline silicon solar cells. *Sol Energy* 76(1):277–283. <https://doi.org/10.1016/j.solener.2003.08.019>
- Magsi K (2014) Bio-inspired photon absorption and energy transfer for next generation photovoltaic devices. Stony Brook University
- Miles RW, Zoppi G, Forbes I (2007) Inorganic photovoltaic cells. *Mater Today* 10(11):20–27. [https://doi.org/10.1016/S1369-7021\(07\)70275-4](https://doi.org/10.1016/S1369-7021(07)70275-4)
- Şahin ME, Okumuş HI (2016) Physical structure, electrical design, mathematical modeling and simulation of solar cells and modules. *Turk J Electromech Energy* 10680
- Silicon Pyramid Structure as a Reflectivity Reduction Mechanism. <https://scialert.net/fulltext/?doi=jas.2017.374.383>. Accessed 8 Aug 2022
- Sunwize, PV module bypass diodes—what are they and what do they do? <https://www.sunwize.com/tech-notes/pv-module-bypass-diodes-what-are-they-and-what-do-they-do/>
- Swart AJ (2018) Analyzing the performance of identical PV modules in a semi-arid region over a 2-year period. In: International conference on multidisciplinary research, pp 94–108
- UAE-based Mulk Holdings International pens JV agreement to enter US market (2021) *Arabian Business*. <https://www.arabianbusiness.com/industries/construction/467119-uae-based-mulk-holdings-international-inks-deal-with-park-international-investments-silver-heights-real-estate>



Second-Generation Photovoltaics: Thin-Film Technologies

Abdul Hai Alami^{ID}, Shamma Alasad^{ID}, Haya Aljaghoub^{ID},
Mohamad Ayoub^{ID}, Adnan Alashkar^{ID}, Ayman Mdallal^{ID},
and Ranem Hasan^{ID}

Abstract

The thin-film technologies are a direct answer to the monopoly of silicon materials in the PV market. With the silicon manufacturing processes being refined as art, the competition for high quality and low price has rendered small manufacturers incapable of competing in the silicon market. A new set of technologies and manufacturing processes have come to existence to allow a brand-new niche to flourish. The thin-film technologies use materials that can be applied directly to a substrate to form active photovoltaic layers that are independent of the silicon refining procedures of the past. This chapter features these manufacturing technologies.

1 Introduction and Importance

The dominance of first-generation solar cells (monocrystalline) is due to their unparalleled power conversion efficiencies (on average 20%), robustness, material abundance

and non-toxicity, and high-power output. Additionally, their production is heavily influenced by the long-gained experience in manufacturing them. Moreover, any new technology that has the potential to break into the solar cell scene is faced with the challenge to overcome mass production of monocrystalline silicon solar cells and compete with their figure of merit. Hence, second generation of solar cells, manifested in the form of thin-film solar cells, are fabricated by stacking one or more thin-film layers on cheap substrates such as conductive oxide-coated glass or plastic. The production of monocrystalline silicon solar cells is both resource and energy intensive, which is why multi-crystalline silicon solar cells, that have an average efficiency reaching 14%, an area of 150–250 cm², and a thickness ranging between 180 to 300 μm, cost about 1.3 euros/cm², and 10 g Silicon/W, are considered a viable alternative with lessened costs.

The core principle behind thin-film solar cells is to reduce the thickness of a given device, allowing to maximize the active photovoltaic area produced from the same amount of feedstock. However, thin-film solar cells can go as low, in terms of thickness, as the minimum thickness that dictates the breakage tendencies. In general, large-area thin-film solar cells require thicker layers/substrates in order to attenuate the risk of wafer breakage. For instance, a wafer with an area above 400 cm² will require a thickness not below 100 μm. Additionally, a conventionally overlooked source of silicon losses, which is sawing, is increased with decreasing the thickness of the thin-film solar cells. Due to less materials utilized to fabricate these cells, their costs can go as low as 1 euro/W. Moreover, an advantage of thin films is that they are not bound by a maximum area (i.e., 300 cm²), contrary to monocrystalline silicon, which means that these technologies can be modulated and connected in a more cheap and flexible way. Despite these opportunities, both the power conversion efficiency and the lifetime stability of thin-film PV modules are lacking.

A. H. Alami (✉) · H. Aljaghoub · M. Ayoub · A. Mdallal ·
R. Hasan
University of Sharjah, Sharjah, United Arab Emirates
e-mail: aalalami@sharjah.ac.ae

H. Aljaghoub
e-mail: haljaghoub@sharjah.ac.ae

M. Ayoub
e-mail: mohamad.ayoub@sharjah.ac.ae

A. Mdallal
e-mail: ayman.mdallal@sharjah.ac.ae

S. Alasad · A. Alashkar
American University of Sharjah, Sharjah, United Arab Emirates
e-mail: g00070854@aus.edu

A. Alashkar
e-mail: b00028197@alumni.aus.edu

The film thickness of a thin-film solar cell differs from a few nanometers (nm) to tens of micrometers (μm), that is much thinner than a commercial silicon wafer ($\sim 200 \mu\text{m}$), which are the base for fabricating conventional silicon solar cells. Thin-film cells are thus thinner, lighter, and have less drag to counter breakage rates. Consequently, thin-film solar cells have expanded the horizon of the types of substrates that can be used reaching out to flexible substrates, which have lucrative and practical advantages including the use in photo-generating glazing materials as a replacement for drapes and conventional glass, as well as the integration of photovoltaics in buildings' exteriors. The supporting material on which the silicon is deposited on can either act as a substrate or superstrate. Consequently, the two basic configurations of thin-film solar cells are the substrate and the superstrate configuration. Both configurations rely upon the sequence of the deposition of the silicon layers. A superstrate configuration follows the p-i-n sequence, which means that the energy bearing photons have to permeate through the supporting material, which has the requirement to be highly transparent to facilitate their transmittance, and ultimately act as a cover or an encapsulating material for the case of modules. On the other hand, a substrate configuration follows the n-i-p deposition sequence, where the supporting material forms the backside of the solar cell. Additionally, supporting materials are classified based on their associated temperature endurance. For instance, a standard low-temperature superstrate for a thin-film solar cell is soda-lime glass with a modified iron composition to obtain low emissivity to allow the penetration of light. A standard low-temperature supporting material costs 10 euros/ m^2 for a thickness range of 3–4 mm. Low temperature/low-cost supporting material pose as an advantage for thin-film solar cells, as there has yet to be a method for producing monocrystalline silicon solar cells with competing temperature and cost benchmarks. Other supporting materials, such as borosilicate float glass, can withstand intermediate-temperature strain. Borosilicate float glass is an intermediate-temperature superstrate with thicknesses ranging from 3 to 5 mm and cost around 25 euros/ m^2 have had an influence on PV manufacturing during the last decade. Moreover, high-temperature supporting materials such as c-Si wafers, ceramics (i.e., alumina and mullite), glass ceramics, graphite, and steel suffer from the poor associated figure of merit (euro/ m^2). Nevertheless, properties such as the crystallographic and electronic quality of c-Si films are enhanced by increasing the temperature of the crystal growth/deposition. Although the data in Fig. 1 is for the United States of America, it is quite indicative of the share and importance of thin-film technologies in the market. Figure 2 shows a more comprehensive overview of the share of each PV technology available.

2 Overview of Manufacturing Techniques

As new technology emerges, different production techniques are used. One of the most widely known and established methodologies available for depositing thin films and obtaining epitaxial growth, also known as vertically structuring the deposited layers, is the chemical vapor deposition (CVD) method. The CVD method is popular due to its high success rate and simplicity. In the CVD method, several gasses interact with each other in a furnace tube with a substrate. During the CVD process, gasses such as hydrogen and silane flow into the tube and interact with each other. To enhance the reactivity inside the tube chlorine is added, this in return results in producing dichlorosilane (SiH_2Cl_2) or trichlorosilane (SiHCl_3) gasses. The chlorosilane gas is a much safer and cost-effective alternative for increasing the reactivity of the CVD process. The CVD process can be enhanced by adding plasma, heat, or radio frequencies at both atmospheric and low pressures. Due to the challenges faced in acquiring the silane gas, occasionally, it is preferable to look at the liquid phase epitaxy of the silicon and produce molten silicon. Molten silicon can be obtained at temperatures between 700 and 1000 °C. There are two ways to deposit liquid silicon onto the substrates, the first method is the Traveling Solvent Method (TCM). The TCM represents a sandwich with a solvent between a polycrystalline silicon carbide (SiC) source platelet and a substrate. The solvent is inserted between the substrate and the source material, and between the substrate and the source, there is a relative motion with a temperature gradient. The temperature at the source material is much higher than the temperature at the substrate prompting the SiC to dissolve and deposit on the substrate. The conventional first-generation methodologies are not suitable for depositing thin films because compared to first-generation solar cells, thin films' thicknesses are about 1000 times smaller. As a result, for thin-film deposition, substrates are necessary. These substrates are most likely transparent and made of lime glass. Due to the small thicknesses of thin-film solar cells, the texture of the surface of the cells must be altered in a way to ensure that the cell has high absorbance.

3 Available Thin-Film Photovoltaic Technologies

The main technologies representing the thin-film photovoltaic solar cells include:

1. Cadmium telluride (CdTe) cells.
2. Copper indium gallium selenide (CIGS) cells.
3. Amorphous silicon (a-Si) cells.
4. Gallium arsenide (GaAs) cells.

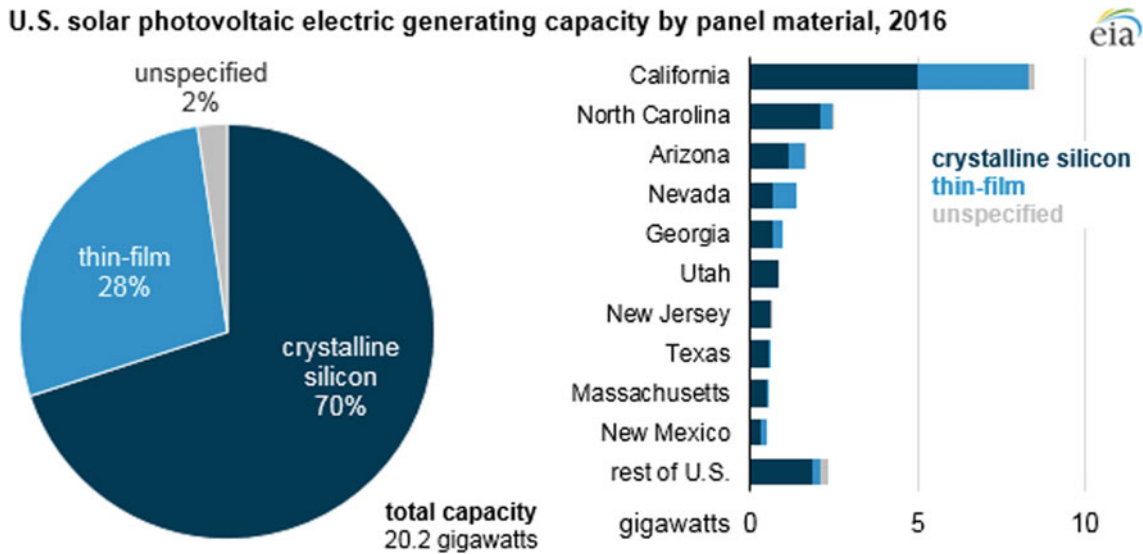
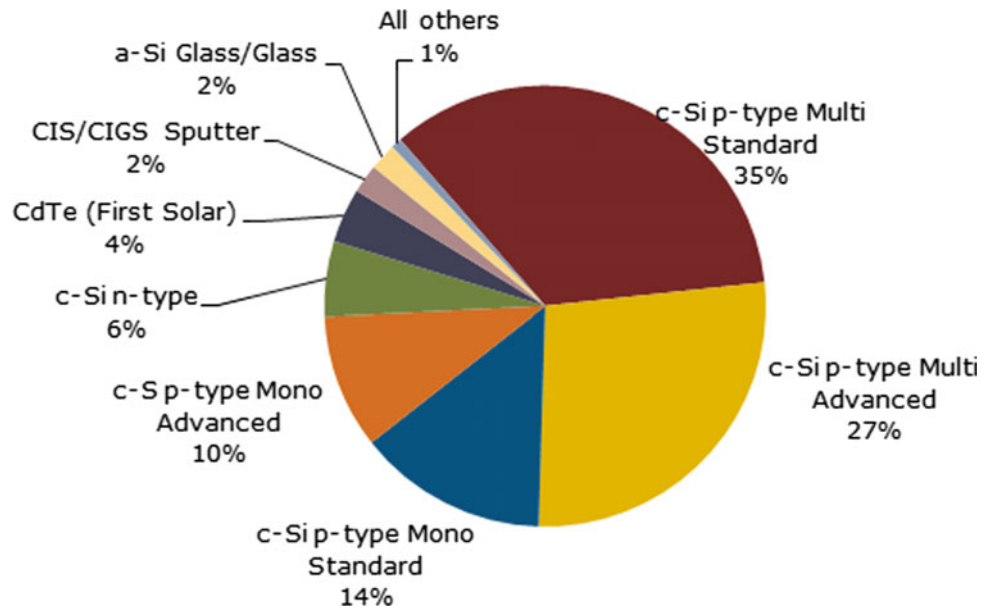


Fig. 1 Photovoltaic electric generation capacity by panel material in the United States of America (EIA: U.S Energy Information Administration 2017)

Fig. 2 Thin-film (CdTe, CIGS, and a-Si) percentage among other types of cells (50 GW Solar Production: A 2014)



3.1 Cadmium Telluride (CdTe) Solar Cells

The history of CdTe solar cells dates back to the 1950s. CdTe-based active material has a novel match with the photon distribution in the light spectrum within the atmosphere with a bandgap of about 1.5 eV depending on the purity of the end material. A heterojunction design for a solar cell device where the CdTe layer acts as a p-type junction for holes majority carriers’ diffusion, matched with an n-type junction for electron carrier diffusion that is represented by a cadmium sulfide (CdS) layer, along with contacts on both ends of the device. GE, kodak, and

AMETEK (along with various pioneers of this technology through its timeline) have revolutionized the CdTe-CdS P–N junction solar cells. CdTe cells are the only thin-film technology that are cheaper than the commercial solar cells consisting of crystalline silicon in multiple kilowatt systems. CdTe photovoltaics are utilized in well-known solar farms that are reshaping the photovoltaic implementation scene, like the Topaz Solar Farm in Arizona, USA, shown in Fig. 3. The total annual production of the Topaz solar farm was valued at 401,308 MWh in 2013 and reached 1,300,788 MWh in 2021 (Electricity data browser—Topaz Solar Farm 2023).

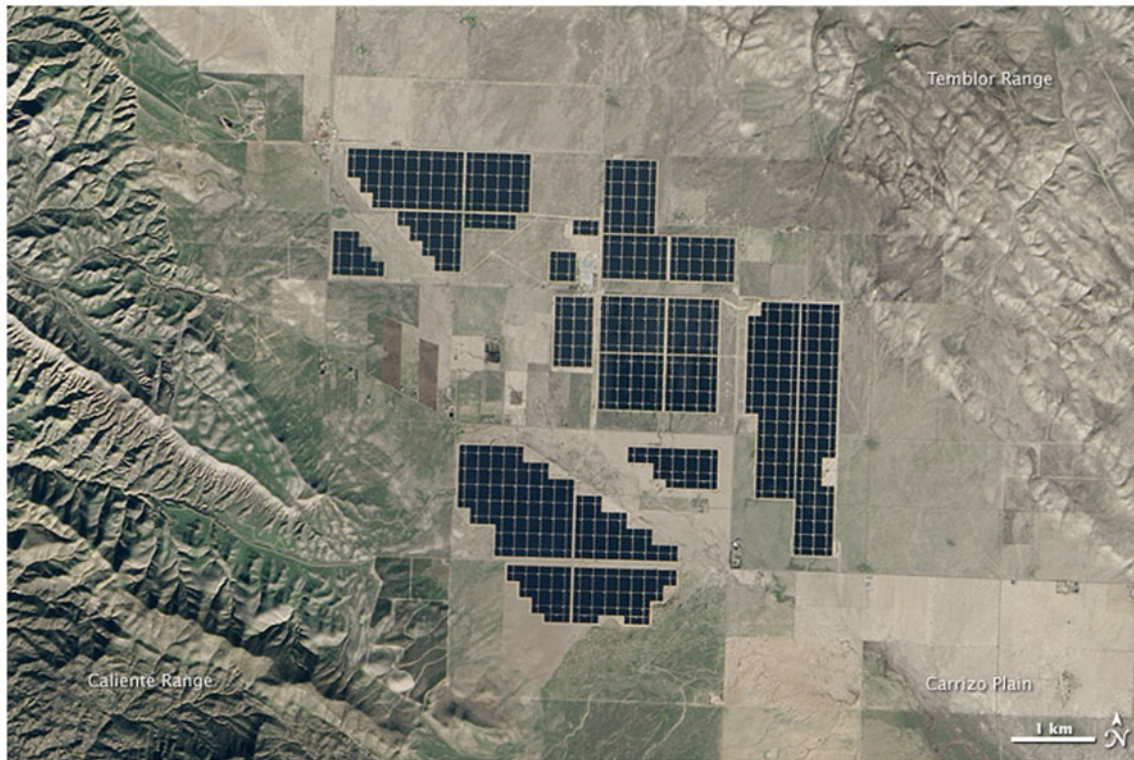


Fig. 3 Topaz Solar Farm in Arizona, USA in 2015 (Topaz Solar Farm 2015)

CdTe technology represents a bit over 50% of the commercially available thin-film photovoltaic modules, accounting for around five percent of worldwide PV production. FirstSolar is a leader in the thin-film photovoltaic modules' market, and their influence has been substantial through managing a large-scale farm like Topaz.

The CdTe technology has intrinsic advantages over other PV technologies and can be considered a potential solution to key ecological issues of solar PV manufacturing and operation. Their energy yield vs. energy required to manufacture them mitigate issues related to climate change, energy security, and water scarcity, across a range of application scenarios. From a lifecycle perspective, CdTe technology has the lowest carbon footprint, lowest water requirement in manufacturing processes, and, most importantly, the shortest-lived breakeven period among other competing solar photovoltaic technologies. This manifests as more carbon reductions in a shorter period of time without short-term energy loss.

The cell structure is generally similar to other thin-film cells that are deposited upon a transparent substrate from soda-lime glass, with its intrinsic straight and smooth surface, as shown in Fig. 4.

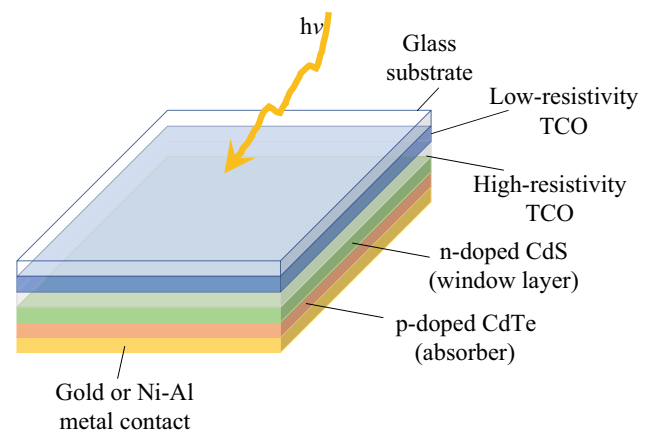
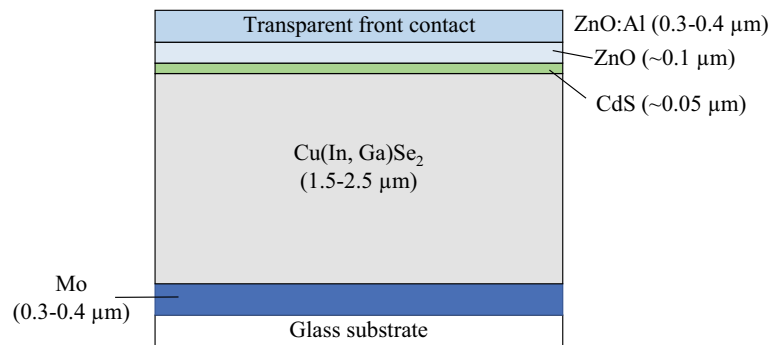


Fig. 4 Structure of cadmium-telluride (CdTe) solar cell

3.1.1 CdTe Cell Efficiency

FirstSolar inducted CdTe in the high-end efficiency cells with their report of a CdTe cell that reached 21.1% in 2014, and it was not long before this record was beaten with a 22.1% cell that was reported 2 years later (Solar 2014). In terms of modules, in 2014 modules operated at 16.1–17.0% efficiencies. Average production line module

Fig. 5 CIGS cell structure

efficiency was projected to be 17% by 2017, only to raise this projected figure to 19% by 2016. Overall, CdTe cells have reached a certified record efficiency of 22.1% (Best Research-Cell Efficiency Chart | Photovoltaic Research | NREL 2023).

The secret behind these record efficiencies reported is mainly a manufacturing one. Alloying of different elements that make up the cells is used to allow band gap grading and tuning. Alloying CdTe and selenium (Se) improves the photo response for this active layer to certain regions of the light spectra that is available within our atmosphere. Moreover, an alloyed active structure (i.e., CdSe_xTe_{1-x}/CdTe) that utilizes magnesium zinc oxide (MgZnO, MZO), where MZO partially replaces the CdS component, where the latter causes inefficient radiation absorption, results in an optimized CdS layer that has a more suitable alignment with CdSe_xTe_{1-x} as well as a better transparency.

3.2 Copper Indium Gallium Selenide (CIGS) Solar Cells

Another thin-film technology, with average reported efficiencies of around 20% that were represented by the National Renewable Energy Laboratory (NREL) (Best Research-Cell Efficiency Chart | Photovoltaic Research | NREL 2023), is known as the copper (Cu) indium (In) gallium (Ga) selenide (Se) (CIGS) solar cell, fabricated by the deposition of a CIGS active layer on a glass or a flexible substrate with electrodes on both ends of the device. The end film possesses a 10⁵/cm absorption coefficient that suits electrons with 1.5 eV energy and above and thus strongly absorbs sunlight in the required visible spectrum for a good PV operation and yield. One advantage of such solar cells is the ability of the bandgap to be tuned depending on the ratio of indium and gallium. For example, in the formula: CuIn_xGa_(1-x)Se₂, the ratio between In and Ga can be optimized according to the desired bandgap of the end film. An active layer with no (In), copper gallium selenide (CGS), has a bandgap of ~1.7 eV that is decreased by increasing the amount of (In) within the structure reaching down to 1 eV

with the extreme case of no (Ga), copper indium selenide (CIS).

Structurally, the copper indium selenide (often referred to “CIS”) solid solution along with (CGS) results in a chalcopyrite crystal structure with tetrahedral bonds. An illustration of the cell layers is shown in Fig. 5, showing the microscale of the cell construction (maximum of 3.5 μm of active material deposited over the glass substrate).

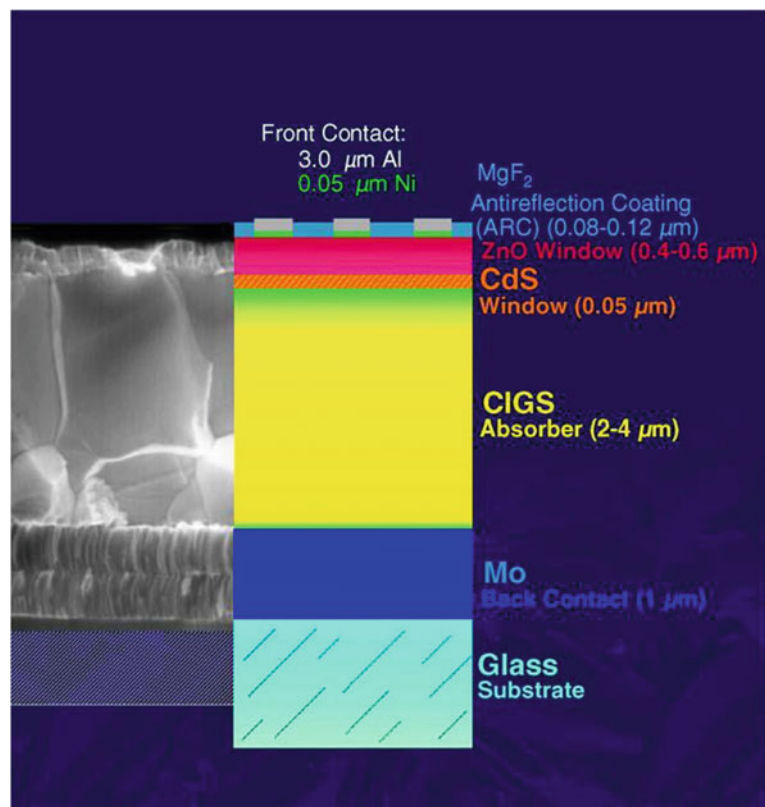
3.2.1 Cell Manufacturing Considerations

A substrate of soda-lime glass with a thickness of 1–3 mm coated with molybdenum (Mo) on one side to serve as metal back contact. The CIGS/CdS heterojunction are enhanced with an undoped zinc-oxide (ZnO) layer that precedes an aluminum-doped ZnO layer that acts as a top electrode. The CIGS layer has to meet the minimum penetration depth requirements that set the absorbance properties of any active layer with bandgaps ranging between 1.02 eV and 1.65 eV with varying the Indium and Gallium contents indicated by CuInSe₂ and CuGaSe₂, respectively. The upper window layers from doped ZnO have larger bandgaps: where the ZnO and CdS bandgaps are 3.2 eV and 2.4 eV, respectively, and allow more light to pass while simultaneously serving as a front contact for current collection. The cell structure is shown in Fig. 6.

3.2.2 Device Structure and Construction

Soda lime glass is utilized as a substrate since it includes sodium (demonstrated to give a significant improvement in open-circuit voltage) by the passivation of surface and grain boundary defects. Such glass substrates can be replaced by substrates made of metal foils or polyimide that are thinner and more flexible. A coating of molybdenum is created (mostly by sputtering) to serve as the back contact and returns the majority of the light that has not been absorbed into the absorber. This is followed by one of several distinct techniques used to create a hole majority diffusion CIGS absorber layer. Above the absorber is a thin n-type buffer layer. Generally, cadmium sulfide (CdS) buffer is deposited using a chemical bath. A thin coating of a middling undoped zinc oxide (i-ZnO) covering the buffer is followed by a

Fig. 6 CIGS scanning electron microscope image of the cell with superposed cell components (Kazmerski 2022)



larger layer of ZnO that has been doped with aluminum (Al). Note that when a ZnO:Al window layer is being deposited, the intrinsic zinc-oxide layer acts as a shield that protects the substrates and active layers, represented by the heterojunction, from sputtering damage while depositing ZnO:Al.

3.2.3 History of Device Efficiency

The highest efficiency was 20.8% as of October 2013. By altering the CIGS surface to resemble CIS, researchers at the NREL reached a ground-breaking efficiency record of $\sim 20\%$ (Mansfield 2019). These samples were deposited on glass; therefore, they lacked mechanical flexibility. Following on their footsteps, researchers at Empa fabricated a slightly better performing CIGS cell at $\sim 20.4\%$ (Hall 2013). The current best certified cell efficiency stands at 23.4% (Best Research-Cell Efficiency Chart | Photovoltaic Research | NREL 2023).

On the side of larger area modules, NREL was able to fabricate a 13.8% CIGS module with an area of 1 m². Manz AG, a Dutch company, was able to commercially mass produce a 14.6%-efficiency CIGS module back in late 2012 on the total surface area and $\sim 16\%$ on its aperture. MiaSolé and Solar Frontier were able to fabricate a 15.7% and a 17.8% on a 1 m² and a 0.09 m², respectively. Concentrated photovoltaics have also been utilized into achieving extraordinary efficiencies reaching 30%. Improving

performance parameters can be achieved by optimizing the bandgap of the active material (CIGS, CIS or CGS), such as the open-circuit voltage, depending on the optical behavior that is practically beneficial.

3.2.4 Manufacturing Technologies

For film production, vacuum-based techniques allow the co-evaporation or co-sputtering of Cu, Ga, and In onto a substrate at room temperature. This is easily done as most of these materials are evaporated in their elemental form with minimal contamination of the apparatus. This step is followed by annealing the resultant film in a stream rich in selenide (Se) vapor. Co-evaporating Cu, Ga, In, and Se onto a hot substrate in a CVD furnace as shown in Fig. 7 is an alternate method.

In this process, selenium is provided in gaseous form, dihydrogen selenide H₂Se, or pure gaseous Se, at a controllable temperature for Se diffusion reaction activation, also known as chalcogenization. A chalcogenide is created by a series of complicated interactions, including the creation of CuInGa intermetallic alloys, the creation of intermediate metal-selenide binary compounds, and the phase segregation of differently ratioed CIGS compounds. The characteristics of the CIGS film are challenging to regulate due to the wide diversity and complications of the reactions. The selenium supply has an impact on the qualities of the

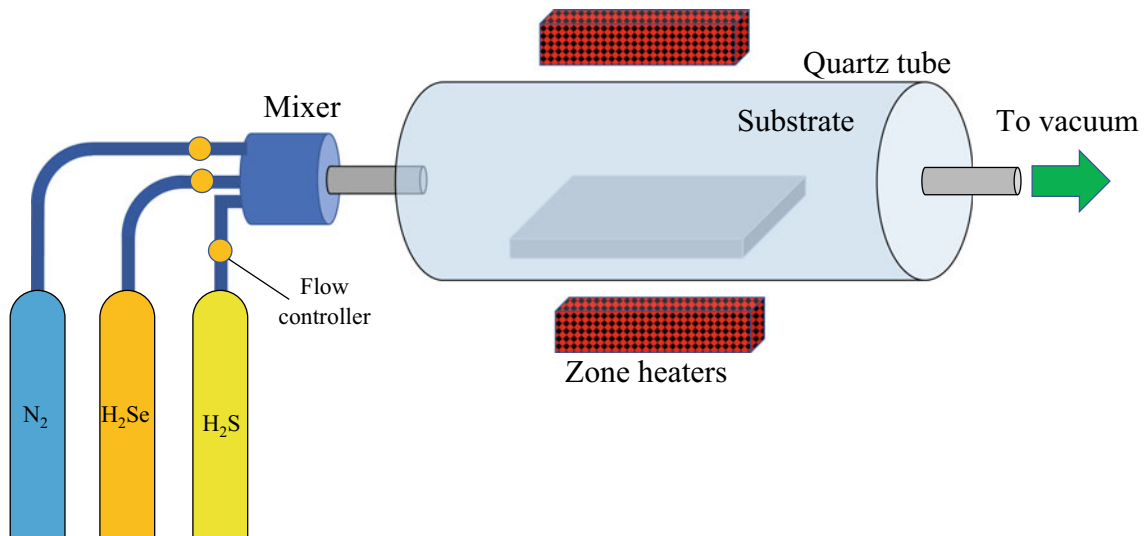


Fig. 7 Chemical vapor deposition of CIGS solar cells on glass substrate

resultant films. H_2Se delivers the quickest selenium incorporation into the absorber, and CIGS films can attain 50% selenium at 400 °C.

Only at reaction temperatures greater than 500 °C, the elemental Se can be fully incorporated. Films made from elemental Se at lower temperatures were Se deficient but contained several phases, such as metal selenides and different alloys. The biggest grain sizes and finest compositional uniformity are obtained when using H_2Se ; however, it is extremely poisonous and is regarded as an environmental concern.

Metallic layer sputtering, followed by selenization, can also be used, and compared to co-evaporation, this technique has a greater throughput and is easier to attain compositional uniformity. A sputtering process that utilizes copper indium and gallium simultaneous targets is used to deposit a 3-components film on a desired substrate that is later annealed in a selenium atmosphere. Moreover, rather than sputtering a sole subsequent order of CIS or a CGS layer, a stacked layer of repetitive simultaneous sputtering achieves an improved crystallinity in the film as well as an overall better root-mean-square roughness. However, this method of depositing the CIGS active layer requires a feasibility study to justify the suitable equipment as well as the degree of enhancement that is achieved.

Alternative non-vacuum-based processes deposit the base (precursor) material nanoparticles onto the substrate and sinters them (joins their grains) there. Electroplating, for example, is another inexpensive option for applying the CIGS layer which can be followed by selenization. The electroplating setup is shown in Fig. 8.

The electroplating process is governed by Faraday's law. The amount of material, w , in grams, that is uniformly removed/deposited from anode/or on the cathode in an

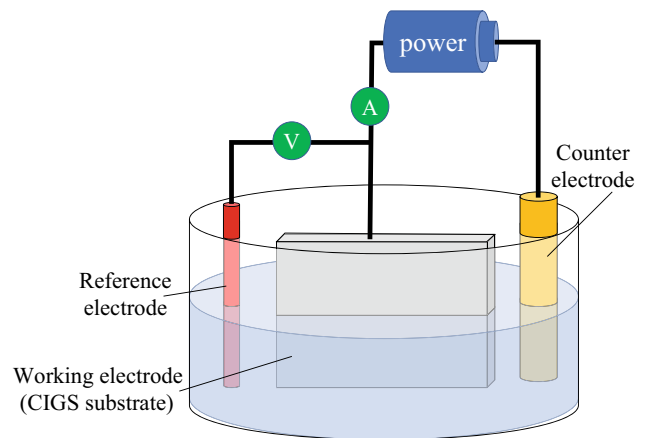


Fig. 8 Electroplating process for CIGS solar cells

aqueous solution over a period of time is found using Faraday's equation:

$$w = \frac{ItM}{nF} \quad (1)$$

where I is the current flow in A, M is the atomic mass of the deposited metal in g/mol, n is the number of electrons/atoms produced/consumed (usually 2) and F is Faraday's constant (96,000 C/mol or 96,500 A.s/mol).

Metal foils provide a suitable substrate for electrodeposition, which demands for conductive electrodes. A 3-electrode system comprises of a working (Cathode), counter, and reference electrodes where they are all used in simultaneous deposition. Electrodeposition followed by selenization alleviates the difference in electronegativity of electrodes by injecting ions into the solution for each

element (Cu^{2+} , Se^{4+} , In^{3+} , and Ga^{3+}), thus altering the tendency of gaining an electron of a specific ion species. The copper-selenium system has a complex behavior, and the composition of the film relies on the ratio of the $\text{Se}^{4+}/\text{Cu}^{2+}$ ion flux which can form a gradient throughout the film's surface requiring an optimization step to determine the concentration of the precursor used and the deposition potential. The characteristics of the produced films are copper richness and small grain sizes, and include $\text{Cu}_{2-x}\text{Se}_x$ phases as well as contamination from the solution. The crystallinity of the film is enhanced further by annealing.

3.3 Gallium Arsenide Thin-Film Cells

For single-crystalline, costly, thin-film solar cells, an active layer consisting of gallium arsenide (GaAs) is employed, producing a competing semi-conducting material. GaAs cells are relatively expensive, yet they have the best single-junction solar cell efficiency in the world at 28.8%. This technology is frequently utilized in spacecrafts given that they behave competitively in pre-existing spacecrafts and stations (i.e., international space station ISS), as they were optimized at suitable conditions including AM0. Conventional GaAs cells consist of a InGaP/(In)GaAs/Ge cells structure.

They are also employed in concentrated PV, a new technology that suits areas with abundant sunlight and concentrates sunlight through lenses onto a much smaller, cheaper GaAs concentrator solar cell.

3.4 Amorphous Silicon Solar Cells (a-Si)

Amorphous silicon technologies are based on a distorted non-crystalline type of silicon. These technologies are, by far, the well-established and high-performance achieving thin-film technology. A viable candidate to replace the conventional and commercially backed-up crystalline silicon, also due to the vast global adversities that accompany extracting and refining silicon. Although CdTe-based thin films cells have had their fair share of research and development, silicon-based thin-film cells continue to be of interest to the industry. Devices made from silicon present less environmental and ecological challenges, contrary to CdTe and CIS-based technologies, as the latter technologies bring up toxicity and humidity concerns as well as low manufacturing yields of CIS as a result of material complexity. Three main silicon-based PV modules arise within the context of market domination, namely (i) amorphous silicon cells, (ii) amorphous / microcrystalline tandem cells, and (iii) glass supported thin-film polycrystalline silicon.

3.4.1 Manufacturing Technologies

Thin-film silicon cells can be manufactured by chemical vapor deposition, specifically those that are plasma aided. This technique applies an extremely thin coating of silicon—only 1 μm thick—to transparent conductive oxide-coated substrates, using a blend of silane (SiH_4) and hydrogen (H_2) gasses. Amorphous silicon operates exceptionally well at weak light due to its bandgap of 1.7 eV, which allows it to absorb a large portion of the light spectrum (including some ultraviolet and infrared). Contrary to crystalline silicon cells, amorphous silicon-based solar cells can take advantage of the more abundant diffuse irradiance that penetrates through our atmosphere, behaving and performing in a better manner in the periods of early mornings and late afternoons.

The cell structure is based on a p-i-n junction, where i stands for intrinsic (middle). Charge carriers are expected to have low lifetimes within amorphous silicon structures due to the normality of dangling bonds within them, which act as recombination hubs and pin the Fermi level, making it impossible to dope the substance to the n- or p-type. The electron mobility in hydrogenated amorphous silicon, a-Si:H, compared to that of holes is approximately 1–2 times, which means that the collection rate of electrons drifting from the n to p-type contact is superior to that of holes that are being transferred from the p to the n-type contact. Which further dictates the overall structure of the cell where the p-type layer should be positioned where the photons are incident in order to ensure that the minority carriers (electrons) are able to pass the junction.

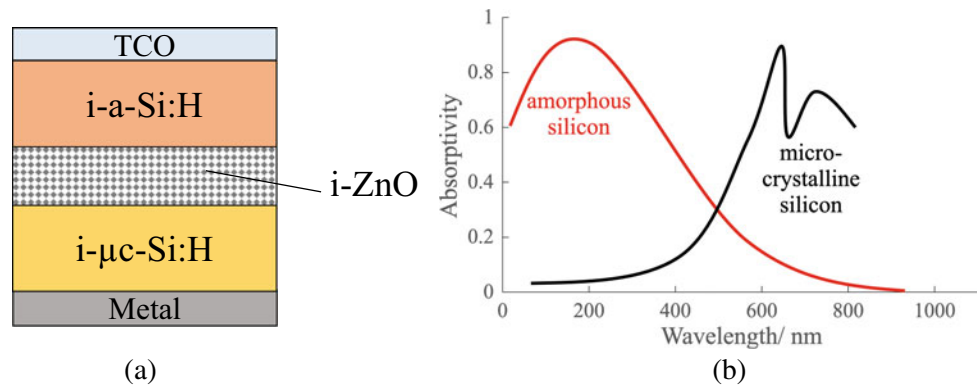
3.4.2 Cell Efficiency

The first six months of operation see a considerable decline in an a-Si cell's efficiency of between 10 and 30 percent. This is known as the Staebler–Wronski effect (SWE) due to the fluctuation of light and dark periods that change the behavior of these semi-conducting materials, accordingly, also known as light-soaking. A counteract for this dip in performance is to heat the silicon wafers at temperatures reaching 150 °C, to reform the crystal structure into a slightly ordered one.

3.4.3 Tandem-Cell Using A-Si/ $\mu\text{c-Si}$

A tandem solar cell device can be fabricated by forming a heterojunction based on an amorphous silicon layer and a slightly more ordered silicon type, such as microcrystalline silicon ($\mu\text{c-Si}$) (micromorph structure), and due to the difference in crystallinity, the momentum of the crystal structure influences the bandgap and creates a difference between the two, as shown in Fig. 9a. The point behind tandem structures is to increase the range of the solar spectrum that is absorbed by the cell's respective active layer; in the previously mentioned example, the amorphous

Fig. 9 Tandem amorphous-crystalline solar cell **a** structure and **b** generalized absorption regimes



and the multi-crystalline silicon layers absorb high energy and infrared photons, respectively, as shown in Fig. 9b.

The micromorph stacked-cell technology was created and registered under a patent at the Institute of Microtechnology (IMT) at Neuchâtel University in Switzerland. Currently, it is licensed to TEL solar. Moreover, an independent validation of the micromorph stacked cell was carried out in 2014, resulting in a world record efficiency at 12.24%.

All of the layers are silicon-based; therefore, PECVD can be used to manufacture them. The a-Si bandgap is 1.7 eV, while the c-Si bandgap is 1.1 eV. Infrared and red light are both absorbed by the c-Si layer. The transition between a-Si and c-Si can produce the highest efficiency. Nanocrystalline silicon (nc-Si), which has a bandgap close to c-Si, can take the place of the latter.

3.4.4 Polycrystalline Silicon on Glass

In an effort to combine the benefits of thin-film devices with those of bulk silicon, a thin-film multi-crystalline silicon can be obtained on a glass substrate by post-treatment of amorphous silicon that is deposited via cheaper and more attainable thin-film deposition technologies. Modules can be constructed by depositing an ARC layer along with doped silicon onto glass substrates that can be textured. One process used for this purpose is CVD or its plasma-enhanced cousin PECVD. The roughness (texturing) of the glass will increase the cell efficiency by 3% via light trapping within the cell through multiple internal refractions.

Multicrystalline silicon is produced by subjecting the thin silicon film to temperatures between 400 and 600 °C. This annealing process enhances the device power conversion efficiency by 8% and increases the production yields to more than 90%.

Crystalline silicon on glass (CSG), where multi-crystalline silicon grows to 1–2 μm is known for its resilience and toughness. These modules do not require a TCO layer, and thus, their manufacturing process is

simplified by eliminating a step and also by avoiding the complex contact deposition process. This also reflects on lower production cost.

3.4.5 Doping of Amorphous Silicon

Gases including phosphine (PH₃) and diborane (B₂H₆) have been utilized to enhance the conductivity of amorphous silicon, by mixing with the silane gas precursor, similar to how it is done for crystalline silicon. Phosphorous and boron doping enhance the mobility of electron and hole charger carriers, respectively, forming what are known as n- and p-type amorphous silicon materials.

Optoelectronic properties of amorphous silicon are heavily influenced by the type of deposition technique that is used, where plasma-enhanced deposition produces better films in comparison to sole chemical vapor deposition. The percentage of hydrogen present within the amorphous silicon structure and the amount of hydrogen links affect the electronic properties of the semiconductor positively. Hydrogenated amorphous silicon (a-Si:H) is sometimes used as an electron filtration layer, that has a relatively higher electron mobility than conventional a-Si.

3.4.6 Amorphous Silicon Manufacturing Techniques

The goal in a-Si manufacturing is to arrive at the PIN structure. The core photodiode in an amorphous silicon solar cell comprises of subsequently deposited layers following either of the two structures p-i-n or n-i-p.

These three layers are as follows: (i) very thin p-type layer, typically 10 nm is thickness, (ii) an intrinsic layer (i-layer) that is significantly thicker, measuring in the hundreds of nanometers, and (iii) a thin n-type layer. The structure is shown in Fig. 10. The operational mechanism starts when incident light hits the cell and causes electrons and holes to diffuse to their opposition due to concentration gradients, leaving behind a forbidden region with an electric

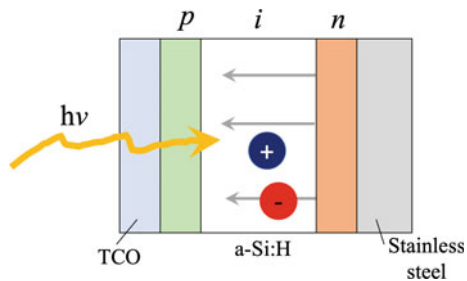


Fig. 10 Schematic of the p-i-n structure of amorphous silicon

field reaching greater than 10^4 V/cm. Conventionally, incident solar radiation on the solar cell allows the permeation of photons through the p-type layer (window layer) and are absorbed in the i-layer due to its relatively larger thickness (meets the penetration depth requirement for absorption). The photocarriers are then drifted by the built-in electric field to the n- and p-type regions/layers causing photogeneration.

3.4.7 Deposition Techniques for Amorphous Silicon

The deposition techniques for amorphous silicon are variants of the chemical vapor deposition (CVD) process, where a plasma is used (plasma-enhanced CVD) along with another source of energy to ensure proper deposition on the location of the glass substrate within the deposition system. These variants include:

1. Radio-frequency, plasma-enhanced CVD (RF-PECVD).
2. Direct current, plasma-enhanced CVD (DC-PECVD).
3. Very high frequency, plasma-enhanced CVD (VHF-PECVD).
4. Microwave assisted PECVD.
5. Hot wire, plasma-enhanced CVD (HW-PECVD).

Spear and LeComber utilized radio frequency (RF) to create SiH_4 -based glow discharge, which is currently known as plasma-enhanced chemical vapor deposition (PECVD). The following list defines the main components of PECVD:

1. Gas delivery system: regulators and controllers for pressure and mass flow rate, respectively, and gas valves for gas flow direction.
2. Deposition chamber: substrate holder, heating element, RF power, high-quality vacuum environment, and deposition electrodes.
3. Pumping system: a turbomolecular pump which is capable of achieving high-quality vacuum for a better deposition process, with its shortcomings backed up by an extra mechanical pump, and a process pump to extract by-products and other gasses.

4. Pressure control system: manometers, throttle valves, and gauges to monitor and control the pressure inside the deposition chamber.
5. High-frequency power supply (RF or very high frequency (VHF) supply with impedance matching network).
6. Exhaust system: where process gasses and by-products are extracted and are typically chemically treated or burnt to neutralize and pyrolyze them, respectively.

The conventional method for producing amorphous silicon-based materials is through PECVD with VHF, hot wire (HW) catalytic deposition, and RF-PECVD with 13.56 MHz excitation. A silicon-containing gas, such as a combination of SiH_4 and H_2 , is often used in the mechanism as precursor in a vacuum-aided deposition where two electrodes are powered by an external RF source. For a specific RF voltage across the plates, there is a gas pressure operating range where plasmas are developed.

The gas in the chamber is excited and decomposed, and generates radicals and ions by the plasma. On one or both of the electrodes, substrates can be put, and when these radicals diffuse onto them, the hydrogenated silicon thin film starts a chain-growth process and crystallizing to a certain degree. To get the best film quality, the substrates are heated ($150\text{--}300^\circ\text{C}$); this effect is explained by the increase in adatoms diffusion within the growing film.

The ideal separation between the RF electrode and the targeted substrate is 1 and 5 cm for a-Si deposition. While a bigger gap makes it simpler to maintain a plasma, a smaller distance is preferable for a uniform deposition. Residue silicon atoms are trapped and deposited onto the chamber boundaries, while the remainder are disposed through the exhaust/venting system. For a given RF power, both the pressure and the gas flow rate have an influence on the residence time of molecules for specific species, which in turn determines the deposition rate.

The setup for a HWCVD system is comparable to that for the RF-PECVD system, with the exception that a heated filament is used in place of the RF electrode. Sole SiH_4 gas, or a blend between SiH_4 and other gasses such as hydrogen or helium, is directed into the chamber. A filament that is temperature durable, usually made out of platinum (Pt), tungsten (W), or tantalum (Ta) metals, is heated to about $1800\text{--}2000^\circ\text{C}$ catalytically exciting the gas into radicals or ions. The silicon radicals then rise within the chamber and are accumulated (deposited) onto a substrate that is positioned a few centimeters away, which is exposed to heat regulation to control the temperature between 150 and 450°C . In comparison with RF-PECVD films, HWCVD a-Si materials exhibit a relatively lower H concentration in the

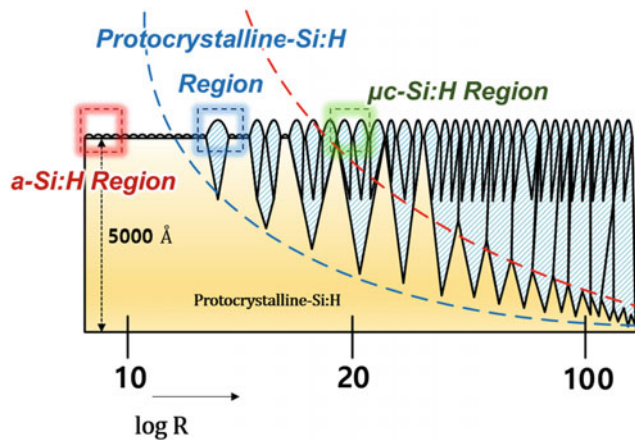


Fig. 11 Range of film structures (schematic), obtained with different PECVD parameters, for films deposited on glass substrates; the dashed lines indicate the transitions between amorphous and mixed-phase material, as well as between mixed-phase material and highly crystalline material. The x-axis is $\log R$, calculated as $\log [H]/[SiH_4]$ (Han et al. Aug. 2017)

film and better durability against light-soaking (degradation due to light exposition).

It has been discovered that hydrogen dilution of the silane gas mixture during a-Si deposition reduces the density of defect states and enhances the material's stability against light-soaking effects. It is quite easy to calculate the dilution ratio, R , that has such potent effect on the resulting layer as follows:

$$R = [H_2]/[SiH_4] \quad (2)$$

where the terms $[H_2]$ and $[SiH_4]$ indicate the flow rate of each respective gas. Solar cells with i-layers deposited using high H_2 dilution ratios exhibit improved performance and stability.

It is also noted that the deposition rate drops with higher R values, and when R is high enough, the obtained silicon films become nanocrystalline.

Films are generally amorphous at lower dilutions ($R = 10$); however, there is a phase change and a transition into a rougher region after a certain thickness limit. As dilution is increased, this roughening transition is suppressed. For increasing dilutions, a regime known as “protocrystalline” begins with the expanding thin film adopting an amorphous structure. Crystallites develop in the amorphous matrix as the film thickens (producing a “mixed phase”). This is shown in detail in Fig. 11.

References

- 50 GW Solar Production: A 2014 Reality?—SolarFeeds Magazine. <https://www.solarfeeds.com/mag/50-gw-solar-production-2014-reality/> (Accessed 10 Feb 2023)
- Best Research-Cell Efficiency Chart | Photovoltaic Research | NREL. <https://www.nrel.gov/pv/cell-efficiency.html> (Accessed 10 Feb 2023)
- EIA: U.S Energy Information Administration (2017) Utility solar photovoltaic capacity is dominated by crystalline silicon panel technology
- Electricity data browser—Topaz Solar Farm. <https://www.eia.gov/electricity/data/browser/#/plant/57695> (Accessed 10 Feb 2023)
- First Solar (2014) First solar builds the highest efficiency thin film PV cell on record. Krum, Steve
- Hall M (2013) EMPA announces 20.4% efficient thin film CIGS-on-polymer cell
- Han S et al (2017) A study on crystalline silicon solar cells using tunnel oxide layer for carrier selective contacts. *New Renew Energy* 13 (3):4–9. <https://doi.org/10.7849/ksnre.2017.9.13.3.004>
- Kazmerski L (2022) Structure of a CIGS device. CdS is used optionally and some CIGS cells contain no cadmium at all
- Mansfield L (2019) Manufacturing and reliability science for CIGS photovoltaics. [Online]. Available: www.nrel.gov/publications
- Topaz Solar Farm, California (2015) Accessed 10 Feb 2023. [Online]. Available: <https://earthobservatory.nasa.gov/images/85403/topaz-solar-farm-california>



Third-Generation Photovoltaics: Dye-Sensitized Solar Cells (DSSC)

Abdul Hai Alami[✉], Shamma Alasad[✉], Haya Aljaghoub[✉],
Mohamad Ayoub[✉], Adnan Alashkar[✉], Ayman Mdallal[✉],
and Ranem Hasan[✉]

Abstract

The investment in new PV technologies is important and is done by exploiting novel materials, materials processing, and manufacturing techniques to achieve performance levels that supersede those attained by classical counterparts. This chapter covers the unique materials and procedures utilized to produce dye-sensitized solar cells of the third-generation technologies. The chapter also includes a do-it-yourself project to provide the reader with a chance to build and test a dye-sensitized solar cell.

1 Introduction

Third-generation photovoltaics technologies have emerged recently to replace conventional silicon-based ones. Using alternative materials and processing technologies is important to explore higher device efficiencies at lower costs. The manufacturing technologies, however, will utilize thin-film (second-generation deposition) techniques with minimal

modifications. The main goal remains to minimize the cost per Watt peak, in addition to using nontoxic and abundant materials, just like the traditional Si-based solar cells, and second-generation thin-film technologies (Conibeer 2007).

According to findings from a study conducted by the National Renewable Energy Laboratory on the top efficient cells in the renewable energy industry, there are three main varieties of third-generation solar cells (and their modified variants): (i) Dye-sensitized solar cells (DSSC), (ii) Organic photovoltaics (OPV), and (iii) Perovskite solar cells (PSC). The variants are enhancements for the above three, such as monolithic, organic tandem, copper zinc tin sulfide (CZTSS), and quantum dot cells.

With the independence from silicon and its processing equipment and technologies, chemical companies such as the Canadian giant DuPont entered the PV materials market. They focused on allocating some of their product lines to be suitable and compatible with equipment and processes to produce third-generation solar PV cells, especially OPV. What the NREL-reported results lacked was the association of output power or efficiency with the associated costs of producing the cells. Figure 1 shows this association for all three PV generations, with first generation cells having high production cost and consistent, but low efficiency. Second-generation technologies have low cost and low efficiency. The technologies that have the best promise are third generation which reside in the low cost/high efficiency quadrant (CleanEnergyWIKI 2022).

The first gray area in the graph of Fig. 1 is the thermodynamic limit (theoretical limit) which cannot be exceeded. It is similar to the Carnot cycle efficiency limit. The second gray area represents the single bandgap limit for a single heterojunction cell. To have more than one bandgap means to build and test a tandem solar cell, where the light absorbers are arranged in a layered way, with the one with a bigger bandgap being placed at the top.

A. H. Alami (✉) · H. Aljaghoub · M. Ayoub · A. Mdallal ·
R. Hasan
University of Sharjah, Sharjah, United Arab Emirates
e-mail: aalalami@sharjah.ac.ae

H. Aljaghoub
e-mail: haljaghoub@sharjah.ac.ae

M. Ayoub
e-mail: mohamad.ayoub@sharjah.ac.ae

A. Mdallal
e-mail: ayman.mdallal@sharjah.ac.ae

S. Alasad · A. Alashkar
American University of Sharjah, Sharjah, United Arab Emirates
e-mail: g00070854@aus.edu

A. Alashkar
e-mail: b00028197@alumni.aus.edu

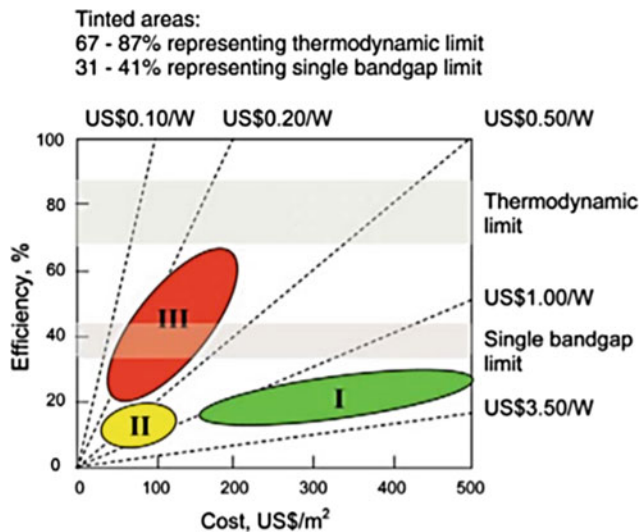


Fig. 1 Cost-efficiency graph, where costs are modules per peak W (CleanEnergyWIKI 2022)

1.1 Roll-To-Roll (R2R) Manufacturing

Thus, the main goal of developing third-generation photovoltaics is to reduce the cost and provide consistent efficiency. This should be done via manufacturing processes amenable to mass production, or what is known as roll-to-roll (R2R). If this is done, the PV modules can be printed in ways similar to how newspapers or magazines were printed decades ago. Instead of the Cyan, Magenta, Yellow, and Black (CMYK) colors, active precursors are used through nozzles and slots on temperature-controlled substrates and different processing conditions. It is said that if the PV rolls are produced at 60 km/hr, then one year would be enough to produce PV modules to cover the world energy needs.

The major problems that preclude these technologies from achieving their desired status include their limited lifetime and compatibility, since these solar cells are not guaranteed to last for 25 years as their silicon counterpart. Also, most of the technologies require a strictly pristine and controlled environment (i.e., in a Glovebox), which means that their operation in their real environment cannot be predicted. It is, however, interesting to mention that it is possible that third-generation solar cells may achieve efficiencies higher than the 31–41% power efficiency range established by the Shockley–Queisser limit, since their bandgap can be tuned and manipulated, which keeps the door open for R&D work to allow their performance and economics to be truly competitive.

1.2 Third-Generation PV Cell Structure

Third-generation photovoltaics can be considered as electrochemical devices. This is a main difference between them and the strictly solid-state silicon solar cells, as shown in Fig. 2. For third-generation photovoltaics, there are two mechanisms of charge transfer after the charge generation due to incident solar radiation. The first mechanism occurs after incident radiation produces the electron/hole pairs and electrons are guided to the external circuit directly. The second mechanism involves a series of redox reactions at the surface of the photoanode and the electrolyte as well as at the interface between the electrolyte and the counter-electrode that will receive the electron after it passes through the external load.

From a manufacturing point of view and as will be seen later, most third-generation photovoltaic materials are built upon a transparent glass substrate. This substrate allows subsequent strata of active materials to be deposited on a smooth and perfectly straight base. Titanium dioxide (TiO_2) or titania is another common denominator for all third-generation technologies. Titania is a very porous material upon which active materials can intercalate and attach. Also, to make the transparent photoanode conductive, a transparent conductive oxide (TCO) layer is added. This layer is composed of indium-tin oxide (ITO) or fluorine-doped tin oxide (FTO) and deposited on the nonconductive glass. Such oxides have sheet resistance less than $30 \Omega/\text{square}$ and reflectivity of around 10%. Making such layers more transparent and more conductive requires a strict balance of two opposing factors. To be more conductive, an opaque metal is ideal, but this takes the transmission down to zero, and thus, an optimization has to be made.

2 Dye-Sensitized Solar Cells (DSSCs)

From a manufacturing standpoint, the most straightforward third-generation solar cell technology is the dye-sensitized solar cells. There is a biomimetic aspect to how light interacts with the solar materials that is similar to photosynthetic activities in plants and some aquatic creatures. The titanium dioxide in the photoanode is “sensitized” when a dye is introduced to shift the material’s absorbance from the UV “Ultraviolet” to the visible spectrum range. Figure 3 shows the absorbance of TiO_2 under UV radiation, which happens in a strictly narrow range. Since the target range is around 500–600 nm, a dye is added to the titania to allow this shift and utilization of incident solar radiation.

Fig. 2 **a** General structure of a solid-state silicon photovoltaic technologies and **b** photo-electrochemical third-generation technologies

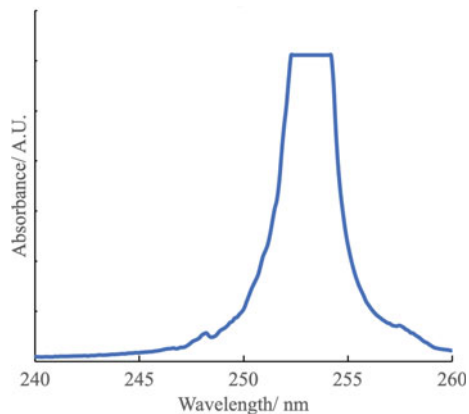
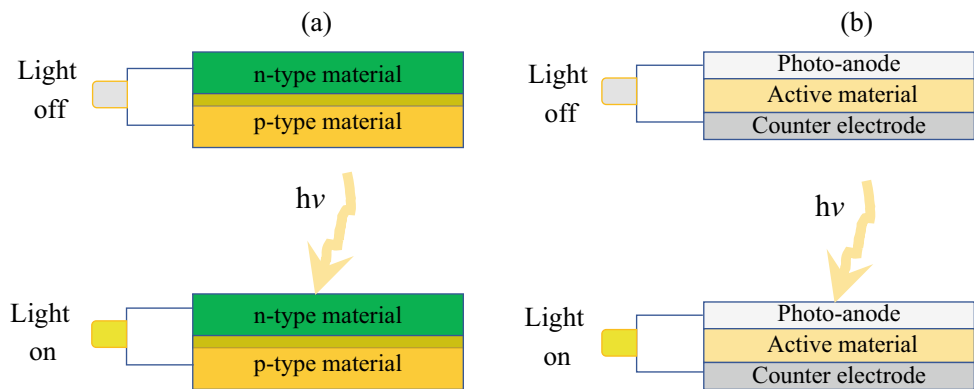


Fig. 3 Titanium dioxide (TiO_2) absorbance in the UV range

Dyes are ligands, which are ions or neutral molecules that function as Lewis bases (electron pair donors) and bond to a central metal atom or ion, also behaves as a Lewis acid (electron pair acceptor). A covalent bond is formed with the central atom using ligands consisting of at least one donor atom with an electron pair. Ligands allow for the production or consumption of electrons in the ionic state and can attach to the surface of the TiO_2 material and allow for the shift in its absorbance from UV to Vis as will be detailed later. When a semiconductor is sensitized, sensitizers are adsorbed on its surface. They are responsible for the absorption of visible light, which results in the subsequent injection of excited electrons into the conduction band of the semiconductor electrodes.

2.1 Grätzel Cell

These biomimetic devices are a major shift from conventional silicon solar cells and were produced in 1992 by Michael Grätzel at the Ecole Polytechnique in Switzerland (O'Regan and Grätzel 1991). There was no boron or phosphorus doped Si p-n junction present in this cell. The result is a photo-electrochemical cell, which functions similarly to

a photosynthetic plant cell. Since the Grätzel cell is so cheap and simple to produce, it has attracted a lot of interest and served as a foundation for further research.

The cell structure is based on the following main components:

1. Photoelectrode (photoanode)
2. Electrolyte (reduction/oxidation)
3. Dye (in the heart of the cell)
4. Counter-electrode.

The operation at a glance:

In a dye-sensitized solar cell, the dye is the engine that drives the device (operates like chlorophyll in a photosynthetic plant cell). The dye is often an organometallic complex based on ruthenium, but other natural sensitizers can be used; however, they bear lower efficiencies. In order to capture photons, the dye is essential (by generating excitons), i.e., when a photon hits the dye, an electron is excited from the ground state (HOMO) into the first excited state (LUMO), leaving behind a hole. For the semiconducting layer, titania is not the only option as zinc oxide (ZnO) and tin oxide (SnO_2) can also be used. TiO_2 is the most prominent one for use in cell manufacture because of its ultra-porosity, which provides anchoring locations for dyes as well as ample area for redox reactions to take place.

2.2 DSSC Cell Structure

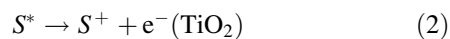
The cell building takes place over a lime soda glass substrate. Although it is a nonconductive material, it allows solar radiation to pass into the active material. Once the light hits the active material (TiO_2), it will start to produce electrons. In order to collect the electrons, it is necessary to apply a transparent conductive oxide (TCO) to the glass in the form of indium-tin oxide (ITO) or fluorine-doped tin oxide (FTO) so that charge can be conducted. ITO is transparent, conductive, and has sheet resistance of $30 \Omega/\text{square}$, while

the fluorine doping reduces the sheet resistance further to 15 Ω /square. The counter-electrode (Al, Au, Ag, etc.) is put on top of the TiO_2 , and in between the electrolyte is injected which helps to close the circuit electrochemically. The dye operates like chlorophyll in a photosynthetic cell. Dyes could be natural sensitizers or synthetic. Ruthenium-based organometallic synthetic dye is often used and is responsible for harvesting the photons and generating excitons (electron/hole pairs). Figure 4 shows the cell structure.

Once a photon hits the dye, an electron will be excited from the ground state, which is located in the highest occupied molecular orbital (HOMO) and will move into the lowest unoccupied molecular orbital (LUMO), producing excitons and leaving behind a hole. The most significant thing in DSSC is that the generation of e^- and h^+ are occurring in two different locations. As will be seen later in this chapter, the substrate and enhancer selections have a significant impact on the resulting voltage levels in practice.

3 Operating Mechanism

The TCO-coated electrode (e.g., SnO_2 /glass) consists of a nanocrystalline oxide semiconductor thin-film electrode (TiO_2 or ZnO), a sensitizer (dye) is adsorbed on the surface of the TiO_2 electrode, and the TiO_2 electrode absorbs the incoming photons, causing a transition from the ground state (S) to the excited state (S^*). An electron moves from the sensitizer's HOMO to its LUMO during photoexcitation. Here are the equations for how the oxidation of the sensitizer molecule occurs, as a consequence of the of the propulsion of the excited charge carriers from the valence band to the conduction band of the TiO_2 layer (photo-electrode). The redox ions are contained inside the electrolyte.



Electrons are not only transferred from singlet states, where all electrons are paired, but also from triplet states that include two unpaired electrons. This is due to the high energy states. Next, the injected electrons permeate through

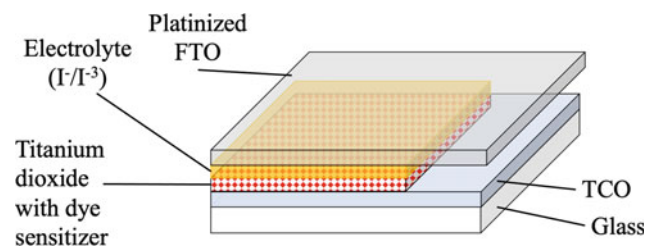


Fig. 4 Simplified DSSC cell structure

the TiO_2 electrode to the transparent conducting oxide (TCO) electrode. The ground state of the oxidized sensitizer is regenerated when it is reduced by the I^- ions that are present in the electrolyte, and the I^- ions themselves are oxidized into I_3^- ions during this process. Because of this, I_3^- ions move toward the opposite electrode, where they are reduced to I^- ions. Figure 5 depicts the operation of DSSC under illumination.

4 Energy Levels and Recombination Prevention

If the hole and the excited electron are not separated by two different and separate media, then recombination will occur. Keep in mind that the anode, composed of nanostructured titania (TiO_2), serves as the electron transport layer (ETL) and receives the excited electrons. Titania is a mesoporous material that is annealed to be in its anatase structure (rather than rutile), and the pore structure of titania ranges from 2 to 50 nm in size. The titania matrix receives dye molecules, where ligands bond to titania. Electrons can then transfer quickly from the LUMO of dye molecules to the lower energy of titania conduction band. Figure 6 below displays a typical energy diagram.

The hole should be directed to the opposite side of the cell (the cathode). This is also referred to as the hole transport layer (HTL). An iodide/triiodide (I^-/I_3^-) redox couple was used in the first Grätzel cell. The iodide would regenerate the oxidized dye molecules and the resulting oxidized species (triiodide) are transported to the cathode via diffusion, where they are reduced back into iodide. Since diffusion is a physical phenomenon, it is sensitive to the density,

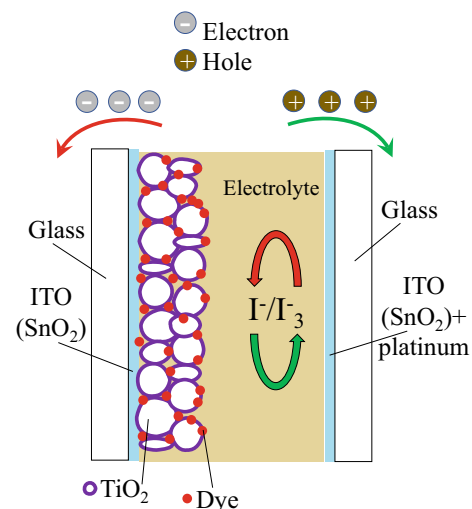


Fig. 5 Dye-sensitized solar cells principle of operation

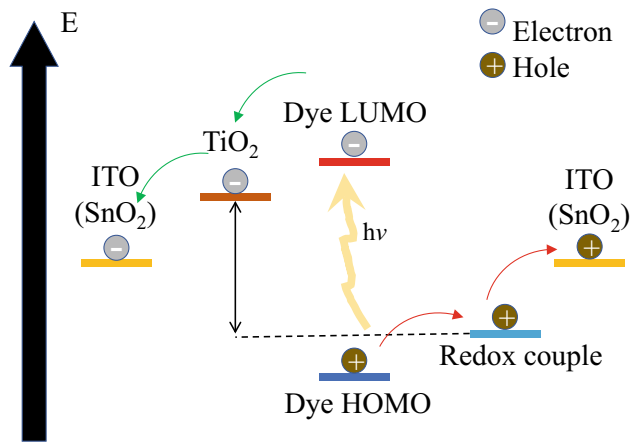


Fig. 6 Dye-sensitized solar cell's typical energy diagram

concentration, and viscosity of the electrolyte (solute/solvent ratio and type).

5 Generated Voltage

The open-circuit voltage in DSSC depends on the interaction between different material layers and their work functions under illumination. The effective voltage obtained is measured between redox couple and dye LUMO, and hence, any enhancements of this voltage have to happen at this interface. The difference in energy that exists between the Fermi energy of the electrons in TiO_2 , and the redox potential of the liquid electrolyte is what determines the maximal photovoltage that may be achieved. TiO_2 's conduction band and the HOMO level of the hole transport layer (HTL) material combine to provide the highest possible voltage for a solid-state device. The practical voltage values depend on many factors such as the type of material used. The maximum V_{oc} obtained is 0.7 V, and the maximum efficiency is 11% (13% in 2022). In cells that utilize Poly(3,4-ethylenedioxythiophene) poly(styrenesulfonate) (PEDOT:PSS) and poly(4-undecyl-2,20-bithiophene) (P3PUT), the photovoltage is differed by 0.7 V, although their HOMO levels are 1 eV apart.

Recombination is the leading cause for fewer electrons to perform the desired work. It also reduces the anode's voltage and Fermi energy of electrons. Furthermore, the less holes that reach the cathode, the more energy the electrons will gain at the cathode. This adversely affects the photovoltage, measured from the difference between two electrodes.

Grätzel cells still have not reached their full industrial potential, but improvements to their three main components (Dye, ETL, HTL) as well as increased reliability and a longer lifespan will help get them there. These factors are discussed the following sections.

6 Space Charge and the Electric Field

In silicon solar cells that utilize p-n junctions, the active junction is formed when electronic charge carriers from different components balance out, creating a space-charge region. In the space-charge layer, the electric field effectively separates the photogenerated charges.

In third-generation PV and in DSSC in particular, there are no space-charge effects as there is no long-range continuum of host material. The titania has individual particles with nano-dimension size (~ 20 nm), which is not thick enough to produce a space-charge layer. Also, cations at the counter charges of I^-/I_3^- redox couple in electrolytes act as a filter for electrons in the electrode, which results in the absence of a potential gradient in the electrode. The first step in the process of charge separation is completed when electrons are injected into the semiconductor (titania) and holes are injected into the electrolyte.

7 Depletion Zone/Charge Separation

Contrary to conventional PV cells, where the charge carrier separation happens under the influence of a built-in electric field, the charge separation in DSSC happens due to the chemical interface and energy level differences between the different layers. For example, once the electrons are generated in the sensitizer media, they are transferred into the TiO_2 layer and subsequently into the transparent conductive oxide layer (i.e., ITO). Moreover, the consequently generated holes are transferred via the I^-/I_3^- electrolyte and finally to the counter-electrode. A similar phenomenon can be found in the photosynthesis process in plants, where a synthesizer (chlorophyll) generates charge carriers that are transferred via a membrane in the living organism.

For all solar cells, the following equation may be used to determine their individual efficiency (%) in transforming solar energy into electricity:

$$\eta(\%) = \frac{J_{sc} [A \cdot m^{-2}] \times V_{oc} [V] \times FF}{I_0 [W/m^{-2}]} \times 100 \quad (3)$$

where I_0 is photon flux (100 mW cm^{-2} for Air Mass 1.5G (AM 1.5 G)), J_{sc} is the short-circuit current density (at no voltage) when under illumination, V_{oc} represents the open-circuit voltage, and FF is the fill factor.

8 Open Circuit Voltage Considerations

The energy gap between the Fermi level and the TiO_2 electrode is used to measure the open-circuit voltage of the cell (which is located near the conduction band potential or

E_{CB}) and the redox potential of the I^-/I_3^- in the electrolyte. See Fig. 7 for an illustration of where the voltage is measured. The yellow stripes indicate a voltage measurement point. Redox couples have an energy separation of (ΔE_1), which is taken into account as the driving force for electron injection. Therefore, I^- oxidation results in the regeneration of the dye-cation. The HOMO has to be highly positive than the I^-/I_3^- tendency to gain/lose electrons in order to receive electrons efficiently. The value of ΔE_2 represents the difference between these two values. For improved DSSCs with TiO_2 and I^-/I_3^- , ΔE_1 and ΔE_2 are around 0.2 and 0.5 eV, respectively.

Both the E_{CB} value of the TiO_2 electrode and the redox potential in the electrolyte are strongly dependent on the nature and concentration of the electrolyte components and are generally between -0.5 and 0.4 V against normal hydrogen electrode (NHE), respectively. Currently, optimized DSSCs show V_{oc} in the range of 0.75 – 0.85 V, whereas the greatest V_{oc} achieved for DSSCs with a TiO_2 electrode and the I^-/I_3^- redox medium is typically around 0.9 V.

9 Short Circuit Current Considerations

The short-circuit current density J_{SC} is determined by the product of the charge injection efficiency φ_{inj} , the charge collection efficiency η_c , and the light harvesting efficiency (LHE) which is given by the following formula:

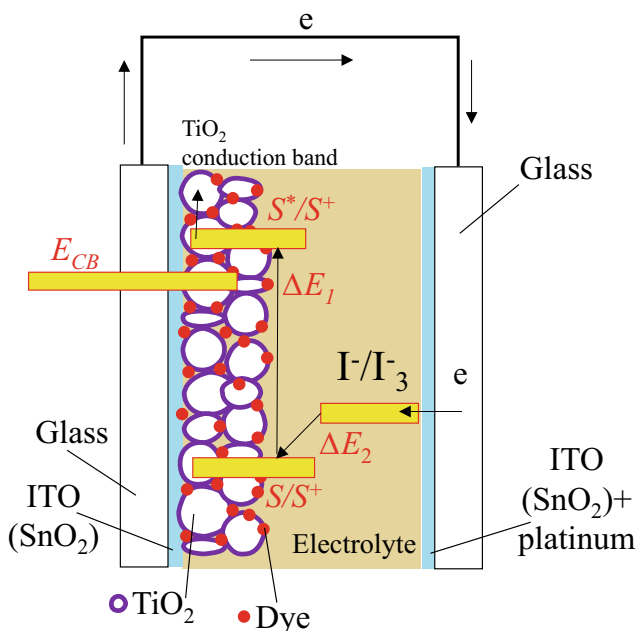


Fig. 7 A typical DSSC construction with voltage reference points highlighted in yellow

$$LHE = 1 - T = 1 - 10^{-A} \quad (4)$$

where T represents radiant transmission and A represents radiant absorption. The LHE is obtained by determining the electrodes effective absorption coefficient. TiO_2 electrode thickness, adsorbed dye concentration, and sensitizer extinction coefficient each have a contribution.

The photo response range of the cell is set by its bandgap (HOMO–LUMO difference). The higher the bandgap, the better in order to allow higher energy to go to the cell. In order to take advantage of a larger spectrum of solar radiation, it is necessary to have a narrow HOMO–LUMO energy gap. The LUMO must be more negative compared with E_{CB} to have high φ_{inj} .

10 Surface Area Considerations

High LHE is obtained when incident photons are completely absorbed by the sensitizer. TiO_2 nanoparticles offer a huge surface area for dye molecules to adhere. In fact, TiO_2 electrodes have a surface area that is almost a thousand times bigger than their apparent surface area, as measured by a roughness factor (r_f). In other words, the actual surface area of a TiO_2 film measuring 1 cm^2 with a thickness of 10 μm is 1000 cm^2 . This also means that if the r_f of the nanoporous TiO_2 film is high, the dye adsorption will be very high (by a quantity of the order of 10^{-7} mol cm^{-2}), resulting in almost complete absorbance at the dye spectrum absorption's peak wavelength.

11 Charge Collection Efficiency

Electron diffusion length (L) is used to determine charge collecting efficiency:

$$L = \sqrt{D[m^2/s] \cdot \tau[s]} \quad (5)$$

where D is the diffusion coefficient for electrons in nano-sized pores in semiconductor electrodes, and τ represents the electron lifetime in the electrode, which is measured by the rate of recombination at the interface between the electrode, dye, and electrolyte.

Due to the different nature of liquid-based and solid-state DSSC, the diffusion length of the electrons with them varies accordingly. As to capture the generated electrons, their diffusion length must be higher than the cell's materials thickness. For liquid-based DSSC, the diffusion length is in the tens of micrometers; in an optimized DSSC, the resultant collection efficiency would be bordering 100%. However, in solid-state DSSC, the diffusion length is shorter, which is

why they require more efficient sensitizers to make up for any potential collection losses.

12 The Fill Factor

The fill factor (FF) is affected by the solar cell's shunt and series resistances. In addition to charge recombination at the TCO/electrolyte interface, interfacial charge recombination contributes to the shunt resistance. Shunt resistance should be decreased, which is achieved by finding materials that are better compatible with each other. The electrolyte thickness may be decreased, the concentration can be increased, and the surface area of the platinum counter-electrode can be increased in order to decrease the series resistance. The FF may also be connected to the rate of potential-dependent electron transfer or transport when exposed to light.

13 Components of DSSC

To construct a functioning DSSC, the following components should be present, and their interactions optimized:

1. TCO Electrode
2. Nanocrystalline TiO_2 Photoelectrode
3. TiO_2 nanoparticle
4. Ru-complex photosensitizer
5. Redox electrolyte
6. Counter-electrode
7. Sealing materials, used to eliminate leakage of electrolyte and solvent evaporation. For example, co-polymers such as Surlyn Du Pont, which is a mixture of ethylene and acrylic acid, are used.

13.1 TCO Electrode

Substrates for TiO_2 photoelectrodes typically consist of TCO-coated glass. High solar cell performance is achieved by ensuring the TCO substrate has a high conductivity (low sheet resistance) and transmittance (transparency). Sintering of the TiO_2 electrode typically takes place between 450° and 550°C ; therefore, the conductivity should be temperature independent up to these temperature extremities. The TCO resistance is measured by the four-point probe technique. A multimeter is a handy tool to know which surface has the TCO deposition, and it can also be used to estimate the resistance between the two multimeter probes knowing the distance between them. This procedure carries many sources of errors, and thus, a four-probe setup like the one shown in Fig. 8 has a pre-set distance (x) between the probes and

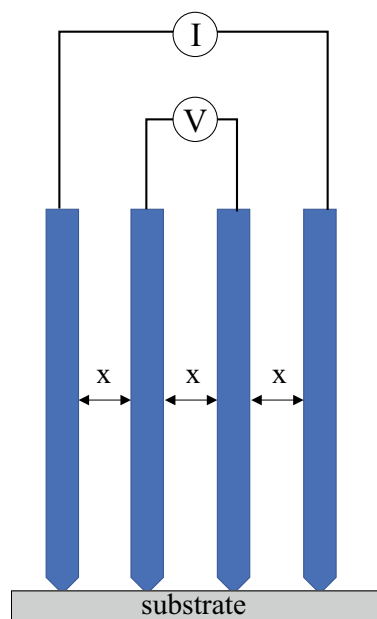


Fig. 8 Four-probe test to determine the sheet resistance of glass with TCO

offers separate voltage and current readings to enhance the accuracy.

Indium-tin oxide (ITO) is the most common TCO material. Despite its low resistance at room temperature, ITO has a poor thermal stability of resistance. Nippon Sheet Glass Co. and other manufacturers employ FTO (fluorine-doped SnO_2) as the TCO substrate for DSSC. (nsg.com), or Asahi Glass Co. Ltd. (agc.com) that produce glass with sheet resistance in the range of $R = 8\text{--}10 \Omega/\text{square}$. Plastic DSSCs may employ ITO-coated poly(ethylene terephthalate) (PET) or poly(ethylene naphthalate) (PEN) as a substrate if TiO_2 electrode preparation can be done at temperatures under 200°C .

13.2 Nanocrystalline TiO_2 Photo-Electrode

In this and any other electrochemical system, the essential function of an electrode is to offer adequate surface area for dye adsorption, which is why porous electrodes are preferred over their counterparts, to transport all injected electrons to TCO, and to enable redox reaction to take place. Electrodes have to be transparent in order for visible and near-infrared radiation to pass through (wavelengths between ~ 380 and 1000 nm). The absorption coefficients of the sensitizers dictate the required penetration depth for the photons to be absorbed, which is why the porosity of the electrode (measure of the present surface area) and its thickness are important parameters (while taking into account the diffusion length of electrons).

For typical cells, the best thickness of porous electrodes is 10–20 μm . Electrodes utilize commercial nanocrystalline TiO_2 , such as P25 Degussa/anatase (see sigmaaldrich.com) and ST-21 from Ishihara Sango Kaisha Ltd. (see <https://www.iskweb.co.jp>). TiO_2 has to be in nanoparticles form with maximum particle size of 20 nm that can be obtained from the hydrolysis of Ti (IV) alkoxides. It is necessary to exercise control over the hydrolysis and condensation kinetics in order to generate monodispersed particles of the required size. Acetic acid (or acetyl acetonate) treatments are carried out on titanium alkoxides to obtain colloids with relatively large porosity-induced surface area density, with values reaching 200 m^2/g . However, an adverse effect is witnessed on the particle size, where a reduction up to a diameter of 7 nm was present.

13.3 Preparation of the TiO_2 Electrode

To begin the process of preparing the TiO_2 electrode, initially a TCO substrate is covered with the TiO_2 paste employing screen printing, spin coating, or doctor blading and then heated at temperature in the range of 450–550 $^\circ\text{C}$ to transform the TiO_2 into the desired porous anatase structure. The target thickness of the TiO_2 is around 10 μm , which requires multiple runs in the spin coater or doctor blading. In screen printing, film thickness can be controlled by (i) proper paste composition selection (i.e., TiO_2 nanoparticles wt % in the paste), (ii) screen mesh size, and (iii) printing repetition. It is also important that the TiO_2 film is porous enough to enable the electrolyte holding the redox ions to permeate it, allowing the redox ions to access all the adsorbed dyes and diffuse again to the counter-electrode. Some enhancements to film production such as the addition of a polymer (polyethylene glycol (PEG) and ethyl cellulose (EC) into the TiO_2 paste control the porosity of 50–70% in the sintering process. Adding surfactants also helps enhance the surface adhesion and can be fired away during sintering operation.

13.4 Adsorption Properties of Dyes

Dye is added to enhance the sensitivity of the cell and absorption of longer wavelengths. This is true for all types of dyes, natural and synthetic. The former can consist of either chlorophyll (green) or anthocyanin (red), and the latter uses Ru-complex sensitizer. Being adsorbed onto the TiO_2 surface, it aids in the initial processes of photon absorption and the subsequent injection of electrons. Grätzel's typical Ru-complex sensitizers' chemical structure is seen in Fig. 9a, and their absorption (solid lines) and transmission (dashed lines) properties are illustrated in Fig. 9b (Nazeeruddin et al. 2004).

The metal-to-ligand charge-transfer (MLCT) transition is responsible for these dyes' absorption in the visible and near-IR ranges. The d-orbital of the Ru metal and the π^* of the ligand provide the basis for the HOMO and the LUMO, respectively. The absorption characteristic of the complex is shifted toward the red because the NCS ligand accepts electrons from iodide ions and causes a negative HOMO level shift.

Among the visible wavelengths of light, blue has the greatest frequency while red has the lowest. A redshift occurs when an object moves away and the light is stretched to lower frequencies and longer wavelengths. On the other hand, a blueshift occurs when the wavelength is decreased, which is associated with an increase in frequency of electromagnetic waves. The color is changed in visible light, moving from the red to the blue ends of the spectrum.

13.5 Dye Preparation

As will be further discussed in the case study at the end of this chapter, the steps for dye preparation are as follows: The Ru-complex sensitizers are dissolved in a 1:1 mixture of ethanol or tert-butanol and acetonitrile at a concentration of 0.2–0.3 mM. After the electrodes have been preheat-treated and coated with TiO_2 , they are submerged in the dye for more than 12 h at 25 $^\circ\text{C}$ to enable the dye to adsorb to the TiO_2 surface. Because of the strong electrical interaction between the ligand and the TiO_2 conduction band, electrons may be effectively injected from the Ru-complex into the TiO_2 upon attachment of the carboxyl groups of the Ru-complex to the TiO_2 surface. Analysis of FT-IR absorbed energy show that the Ru-complex is adsorbed on the TiO_2 surface through carboxylate bidentate coordination or ester bonding. Because of the TiO_2 surface area and the dye quantity, the N3 dye covers approximately 100% of the TiO_2 surface.

13.6 Redox Electrolyte

Electrolytes utilized in DSSCs include I^-/I_3^- redox ions, which enable the transfer of electrons between the sensitizers and the counter-electrode. Lithium iodide, sodium iodide, potassium iodide, tetraalkylammonium iodide (R4 NI), and imidazolium-derived iodides in nonprotonic organic solvents at concentrations of 0.1–0.5 M (M: molar concentration) and 0.05–0.1 M I₂ are all examples of iodide mixtures. DSSC often makes use of nitrile solvents, which are organic solvents with a relatively low viscosity. Some examples of these solvents are acetonitrile, propionitrile, methoxyacetonitrile, and 3-methoxypropionitrile. Solvent viscosity is very important as it impacts the electrolyte ionic

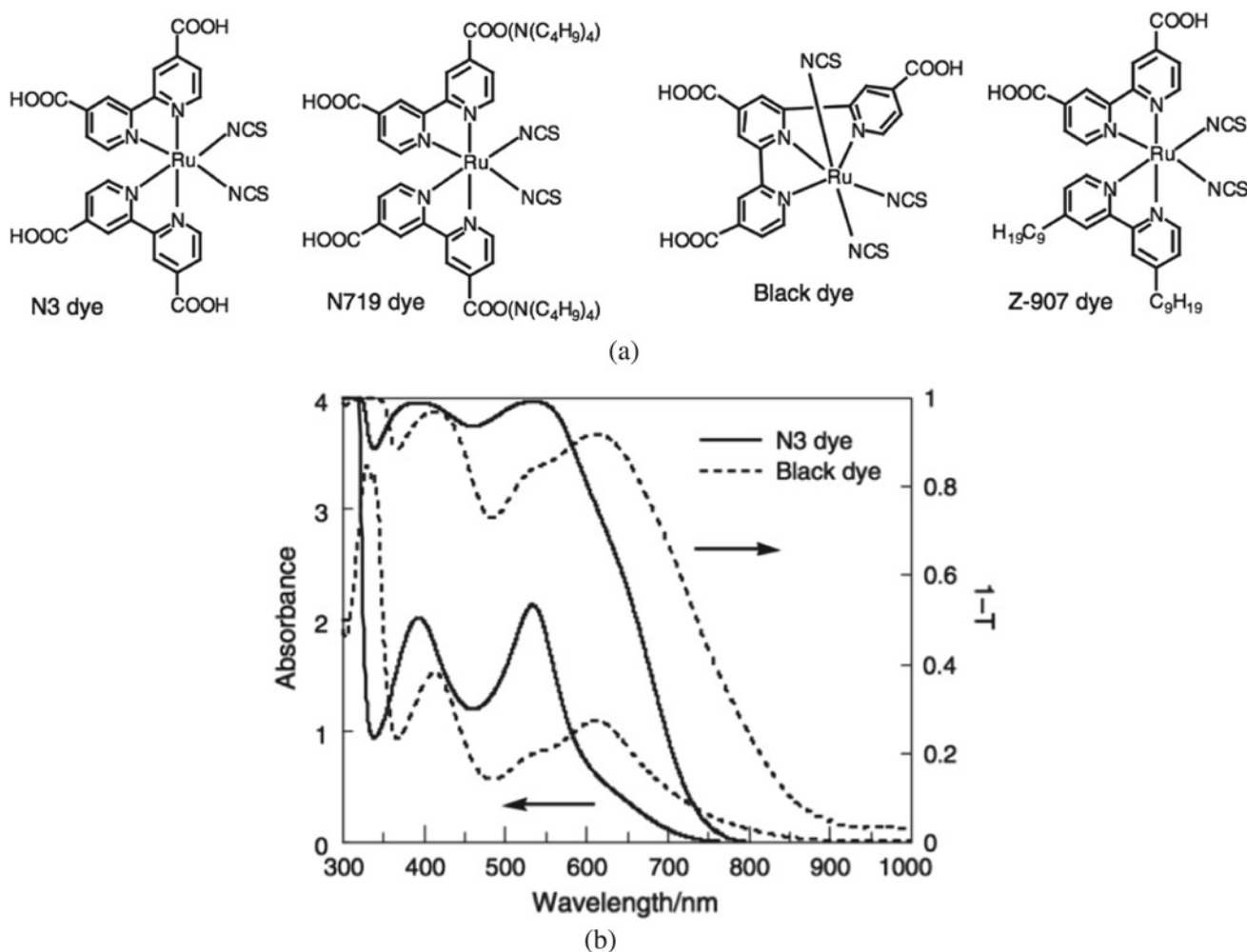


Fig. 9 a Chemical structure of ruthenium-based synthetic sensitizers and b absorbance in the UV–Vis region for the N3 and black dyes (nm) (Nazeeruddin et al. 2004). (With permission 5,364,120,164,714)

conductivity and hence, the solar cell's performance. Low viscosity is desired to enhance the J_{sc} of the solar cell, but the problem is that it is going to evaporate, and whose long-term seal is similarly difficult to achieve. On the contrary, high viscosity results in harder ionic motion and thus low current. The diffusion coefficient of I^{-3} in methoxyacetonitrile = $5.4 - 6.2 \times 10^{-6} \text{ cm}^2\text{s}^{-1}$, which is the best range.

13.7 Counter-Electrode

At the counter-electrode, the triiodide ions I_3^- , which are produced when dye cations are reduced with I^- ion, are oxidized back to I^- ions. The electrocatalytic process involving the reduction of triiodide ions requires a counter-electrode with a high level of electrocatalytic activity. The counter-electrode functions as a collector of the positive charges (holes), and this is where the reduction of

the electrolyte takes place. A good conductive material which has a good catalytic activity should be utilized. The material used as a counter-electrode could be 100% platinum, but its main issue is the high cost. The counter-electrode consists of sputtered Pt coated on a TCO substrate ($5-10 \mu\text{g}\cdot\text{cm}^{-2}$ or around 200 nm thickness). Pt colloids are formed on the surface of a TCO substrate with a sputtered layer of Pt on top of it, by dropping a controlled quantity of an alcoholic solution of H_2PtCl_6 over the surface, drying it, and then heating it at 385°C for 10 min. Resistance of the counter-electrode and electrolyte interface have an impact on the solar cell's fill factor. Polymers and carbon-based materials (i.e., PEDOT) are the other alternatives for the counter-electrode instead of Pt. The electrocatalytic activity required for the reduction of triiodide ions corresponds to an exchange current density of $0.01-0.2 \text{ A cm}^{-2}$. Pt is not the only material suitable for use as a counter-electrode; carbon and polymers like PEDOT are other viable options.

14 Performance of Highly Efficient DSSCs

Incident photon-to-current conversion efficiency (IPCE) is calculated from:

$$\text{IPCE}(\%) = \frac{1240(eV \cdot \text{nm}) \times J_{\text{ph}}}{\lambda \times \phi} \times 100 \quad (6)$$

where the constant 1240 has the energy unit of electronvolt (eV) multiplied by the wavelength unit of nanometer (nm), J_{ph} (mA cm^{-2}) designates the short-circuit photocurrent density when exposed to monochromatic irradiation, λ (nm) and ϕ (mW cm^{-2}) are the wavelength and intensity of the external monochromatic light, respectively. The highest IPCE is typically lower than 90%:

$$\text{IPCE} = \text{LHE} \times \phi_{\text{inj}} \times \eta_c \quad (7)$$

where LHE is the light harvesting efficiency, ϕ_{inj} is the electron injection efficiency, and η_c is the collection probability of charge carriers (charge collection efficiency).

14.1 Performance of Ru Sensitizer-Based DSSCs

Ru sensitizer are standard and give the best FF and η . The high η values, more than 11% were obtained with DSSC, e.g., with N719 dye ($J_{\text{sc}} = 17.7 \text{ mA cm}^{-2}$, $V_{\text{oc}} = 0.846 \text{ V}$, FF = 0.75), and with black dye ($J_{\text{sc}} = 20.9 \text{ mA cm}^{-2}$, $V_{\text{oc}} = 0.736 \text{ V}$, FF = 0.72).

14.2 Mechanism of Dye to Metal Oxide Electron Injection

Being an electrochemical device, it is important to analyze not only the electronic motion in wires and contacts, but also their physical diffusion behavior across all different layers of the cell. An intramolecular MLCT transition takes place as a consequence of the photoexcitation of a Ru-complex sensitizer. In this transition, the HOMO and LUMO are generated from the d-orbital of the Ru metal and the π^* orbital of the bipyridyl ligand, respectively. Negatively moving the HOMO level (which results in the red shift of the complex's absorbance) is accomplished by the NCS ligands, which are powerful electron donors. In addition, these ligands take electrons donated by iodide ions. Following photoexcitation, excited electrons from the bipyridyl ligands are effectively injected into the TiO_2 electrode's conduction band via the carboxyl groups bonded to the TiO_2 surface.

The oxidation potential of the excited state of the sensitizer is greater, or more negative, than the voltage of the conduction band, E_{CB} , and the difference needed is determined to be larger than 0.2 V as was shown in Fig. 6. Since TiO_2 is nanoporous, it is reasonable to assume that the energy heterogeneity of the nanoporous metal oxide electrode surface is sufficient to produce the necessary ΔE_1 . Ru-based dyes provide quick intersystem crossover from singlet to triplet excited states, followed by injection from the triplet excited state to the conduction band, and thus allows for the detection of injection from the excited state of the dye using a TiO_2 electrode. Hence, electrons will transport mainly by diffusion. The charge diffusion equation is governed by:

$$Q = -D \frac{dc}{dx} \quad (8)$$

where D refers to the electrons coefficient of diffusion and c refers to their concentration. The current response to a slight variation in incident light has been used to calculate the nanoporous TiO_2 material's diffusion coefficient D . As measured by the current response, the diffusion coefficients improved from 10^{-8} to $10^{-4} \text{ cm}^2/\text{s}$ as the light intensity increased, while the value in crystal TiO_2 is on the order of $100 \text{ cm}^2/\text{s}$ (Supriyanto et al. 2019).

Since there exist various charged species with opposite electrical charges, the diffusion coefficient is usually affected by the resulting electric field. The electron current is coupled by a cation current, and the slower current dictates the measured (observable) current. In electrolyte solutions with low cation concentrations, the electron diffusion is additionally constrained by the cation diffusion current rather than only the trapping and de-trapping events. This is known as ambipolar diffusion, the coefficient of which is written as:

$$D_{\text{amb}} = \frac{(n+p)}{(n/D_p) + (p/D_n)} \quad (9)$$

Annealing, which is heat treatment of the nanoporous electrodes, is done to enhance the diffusion and ionic motion of TiO_2 anatase that needs high temperature, unlike TiO_2 Rutile. This process also allows the electron lifetime to be increased with increasing temperature. This is related to the formation of traps at the boundary. Figure 10 shows the electron transfer process through a typical DSSC, along with the mechanism and the time scale at which the transfer can occur. The sensitizer in this case is an N3 one (see <https://www.solaronix.com/materials/products/ruthenizer/>). Figure 10 is a schematic depicting the injection process.

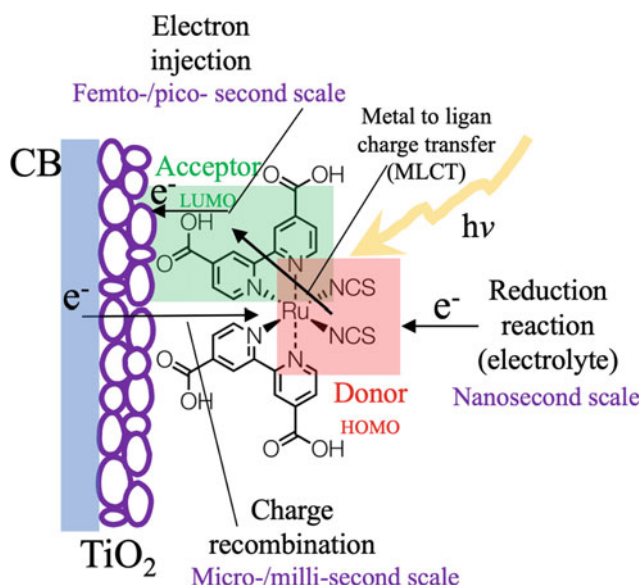


Fig. 10 Electron transfer process in DSSC

14.3 Commercialization

Many aspects have to be perfected in the development of DSSC technologies before they can be commercialized. The high sheet resistance of the TCO electrode on scale-up of the DSSC, which causes a loss of efficiency, is one of the obstacles that has to be solved, along with the primary issues of fill factor, stability, and lifespan in severe environmental conditions. There is also the decision on what size should the DSSC cell be within a module. In Si-based technologies, the wafer size was determined according to restriction of production processes or material properties (surface tension).

Among the many advantages of DSSC production technologies is the ability to deposit the layers on almost any substrate. For example, flexible DSSC deposited on flexible TCO-covered PET substrate is a stark advantage over silicon solar cells. Also, since cell size is not bound except by the substrate size, fabricating large area DSSCs can be done by two ways: either by making small solar cells and connecting them together or by producing large size cells. All the components should have high quality TCO with low resistance. When the DSSC is scaled up, the TCO substrate's sheet resistance rises, which reduces the device's efficiency, specifically its fill factor. In comparison, the efficiency of a cell measuring 3 cm² was 7.6%, while the efficiency of a cell measuring 1 cm² was 8%. A module made up of 12 connected cells with a total size of 112 cm² was able to attain a rate of 7% efficiency. The optimization of cell connectivity remains a topic for future research for third-generation photovoltaics.

14.4 Connectivity Options

There are two main types of module connectivity are the Z-type and the W-type, as shown in Fig. 11. Each TCO substrate has a three-step deposition process consisting of a Z-type connection, a TiO₂ electrode, and a counter-electrode. Because the TCO substrate and separator have been scribed to provide electrical isolation between the cells, it is essential that the cells be connected to one another. For each TCO substrate, a TiO₂-based photoanode and a corresponding counter-electrode are printed, in a W-type connection, eliminating the need for interconnecting them. Because light is illuminated via the counter-electrode in this type, the counter-electrode should be transparent.

15 Do-It-Yourself (DIY) Project and Case Study

The process of constructing a DSSC is simple. This section highlights the most important steps to do so for educational and testing purpose. The project is best executed in a lab setting under a fume hood as it entails using solvents and sintering using heating plates (at 550 °C). The required equipment is detailed below, but said equipment are not difficult to acquire. The authors have also recorded the steps in a video on YouTube (<https://youtu.be/jjpoMzrWrPk>), and simplified procedural steps are given next. A list of materials is presented in Table 1.

- Anionic liquid detergent/deionized (DI) water is used to clean the conductive glass (FTO) substrate before being placed in an ultrasonic bath for 20 min. Following this, the samples are cleaned and immersed in DI water once more before being returned to the ultrasonic bath for another 15 min. The samples are dried in an oven at 70 °C after being rinsed with ethanol, such as shown in Fig. 12.
- Place the electrodes in UV-Ozone treatment for 20 min.
- Prepare TiO₂ paste by mixing TiO₂ powder and polyethylene glycol (1:1 mass ratio), and a drop of surfactant in a mortar.
- Take a swab of TiO₂ paste and blade (spread) it on the FTO electrode.
- Coated photo-electrode to be heated (ramp heating) on a hot plate for 30 min to reach 500 °C and let it cool to 70 °C, the process is shown in Fig. 13.
- Soak TiO₂-coated samples in ruthenium dye solution (ruthenium dissolved in ethanol) for a day (in a dark environment) and then take them out and dry them using a clean tissue; steps are shown in Fig. 14.

Fig. 11 DSSC module connectivity, Z-type (above) and W-type (below)

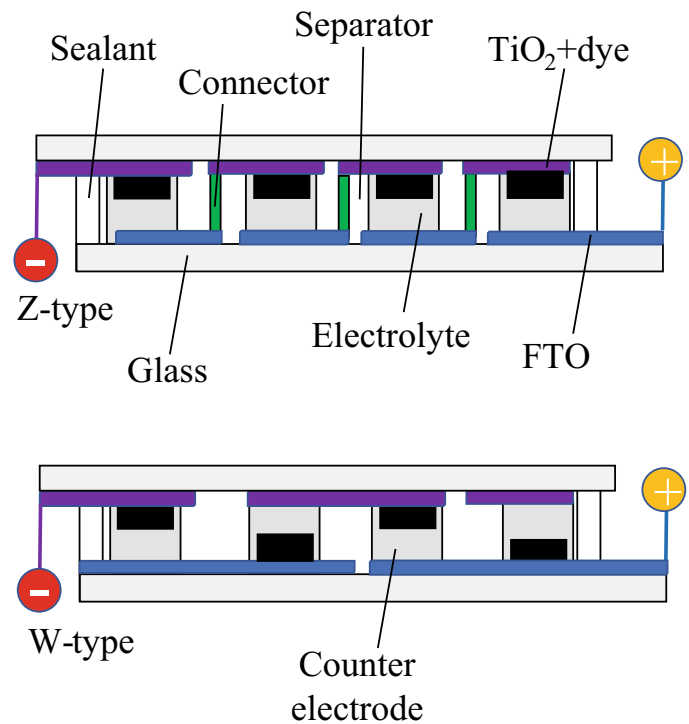


Table 1 DSSC DIY materials and usages

Material	Usage
<i>Electrode</i>	
FTO-coated glass	Substrate
Di water	Cleaning
Anionic liquid detergent	Cleaning
Ultrasonic bath	Cleaning
Ethanol	Cleaning
Oven	Drying
<i>Photoanode</i>	
TiO ₂ powder	TiO ₂ paste preparation
Polyethylene glycol	TiO ₂ paste preparation
Mortar	TiO ₂ paste preparation
Doctor blading	TiO ₂ paste Deposition
Hot plate	TiO ₂ layer processing
Ruthenium	Dye preparation
Ethanol	Dye preparation
<i>Cell assembly</i>	
Iodide/Triiodide	Electrolyte
Syringe	Electrolyte injection
Pt-coated glass	Counter-electrode
Paper clips	Sandwiching cell parts
<i>Cell testing</i>	
Solar simulator	Light source
Potentiostat	Data acquisition

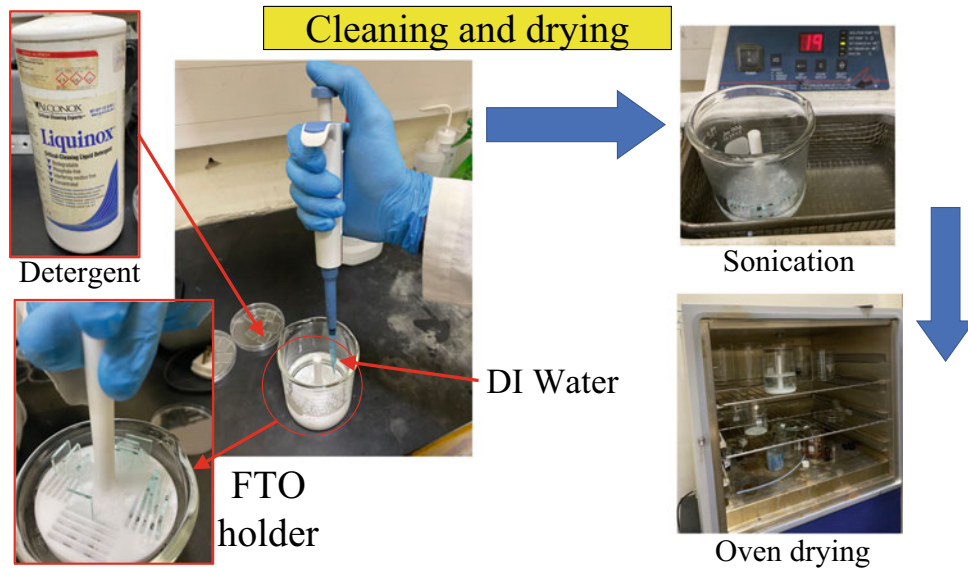


Fig. 12 Cleaning process for TCO substrates

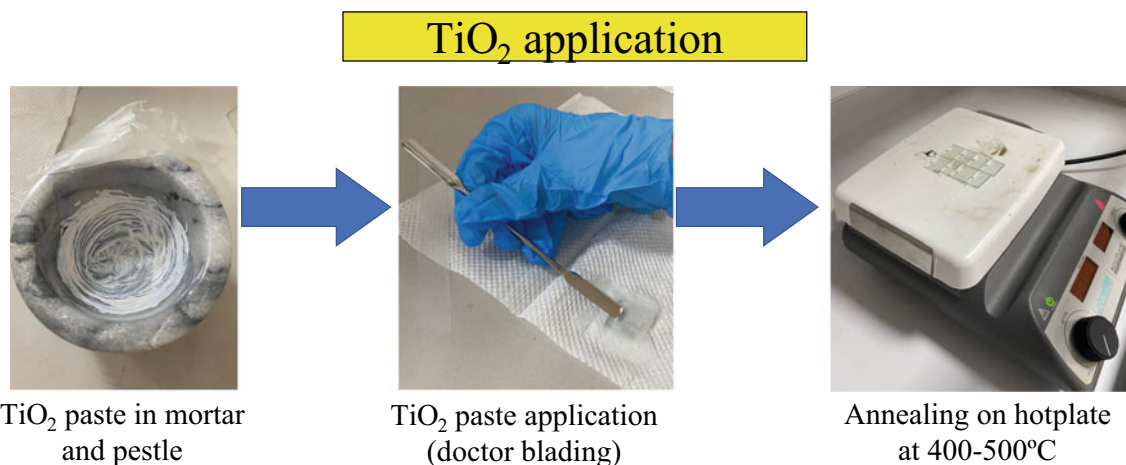


Fig. 13 TiO₂ paste preparation, deposition, post-treatment (annealing)

- Tape the area that is not covered with the TiO₂ while leaving a small region that has the exposed FTO, so that there is no short-circuiting between the sample and the counter-electrode.
- Take out a drilled counter-electrode and place it on the top with Pt surface facing the photo-electrode.
- Use a syringe to inject electrolyte between the two electrodes.
- Clean excess solution and flip it upside-down, and steps are shown in Fig. 15.
- Cell is done!
- Make sure you have a light source and a reference cell, use a potentiostat, and connect a terminal to each side of the cell, and you are ready to do the measurements (J-V test); steps are shown in Fig. 16.

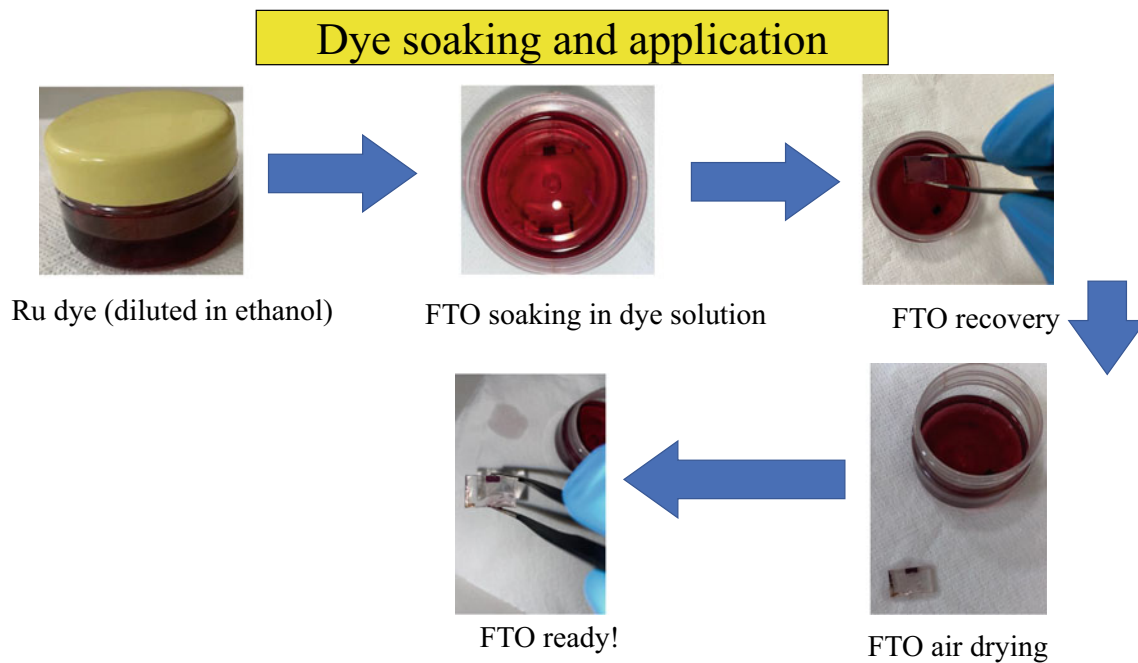


Fig. 14 Dye deposition on TiO_2 substrates

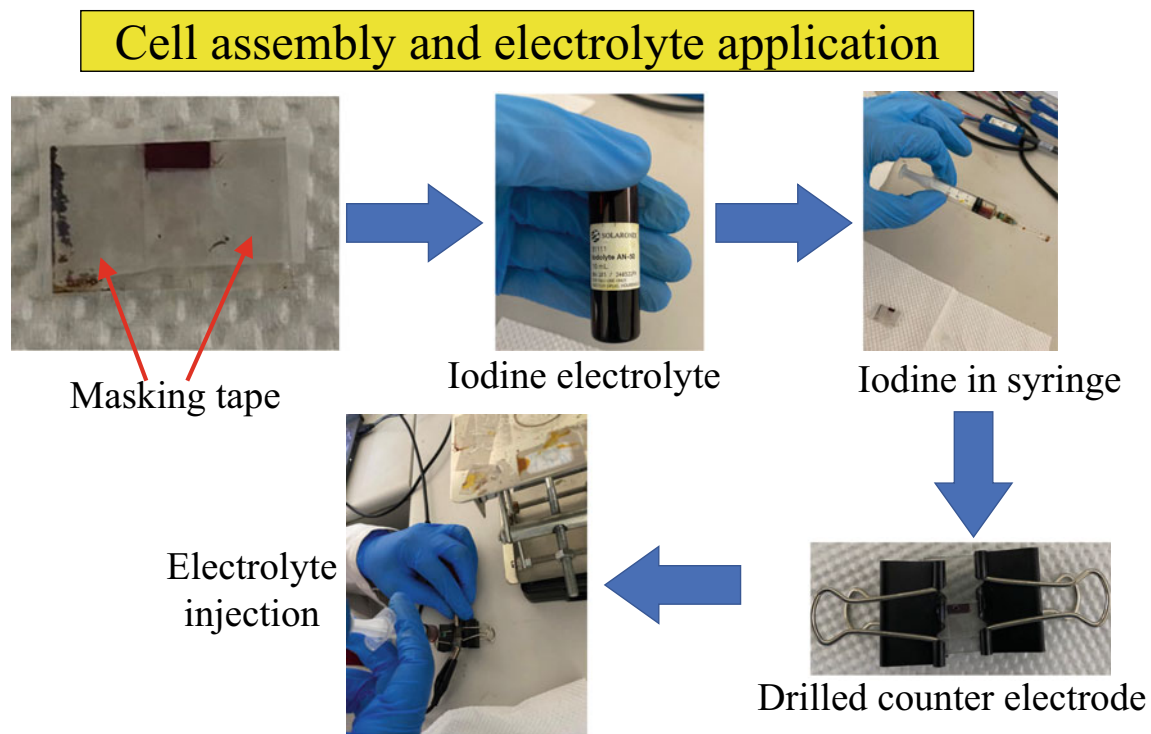


Fig. 15 Cell finalization and electrolyte injection

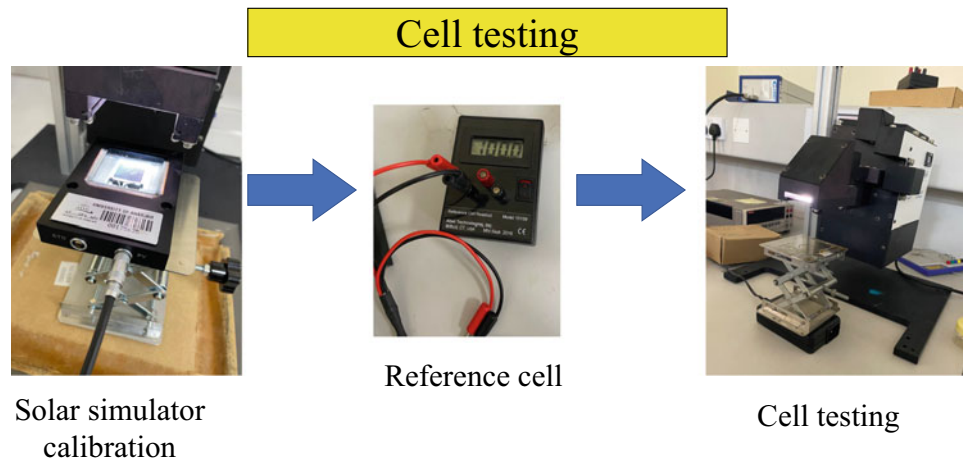


Fig. 16 Dye-sensitized solar cell testing setup

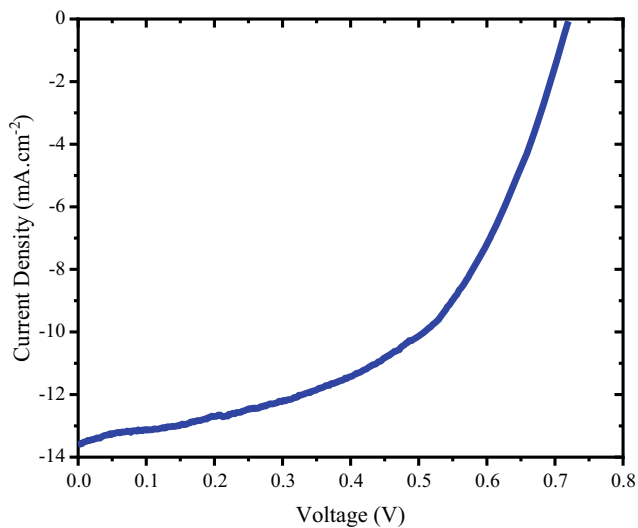


Fig. 17 Dye-sensitized solar cell J-V curve

- Figure 17 shows the J-V curve for a dye-sensitized solar cell with an efficiency of 5.11%.

References

- CleanEnergyWIKI. <http://cleanenergywiki.org/index.php?title=Special:ListFiles&offset=20110615223058%7CRamanmic.swf> (Accessed 07 Aug 2022)
- Conibeer G (2007) Third-generation photovoltaics. *Mater Today* 10 (11):42–50. [https://doi.org/10.1016/S1369-7021\(07\)70278-X](https://doi.org/10.1016/S1369-7021(07)70278-X)
- Nazeeruddin MK et al (2004) Stepwise assembly of amphiphilic ruthenium sensitizers and their applications in dye-sensitized solar cell. *Coord Chem Rev* 248(13–14):1317–1328. <https://doi.org/10.1016/j.ccr.2004.03.012>
- Supriyanto E, Alviati N, Kartikasari HA, Rohman L, Triyana K (2019) Simulation of electron diffusion coefficient interpretation on the optimum thickness of TiO₂ photoanode in dye-sensitized solar cell (DSSC). In: *IOP conference series: materials science and engineering*. 515(1). <https://doi.org/10.1088/1757-899X/515/1/012058>



Third-Generation Photovoltaics: Organic Photovoltaics (OPV)

Abdul Hai Alami[✉], Shamma Alasad[✉], Haya Aljaghoub[✉],
Mohamad Ayoub[✉], Adnan Alashkar[✉], Ayman Mdallal[✉],
and Ranem Hasan[✉]

Abstract

The investment in novel PV technology is an important tool to exploit novel materials and material processing and manufacturing technologies to achieve performance levels that supersede those attained by classical materials and processes. The following chapter highlights the novelty of materials and processes used to produce the third-generation technology of organic solar cells and latest manufacturing technologies.

1 History and Background

Organic photovoltaics (OPV) are a type of third-generation solar cells that have paved the way for solution state deposition techniques that have since increased the chance of these technologies to break into their commercialization stage. Mass production of OPV from solution-based precursors will help in driving their cost down on, but on behalf of their efficiencies. However, utilizing these technologies in multi-junction devices that are based on the difference in bandgap of different junctions can drastically increase their

respective efficiencies with a slight increase in cost. A global aim is set by researchers to accommodate to both high throughput production of PV, specifically OPV, and similar third-generation technologies using roll-to-roll compatible techniques while retaining relatively good efficiencies in comparison with the devices that are produced in research and development centers, with utilizing solution processing methods at low temperatures and eliminating the use of expensive vacuum techniques.

The term organic refers to the existence of hydrocarbon molecules, with less than a 10,000 molecular weight, or chains (polymers), with more than 10,000 molecular weights of hydrocarbons inside a specific compound. The discovery of the organic semi-conducting material is accredited to John McGinness through his utilization of it in the “melanin (polyacetylenes) bistable switch”. Along the organic semi-conducting material timeline, anthracene which is a solid polycyclic aromatic polymer (three fused benzene rings), was used as the first organic light-emitting device. Moreover, a breakthrough in the 1980s occurred when Kodak reported the first organic light emitting and solar cell device (A brief history of OLEDs).

There are different aspects to tackle in OPV, just as mentioned earlier going from lab to commercial scale production is going to be a crucial turning point in this technology's future, selecting the appropriate tools and processes can be thought of as the initial step into achieving this sought-after goal. However, characterization and testing techniques such as a certified STC sun simulator to ensure the integrity of the produced cells, UV-Vis tests, scanning electron microscope tests, cyclic voltammetry, etc., must be utilized in the optimization process before the mass production of these technologies in order to provide a consumable-worthy product. OPV are a work in progress, with a current champion efficiency of 18.2% according to the national renewable energy laboratory (NREL) (Organic Photovoltaic Solar Cells). OPV are based on organic active layers sandwiched between two electrodes. Light passes

A. H. Alami (✉) · H. Aljaghoub · M. Ayoub · A. Mdallal · R. Hasan

University of Sharjah, Sharjah, United Arab Emirates
e-mail: aalalami@sharjah.ac.ae

H. Aljaghoub
e-mail: haljaghoub@sharjah.ac.ae

M. Ayoub
e-mail: mohamad.ayoub@sharjah.ac.ae

A. Mdallal
e-mail: ayman.mdallal@sharjah.ac.ae

S. Alasad · A. Alashkar
American University of Sharjah, Sharjah, United Arab Emirates
e-mail: g00070854@aus.edu

A. Alashkar
e-mail: b00028197@alumni.aus.edu

through a transparent substrate which could be a transparent conductive oxide (TCO)-coated glass or a flexible substrate; however, it is favorable to use a flexible material since it can be processed at low temperatures which reduces the overall power consumption. On flexible substrates, indium tin oxide (ITO) is deposited, usually via sputtering, which allows holes to be collected. This part allows the light to pass, and any electrons generated will be conducted through the ITO. PEDOT:PSS is one of the most important materials utilized for the motion of holes, as it is a hole transport material (HTM) and once the light hits it, holes are allowed to pass while electrons are blocked. The active material is an organic donor/acceptor blend, as will be discussed later. A photon comes with a certain amount of energy $h\nu$, hits the surface of the active material inside an organic solar cell (OSC), where an electron and a hole are generated. The donor donates electrons, leaving holes behind, and the acceptor accepts the electrons that would fill the intrinsic concentration of the holes available. Aluminum is usually used as a cathode for electrons collection from the device, silver, or calcium.

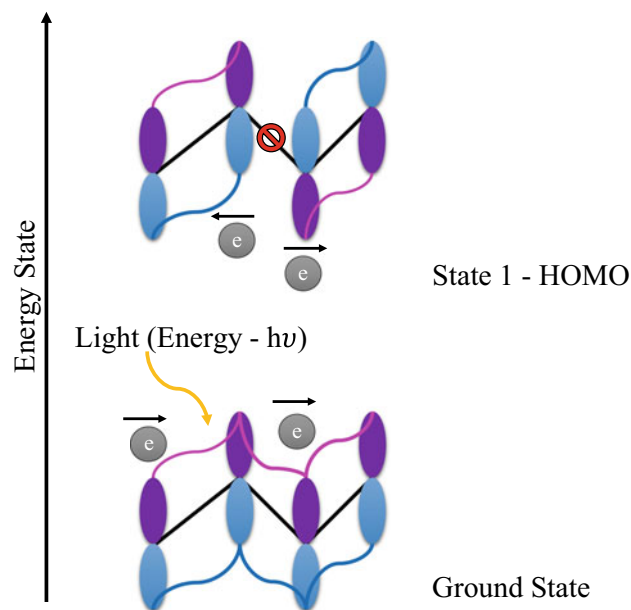


Fig. 2 Energy states and π^* orbitals' shift with added energy—ground and state 1

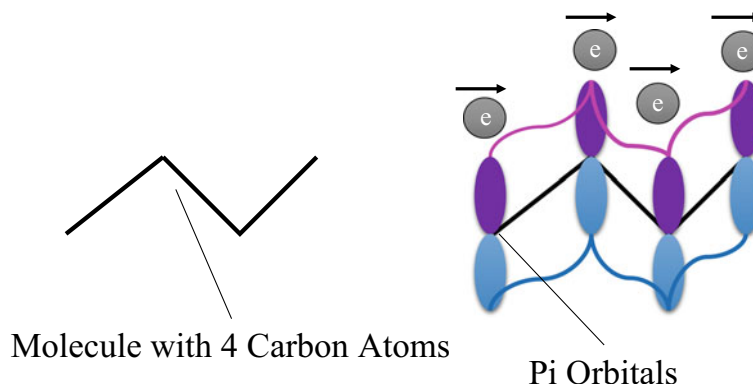
2 Physics of Organic Photovoltaics

In a conjugated organic system, each carbon atom corresponds to a π^* orbital that allows electrons to hop across the molecule. For a system with n carbon atoms, at the lowest energy state, there are n π^* orbitals that are perfectly aligned and allow electrons to meander throughout the organic molecule, such as shown in Fig. 1. When energy is added to the organic molecule, via light absorption for instance, corresponding nodes pop up in between the π^* orbitals creating an unsymmetrical path for electrons (an anti-parallel formation), such as shown in Fig. 2. Given that out of these two states (the occupied energy levels), state 1 has a higher energy level, and in the case of light absorption, electrons are most likely to be divided between these two states,

making state 1 the highest occupied molecular orbit (in terms of energy), also known as the HOMO level.

Adding further energy to an organic molecule will split the π^* orbitals even further, creating a parallel formation with only one couple of π^* orbitals, singling out the other two. This will further block the motion of electrons by creating an extra node in the organic molecule. By going further and adding extra energy, more nodes are created between the π^* orbitals until all the orbitals are singled out and electrons are exclusive to their home orbital such as shown in Fig. 3. Out of the top two energy states (the unoccupied energy levels), state two has the lowest energy level, making it the lowest unoccupied molecular orbit when there is excess energy within the organic molecule system, also known as the LUMO level.

Fig. 1 Ground state molecule with aligned π^* orbitals



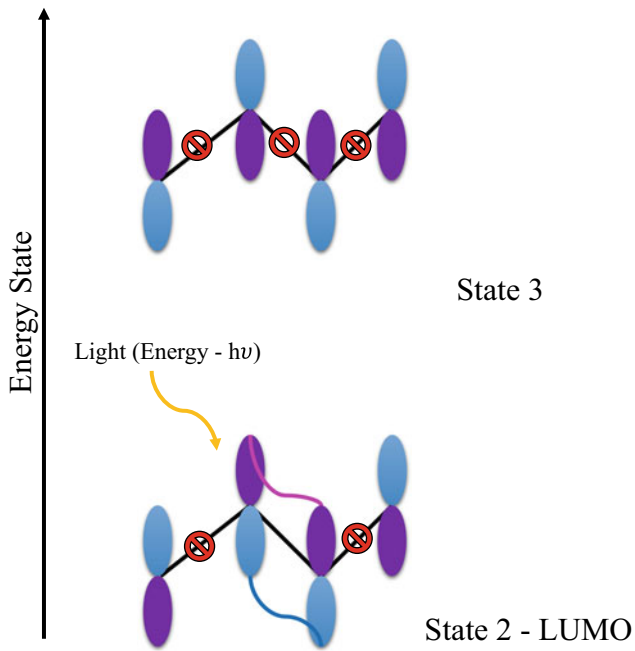


Fig. 3 Energy states and π^* orbitals' shift with added energy—state 2 and state 3

The difference between the HOMO and LUMO levels of an organic molecule is equivalent to the bandgap in non-organic materials, which is the energy barrier required to free an electron from the ground state to a state that can allow the collection of electrons in the form of electric

current, shown in Fig. 4. Since both the HOMO and LUMO levels are so close in energy, and with the vacancies available in the LUMO level, electrons are easily excited and transition smoothly between these states, with the gain and loss of energy.

3 Organic PV Cell Structure

The highlight of third-generation solar cells in general, and specifically OSC in this case, is the deviation from the conventional P–N junction that is utilized in first generation crystalline silicon and second generation thin-film technologies. With conventional P–N junction structures, the diffusion length of minority carriers, electrons in P regions and holes in N regions, is very short, leading to recombination events that ultimately decrease the amount of electrical current and power extracted from a given cell. However, in third-generation solar cells, this issue has been widely studied and alternatives were implemented. Throughout the development OPV, three structures have played major roles in allowing this technology to reach the condition it is in today. The single layer organic solar cell (OSC) consists of a substrate (usually ITO- or FTO-coated glass), a semi-conducting polymer and a metal contact, such as shown in Fig. 5. In this structure, a relatively weak electric field is produced between the metal contact and the transparent conducting oxide (TCO), and the semi-conducting organic material (the polymer) is used as an

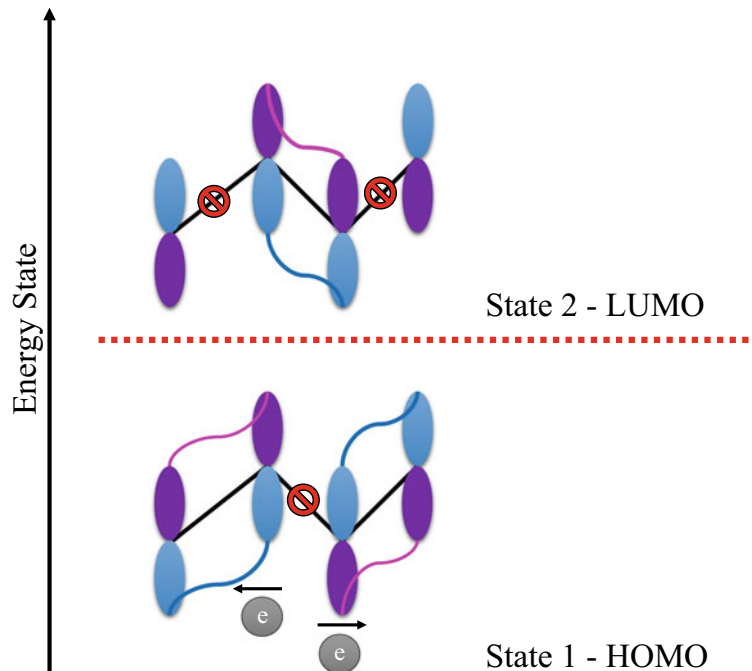


Fig. 4 HOMO and LUMO levels

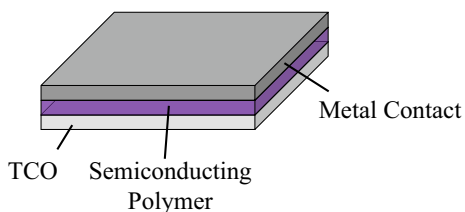


Fig. 5 Single layer OSC structure

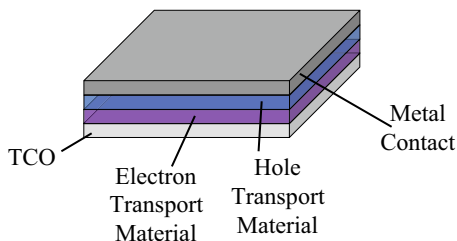


Fig. 6 Bilayer OSC structure

electron and a hole diffusion layer. This structure performs weakly due to the insufficient electric field intensity for charge separation, which leads to more recombination events and loss of electrons which subsequently leads to loss of efficiency.

Next in line comes the bilayer OSC, which contrary to the single layer OSC, the single layer polymer is split into electron and hole diffusing layers which provide a relatively better electric field and ensures a better separation process, such as shown in Fig. 6. The short diffusion length of minority carriers (electrons in the hole diffusing layer or holes in the electron diffusing layer) acts as an adversity that accompanies this scheme of device design. In addition to these layers exists the metal contact and the TCO for charge collection.

Currently, the dominant structure in research for OSC is the bulk-heterojunction (BHJ). It was first investigated by Heeger and Friend (Yu et al. 2014), where they reported the use of a mixture consisting of solid state donor and acceptor that provides a nanostructured morphology. In BHJ-OSC, the short diffusion length of minority carriers is overcome by creating an interconnected electron and hole transport materials which interact in the form of a network, such as shown in Fig. 7a, c. The generated electrons and holes are injected in their respective diffusion layers and move across the OSC at an instant, providing high separation efficiency and a better chance for these charges to be collected using the metal and the TCO at both ends of the OSC and a PEDOT-hole transporting layer into the top contact. An aligned BHJ-OSC was also introduced which ensures that island regions of sole hole or electron diffusing materials are avoided, such as shown in Fig. 7b, d.

4 Materials and Fabrication Techniques

Currently, research is mainly done on two materials for the BHJ active layer consisting of P3HT and PC₆₀BM. These two materials are commercially obtained in powder form, and the precursor is prepared by dissolving these powders into solvents such as chlorobenzene (CB), that is after optimizing their ratios and the amount of solvent used. The mainstream deposition techniques for OSC in research and development is spin coating and to a lesser extent, slot-die deposition, although other techniques have been devised as well, and are compared in terms of layer thickness accuracy, amenability to roll-to-roll production and material waste. Spin coating heavily depends on the wetting of the substrate, the viscosity of the precursor used, the speed and time at which the spin coater rotates. Post-treatment is usually required and its conditions include annealing (heating the deposited layer), anti-solvent treatments, quenching, etc. This information will be discussed in detail in the dedicated manufacturing techniques chapter.

4.1 Solvents

An issue arises with the use of the previously mentioned solvent, CB, and di-chlorobenzene (DCB), which is also commonly used in OPV, as they present health and environmental hazards. Working with either CB or DCB limits the production of OSC to controlled environments such as that provided by a glovebox, and it also draws back the commercialization of this technology given the direction the world is headed into preserving the environment and controlling pollution levels. Although the end devices while using CB or DCB as precursor-solvents are relatively good, alternatives must be sought to counter these issues.

Poly(3-hexylthiophene-2,5-diyl), also known as P3HT, is a polymer that is extensively used in OPV applications, as well as organic light-emitting diode (OLED) and organic field-effect transistor (OFET) applications, P3HT's chemical structure is shown in Fig. 8, with the chemical formula (C₄H₂S)_n. P3HT has a low bandgap (~1.9 eV (Murali et al. 2015)), which means that it absorbs a wide range of the ultraviolet and visible light spectrum. In a BHJ active layer blend, P3HT acts as the donor material, providing a pathway for holes to be transferred across the OPV cell. P3HT is highly soluble in the previously discussed solvents CB and DCB, and with its fast drying characteristics, it results in a highly crystalline absorption thin film (Polymer).

Fullerene derivative (Brinkmann et al. 2010; Brinkmann et al. 2010)-phenyl-C₆₁-butyric acid methyl ester (C₇₂H₁₄O₂), known as PCBM, is a soluble derivative of C₆₀, that is commonly used in OPV, and has a chemical structure

Fig. 7 **a** Bulk-hetero junction OSC, **b** Aligned bulk-hetero junction OSC, while **c** is a depiction of BHJ and **d** is that of aligned BHJ

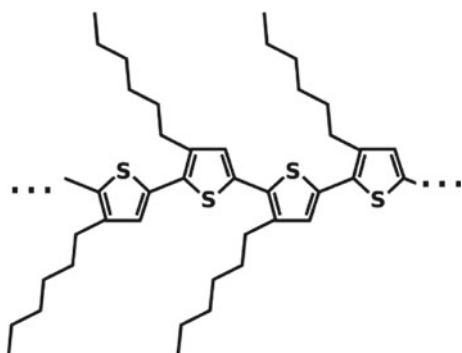
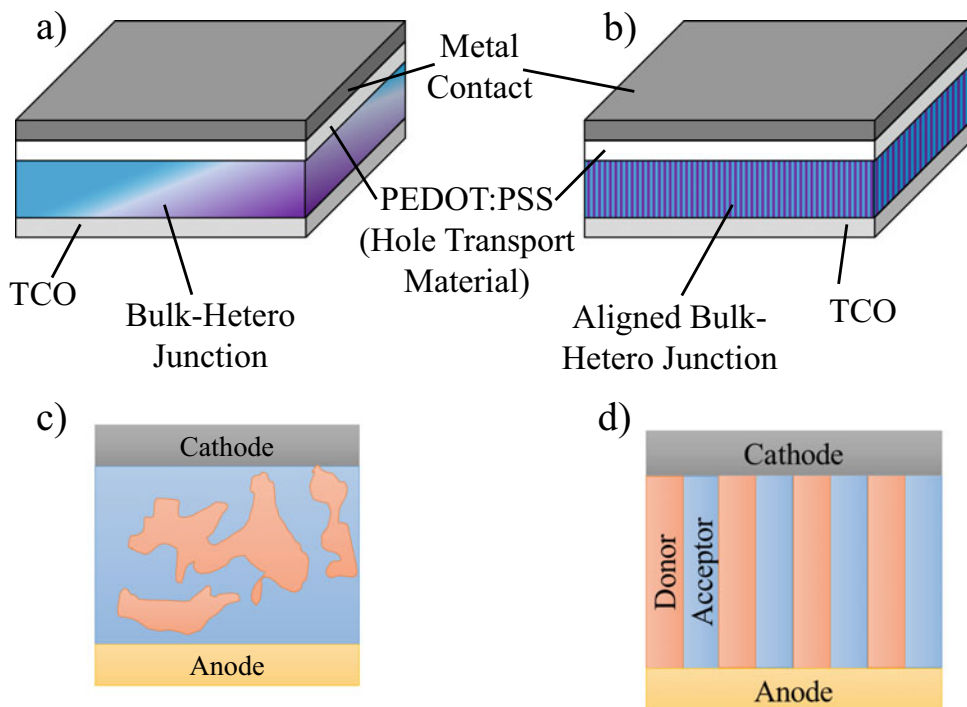


Fig. 8 P3HT chemical structure (Brinkmann et al. 2010) (<http://gisaxs.com/index.php/Material:P3HT>)

such as shown in Fig. 9. PCBM is an electron acceptor, that is used as an electron transporting material inside BHJ structures of OSC, it has a bandgap of 2.4 eV with a high electron mobility for efficient charge transfer across an OSC. It is easily soluble in donor polymer solvents such as CB and DCB and mixes well with other materials such as P3HT to create a state-of-the-art BHJ absorption layer.

4.2 Hole-Transport Materials

In OSC, a hole transporting material (HTM) is usually deposited on top of the BHJ layer, in order to enhance the mobility of the holes and increase the chances of

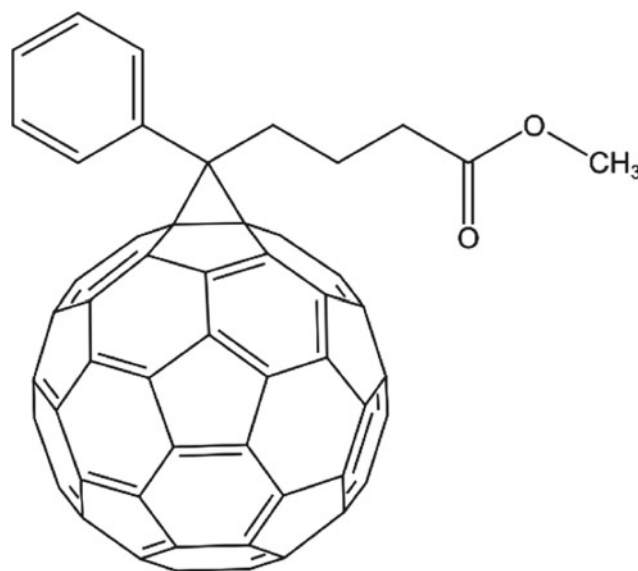


Fig. 9 PCBM chemical structure (“Phenyl-C61-butyric acid methyl ester” 2021)

collecting them using the top electrode (Silver, gold, ITO, etc.). Poly(3,4-ethylenedioxythiophene) polystyrene sulfonate, known as PEDOT:PSS, with the structure shown in Fig. 10, is a common transparent conducting polymer that is used as an HTM. It has a high conductivity and a desirable level of transparency, along with a solution-metering capability making it a key material for OPV applications.

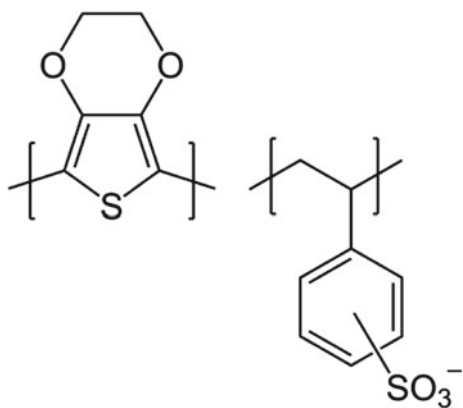


Fig. 10 PEDOT:PSS chemical structure (Brinkmann et al. 2010) (https://en.wikipedia.org/wiki/PEDOT:PSS#/media/File:Polythiophenes_Pedotpss.png)

4.3 Deposition on Substrates

OSC substrates have some requirements that have been standardized to ensure a high-performance of the end devices. A high-quality optical transparency is essential to allow for a high-intensity of the incident light to reach the photoactive layer with its different designs (single junction, bilayer and bulk-heterojunction), given that OSC are usually operated in a flipped position relative to the deposition sequence. In some cases, OSC are manufactured using non-transparent substrates. However, the architecture of the device can be affected by the utilization of non-transparent substrates due to the requirement of top electrodes to be transparent with a transparent top barrier (stuck to the substrate). While by using transparent substrates, the transparent electrodes often combined with it can be placed either on top or on the bottom or on both sides for semi-transparent cells. The smoothness of the substrate is also an important parameter to consider, more importantly, the rms roughness of the substrate, which controls the nucleation and crystallization rate of the subsequent layers with positive effects to the interface resistance. Thickness up to the nanometer range is fine for the case of glass or PET to enhance high-quality deposition of the subsequent layers. Roughness of the surface should not be high when the distances of structures are not long since it produces shorts in the device. When the distances are long, moderate roughness can be accepted. An example of rough substrates over short and long distances are metals, while substrates composed of plastics are only rough at long distances. Being thermally resistant is a must for OSC substrates, given that the deposited layers (ETMs, active and HTMs) are processed “annealed” at high temperatures, reaching up to 500 °C, which also corresponds to a high dimensional stability. Chemical resistance to what is considered to be lethal components that make up OSC, is

something that must be considered with the highest regard, given how effective the solvents that are used in penetrating through surfaces. Low water absorption is taken into account for the long-term operation of OSC, due to the adverse effects water molecules have on the active materials in OSC, and having a low water absorption will ultimately increase the lifetime of the fabricated devices.

4.3.1 Glass Substrates

Fluorine-doped tin oxide, or indium tin oxide-coated glass is a conventional substrate that is used for OSC applications. With a 92% transmission in the visible light spectrum and 600 °C maximum processing temperature, it makes for a convenient device fabrication. The relatively lighter weight of glass substrate can be an advantage in comparison with metal substrates (stainless steel), 220 mg/m² versus 800 mg/m², respectively. Stainless steel substrates are also a setback in terms of visible light transmission at 0%, but have a high tolerance for higher temperature processing if required. (Fthenakis 2012). The problem associated with using glass is its brittleness and ability to break while processing. However, substrates like glass can be used in many applications in the context of housings’ exterior, such as windows. Glass substrates are preferred over plastics, which will be discussed in the following section, due to their high transparency in the visible spectrum and high resistance to UV. The low light transmission of stainless steel eliminates its use as a photoanode to allow the light to pass in. However, stainless steel can be used when the operating temperature exceeds the limit of that of glass substrates (>1000 °C). Stainless steel also shows better dimensional stability than glass or plastic substrates. Metal foils can also withstand high processing temperatures and are dimensionally stable, but their use is limited since they are non-transparent and have a high surface roughness, which can be overcome to some extent using polishing techniques. However, metal foils with no transparency can be utilized when the light is incident on the cell in its top position.

4.3.2 Flexible Substrates

Flexible substrates are utilized for roll-to-roll production lines to bring down the overall cost of OSC. Polyethylene terephthalate (PET) substrates are optically transparent to visible light, with an 89% transmission, and have outstanding low moisture absorption at 0.14% and high-quality mechanical properties with a 5.3 GPa (Fthenakis 2012) Young’s modulus and a 225 MPa (Fthenakis 2012) tensile strength. Polyethylene naphthalate (PEN) is a polymer with comparable properties and used in the same context of PET. However, these substrates have a low maximum processing temperature at 78 and 121 °C (Fthenakis 2012), respectively. For high-temperature processing requirements,

Polyimide (PI) is a polymer with relatively good mechanical properties, that retains a good degree of flexibility, and a novel 410 °C (Fthenakis 2012) processing temperature for high-temperature OSC materials.

4.4 Compatibility with Roll-To-Roll

Operating a roll-to-roll production line is an achievable task and very beneficial on the long run for any process or fabrication that can be easily metered, which is the case for OPV, given that these lines can operate 24/7. However, there are points to be considered before optimizing such a process which are, the type of ink used, wetting and dewetting of the substrate, given that in order to make the roll-to-roll successful it is important to make sure that the material wets the surface, the thickness of the layer to prevent layers from intermixing, managing the self-assembled process, oxidation, contamination, or defects are reduced or completely avoided.

The choice of the deposition technique in a roll-to-roll line depends on the thickness of each layer, deposition events, annealing conditions, ink properties, solvents, substrates, and viscosity. The choice of the deposition technique mostly depends on the viscosity of the ink that affects its

deposition on the substrates (too low viscosity can cause evaporation or leakage as well as preventing the formation of very sharp edges, and high viscosity makes it very difficult to cover the entire surface). Viscosity of ink in the photoactive layer has to be low due to the limited solubility of the photoactive compounds. P3HT/PCBM (Poly3-hexylthiophene (P3HT) and [6,6]-phenyl-C61-butyric acid methyl ester (PCBM)) active material has a viscosity of 1–5 mP.s. But in the case of other layers such as PEDOT:PSS, it is not limited to a very low viscosity and can reach above 50 mPs. Silver inks can be synthesized with low viscosity and are ink jet printed or can be in the form pastes and subsequently screen printed.

Figure 11 shows the inkjet-printed silver grid where the height is 300 nm from (b) the line profile and (c) the screen printed TEC-PA-010 ink from Inktec (<http://www.inktec.com>) with height of 2000 nm as shown in (d) the line profile (Inktec). The conductivity of grid is higher in (c) due to increased line height. Therefore, it would be good to make sure that the topology or deposition process is going to increase the size of the lines. Figure 12 shows a comparison in the current density of the simple ITO, silver which is highly conductive in honeycomb structure with PEDOT, and silver lines with PEDOT. The I-V curves of

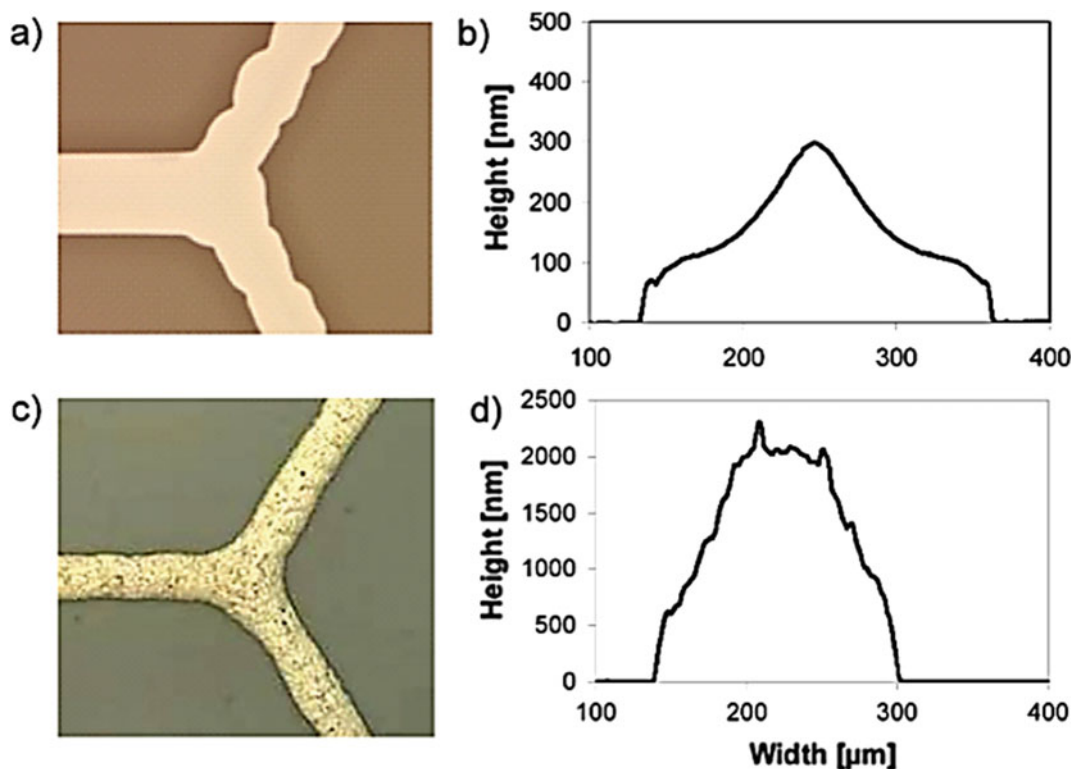


Fig. 11 a Microscopic image of inkjet-printed silver grid on PEN substrate and b its line profile. c Microscopic image of Inktec TEC-PA-010 ink screen printed and d its line profile (Galagan and Andriese 2012)

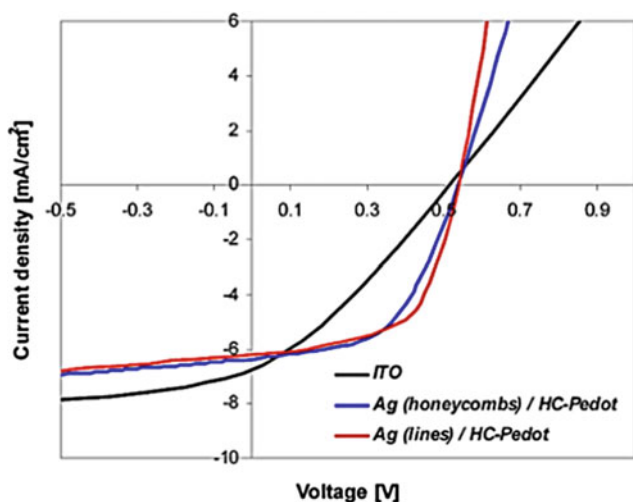


Fig. 12 Comparison between the current density versus voltage for grids and ITO-based devices (Galagan and Andriessse 2012)

the solar cells show that there is a lucrative advantage of using such grids.

4.5 Spin Coating for OPV Manufacturing

In recent days, the processing of OPV utilizes techniques of coating and printing. Developing such solar cells is mostly done by spin coating. This is one of the most important manufacturing processes used in laboratory scale cells, while other coating and printing techniques are analytic to the parameters associated to the ink and the surface interaction. Spin coating is not analytic which is a major advantage. This technique is, however, not compatible with roll-to-roll processing which involves processing of the solar cells in liquid form or in solution, to be able to deposit one layer after another on a substrate. OPV devices are mostly distinguished by roll-to-roll production lines. Although they can be handled simply and are fast to process, it is still difficult to transform all the lab-scale

processing parameters to large scale, specifically with techniques not compatible with roll-to-roll (Arbouch et al. 2014). Figure 13 shows the operation of spin coating where the solution is deposited on the top of a rotating disk. Due to centrifugal force, the material spreads on the whole surface. Only a little amount of the material is needed, after spinning, it covers the whole exposed surface and then it is heat-treated/annealed to have a homogeneous and a low-resistance layer.

Spin coating and annealing parameters can both be optimized to result in an efficient active organic layer. The optimization is carried out by testing different spin coating frequencies and durations, as well as annealing temperatures and time. Shaban et al. (2021) studied the effects of these parameters on a P3HT:PCBM active layer blend where the spin coating frequency ranged from 900 to 3000 rpm and the annealing temperature ranged 130–190 °C. Not only does the energy efficiency of an OSC get affected by these conditions and parameters, but the optical efficiency, which depends on the thickness of the end layer, is noticeably variable, such as shown in Fig. 14. Optimum performance values, based on their obtained J-V curves, correspond to 3000 rpm spin coating frequency and 160 °C annealing temperature. With increasing the annealing temperature starting from 130 °C, J_{sc} , V_{OC} and power conversion efficiency (PCE) values increase from 8.82 mA/cm², 0.597 V, 1.95% to a threshold of 10.78 mA/cm², 0.640 V and 3.68% at 160 °C, and reaching a low of 8.24 mA/cm², 0.664 V and 2.21% at 190 °C.

Using an Mg–Al cathode blend and ranging the spin coating frequency from 900 to 3000, the performance values J_{sc} , V_{OC} , and PCE increase from 8.649 mA/cm², 0.639 v and 2.61% to 12.01 mA/cm², 0.660 V and 4.65%, respectively. The effects of annealing on different solvents for organic active layer blends are also worthy of being studied. Figure 15 and Table 1 show the effect of annealing on the absorbance and J-V curves for blends that utilize chlorobenzene and o-Xylene, where enhancement is found in both compositions after annealing.

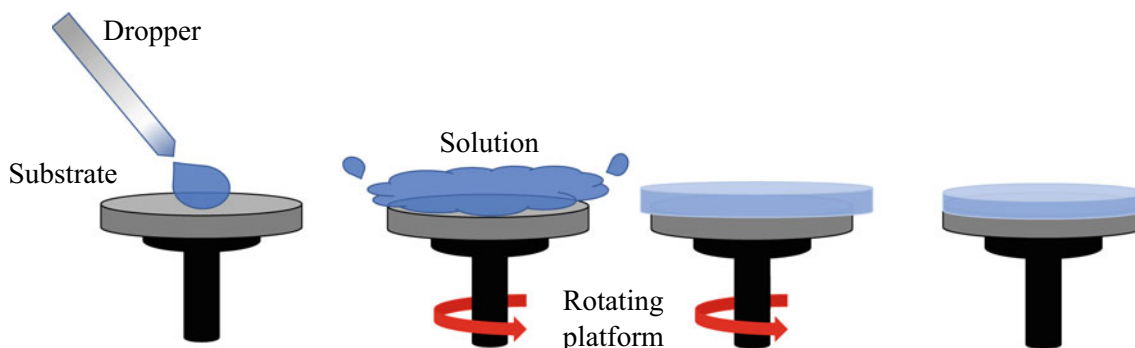


Fig. 13 Spin coating process

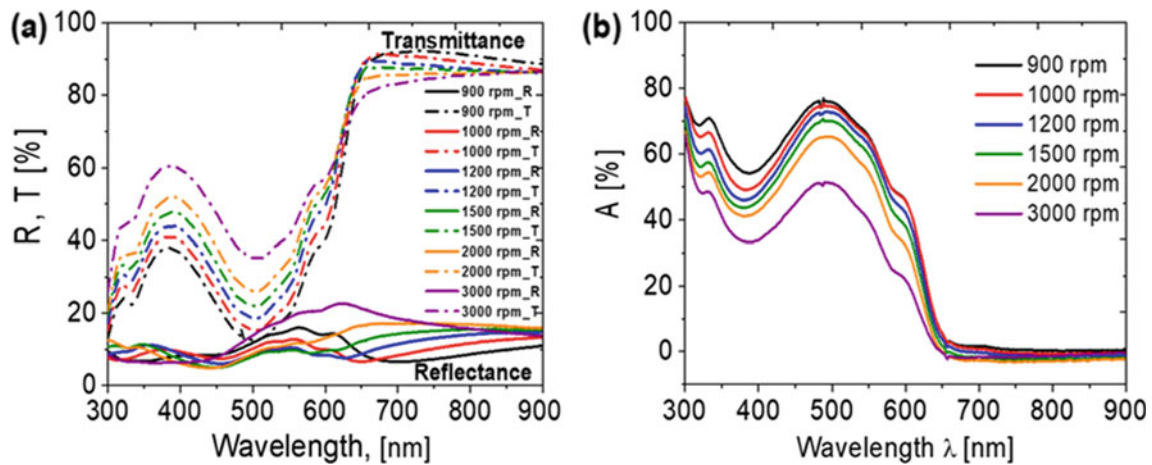


Fig. 14 a Reflectance and transmittance b Absorbance for P3HT:PCBM blend at different spin coating frequencies and annealed at 160 °C for 5 min (Shaban et al. 2021)

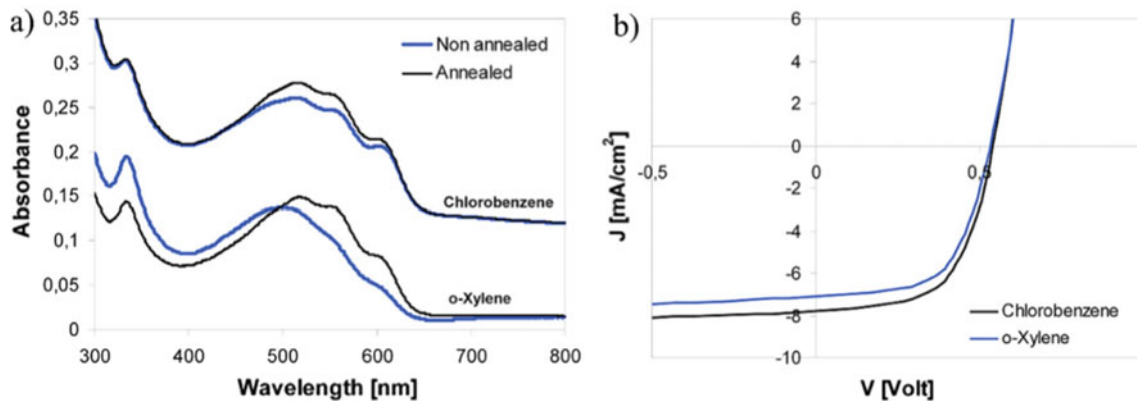


Fig. 15 a Effect of annealing on absorbance and b J-V characteristic curves (Galagan and Andriess 2012)

Table 1 Effects of annealing temperature on organic active blends' performances (Galagan and Andriess 2012)

Solvent, annealing	J_{sc} (mA/cm ²)	V_{oc} (Volt)	FF	η (%)
Chlorobenzene, not annealed	3.64	0.572	0.296	0.62
Chlorobenzene, annealed	7.75	0.546	0.572	2.42
o-Xylene, non-annealed	4.71	0.507	0.332	0.79
o-Xylene, annealed	7.05	0.535	0.581	2.19

4.6 Slot-Die Coating

A roll-to-roll compatible technique is slot-die coating, where a material is added using a die head that allows the material to fall down in a vertical direction through its slot, while the slot-die head is moving relative to a stationary stage. This coating technique allows for roll-to-roll coating of the hole transport layer (PEDOT:PSS) and the photoactive layer (P3HT/PCBM). Layers deposited with slot-die can have very low thickness and be uniform. 1-D patterning can be used to make the OPV modules. The deposition

profile, shown in Fig. 16, can be characterized by applying different techniques including Atomic Force Microscopy (AFM), which consists of a small needle that moves right and left on the surface. If the surface is smooth, a flat line is produced, and if there were rough particles, it will be shown from the diagram. The average thickness of the layer is about 110 nm for the PEDOT:PSS using the speed of about 10 m/min (the optimum one) and using a drier at 110 °C. The other way of measurement is using the ellipsometry where the index of refraction of the material is measured to get the thickness.

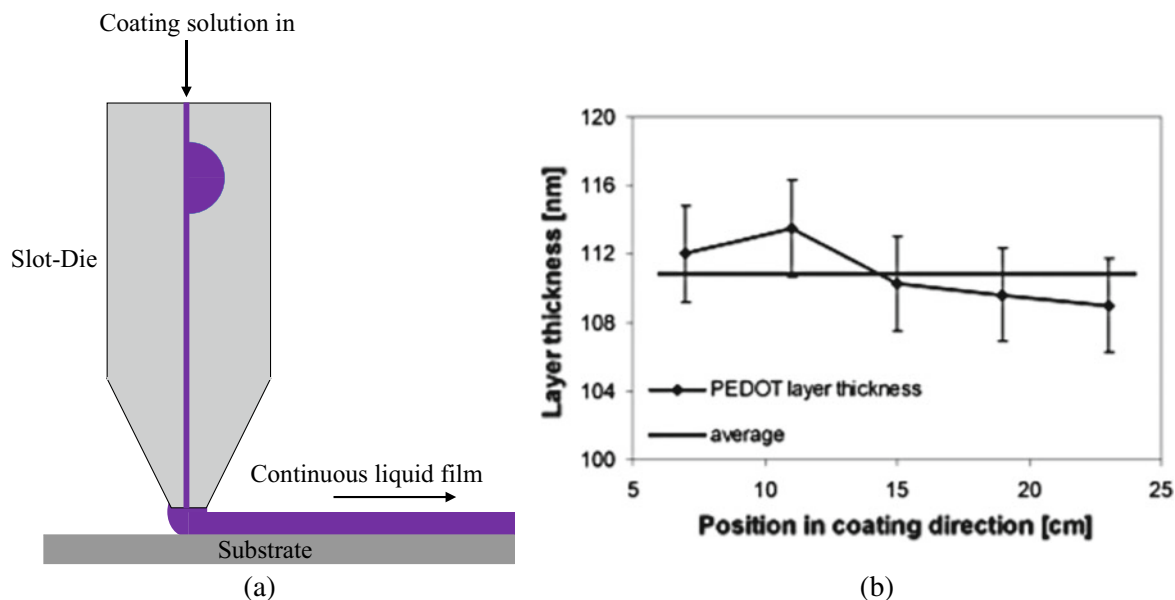


Fig. 16 a Depiction of the slot-die deposition process and b layer thickness versus position in coating direction (Galagan and Andriesse 2012)

4.7 Overall Fabrication Process

Fabricating an OSC comprises of different stages that are mostly done in controlled environments. To begin with, an FTO or ITO-coated glass is cut and cleaned in preparation for a residue-free process. Then using chemical etching, a narrow region on the coated glass substrate is removed to allow for latter top contact deposition. The layers that make up an OSC are deposited (mainly using spin coating), where it goes as follows, electron transport layer (ETM), usually Titanium Dioxide (TiO_2), organic active blend (the BHJ), an HTM (PEDOT:PSS), and a thermally evaporated silver or gold contact, with the addition of annealing steps in between different layers' depositions for better sintering, crystallization and formation of the desired end materials.

4.8 Scaling up OPV for Commercial Use

One of the things researchers are interested in is scaling up. Scaling up means going from a lab-scale product to a commercial one, with a larger active area is required. However, as a consequence, there may be a lot of losses that will arise from the larger thicknesses that the ions or the electrons/holes (charge carriers) have to pass, such as recombination. These losses mainly depend on the sheet resistance of the electrode. Testing a cell with an active area

of 0.09 cm^2 can yield an efficiency of 2.42%. By scaling up and having a higher active area of 6 cm^2 , the current will decrease, and voltage will decrease slightly but the fill factor will be affected significantly, and hence, the overall efficiency will show a sharp drop indicating a worse performance. In this case, an efficiency loss of around 20% is witnessed using devices based on ITO-coated glass substrates and shows the performance of devices with active areas of 0.09 cm^2 and 6 cm^2 as shown in Table 2.

As interconnecting solar cells provides high voltages, the coating and printing processes can be used to establish direct patterning. Patterned printing has emerged to manufacture modules with internal interconnecting. The easier way of connecting cells/modules is having a common internal connection, where a photoanode and one common back surface field are utilized. All of the components share the substrate but each of them has unique/individual active areas and modules printing may offer a significant reduction in the manufacturing cost and increase the stability of the modules.

In ITO, the cell's width is restricted between 0.5 and 1 cm as a result of the high sheet resistivity; hence, ohmic losses are decreased. However, bigger areas are essential to get more energy from solar radiation. Interconnection of individual cells serves as an alternative to accomplishing high efficiency rather than increasing the size of the cells. The performance for the two cells with 0.09 and 6 cm^2 is shown in Fig. 17, and the efficiency for the smaller cells

Table 2 The performance of devices with active areas of 0.09 and 6 cm^2 (Galagan and Andriesse 2012)

Active area (cm^2)	J_{sc} (mA/cm^2)	V_{oc} (V)	FF	η (%)
0.09	7.75	0.546	0.572	2.42
6	7.46	0.530	0.478	1.89

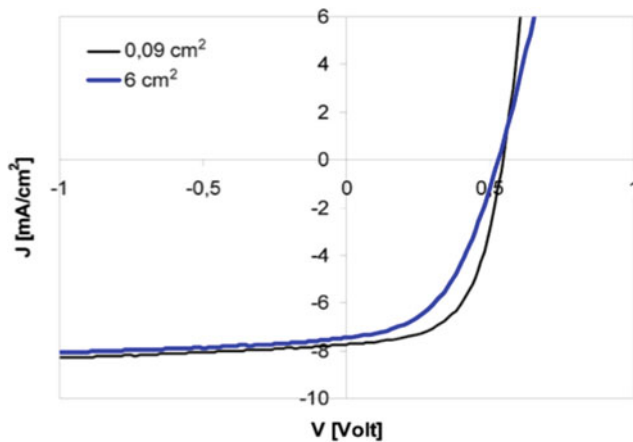


Fig. 17 Performance of two organic cells of different areas (Galagan and Andriess 2012)

interconnected together is 20% higher than the one big cell (seen from the higher energy). By increasing the width of the cell above 1 cm, the losses in efficiency increase significantly.

4.9 Recent Progress of Organic Solar Cells

Over the past 3 decades, OPV have showed decent progress due to their low cost of fabrication, easy processing techniques, with liquids metering and roll-to-roll production lines, and flexibility. The efficiency for this technology has exceeded 18.2% (Best Research-Cell Efficiency Chart) for single junction devices and 14.2% (Best Research-Cell Efficiency Chart) for multi-junction tandem device structures (Sharma et al. 2022). OPV have been implemented in a variety of applications so far. Indoor power generation is one of the main applications for OPV given the advantages that indoors have over outdoor light harvesting conditions (below 1 sun intensity), given that the light spectra of indoor sources match well with the light absorption coefficients of OPV materials, and even if there was a low match, optical properties of these materials are easily tuneable (Ryu et al. 2020). Different active layer blends have been used and ratio-optimized such as PCDTBT:PC₇₁BM and PTB7-Th:PBDB-T:ITIC-Th:PC₇₁BM and have shown efficiencies reaching 16% and 14%, respectively, with indoor conditions based off different light sources and spectrums (fullerene and LED). Increasing the efficiency of OPV devices have been targeted by researchers and attempted by utilizing techniques such as the singlet fission (SF). The singlet fission is a technique that is used to multiply the quantity of photons reacting with the active layer in an OSC, where a singlet excitation energy state is converted into two spin-triplet excitons. The newly multiplied photons carry less energy than the initial incident photon but given

that charge carriers' generation is independent of the energy of a photon and more dependent on the number of excitation events, more carriers are generated and subsequently an increase of current is obtained as well as an increase in efficiency (Sharma et al. 2022). Optimizing the ratio of active layer blends helps in the singlet photon fission regard as well as narrowing down the bandgap of the active material (HOMO–LUMO) energy difference to utilize a larger portion of the light spectrum and increase the excitation events overall.

4.10 Summary for Substrates Selection

Advances are also expected in selecting the most appropriate substrates for deposition. To summarize the previous discussion, the general requirements for successful substrate include the following:

1. Optical quality of transparency to let light reach the photoactive layer.
2. Smoothness in nanometer range to provide a surface that will promote high-quality deposition of subsequent layers and prevent the penetration of potential substrate irregularities into device layers.
3. Ability to support processing at high temperatures.
4. Good dimensional stability.
5. Good resistance to chemicals used during processing.
6. Low water absorption.

Thus, a wide choice of substrates is available and ranges from typical glass, polymers (PET, or polycarbonate) and metals such as stainless steel. Polymers have transparencies that are almost as good as glass and have better elasticity, the fall behind in UV and dimensional stability, as well as processing temperatures. Metals have all the advantages in terms of all physical, mechanical, and chemical properties but they are opaque. Since the efficiency of a solar cell depends on the electrode dimensions and its sheet resistance the sheet resistance of ITO/glass substrate is 10–15 Ω /square, while the sheet resistance of ITO on PET substrate is around 60 Ω /square. A rapid decay of the efficiency was shown upon increasing the width of the solar cell.

References

- A brief history of OLEDs. [Online]. Available: <https://www.nanowerk.com/spotlight/spotid=57140.php>
- Arbouch I, Karzazi Y, Hammouti B (2014) Organic photovoltaic cells: operating principles, recent developments and current challenges—review. *Phys Chem News* 72:73–84
- Best Research-Cell Efficiency Chart. [Online]. Available: <https://www.nrel.gov/pv/cell-efficiency.html>

- Brinkmann M, Contal C, Kayunkid N, Djuric T, Resel R (2010) Highly oriented and nanotextured films of regioregular poly (3-hexylthiophene) grown by epitaxy on the nanostructured surface of an aromatic substrate. *Macromolecules* 43(18):7604–7610. <https://doi.org/10.1021/ma101313m>
- Fthenakis V (2012) Third generation photovoltaics. [Online]. Available: <https://torl.biblioboard.com/content/1c479981-4815-4497-a712-0bcdbfe9860d?organizationId=1f7368e7-f10b-49a1-8ced-2d9476279974>
- Galagan Y, Andriess R (2012) Organic photovoltaics: technologies and manufacturing. In: *Third generation photovoltaics*, InTech. <https://doi.org/10.5772/25901>
- Inktec
- Murali MG, Rao AD, Yadav S, Ramamurthy PC (2015) Narrow band gap conjugated polymer for improving the photovoltaic performance of P3HT:PCBM ternary blend bulk heterojunction solar cells. *Polym Chem* 6(6):962–972. <https://doi.org/10.1039/C4PY01274G>
- Organic Photovoltaic Solar Cells. [Online]. Available: <https://www.nrel.gov/pv/organic-photovoltaic-solar-cells.html>
- Phenyl-C61-butyric acid methyl ester (2021) Wikipedia. [Online]. Available: https://en.wikipedia.org/w/index.php?title=Phenyl-C61-butyric_acid_methyl_ester&oldid=1027259346
- P3HT Polymer, Reduced to Clear CAS 104934–50–1. Ossila. [Online]. Available: <https://www.ossila.com/products/p3ht>
- Ryu HS, Park SY, Lee TH, Kim JY, Woo HY (2020) Recent progress in indoor organic photovoltaics. *Nanoscale* 12(10):5792–5804. <https://doi.org/10.1039/D0NR00816H>
- Shaban M, Benghanem M, Almohammed A, Rabia M (2021) Optimization of the active layer P3HT: PCBM for organic solar cell. *Coatings* 11(7):863. <https://doi.org/10.3390/coatings11070863>
- Sharma T et al (2022) Recent progress in advanced organic photovoltaics: emerging techniques and materials. *ChemSusChem* 15(5). <https://doi.org/10.1002/cssc.202101067>
- Yu J, Zheng Y, Huang J (2014) Towards high performance organic photovoltaic cells: a review of recent development in organic photovoltaics. *Polymers* 6:2473–2509. <https://doi.org/10.3390/polym6092473>



Third-generation Photovoltaics: Perovskite Solar Cells (PSC)

Abdul Hai Alami[✉], Shamma Alasad[✉], Haya Aljaghoub[✉],
Mohamad Ayoub[✉], Adnan Alashkar[✉], Ayman Mdallal[✉],
and Ranem Hasan[✉]

Abstract

The investment in novel PV technology is an important tool to exploit novel materials and materials processing and manufacturing technologies to achieve performance levels that supersede those attained by classical materials and processes. The following chapter highlights the novelty of materials and processes used to produce the third-generation technology of perovskite solar cells and latest manufacturing technologies. The chapter also contains a DIY project that shows a step-by-step execution and manufacturing procedure.

1 History and Definition

Organic–inorganic third-generation perovskite solar cells (PSC) are a promising alternative to current conventional photovoltaic technologies and a competitive option among other third-generation solar cells such as organic (OPV) and dye-sensitized (DSSC). Perovskite materials are basically sensitizers that were inducted into the photovoltaic solar cell scene by Tsutomu Miyasaka in 2009 (Kojima et al. 2009),

where a power conversion efficiency (PCE) of 3.1% was achieved, and perovskite solar cells have since exceeded pre-established technologies in terms of PCE, reaching 25.7% according to the National Renewable Energy Laboratory (NREL) (Best Research-Cell Efficiency Chart | Photovoltaic Research | NREL 2022). Perovskite solar cells are direct descendants of dye-sensitized solar cells in solid-state form. Although, conventional DSSC with liquid electrolyte and dye intercalation processes exhibited promising PCE, the performance was limited and bound by the environmental tolerance of the liquid electrolyte. Long-term stability was one of the main issues, where there was a sudden dissolution of the perovskite in the electrolyte. In DSSC, the biggest challenges were leakage and/or evaporation of the liquid electrolyte, which is why newly fabricated DSSC and their derivative PSC were based off the work of Nam-Gyu Park and Michael Grätzel through their invention of solid-state dye-sensitized solar cells in 2012 (Kim et al. 2012), with their novel device's efficiency reaching 9%. The word perovskite refers to the crystal structure of the formula ABX_3 , where A is a monovalent organic cation, such as methylammonium and formamidinium that are most commonly used in PSC applications, B is a divalent inorganic cation (heavy metal), such as lead or tin (Pb, Sn), and X is a halogen, such as chlorine, iodine and bromine (Cl, I and Br). A and B , organic and inorganic cations, occupy the centers of the cubo-octahedral and octahedral sites where they share 12 and 6 X atoms, respectively, such as shown in Fig. 1.

Different atom categories (A , B or X) play a crucial role in determining the type of perovskite structure and consequently its stability. For instance, changing a methylammonium (A) atom to its formamidinium alternative changes the lattice parameter of the crystal structure and consequently affects the overall stability of it. The same goes for B as well as X atoms, with the goal of achieving a structure tolerance factor of 1, using a compatible combination of these three types of atoms (Frost and Walsh 2016).

A. H. Alami (✉) · H. Aljaghoub · M. Ayoub ·
A. Mdallal · R. Hasan
University of Sharjah, Sharjah, United Arab Emirates
e-mail: aalalami@sharjah.ac.ae

H. Aljaghoub
e-mail: haljaghoub@sharjah.ac.ae

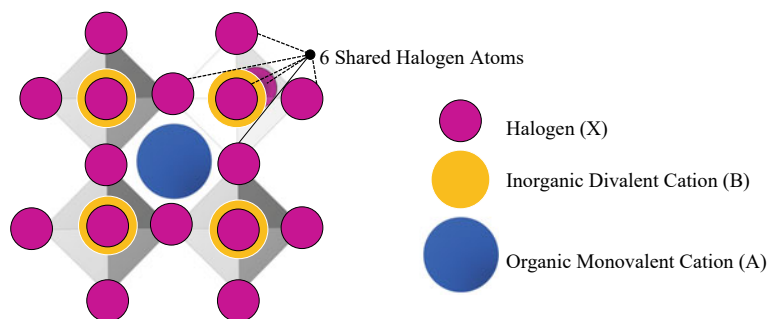
M. Ayoub
e-mail: mohamad.ayoub@sharjah.ac.ae

A. Mdallal
e-mail: ayman.mdallal@sharjah.ac.ae

S. Alasad · A. Alashkar
American University of Sharjah, Sharjah, United Arab Emirates
e-mail: g00070854@aus.edu

A. Alashkar
e-mail: b00028197@alumni.aus.edu

Fig. 1 Depiction of the perovskite crystal structure



2 Perovskite Solar Cell Structure and Operation

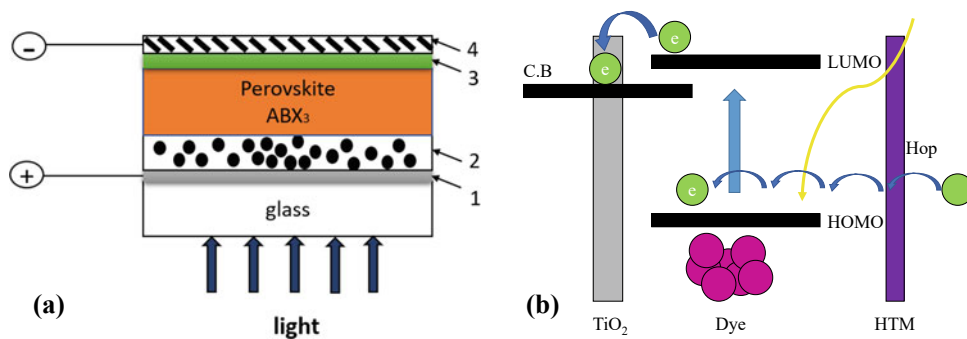
A perovskite solar cell consists of a transparent conductive oxide-coated glass substrate, an electron transport material (ETM), a perovskite active layer, a hole transport material (HTM) and a counter electrode, such as shown in Fig. 2a. The layers are arranged for generating electrons starting from the light passing through the solar cell. The mechanism for electron–hole generation occurs by the following: sunlight is absorbed by the perovskite active layer which excites the electron–hole pairs. The electron is then transferred to the surface of the bottom conductive electrode. Therefore, the transition metal oxides (TiO_2 or SnO_2) in the electron transport layer transfer the electron to the conductive part (FTO). The hole transport material collects the generated holes; however in certain cases, the shifted electrons can be recombined which impacts the PSC performance. Additionally, some buffers or compact layers can minimize the recombination process. This structure in its core represents a solid-state dye-sensitized solar cell, and in terms of base operation, it is very similar. Figure 2b shows how the excited electrons oxidize the perovskite layer (photoanode) and are injected into the electron transport material (TiO_2). The oxidized perovskite layer, which is the “dye” in this case, reduces the hole transport material through electrons hopping from the counter electrode, after the electrons have been dissipated into the external circuit, for it to reach a neutralized state. The PSC structure has evolved over its

development period since 2009. Figure 3a shows a PSC structure of FTO/CL TiO_2 /HTM+ TiO_2 +Perovskite/gold, where the photoanode (TiO_2 +Perovskite) is completely immersed into the HTM. Figure 3b shows a similar structure, however the HTM is separated and acts as a sole layer, and Fig. 3c shows the conventional heterojunction (planar) structure where no layer is immersed or adsorbed onto another layer.

3 Cell Performance and Optical Bandgap

Formamidinium lead iodide (FAPbI_3) can be tested using a UV–Vis spectra device to determine the absorbance across the visible wavelength and subsequently the bandgap of the perovskite layer. A UV–Vis spectrophotometer consists of a source lamp (usually xenon), a monochromator and light detectors. The xenon source lamp provides a continuous illumination throughout the run. The spectrometer used consists of gratings that isolate single wavelengths of photons. When white light is incident on the grating it is diffracted into the whole range of ultraviolet and visible light spectrum wavelengths. As the light is reflected off the grating, light of a single wavelength is allowed to pass through the slit as it leaves the monochromator. During a UV–Vis measurement, the grating is moved slightly to allow for all wavelengths to pass through the slit, thus covering the whole range of the spectrum. Similarly, a prism can be used to convert the white light into single wavelengths of the whole range of the UV–Vis spectrum. Detectors are placed

Fig. 2 a Perovskite solar cell structure and b solid-state dye-sensitized solar cell charge transfer mechanism



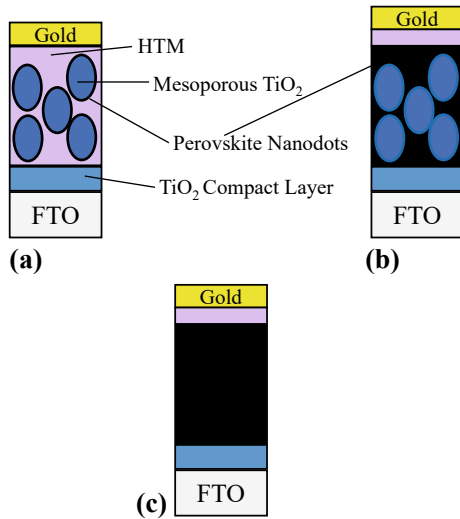


Fig. 3 Perovskite solar cell structural evolution from **a** discrete construction, **b** homogeneous construction and **c** blended construction

behind the targeted samples, such as shown in Fig. 4a, and based off a previously done reference/baseline measurement, the detector measures the attenuation of the intensity of the detected photons and creates a profile of the transmittance based on the concentration of the thin film and the length the light travels through it before being detected such as shown in Eq. (1). The absorbance of the material can then be calculated using Eq. (2), and following Beer-Lambert's law, the absorption coefficient can be directly related to the absorbance, such as shown in Eq. (3), and an absorbance profile is shown in Fig. 4b, where I is the intensity of the light in the tested sample, I_o is the intensity of the light in the baseline sample, α is the absorption coefficient, and d is the thickness of the coated thin film. The absorption coefficient can be calculated using Eq. (4). Then, through Tauc equation, shown in Eq. (5), the bandgap of the perovskite layer can be approximated by extrapolating the x-axis intersection from a linear region in the Tauc plot, where $h\nu$ is the photon

energy, γ is either 1 or 2 depending on whether it is an indirect or a direct bandgap material respectively, and E_g is the bandgap of the semi-conducting material.

$$\text{Transmittance} = 10^{-\text{constant}(\text{concentration} \times \text{length})} \quad (1)$$

$$\text{Absorbance} = \log\left(\frac{1}{\%T}\right) \quad (2)$$

$$I[W/m^2] = I_o[W/m^2]e^{-\alpha[1/m]d[m]} \quad (3)$$

$$\alpha[1/m] = \frac{\text{Absorbance}}{\log e \times d[m]} \quad (4)$$

$$(\alpha[1/m]h\nu[eV])^\gamma = \text{Constant}(E_g[eV] - h\nu[eV]) \quad (5)$$

The associated Tauc plot is shown in Fig. 5.

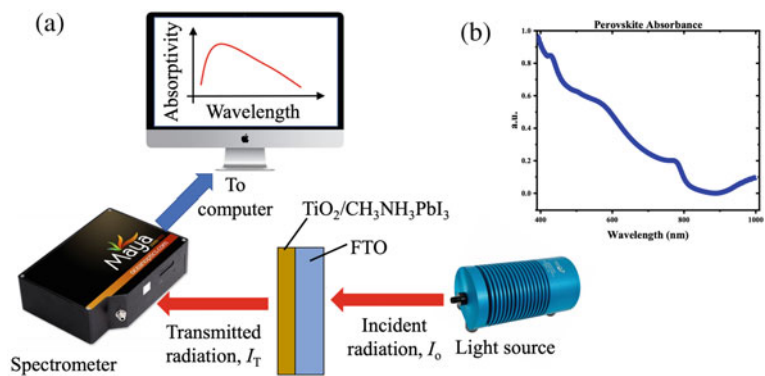
Through Tauc transformation and extrapolating the Tauc plot to the zero-x-axis point (pink line), the bandgap of the perovskite material was approximated to be 2.3 eV which falls into the range of perovskite bandgap. Tuning the bandgap of perovskite materials is a very lucrative advantage given how flexible it makes perovskite materials in utilizing them into photovoltaic tandem structures. It is also essential in determining suitable materials for a single-junction perovskite solar cell and matching the highest occupied molecular orbit (HOMO) and the lowest occupied molecular orbit (LUMO) for electron and hole transport materials, respectively, such as shown in Fig. 6.

4 Progress in Perovskite Solar Cells

4.1 Improving Stability at a High Relative Humidity

An essential aspect to consider in perovskite solar cells is stability. One factor that affects the instability of PSC is humidity. The efficiency of PSC is a function of relative

Fig. 4 **a** UV-Vis setup and **b** typical perovskite absorbance against wavelength



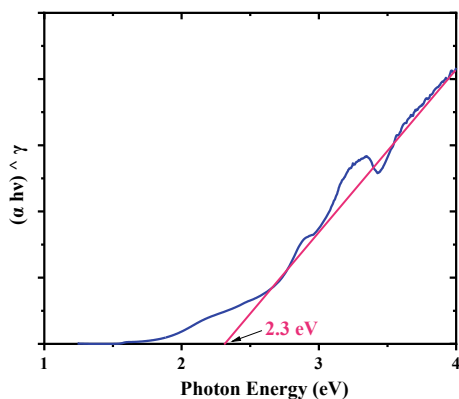


Fig. 5 Tauc transformation plot

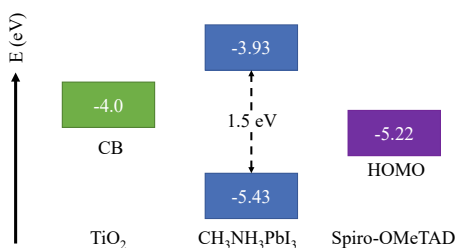


Fig. 6 Perovskite solar cell—energy bands

humidity and the type as well as the ratio of the halogen (X) atoms used; as this ratio increases (higher Br with respect to I), the efficiency has been noted to increase; and therefore, there is no need to stick to a single type of halogen atom, but instead both PbI_2 and PbBr precursor materials can be used. For $x = 0.29$ and higher, the relative humidity does not seem to affect the overall efficiency in a noticeable manner, such as shown in Fig. 7.

4.2 Perovskite Solar Cell Efficiency Progress

Organolead halide perovskites were used for solar cells since 2009. The use of light absorbers of perovskite started from liquid dye-sensitized solar cells to the solid-state type of perovskite solar cells. Figure 8 shows the perovskite power conversion efficiency with time. The efficiency has increased drastically from 3.9 to 25.5% between 2009 and 2020. In addition to the superior performance of light absorption and the desired bandgap, the 1.5 eV bandgap increases the idealization of PSC over the silicon-based solar cells. Further enhancements in large-area fabrication and stability of PSC are essential to be commercialized (Dai et al. 2021).

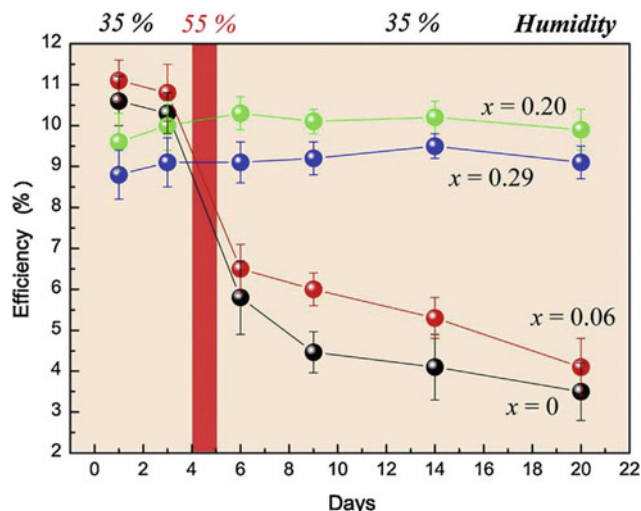


Fig. 7 Perovskite solar cell PCE change with relative humidity and time for $\text{CH}_3\text{NH}_3\text{Pb}(\text{I} - x\text{Br})_3$ ($x = 0, 0.06, 0.20, 0.29$) (Park 2015)

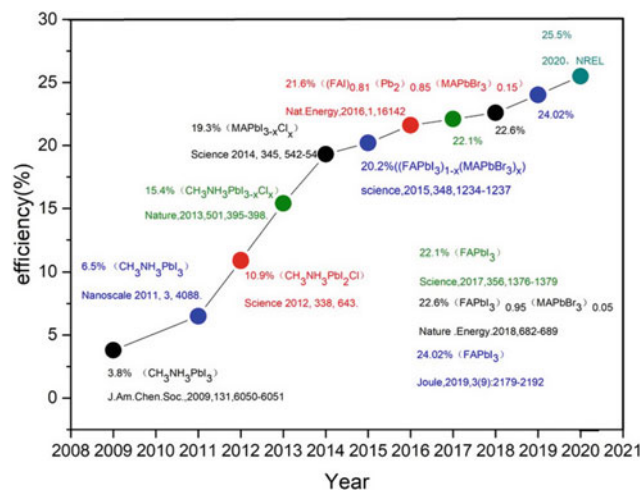


Fig. 8 Change in PSC efficiency between 2008 and 2020 (Dai et al. 2021)

4.3 Available Manufacturing Technologies

There are various pre-established, such as spin coating, and rising manufacturing technologies, such as dip coating and bar coating, that have been utilized for the fabrication of perovskite solar cells. Spin coating is a conventional coating technique that has been used extensively and optimized to achieve PCE results up to 25.5%. The basic operating principle of spin coating is that the resultant centrifugal force causes the solution to spread in a uniform manner across the

substrate, where the end-film result is optimized through rotating time and frequency. Other manufacturing technologies such as dip coating, bar coating, spray coating and slot-die coating have been lately experimented with to tackle issues such as commercialization and automation of the PSC fabrication process. Slot-die coating for instance provides a high throughput along with reproducible film results and poses as a viable option for the future of fully slot-die-coated and roll-to-roll compatible perovskite solar cells.

5 Do-it-yourself DIY Perovskite Project

5.1 Substrate Preparation

PSC can be fabricated using a wide variety of substrates ranging from coated glass to flexible plastics. Fluorine-doped tin oxide (FTO)-coated glass is one of the conventional substrates that are used in PSC fabrication among researchers. Its novel low sheet resistance allows for a highly conductive PSC electrode. FTO glass is first cut into appropriate size, and it is cleaned from any residue that could hinder the integrity of the fabricated PSC. Then, the substrate goes through a process called etching. Etching is a necessary step that removes a part of the conductive oxide from a limited region on the glass substrate to prevent short circuits with the to-be-deposited counter electrode at the end of the fabrication process. A summary of the cell manufacturing process is shown in Fig. 9.

Etching is carried on by covering the targeted region with metal oxide powder, such as zinc oxide (ZnO) and reacting it with an acid, such as hydrochloride (HCl), which essentially removes the FTO and allows for further processing of the substrate, such as shown in Fig. 10. The FTO substrate is then cleaned using a mixture anionic liquid detergent/ deionized (DI) and placed in an ultrasonic bath for 20 min. Then, the samples are rinsed and immersed in DI water again and placed in the ultrasonic bath for another 15 min, after which the samples are rinsed with ethanol and subsequently dried, such as shown in Fig. 11, and the samples are later

Fig. 9 Summary of the steps for PSC manufacturing processes

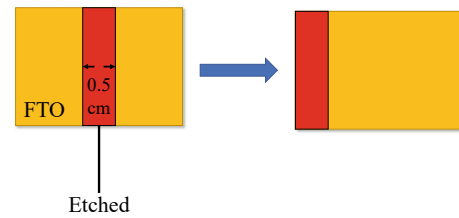
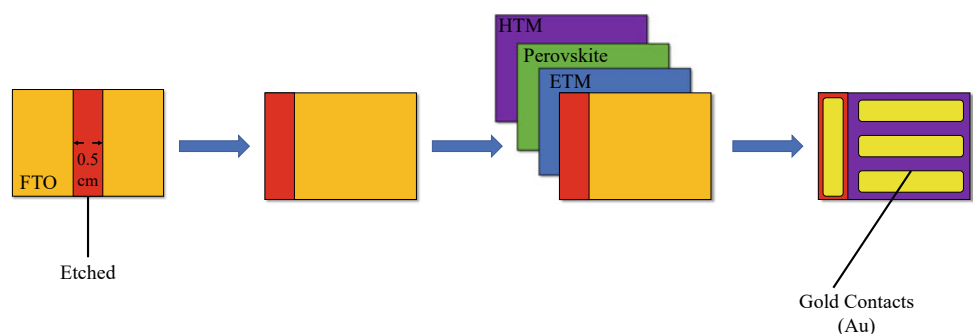


Fig. 10 Etching of FTO substrate

exposed to an ultraviolet source before the subsequent deposition of following layers to enhance the wettability of their surface.

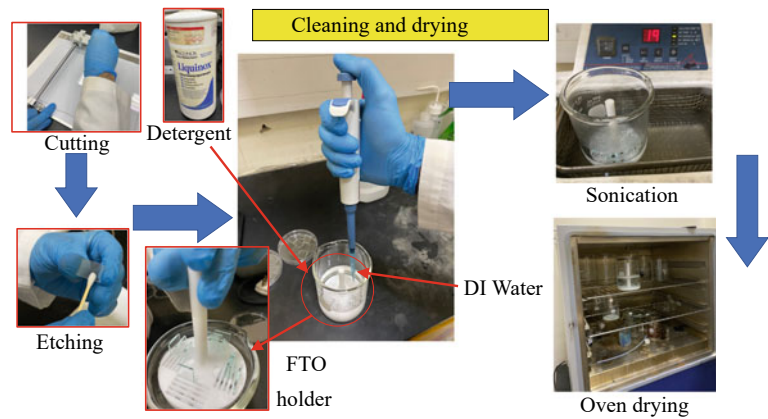
5.2 Electron Transport Layer (ETL) Deposition

Fabrication of PSC requires depositing different layers such as an electron transport layer (ETL) consisting of semiconducting metal oxides, a perovskite active layer (light absorber), a hole transport layer (HTL) and a metal counter electrode contact (preferably gold: Au) layer. To prevent contact between TCO/FTO and the ETL/perovskite (photoanode) and the HTL, a compact layer consisting of TiO_2 is deposited on top of the FTO layer. The compact TiO_2 layer is deposited via spin coating, a spin coater is shown in Fig. 12, just like the rest of the layers that'll be mentioned in this section (except for gold), and then ramp-annealed to reach 500°C for 30–40 min. A mesoporous TiO_2 layer is then deposited and annealed at 120°C for 30–40 min.

5.3 Perovskite Preparation and Deposition

The perovskite active layer is prepared by mixing and dissolving the appropriate amount of base materials such as methylammonium iodide or formamidinium iodide, lead iodide and additives such as methylammonium chloride and cesium iodide for enhanced performance and layer morphology. First off, inorganic components are added and

Fig. 11 FTO substrates preparation



dissolved in organic solvents such as dimethyl sulfoxide (DMSO) and dimethyl formamide (DMF), then they are heated and stirred at 70°C until the powder components are completely dissolved. At the end, the organic components are added to the mixture and left to stir for a couple of hours,

usually 4–5. The perovskite precursor is spread over the substrates containing the ETL and spin coated at a speed of ~ 5000 RPM, and an anti-solvent treatment is carried on by dynamically spin coating chlorobenzene (CB) on the rotating substrate leaving an almost dry film. At the end, the substrates with the deposited perovskite are annealed at 150°C for 20 min. The overall process is shown in Fig. 13.

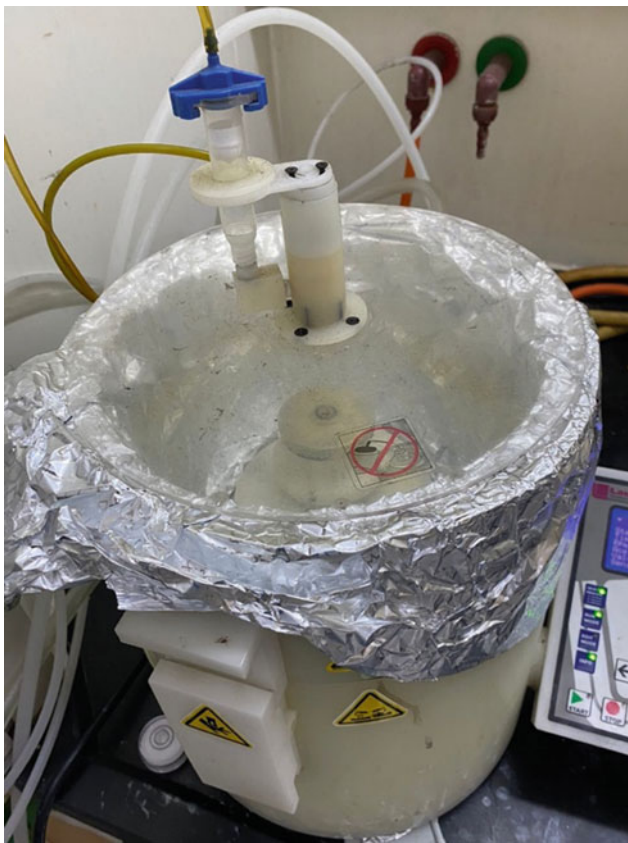


Fig. 12 Spin coating process shows the spin coating machine with disposable aluminum foil to reduce device contamination resulting from solution splash

5.4 Hole Transport Layer and Counter Electrode

Hole transport layer (HTL), commonly Spiro-OMeTAD, is deposited using spin coating, such as shown in Fig. 14a. The mesoporous TiO_2 film pores should be filled with the HTL to induce a heterojunction. For pore filling, a molecular-type HTM such as 2,20,7,70-tetrakis(N,Np-dimethoxyphenylamino)-9,90-spirobifluorene (Spiro-OMeTAD) is preferred. A stock solution of Spiro-OMeTAD is added to a stock solution of Li-TFSI and TBP dissolved in chlorobenzene. The hole diffusion length and conductivity in HTL should be taken into consideration as they restrict the mesoporous TiO_2 film thickness. Then the active materials that lie on top of the previously etched region are scratched off to expose a workable area for the deposition of the gold counter electrode. Finally, the metal contact layer (made from gold, Au) is deposited using thermal evaporation process, with the help of a mask that targets the desired area for contacts, as shown in Fig. 14b. The perovskite solar cells are shown in Fig. 14c, which are ready for characterizations, testing and processing, to extract their power and efficiency figures, such as shown in Fig. 14d.

The following results were obtained for the fabricated solar cells as shown in Table 1 and Fig. 15, where a 14.619% PCE was achieved.

Table 2 provides a summary for the materials that are used in this DIY project and their purposes.

Fig. 13 Flow of perovskite deposition process

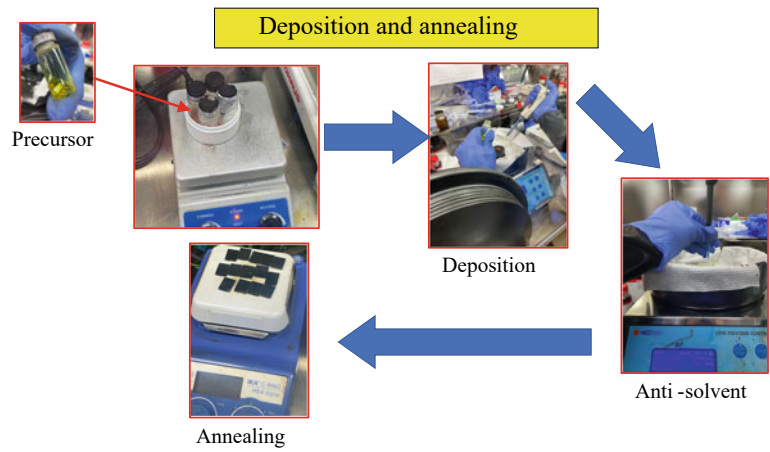


Fig. 14 *J-V* a HTL deposition, b thermal evaporation step, c perovskite cell assembly and d characterization within a solar simulator

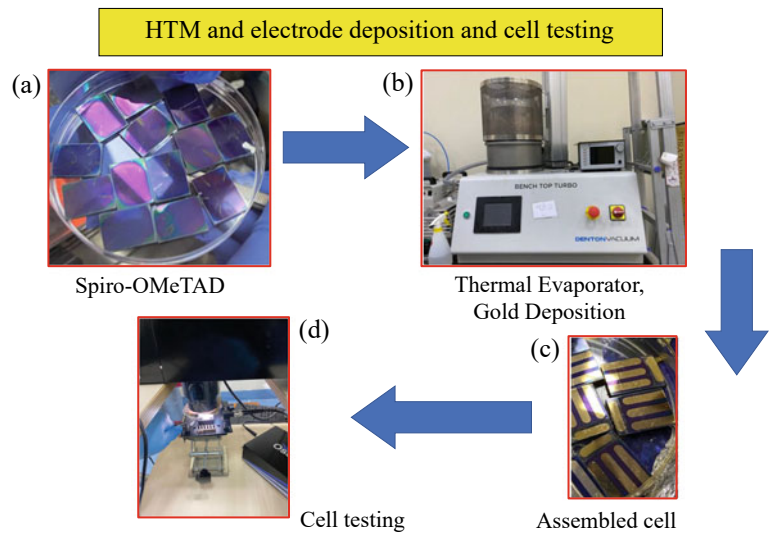


Table 1 Perovskite solar cell *J-V* test results

PCE (%)	FF (%)	J_{SC} (mA.cm ⁻²)	V_{OC} (V)	MP (W)	Rshunt (Ωcm ²)	Rseries (Ωcm ²)
14.619	66.204	- 23.478	0.940	- 14.6193	1119.05	3.906

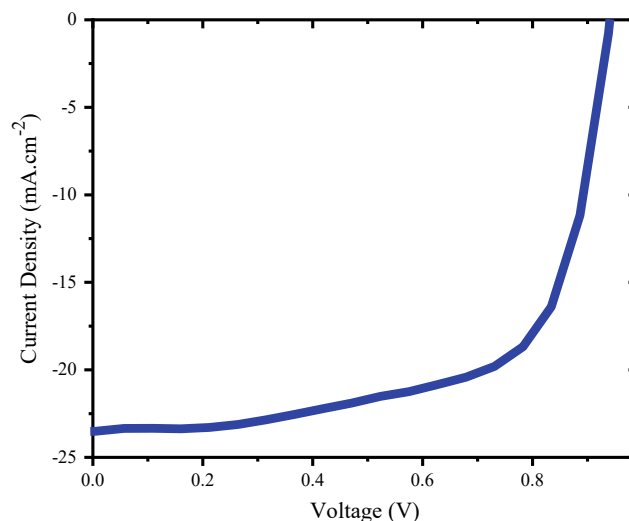


Fig. 15 Perovskite solar cell J - V curve

Table 2 PSC DIY material list








Material	Usage
<i>Electrode</i>	
FTO-coated glass	Substrate/scratching
ZnO + HCl	Etching
Di water	Cleaning
Anionic liquid detergent	Cleaning
Ultrasonic bath	Cleaning
Ethanol	Cleaning
Oven	Drying
<i>ETL-active layer-HTL</i>	
TiO ₂ powder	TiO ₂ precursor preparation
Formamidinium iodide	Perovskite precursor preparation
Methylammonium chloride	Perovskite precursor preparation
Cesium iodide	Perovskite precursor preparation
Lead iodide	Perovskite precursor preparation
Spiro-OMeTAD	HTL preparation
Li-TFSI	HTL preparation
TBP	HTL preparation
Spin coater	ETL-Perovskite-HTL deposition
Hot plate	Annealing ETL and perovskite layer
<i>Counter electrode</i>	
Gold	Counter electrode material
Mask	Counter electrode deposition
Thermal evaporation	Counter electrode deposition
<i>Cell testing</i>	
Solar simulator	Light source
Potentiostat	Data acquisition

References

- Best Research-Cell Efficiency Chart | Photovoltaic Research | NREL. Retrieved from <https://www.nrel.gov/pv/cell-efficiency.html>. Accessed on 17 Jul 2022
- Dai T et al (2021) Strategies for high-performance large-area perovskite solar cells toward commercialization. *Crystals* 11(3):295. <https://doi.org/10.3390/cryst11030295>
- Frost JM, Walsh A (2016) Molecular motion and dynamic crystal structures of hybrid halide perovskites. In: *Organic-inorganic halide perovskite photovoltaics*. Cham: Springer International Publishing, pp 1–17. https://doi.org/10.1007/978-3-319-35114-8_1
- Kim H-S et al (2012) Lead iodide perovskite sensitized all-solid-state submicron thin film mesoscopic solar cell with efficiency exceeding 9%. *Sci Rep* 2:591. <https://doi.org/10.1038/srep00591>
- Kojima A, Teshima K, Shirai Y, Miyasaka T (2009) Organometal halide perovskites as visible-light sensitizers for photovoltaic cells. *J Am Chem Soc* 131(17):6050–6051. <https://doi.org/10.1021/ja809598r>
- Park N-G (2015) Perovskite solar cells: an emerging photovoltaic technology. *Mater Today* 18(2):65–72. <https://doi.org/10.1016/j.mattod.2014.07.007>



Recent Advances in Solar Cells

Abdul Hai Alami , Shamma Alasad , Haya Aljaghoub ,
Mohamad Ayoub , Adnan Alashkar , Ayman Mdallal ,
and Ranem Hasan 

Abstract

This chapter outlines the recent technologies in solar cells and their advancements in supporting various industries to achieve greater efficiency and compatibility. For example, the agrivoltaic technology is discussed. This technology integrates food, energy and sometimes water security. Other topics focus on more novel and sustainable cell manufacturing technologies that will push the utilization of PV technology further, such as tandem cells as well as innovative metallic transparent substrates.

1 Introduction

Photovoltaic technologies can be augmented and incorporated into a multitude of applications, helping to improve the overall performance. The following sections illustrate some of the recent developments in PV technologies. Considering the manufacturing vantage point, redesigning the production of PV would yield ultimate advantages, such as using flexible metallic substrates instead of the brittle glass-based substrates. In addition, employing perovskite/silicon solar

cells aids in the maximum utilization of incident solar radiation due to bandgap differences between the different cells. PV technologies can also be used in agrivoltaic setups, where bifacial solar panels can be used to shade crops and also absorb irradiance from both panel faces.

2 Tandem Silicon/Perovskite Solar Cells

Tandem cells refer to the combination of various solar cells assembled on top of each other. Generally, the upper cell has a high bandgap such as perovskite cells, which converts part of the solar spectrum into electricity, and the rest (infrared) goes through to the bottom cell which is a low bandgap cell such as silicon solar cells. The bottom cell could be a bifacial cell that benefits from the diffused light that falls on the back side of the cell (Akhil et al. 2021; Jošt et al. 2020). Tandem solar cells can be connected either in series or individually, but series-connected cells are easier to manufacture (Tandem Cells 2022). A typical tandem cell is shown in Fig. 1.

There are many types of tandem solar cells, and this includes organic tandem cells: the cheapest and the lowest efficiency of all types with a range of 10–15%. The second type is the inorganic tandem cells, and this form of tandem cell is commercially available and is manufactured from III-V group materials, used in multi-junction cells and has the highest efficiency with 44.4% for the 3-junction cell and 46% for the 4-junction cell. These cells are mainly used in space applications due to their high efficiency and competitive cost. Hybrid tandem cells made of perovskite solar cells have proven to have higher efficiency and reduced cost (What are tandem cells Introduction to solar technology 2022; Yan and Saunders 2014).

2.1 Manufacturing

The deposition process flow and steps of a tandem cell layers are illustrated in Fig. 2. The figure concentrates on the

A. H. Alami (✉) · H. Aljaghoub · M. Ayoub · A. Mdallal · R. Hasan
University of Sharjah, Sharjah, United Arab Emirates
e-mail: aalalami@sharjah.ac.ae

H. Aljaghoub
e-mail: haljaghoub@sharjah.ac.ae

M. Ayoub
e-mail: mohamad.ayoub@sharjah.ac.ae

A. Mdallal
e-mail: ayman.mdallal@sharjah.ac.ae

S. Alasad · A. Alashkar
American University of Sharjah, Sharjah, United Arab Emirates
e-mail: g00070854@aus.edu

A. Alashkar
e-mail: b00028197@alumni.aus.edu

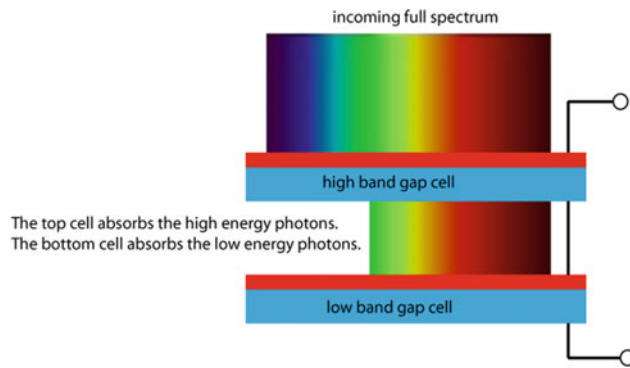


Fig. 1 Series-connected tandem solar cell (Tandem Cells 2022)

manufacturing steps of perovskite tandem and perovskite/Si cells.

The fabrication of perovskite/Si tandem cells is initiated with the deposition of a clear recombination layer on the Si cell (A1) (no reflector or solid metal electrode), and in the second step (A2) the perovskite film is deposited on the previous layer without damaging it or the c-Si cell. In step (A3) a clear and conductive sputter buffer layer is deposited on the perovskite cell. The buffer layer serves as a protection layer, since it protects the perovskite layer in step (A4) when sputter deposition of the transparent electrode occurs on the front side. This electrode is characterized by its high transparency and small sheet resistance. Finally, to reduce the resistance of the conductor, metal gridlines are added (A5) (Leijtens et al. 2018).

In the case of perovskite tandem cells, the process starts with step (B1), where a buffer layer deposited on a wide-bandgap front cell to avoid damage, and after that step (B2) a recombination layer is deposited via sputtering on the top of the buffer layer to protect underlying cell. The rear cell with the small bandgap is deposited through (step B3). Finally, in step (B4) a reflective metal electrode is utilized to

connect the rear cell and increase the light path length (Leijtens et al. 2018).

A recent study at the University of Arizona established a new manufacturing technique regarding tandem perovskite cells which reduces the reflection loss and extends the pathway of the long-wavelength light inside the silicon. The researchers claim that this technique could lead to a 30% efficient perovskite tandem cells. The perovskite layer is deposited with the help of nitrogen blading over a textured silicon substrate with pyramids of 1 μm in height. The existence of the pyramids on the perovskite layer helps in reducing the reflectance. The resulting perovskite layer had thickness of 3–10 μm which is shown in Fig. 3.

The process of blade coating was used to planarize the texture of the silicon layer by filling between the pyramids. Meanwhile the N_2 knife-aided process was used to investigate the capability of the cell to planarize sub-micrometer-textured wafers and coat the poly [bis(4-phenyl) (2,4,6-trimethylphenyl)amine] (PTAA). The knife helps to remove the solvent vapor (Chen et al. 2020; Deng et al. 2019; New manufacturing technique for 26%–efficient tandem perovskite solar cell 2022) (Fig. 4).

2.2 Efficiency

The efficiency varies based on the type of the tandem cell, and the highest achieved efficiency for perovskite/CIGS tandem cell was 24.2 and 25.5% for all perovskite tandem cells (Best Research-Cell Efficiency Chart 2022). Similarly, for the perovskite/Si tandem cells an efficiency of 29.15% was achieved in 2020 (Al-Ashouri et al. 1979), then improved by the research center of Helmholtz Zentrum Berlin für Materialien und Energie (HZB) to 29.8% in 2021 (HZB sets new 29.8% efficiency record for perovskite–silicon tandem solar cells 2022).

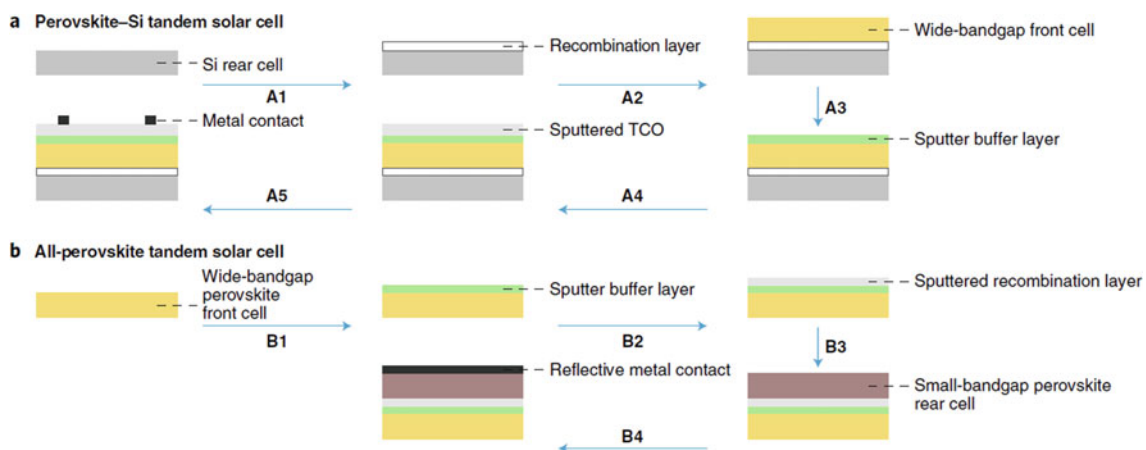


Fig. 2 Typical tandem process flow (Leijtens et al. 2018)

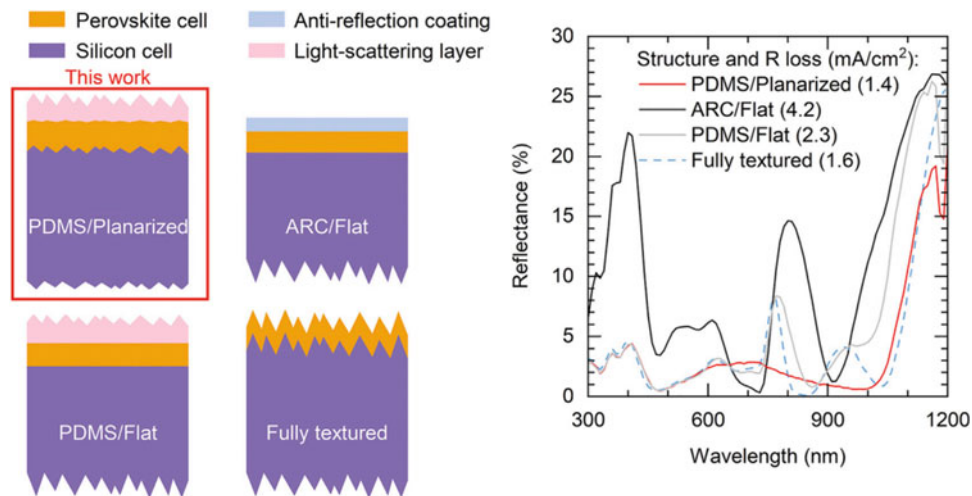


Fig. 3 Architectures of various perovskite/Si tandem cells (Chen et al. 2020)

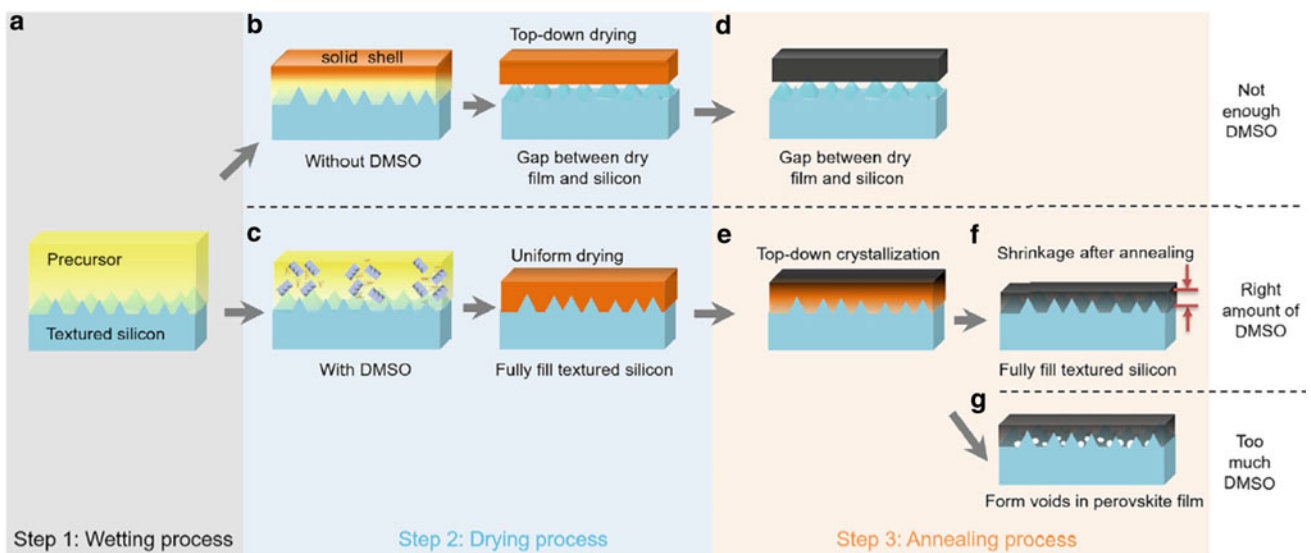


Fig. 4 Various perovskite film formation techniques (Chen et al. 2020)

2.3 Challenges

The commercialization of tandem cells is prevented by numerous challenges in both the architecture and the fabrication aspects.

2.3.1 Transparent Electrodes

Transparent electrodes are the most important components of a solar cell. A great performing electrode must have both high transparency and conductivity. Various materials were used as an electrode for the perovskite cells such as silver (Ag) nanowire, carbon nanotube, graphene and transparent conductive oxides (TCOs) (Rahmany and Etgar 2020). TCOs such as indium transparent oxide (ITO) have proven to improve the device lifetime and provide high

transparency and conductivity (Jung and Guo 2012). However, to achieve that, high treatment temperature (over 300°C) is essential throughout and after the sputtering process (Balasundaraprabhu et al. 2009; Jung and Guo 2012). Yet perovskite materials can't survive under this high temperature (Afroz et al. 2020).

2.3.2 Scalability

Presently, efficiency tests for 1 cm² cells are laboratory tests only. Although, there are many studies that investigate cells with areas exceeding 10 cm² (Afroz et al. 2020). The main issue is the reduction of the lateral conductivity of the TCO-based electrode when compared to other metal electrodes. This effect increases significantly with the increase of the device area (Akhil et al. 2021).

2.3.3 Stability

Tandem solar cells must endure at least 25 years to compete with single-junction silicon. To do so, the instability issues associated with perovskite cells need to be addressed. Since methylammonium is a volatile (unstable) cation, encapsulation was introduced to prevent it from escaping at high temperatures. Formamidinium, on the other hand, demonstrated improved thermal stability as well as higher efficiency (Eperon et al. 2014).

2.3.4 Tin, Lead and Bromide

It has been found that perovskite cells based on tin have short lifetimes, and this is attributed to the fact that the oxidation of tin from Sn^{+2} to Sn^{+4} is carried easily when the cell is exposed to conditions with oxygen and moisture. However, substituting 50% of the halide with an element other than tin (lead (Pb)) improves the lifetime by 10 to 100% (Noel et al. 2014). Another instability problem within the perovskite tandems is the transfer of ions between the various perovskite layers, especially given the fact that the cations of the perovskite structure sites have been proven to be mobile. For instance, it is quite possible for the bromide ions to diffuse within the cells if the diffusion barrier of the recombination layer is not strong. TCOs have provided a good protection (recombination layer), but it must be investigated whether they are suitable for long operations (Leijtens et al. 2018).

2.4 Environmental Impact and Recycling

The presence of lead and tin in perovskite tandem cells raises environmental issues. It has been found that lead is slightly

soluble in water, leading to leak from damaged panels into the environment and groundwater and causing contamination and health hazards. Lead could enter the human body through gastrointestinal and respiratory system causing heavy metal intoxication (Babayigit et al. 2016). In addition, it has been found that chronic exposure to tin is as poisonous as lead and may cause serious damages to the human body (Tin and inorganic tin compounds 2022).

Lead is a valuable material both environmentally and economically, and thus it should be recovered from the waste of perovskites solar cells. Recently, a study developed an economical recycling technique utilizing carboxylic acid cation-exchange resin as lead adsorbent and using thermal detachment to expose perovskite films. Firstly, organic solvents, such as dimethylformamide (DMF), are employed to dissolve the lead. To remove the lead from the organic solvent, it is adsorbed by resin-regeneration process via HNO_3 , then followed by precipitation of PbI_2 by pouring NaI into $\text{Pb}(\text{NO}_3)_2$ containing solution. Figure 5 shows the steps of recycling Pb from that is used in PV cells (Chen et al. 2021).

2.5 Characterization

2.5.1 Morphological, Structural and Compositional Characterization

The characteristics of perovskite cells are vital to identify shunt paths to coarse surfaces of CIGS cells or phase impurities over bandgap modification (Jošt et al. 2019).

Several techniques are used to assess the quality of the layers of the perovskite tandem cells: scanning electron microscopy (SEM), transmission electron microscopy

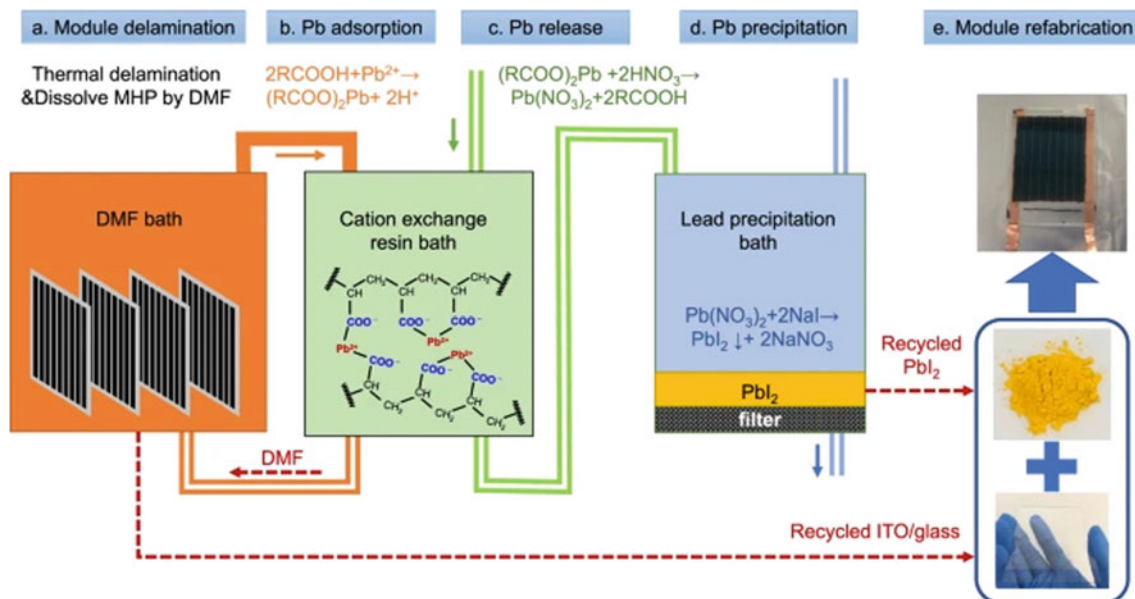


Fig. 5 Flow process and steps for the recycling of perovskite solar modules (Chen et al. 2021)

(TEM), secondary ion mass spectrometry (SIMS) and X-ray diffraction (XRD).

SEM is an electron microscopy mechanism that generates an image of a sample by focusing a beam of electrons on a specific region. The interaction between the beam and the atoms of the samples reveals information on the surface topography and morphology. SEM also provides top and cross-sectional views of the tandem cell that allow the calculation of grain sizes and layers' thicknesses (Jošt et al. 2020).

TEM is similar to SEM with the exception that electrons are transmitted through the sample rather than being scattered or diffracted. This phenomenon can produce images with higher resolution and allows for a more accurate calculation of the layer thicknesses as compared to SEM (Jošt et al. 2020).

SIMS is used to investigate the chemical conformation of samples. SIMS uses a primary beam of ions (Ar^+ , Ga^+ or Cs^+), to collect and analyze the ejected secondary ions.

XRD is employed to study the crystal structure and crystallinity of atoms. It is also utilized to identify the crystalline phases and orientation (Jošt et al. 2020).

2.5.2 Optical Characterization

For perovskite tandem cells, reflection R (%) and transmission T (%) measurements are the main optical characterization using photospectrometer that measures the reflection and transmission of a material as a function of wavelength. The equation $A = 1 - R - T$ can be utilized to calculate the absorption A (%) which in return can help in the optimization of the tandem cells (Jošt et al. 2020).

2.5.3 Radiative Characterization

Radiative characterization helps measure the charge carrier dynamics and recombination at the layers interfaces. In addition, it displays loss mechanisms in a device and provides information on electronic properties of an absorber. To determine the radiative behavior of a PV cell, photoluminescence (PL) is used, where light is emitted from any form of matter after the absorption of photons (Jošt et al. 2020).

2.5.4 External Quantum Efficiency Spectra

Quantum efficiency is the ratio of the charges collected by a solar cell to the number of photons of a specific energy applied on the cell. This method helps in determining the bandgap of the solar cell as well as absorption losses (Jošt et al. 2020).

2.5.5 Current–Voltage Characterization

It is the most common and used characterization technique for most solar cells. It provides information on the overall efficiency of the device. The efficiency depends on the short-circuit current (I_{SC}), open-circuit voltage (V_{OC}) and fill

factor (FF). Both current and voltage are measured under 1.5 air mass (AM) illumination. All these values are required for the plot of the I - V curves (Jošt et al. 2020).

2.5.6 Stability Characterization

Stability characterization is important as it studies the degradation of solar cells due to its interaction with air, moisture and oxygen. Perovskite materials are known to be the most degradable solar cells. Hence, numerous research explored the ideas of stacking and encapsulating cells. Researchers summarized several routes to enhance the stability of the perovskite cells (Jošt et al. 2020):

1. Bulk and surface passivation of perovskite films can enhance the stability of the solar cells by reducing the ionic defects.
2. Applying contact and charge extraction layers enhances the stability and prevents degradation.
3. Proper encapsulation through transparent glass/transparent glass substrates and sealed using curable UV glue.

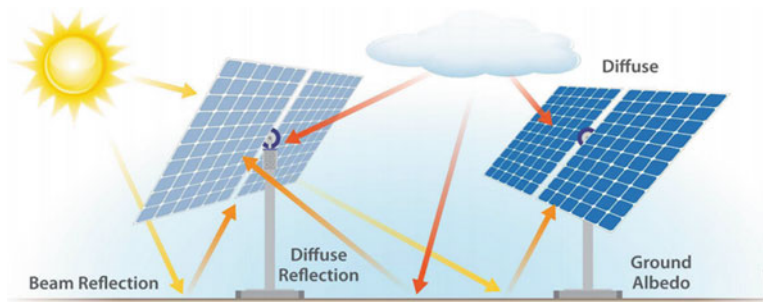
All the characterization methods will be explained in detail in Chap. [Characterization Techniques for Photovoltaics Manufacturing](#) (Characterization techniques for Photovoltaics manufacturing).

3 Bifacial Solar Photovoltaics

The strive to enhance solar radiation utilization within solar photovoltaic panels has resulted in many innovative techniques to reduce reflection, enhance absorption, permit better solar tracking or allow more routes for radiation to interact with the cells. Bifacial solar panels belong to the latter school of thought. They can be thought of as double-sided solar panels capable of generating electricity from either/both sides (front and rear), unlike their conventional counterparts that can only generate from one side. They are usually monocrystalline to achieve the highest possible efficiency, despite being more expensive than polycrystalline ones.

In conventional solar panels light is absorbed by cells with a portion of incident light passing through and being forever wasted. In the case of using bifacial panels, there is still ample chance that the transmitted portion of light to be reabsorbed by rear cells, when it is reflected back by the ground or another material. This reflection effect is called albedo and is a function of the reflecting surface material properties. Generally lighter-color materials will lead to more reflected sunlight than darker materials, and rougher surfaces tend to absorb more than reflect. On the other hand, care must be taken in installing the panels in array form to ensure minimal adverse interference effects of cast shadows.

Fig. 6 Bifacial solar panels' working principle (Deline et al. 2019)



Therefore, small junction boxes, narrow rail supports and vertical supports at the very end of the steel structure are utilized to reduce the shaded area on the rear panels. This type of solar panels comes in different designs: framed and frameless. Also, a number could consist of dual-glass sheets and others of clear back sheets. Figure 6 shows a schematic of how bifacial panels work.

There are several factors that affect the power generation of bifacial solar panels such as mounting height, the further a bifacial module from the ground or a surface the higher chance reflected or diffused light will reach the back of the module. Also, the number of modules in series, and the diffused irradiance fraction which is the ration between the diffused horizontal irradiance (DHI) and the global horizontal irradiance (GHI). Moreover, the albedo of the ground surface is another important factor, a surface covered with snow or ice most likely will reflect more light than soil, or a surface painted with white or silver color will reflect more

light than a surface painted with darker colors. Table 1 shows the albedo values for various surfaces:

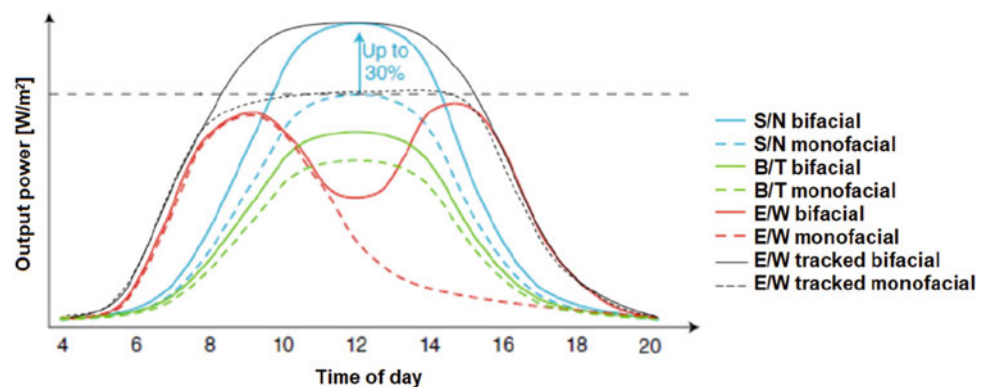
The efficiency of a bifacial solar panel is measured as the ratio of incident luminous power to generated power, and it is measured for front and rear independently. Another important term is the bifaciality factor, which is the ratio of the rear efficiency in relation to the front efficiency when subjected to same irradiance. Due to the existence of another generation source in this type of solar panels, recent researches show that bifacial provides energy yield higher than monofacial by 25 to 30% just from the rear (Dullweber and Schmidt 2016; Sun et al. 2018; Kopecek and Libal 2018) (Fig. 7).

There are two different types of bifacial solar cells: p-type technology that includes the passivated emitter and rear cell (PERC) and the n-type technology that includes passivated emitter rear totally diffused (PERT) and heterojunction with thin layer (HJT). There are many works on other types of p and n-type technologies, but they are still under development and not commercialized yet, such as passivated emitter rear locally diffused (PERL), interdigitated back contact (IBC) and tunnel oxide passivated contact (TOPCon). Table 2 shows a comparison between the different types, and as seen in Fig. 8.

Table 1 Albedo values for various materials (Stein et al. 2021)

Material	Albedo
Grass	0.15–0.26
Snow	0.55–0.98
Black soil	0.08–0.13
Clay soil	0.16–0.23
Sand	0.21–0.60
Asphalt pavement (new)	0.09
Asphalt pavement (weathered)	0.18

Fig. 7 Comparison of power generation curves for monofacial and bifacial modules (Kopecek and Libal 2018)



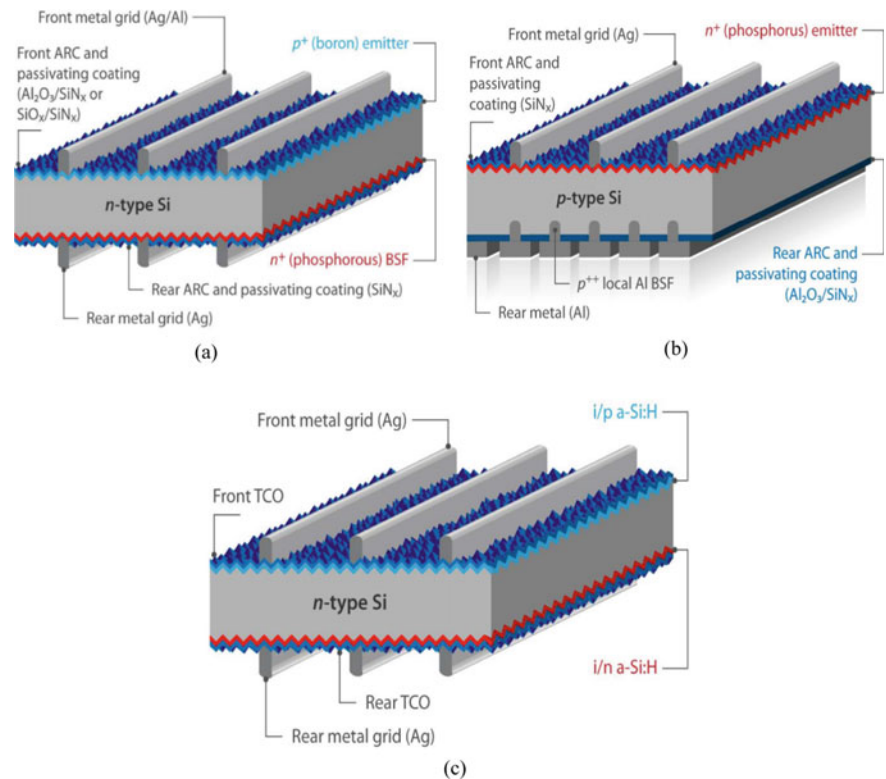
3.1 PERC

It could be used for both concepts: monofacial and bifacial. It is more efficient than traditional solar cells delivering more

Table 2 Comparison between the different types in terms of efficiency and bifaciality (Bifacial solar cells 2022)

Type	Solar cell efficiency (%)	Bifaciality (%)
PERC	21.2	70–80
PERT	22	80–90
PERL	19.8	80–90
HJT	24.7	95–100
IBC	23.2	70–80
TOPCon	22.5	85–90

Fig. 8 Architecture of the different types of bifacial solar cells: **a** PERC, **b** PERT and **c** HJT (Stein et al. 2021)



than 6% higher, in low light and high-temperature conditions. The main difference between this type and a typical monocrystalline solar cell is the existence of a back surface passivation which provides three benefits that boost the efficiency of these cells such as reflection of light back through the cell, reduced electron recombination and reduced heat absorption. The manufacturing processes are similar to the traditional solar cells. Therefore, shifting into this type will not cause a significant increase in the manufacturing costs.

3.2 PERT

Similar to the PERC cells, it can be used as monofacial and bifacial solar cells. The difference between these two types is that PERT back surface is totally diffused whether by boron

(p-type) or phosphorus (n-type), but this requires additional processes, high-temperature POCL and BBR_3 diffusion, which in return results in a more expensive manufacturing process than PERC. On the other hand, this type of cells displays no light-induced degradation (LID) unlike PERC cells.

3.3 PERL

This type of solar cells combines the advantages of both PERC and PERT, where both front and rear monocrystalline cells are passivated; however, the rear cell is locally diffused at the metal contacts to minimize recombination rates yet maintaining electrical contact. This type has many benefits: higher efficiency and energy yield, low process times on the manufacturing process, different configurations on the rear

side could be used (transparent back sheet or glass layer) and similar costs to PERC cells.

3.4 HJT

The heterojunction cells are a new technology, and they have the potential to be the successor to the PERC cells. The novelty of these cell lies in the simple manufacturing process as it requires less steps and lower temperatures. Also, it is compatible with thin wafers allowing for a more facile production and a higher bifaciality potential (Stein et al. 2021).

3.5 IBC

It is one of the HJT configurations with a potential higher efficiency, however accompanied with higher production costs and difficulty in the production processes. This type has several advantages such as lower shading losses, easier connections (no space required between the cells) and lower series resistance.

3.6 TOPCon

Compared to the new technologies such as HJT and IBE, TOPCon can be upgraded from the current PERC and PERT lines. Therefore, the manufactures will only need to

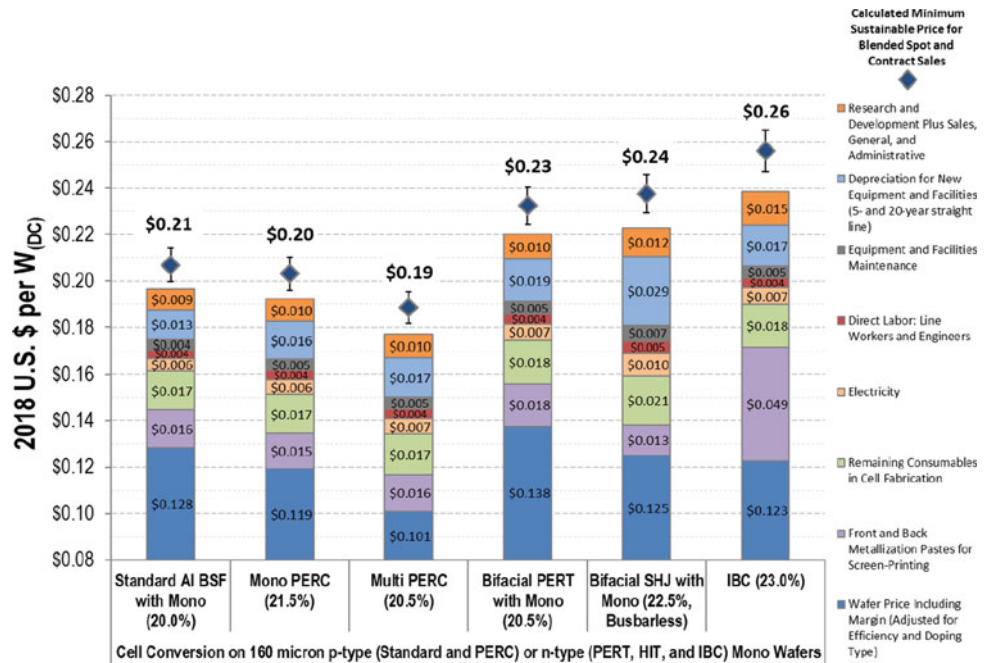
upgrade their existing production lines (lower capital investment). To upgrade n-PERC into n-TOPCon, only additional ultrathin silicon dioxide (SiO₂) to act as a passivation layer between the rear Si surface and the rear contact and a doped poly-Si layer is required to produce a high conductivity layer.

The National Renewable Energy Laboratory (NREL) in 2018 stated that the manufacturing costs of both monofacial and bifacial are relatively close, and this difference is expected to be reduced with coming years with the recent advances in the manufacturing process. Figure 9 illustrates the difference in the manufacturing costs between monofacial and bifacial and its different types (Woodhouse et al. 2019). It can be observed that there is a trade-off between the cost and the efficiency. Nevertheless, the energy yield difference is much higher.

Currently, the monofacial technology is dominating the market share; although there is a reduction in the manufacturing process and many efforts to reduce the usage of aluminum, bifacial cells require only 25% of the aluminum needed for the monofacial type (Photovoltaic Equipment International Technology Roadmap for Photovoltaic (ITRPV) 2019 Results 2019). Figure 10 demonstrates the difference in the amounts of aluminum needed to produce monofacial and bifacial cells.

According to the International Technology Roadmap for Photovoltaic (ITRPV), the shift has already begun. Attitudes are shifting in favor of bifacial technology, it is expected that it will lead the market by the end of 2030 by 70% of the

Fig. 9 Modeled costs and minimum sustainable prices for Al-BSF, PERC, PERT, SHJ and IBC cell technologies (Woodhouse et al. 2019)



market share, which gives an indication on how rapid this technology, and its manufacturing processes are developing (Photovoltaic Equipment International Technology Roadmap for Photovoltaic (ITRPV) 2019 Results 2019). Figure 11 illustrates the expected worldwide market share of the two technologies for the next 10 years.

Bifacial solar panels are still under development. Nevertheless, several large-scale projects were implemented in many countries around the world due it is higher power output by 30% and lower LCOE by 2–6% approximately (Gu et al. 2020). Table 3 illustrates many of these projects with their capacity and the manufacturer.

Due to many advantages, there are several applications for these solar panels that put them ahead of monofacial solar panels. Applications such as: being employed into building integrated photovoltaics (BIPV), agrivoltaics, space stations, large-scale power plants and noise barriers. Table 4 provides the pros and cons of this technology compared with monofacial solar panels.

Fig. 10 Amount of aluminum per cell required for monofacial (blue) and bifacial (yellow) PERC (Photovoltaic Equipment International Technology Roadmap for Photovoltaic (ITRPV) 2019 Results 2019)

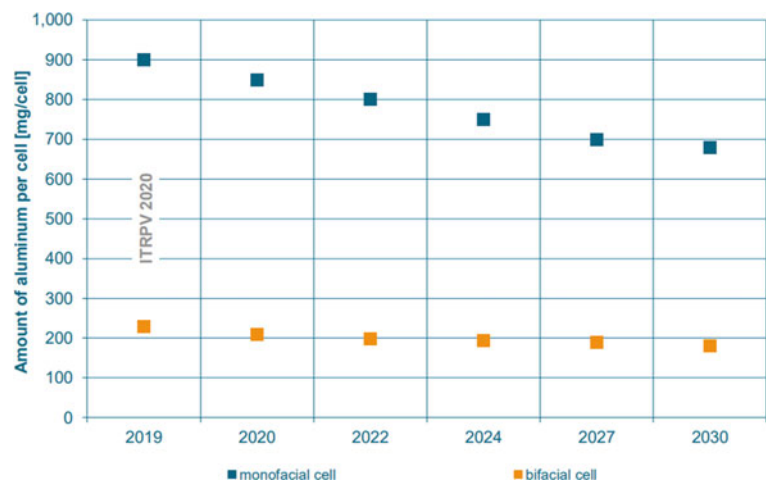
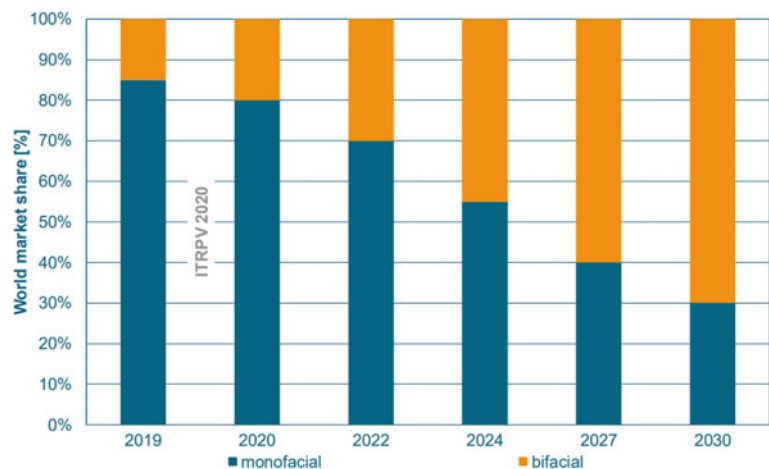


Fig. 11 Worldwide market shares for bifacial technology (Photovoltaic Equipment International Technology Roadmap for Photovoltaic (ITRPV) 2019 Results 2019)



4 Semi-transparent Bifacial

Semi-transparent solar cells are a new type of solar cells that are able to generate electricity from light and visible light transparency. Unlike the conventional solar cells (opaque rear), the back contact acts as a conductive layer instead of a back reflector. Currently, the only commercially available semi-transparent bifacial cells is thin-film silicon technology, and other types such as perovskite and organic transparent cells are still under research and development. The pressing issue with this technology is the need to improve the efficiency while maintaining the targeted transparency (Gao et al. 2017).

Such type of technologies could be used in several applications such as smart energy buildings (architecture), agriculture, automobiles and many other applications, where it can replace regular windows to give an aesthetically pleasing look for buildings, provide passive solar heating, and electricity.

Table 3 Global large-scale bifacial power plants (Greece launches the largest bifacial solar farm in Europe 2022, LONGi and Enel to Build Mexico’s Largest Bifacial Photovoltaic Power Plant 2022, LONGi will supply 224MW of bifacial PERC modules for the largest ‘bifacial + tracking’ project in the United States 2022, Robins Air Force Base Solar 170MW 2022, Taygete I Energy Project 2022, Taygete II Energy Project 2022, Trina Solar ships 600W+ series Vertex modules for a 850 MWp PV project , one of the largest in Brazil 2022)

Year	Country	Installed capacity (MW _p)	Manufacturer
2019	Georgia, USA	224	LONGi solar
2019	Traxscara, Mexico	220	LONGi solar
2021	Taygete I & II, Texas, USA	592	7X energy
2021	Robins air force base in Georgia, USA	170	Georgia power
2022	Kozani, Greece	204	Jinko solar
2022	Juazeiro, Brazil	850	Trina solar

Table 4 Advantages and the disadvantages of bifacial solar cells compared with monofacial

Advantages	Disadvantages
Better performance (higher efficiency)	High installation costs
More durable (UV resistance and prevents moisture permeability)	
Esthetically pleasing	High initial cost
Reduced potential-induced degradation (PID)	
Works well in diffused light	
Lack of aluminum frames	Less flexibility
Longer warranties (up to 30 years)	

In the case of passive solar heating as shown in Fig. 12, the energy during the day is stored in high thermal mass products and items inside the building in order to emit this energy during night to keep the heat inside when it is needed especially for certain types of crops that can’t stand coolness, or during winter for houses and buildings.

For greenhouse applications, certain wavelengths of light are allowed to go through this type of solar cells and are

absorbed by the plants for photosynthesis. Which in return helps in increasing the productivity of the crops. Figure 13 demonstrates a prototype of the combination of semi-transparent cells and greenhouse building.

There are two different types of transparent cells: partially transparent, which has better power output and efficiency but less light transmission; it still enables some sunlight to flow

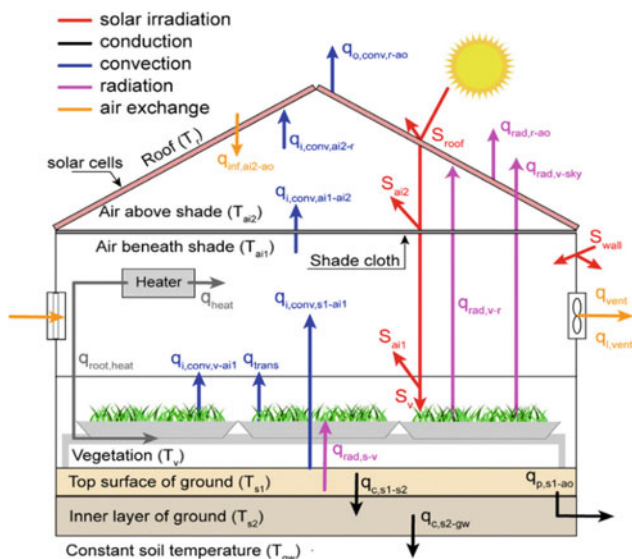


Fig. 12 Schematic diagram of the energy fluxes for OSC greenhouse with shades (Ravishankar et al. 2020)

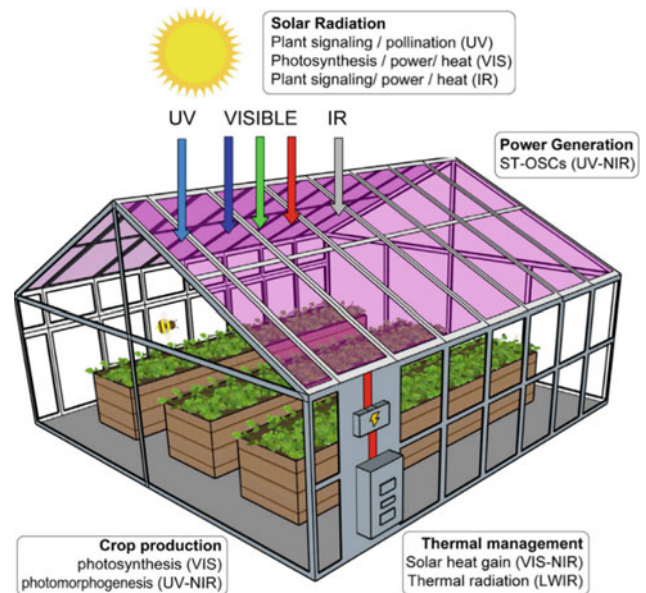


Fig. 13 Depiction of an OSC-integrated greenhouse indicating spectral use of sunlight (Ravishankar et al. 2021)

through the cells. Fully transparent cells, on the other hand, offer a very high level of light transparency but with a very poor efficiency.

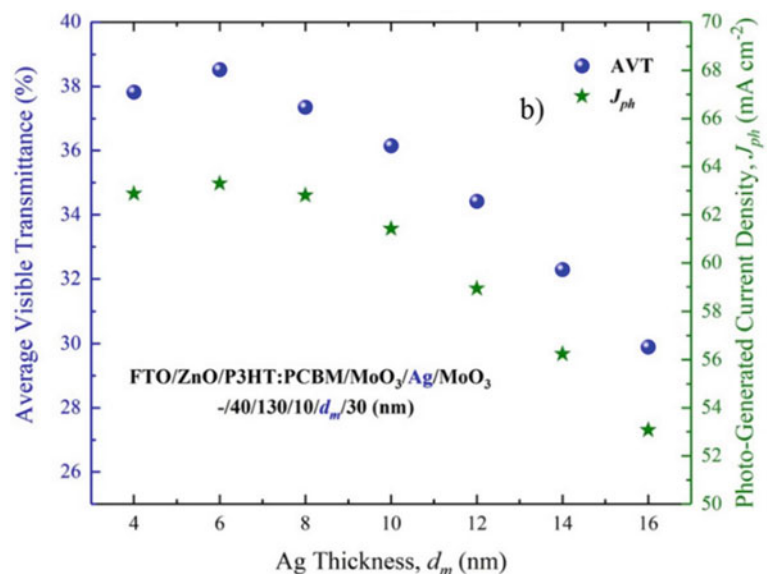
5 Semi-transparent Organic Solar Cells (ST-OSC)

This type of solar cells utilizes organic materials in the active region due to its facile and cheap fabrication process, flexibility and lightness. Recently, organic solar cells (OSC) have achieved efficiencies over 18% (Liu et al. 2020). Semi-transparent OSCs, on the other hand, have reported efficiencies in the range of 8.1 and 10.2%, with an average visible transmittance (AVT) ranging between 23 and 36% (Jiang et al. 2020).

In a recent research, a comparison study between two organic solar cells, the first cell being an opaque organic cell that consists of (FTO/ZnO/P3HT:PCBM/MoO₃/Ag), where Ag is used as a top electrode that has a thickness of 100 nm. The other is a semi-transparent that replaced the opaque Ag with transparent top contact MoO₃/Ag/MoO₃ (dielectric/metal/dielectric), and the inner and outer MoO₃ layers are set to be 10 and 30 nm, respectively (Çetinkaya et al. 2021).

The researchers selected 6 nm as an optimal thickness for the Ag, since it provided the highest current density and average visible transmissivity of 63.30 mA/cm² and 38.52%, respectively, as shown in Fig. 14. The schematic of the semi-transparent organic solar cell in this comparison is illustrated in Fig. 15. The reflectance and absorption in the visible light region increase as the thickness of the Ag layer increases up to 16 nm.

Fig. 14 Variation of the AVT and J_{ph} with respect to the Ag layer thickness for the ST-OSC (Çetinkaya et al. 2021)



From the obtained results it can be observed that there is a slight reduction in the efficiency of the semi-transparent cell (12.5%), but this could be negligible in the case of windows and greenhouses applications.

6 Semi-transparent Perovskite Solar Cells (ST-PSC)

Third-generation solar cells are the most recently developed cells, and only within 11 years the efficiencies were raised significantly, especially for perovskite cells. Perovskite solar cells started with only 3.9% in 2009 and improved up to 25.5% by 2020 (Best Research-Cell Efficiency Chart 2022). Therefore, there is a potential that perovskite semi-transparent cells could achieve high efficiencies with good transmissivity. Currently, the average achieved visible transparency is between 20 and 30% with a power conversion efficiency (PCE) of 8 to 12% (Zhao et al. 2017).

Similar to the ST-OSC, the Ag (opaque layer) of a perovskite cell was replaced with softly deposited MoO₃/Ag/WO₃ (MAW) and MoO₃/Ag/MoO₃ (MAM), Ag thickness was selected to be 12 nm, and then both cells were tested and compared with traditional perovskite cell with Ag as a rear electrode (Liang et al. 2020). The structure of the semi-transparent used in this study is shown in Fig. 16.

Conventional TCOs can are not recommended as rear transparent electrodes due to the high amount of energy and temperature associated with the deposition process. These high temperatures will certainly damage the perovskite and transport layers (Fu 2015).

Fig. 15 Structure of FTO/ZnO/P3HT:PCBM/MoO₃/Ag/MoO₃ (-/40/130/10/6/30 nm) ST-OSC (Çetinkaya et al. 2021)

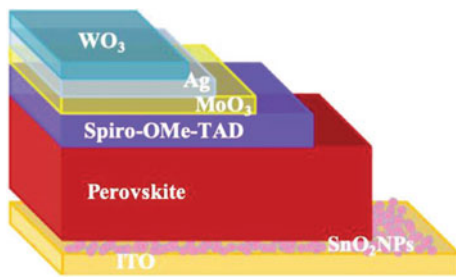
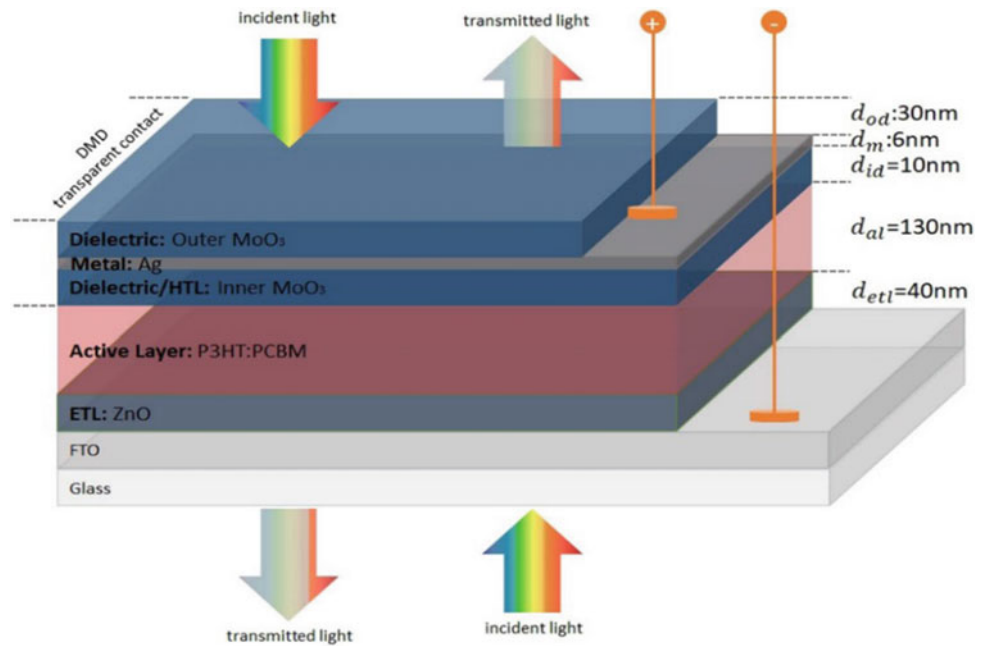


Fig. 16 Structure of (ITO/SnO₂NP_s/perovskite/Spiro-OMe-TAD/MoO₃/Ag/WO₃) ST-PSC (Liang et al. 2020)

The obtained results for the tested cells are illustrated in Table 5. It can be observed that there is a potential to get higher efficiencies from ST-PSC, but this wouldn't occur without a loss in the AVT.

The transmissivity of both MAW and MAM PSC with wavelengths in the range between 400 and 1200 nm was 21.56 and 17.63%, respectively. The AVT of these cells was found to be 10.17 and 6.11%, which is much lower than the ST-OSC, but with huge increase in terms the PCE.

Several researchers studied different rear transparent electrodes for perovskite cells. In Table 6, different works

Table 5 Performance of PSCs with various electrodes (Liang et al. 2020)

Cell	J_{sc} [mA cm ⁻²]	V_{oc} [V]	FF (%)	Power conversion efficiency (%)
ITO-MAW	22.8	1.03	66.0	15.4
ITO-MAM	21.5	1.06	62.4	14.22
Opaque cell	23.7	1.02	71.6	17.3

Table 6 Performance for recent PSCs based on different rear transparent electrodes (Giuliano et al. 2019; Kim et al. 2016; Kim and Tatsuma 2017; Lee et al. 2021; Ying et al. 2019; Zhao et al. 2017)

Rear transparent electrode	AVT (%)	PCE (%)
Bep/Ag/MoO ₃	17.80	9.73
MoO ₃ /Au/ MoO ₃	14.98	13.13
MoO ₃ /Ag/ZnS	7.42	13.30
ZrAcac/PEI/Ag/Ta ₂ O ₅	12.47	13.40
SnO _x /Ag/SnO _x	17.00	11.20
MoO ₃ /Au/Cu/MoO ₃	5.00	12.50

are shown with different results in terms of transmissivity of the layer and the PCE.

7 Agrivoltaic Applications: Large-scale Projects in Arid Areas

PVs offer an efficient way of harnessing solar energy than the natural photosynthetic processes. Additionally, establishing PVs in open areas reduces the installation costs. However, the use of land areas for large-scale PV modules has raised concerns associated with the loss of agricultural lands to increase the profits out of power production from PVs (Weselek et al. 2019). The International Energy Agency (IEA) estimated that in 2050, 16% (6000 TWh) of the global power will be generated from PV, to fulfill societies' requirements. To supply the total demand of PVs, large surface areas are required due to the diffusion of solar energy. Due to the increasing number of people living in densely populated areas and mountainous regions, the land competition in these regions has become more intense (Dinesh and Pearce 2021). Agrivoltaic systems, also known as agrophotovoltaics, serve as a way for the development of PV without affecting food production; in fact, these systems have shown to benefit land productivity. Goetzberger and Zastrow were the first to introduce this technology a few decades ago. They proposed increasing the solar collectors' heights to 2 m above the ground to minimize the effects of excessive shading and noted that the current generation of these systems only requires about a third of the radiation coming from the sun. The technology has already been implemented in commercial and small-scale projects. According to calculations, the implementation of this approach could raise farms' profits by up to 30% (Weselek et al. 2019). Figure 17 shows a timeline for the implementation of agrivoltaics between 2010 and 2021 (Trommsdorff 2021). In 2011, Dupraz and colleagues used the land equivalent ratio to evaluate the productivity of intercropping systems using a dual-use agrivoltaic system. Their simulations showed that the system can increase the overall land productivity by about 70% (Weselek et al. 2019).

Agrivoltaics are even more attractive for deployment in semi-arid and arid areas that suffer from extreme solar

radiation that affects crop production and leads to water losses. Due to efficient water use for irrigation and PV cleaning, high crop yield with reducing solar radiation by solar panels, less soil evaporation and high power generation that adds to the profits of farming, agrivoltaics is the best choice to increase food production with simultaneous electricity production (Mamun et al. 2022; Weselek et al. 2019).

8 Agrivoltaic Case Studies

8.1 India

The Indian economy is considered to be supported by the agricultural sector. According to the most recent study, which was performed in 2011, 70% of the residents were employed in agriculture. According to a survey carried out by the nation's Labor Bureau in 2015–2016, almost 47% of the workforce was engaged in jobs pertaining to agriculture. About 18% of the nation's greenhouse gas (GHG) emissions are attributable to the country's extensive agricultural industry and its Gross Domestic Product (GDP) contribution. The use of antiquated and undependable farming methods is the main cause of this. Furthermore, overuse of government-funded fertilizers led to the destruction of farms. The IPCC Report from 2019 states that land degradation increases GHG emissions and decreases carbon capture rate, which in turn accelerates climate change. Therefore, for India to attain a greater development rate and give its expanding population a place to work, self-sustaining and growth-driven agriculture is crucial (Mahto et al. 2021).

Numerous studies on solar energy and Indian agriculture have previously been published, providing a variety of uses for the technology that can generate Climate Smart Agriculture (CSA). An irrigation system powered by solar energy for sustainable agriculture in India was investigated by the authors of Chel and Kaushik (2011); Kanna et al. 2020). A plant for crop and grain drying driven by solar energy was also planned for Rajasthan. The same study highlighted the use of solar energy for air and water heating. Additionally, in the rural parts of the Kaudikasa village in India, drinkable water was obtained, and sewage was treated using a solar-powered system. These examples show how solar

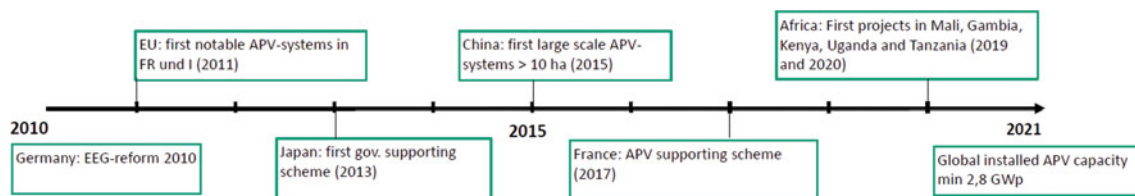


Fig. 17 Timeline for the implementation of agrivoltaics between 2010 and 2021 (Trommsdorff 2021)

panels can be used to support and improve agriculture activities in India (Mahto et al. 2021).

The solar radiation reaching India is enough to generate 500,000 TWh annually. Approximately 10% of the power production is taken into consideration when calculating production. The development of solar manufacturing techniques and enhancements to the maximum power point tracker will inevitably result in a rise in energy production. Figure 18 displays the predicted potential of solar energy for India as a whole according to the National Institute of Solar Energy (NISE) (Mahto et al. 2021).

Agrivoltaics, according to Worringham, might speed up India's implementation of renewable energy by dispersing it throughout the nation. He points out that studies conducted in other countries have revealed that some crops can withstand light shadowing and that, in times of intense heat, some may even profit from reduced temperatures and better soil moisture. He adds that India has already begun to identify the specific techniques, crops and conditions that work best with nearly 20 projects utilizing a variety of panel structures under way. Various policy barriers must be resolved if the agrivoltaics industry is to realize its full potential (Gupta 2021). Jain Irrigation Systems Limited (JISL) and Abellon Energy are both recognized as the originators of agrivoltaics in India. With the first pilots commencing in 2012 and crops being cultivated also underneath the solar structures, JISL has given agriculture

greater importance. Table 7 shows the applied agrivoltaic pilot projects in India (Pulipaka and Peparthy 2021).

8.2 Africa

The International Renewable Energy Agency (IRENA) estimates that by 2040, the potential for renewable energy in Africa will be 1,000 times more than its anticipated electricity demand. By then, renewable energy in Southern and Eastern Africa could increase from a fifth in 2016 to 63%. Figure 19 shows the potential for solar energy to meet the demand in Africa (Edmond 2022).

In East Africa, the distribution of electricity is not equitable, with about twice many more urban than rural towns receiving electricity, despite the fact that these latter areas are generally distant geographically. Owing to the absence of electricity, the majority of rural homes must use biomass for heating and cooking which has negative effects on human health, forest degradation and climate change (Randle-Boggis et al. 2021).

The agriculture industry contributes between 24 and 44 percent of the GDP in East African countries, supporting the income of 80 percent of the population. More than 100,000 people are now employed in sub-Saharan Africa's solar energy sector, which is developing to address electricity concerns. However, this growth calls for creative business approaches to penetrate emerging markets. Specifically in rural areas without current new infrastructure, agrivoltaics will also create new, specialized job opportunities for agrivoltaic manufacturing, application and maintenance. These jobs will increase wages and improve food security while addressing rural unemployment (Randle-Boggis et al. 2021).

Recently, a collaboration between the Universities of Sheffield, York and Teesside in the UK, the Stockholm Environment Institute, World Agroforestry, the Centre for Research in Energy and Energy Conservation and the African Centre for Technology Studies has led to the launch of the first agrivoltaic system in East Africa in Insinya, Kenya, at the beginning of 2022 (Best Research-Cell Efficiency Chart 2022).

Adoption of agrivoltaics in Mali might be quite advantageous. Owing to its geographical location, Mali has among the highest amounts of yearly radiation in Africa, with an average of 2,200 kWh/m² annually (Cheo et al. 2022).

For rural communities in Mali and Gambia, arable land is becoming increasingly scarce which will pose serious issues related to climate change. APV-MaGa is a research and development (R&D) project that intends to create agrophotovoltaic systems that offer local residents with food, water and electricity while boosting the agriculture sector's tolerance to climate change. It is established to ensure that the communities' crop yields are profitable and that the

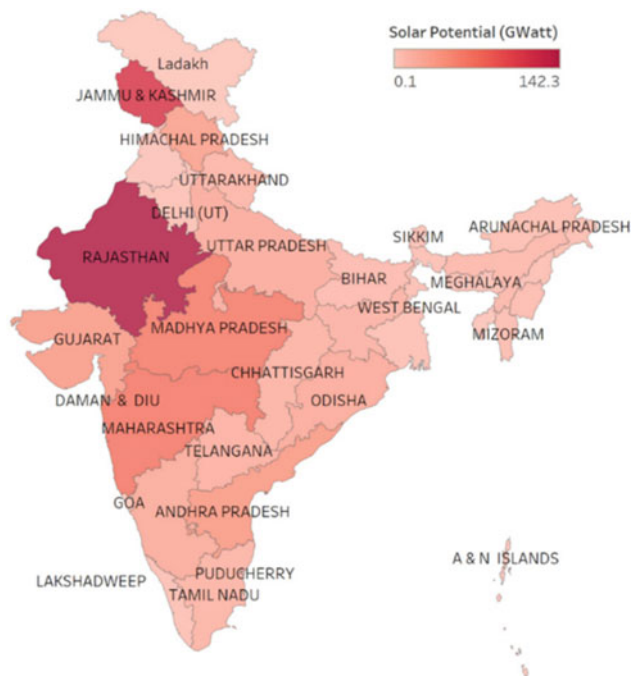


Fig. 18 Potential for producing power in India, according to the National Institute of Solar Energy (NISE) (Mahto et al. 2021)

Table 7 Applied agrivoltaic pilot projects in India (Pulipaka and Peparthy 2021)

Project	Year of commission	Capacity (kWp)	Location	Project type
Amrol distributed solar power	2016	1000	Gujarat, Amrol	Commercial
1 MW GSECL STPS solar	2016	1054	Gujarat, Sikka	Commercial
1 MW Agri base solar power plant	2016	1054	Panandhro	Commercial
N/A	2017	105	Rajasthan, Jodhpur	Research
N/A	2017	10	Noida	Research
N/A	2020	200	Agra	Research
N/A	2017	7.2	Gujarat, Junagadh	Research
Solar-agri electric model	2012	3000 (~ 1000 kWp with agriculture)	Modasa Taluka	Commercial
Clean solar private limited	2016	36.6 MW (~ 400 kW with agrivoltaics)	Gingurthy Village	Commercial/partially research
AgroPV model plants by Jain irrigation	2014	14.4 (banana pilot), 9.6 (rice pilot) and 50.4 (cotton pilot)	Jalgaon	Research
N/A	N/A	100	Haryana, near Gurgaon	Research
Cochin international airport limited (CIAL)	2015	12,000 (partially with agriculture) Total in 2020: more than 26,000	Kerala	Commercial
Krishi vigyan kendra ujwa solar farm	2021	110	Delhi	Research
Residential agri-PV rooftop	2019	3	Delhi	Commercial

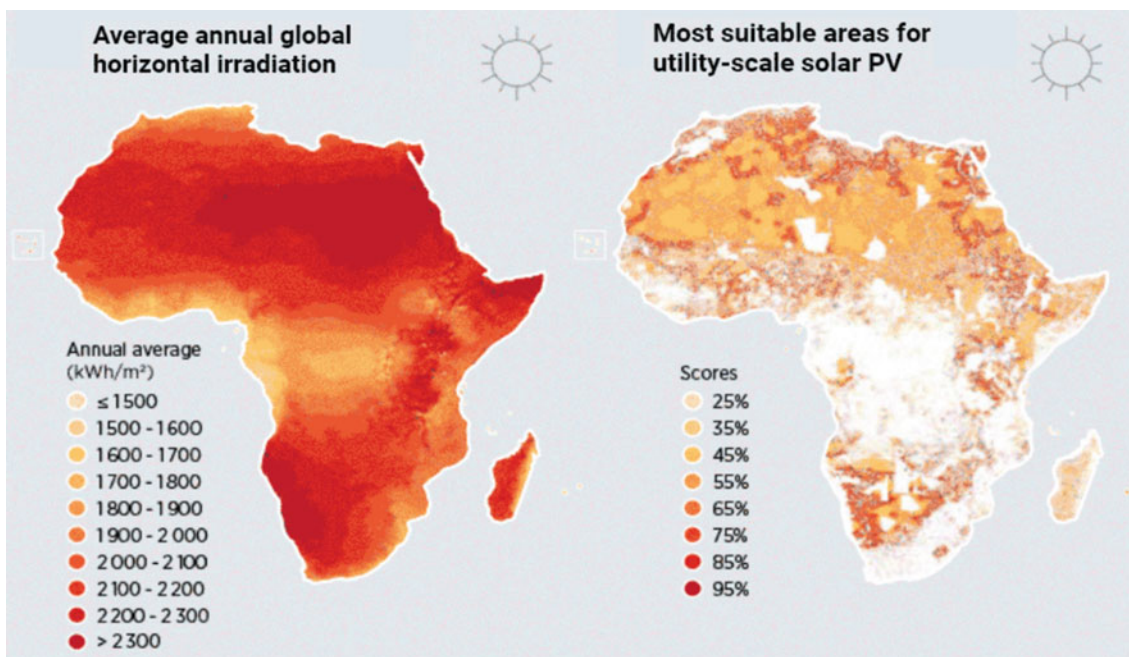
**Fig. 19** Solar energy potential in Africa (Edmond 2022)

Fig. 20 Location of University of Djilali Bounaama in North Algeria (Trommsdorff 2021)



electricity produced is used as efficiently as possible. The project is expected to end in 2023 (United Nations University 2022).

Many agricultural crops grown under agrivoltaics are predicted to increase yields in dry, hot and sunny climate regions like Mali because the partial shading prevents extreme solar radiation, heat and extreme weather conditions from affecting them and benefits the quality of the crop. Rainwater might also be collected directly from the PV panels for irrigation or other uses in farming (Cheo et al. 2022).

In Algeria, WATERMED4.0 project was installed in April 2021 through partnership with European research centers and agencies for the purposes of employing new irrigation techniques to conserve nutrients and water. It is located in the University of Djilali Bounaama in North Algeria as shown in Fig. 20 for conducting experiments by the research laboratory of agricultural production and sustainable development. The pilot project aims at increasing the productivity of crops by 25% (Trommsdorff 2021).

8.3 Agrivoltaics Projects in Europe

In Europe, several enormous agrivoltaics projects were implemented in many countries: Spain, Greece, France, Germany and Netherlands. BayWa is a German company that has undertaken several agrivoltaics projects across Germany and Netherlands, focusing on different types of crops such as wheat, blackberries, strawberries, blueberries, red currants, raspberries, celery and potato.

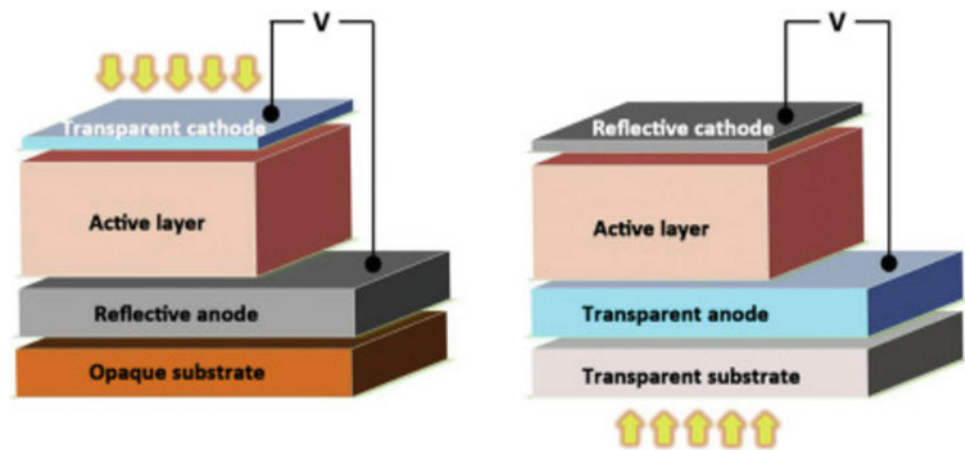
BayWa has built one of the largest agrivoltaics plants across Europe in Babberich and other four test projects across the Netherlands. The project's size was expanded last year to 2.7 MW_p in capacity to cover up to 3.2 hectares using 10,250 solar panels that deliver power to nearly 1250 households (Benefits of Agrivoltaics and 5 real-life examples of successful implementations 2022).

They proved that during hot days, the temperature beneath the solar panels was lower by two to five degrees. This leads to a huge reduction in the evaporation rates, which in return reduces water demand. In addition, during night, the heat got retained better than plastic covering that is used to protect the crops from the cold, in turn decreasing the utilization of plastic in farms (Benefits of Agrivoltaics and 5 real-life examples of successful implementations 2022).

Endesa & Enel are planning to implement the Carmona solar plant project in Spain, with a capacity of 100 MW_p covering up to 100 hectares to be combined with 3 hectares of aromatic plants: sage, rosemary, oregano and coriander in addition to beekeeping. They say that beekeeping helps in improving the productivity of the crops by increasing the degree of pollination (Benefits of Agrivoltaics and 5 real-life examples of successful implementations 2022; The place where bees, crops and photovoltaic panels coexist 2022).

Sun'Agri has installed 84 kW_p in the wine-growing area in Piolenc, France, to test the performance of the agrivoltaics where over 600 m², and 280 solar panels were used at 4.2 height (Benefits of Agrivoltaics and 5 real-life examples of successful implementations 2022; Viticulture results–Sun' Agri 2022). This combination provided several benefits:

Fig. 21 Architecture of a flexible solar cell with two electrodes and an active layer (Elsevier, Open Access) (Li et al. 2021)



limiting excess solar radiation and high heat, reducing water demand by 12 to 34%, improving water comfort while limiting irrigation, pooling additional protection solutions and leading to a better aromatic balance of the wine produced (Viticulture results–Sun’ Agri 2022).

Enel implemented many projects around Greece (Pezoulitika, Polysitos I and Polysitos II, Pezoulitika, Herodasos and Sounio), these power plants were not designed for the purpose of agrivoltaics specifically, but Enel utilized sheep to guarantee that plants don’t intervene with the operation of the solar panels. In addition, with the help of the sheep, the vegetation was kept under control and prevented the spread of fire by providing a natural firebreak. Also, it saves the needed fuel to use mechanical machines for cutting (Benefits of Agrivoltaics and 5 real–life examples of successful implementations 2022).

9 Flexible Solar Cells

Manufacturing flexible solar cells presents an expansion to the conventional applications of photovoltaics. Flexible solar cells can be applied in buildings, vehicles, garments and many more applications. Thin-film solar cells are characterized by their lightweight and flexibility, especially when compared to classical crystalline silicon first-generation solar cells (Zhang et al. 2022). Thin-film solar cells are effortlessly folded into different forms and dimensions based on the required application. These flexible thin-film solar cells present novel energy generation solutions for various outdoor and indoor applications in which weight resilience is essential. Thus, flexible thin-film solar cells can be manufactured on opaque or transparent substrates. Generally, manufacturing flexible photovoltaics is similar to that of the thin-film second-generation solar cells. Thin-film solar cells are constructed through the deposition of several functional layers above a flexible substrate by utilizing methods

including spin coating, printing and vacuum deposition. The flexible substrate offers substantial mechanical support and an overall environmental shield of the solar cell. Figure 21 illustrates the different materials employed to construct a flexible thin-film solar cell; the figure on the right represents the solar cell structured on a transparent substrate; and the figure on the left shows the structure of solar cell on an opaque substrate. To construct a flexible solar cell, two electrodes are integrated to obtain photoelectric charge carriers. In order to for the semiconductor layer to absorb light, one of the electrodes needs to be transparent, and once light is absorbed it is converted to energy through the photovoltaic effect. The main element of flexible solar cells is the active material which plays an essential role in the power conversion efficiency, where this material can either be inorganic, organic or an inorganic–organic semiconductor. Examples of inorganic semiconductors include cadmium telluride, amorphous silicon and copper indium gallium diselenide. Amorphous silicon is primary applicant of flexible photovoltaics owing to their flexible manufacturing processes. Organic semiconductors are classified based on the molecule size, and they contain donor and acceptor compounds. Metal halide perovskite is among the popular types of hybrid semiconductors employed in flexible solar cells. Figure 22 reveals the efficiency of the most recent flexible solar cells along with their materials. Due to the recent swift advancements in material systems, the commercialization of flexible solar cells in many products is anticipated (Li et al. 2021).

9.1 Substrate Types for Flexible Solar Cells

Flexible substrates are of great importance for developing flexible photovoltaics. Substrates are an essential part of the electrode that have great effects on the electrode itself and the overall solar cell performance (Zhang et al. 2022).

Fig. 22 Documented records of the reported efficiencies of different active layers applied in flexible solar cells (Elsevier, Open Access) (Li et al. 2021)

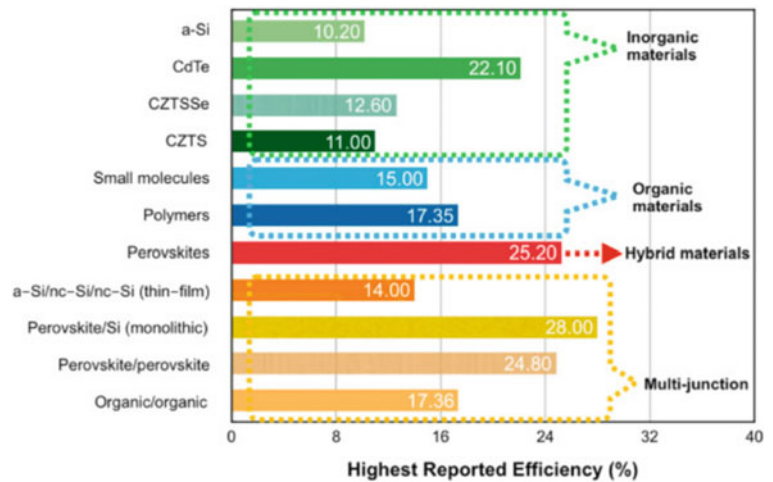


Fig. 23 Depiction of the most utilized substrate material for flexible solar cells organized in a chronological order (Elsevier, Open Access) (Li et al. 2021)

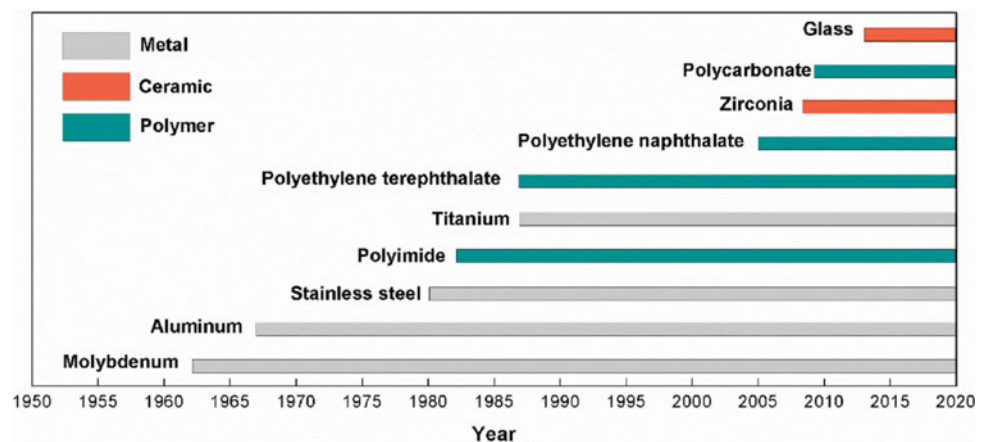


Figure 23 demonstrates the most commonly used flexible substrates classified based on the utilized material. Metal, ceramic and plastic materials are common substrates for flexible cells (Li et al. 2021).

9.2 Metal Substrates

Thin metals that are less than 125 μm foils that can be utilized as flexible substrates for creating flexible solar cells (Wong and Salleo 2009). The high flexibility of the metal substrate is a result of the metal's high ductility. Metal substrates have high thermal stability and chemical erosion resistance (Zhang et al. 2020). Stainless steel metals are the most popular type of metal substrates as they are both cost-effective and have great chemical and thermal stability (Williams et al. 1980). Other than stainless steel metals, aluminum alloy metals and titanium metals have been presented as flexible electrodes for fabrication of flexible solar cells. Titanium metals have been utilized precisely for the fabrication of perovskite solar cells (Kim et al. 2015; Xiao

et al. 2016). Titanium metal substrates in perovskite solar cells allow for to attainment of a PCE of around 13.07% (Wang et al. 2015). Despite these advantages, the high costs of titanium metal substrates limited their wide commercialization. Metal foils in general are associated with high optical reflectance of the visible light spectrum, while the solar cell's top electrode must be optically transparent to allow the transmittance of light to the active materials (Yun 2017).

9.3 Ceramic Substrates

Ceramic substrates are usually made from glass, and they have high thermal stability and chemical erosion resistance. Unlike metal foils, glass does not possess high ductility, and this in return adversely impacts the flexibility resulting in a smaller bending radius (Wong and Salleo 2009). To compensate for their low ductility, the thickness of glass should be thinner than 100 μm to exhibit high flexibility. A perovskite solar cell fabricated on a glass substrate has a power conversion efficiency of 18.1% (Dou et al. 2017). Other than

glass substrates, zirconia ribbon ceramics can also be utilized as flexible substrates for solar cells (Ishizuka et al. 2010).

9.4 Plastic Substrates

Plastics or polymers are cost-effective and lightweight materials that are widely utilized as flexible substrates for flexible solar cells. The most popular types of plastic substrates are polyethylene naphthalate (PEN) and polyethylene terephthalate (PET) because of their high transparency, mechanical robustness, cost-effectiveness and lightweight (Zardetto et al. 2011). It was recently shown that PEN substrates in perovskite solar cells produce a power conversion efficiency up to 19.1% (Yoon et al. 2016). On the other hand, plastic substrates have low thermal stability, lower than 250°C, even though the fabrication processes of solar cells are associated with high temperatures (Zardetto et al. 2011). However, colorless polyimide (cPI) substrates have high thermal stability and resistance and light transmittance (Yi et al. 2020). Moreover, due to the low density of plastic substrates, they have high oxygen and water permeability (Jung et al. 2019). These negative consequences of plastic substrates adversely affect the lifespan of the solar cell (Yi et al. 2020). Nevertheless, this issue can be solved by coating the barrier of the layers of the plastic substrates (Li et al. 2020).

9.5 Electrode Materials for Flexible Solar Cells

After selecting the substrate, the rest of the electrode will be developed on the selected substrate. A flexible solar cell comprises a conducting electrode, an active material and a reflective electrode. Transparent solar cells are made up of only transparent electrodes.

9.5.1 Thin-film Metals

Thick metal layers made up of Al, Mg or Ag with thicknesses higher than 100 nm and high electrical conductivity have been employed as the reflecting electrodes in solar cells. However, when the metal's thickness is thinned down to thinner than 20 nm, the metal film becomes semi-transparent (Wang et al. 2013). Much research has been conducted to enhance the performance, transparency and conductivity of these ultrathin films (Chen et al. 2012).

Metal grids are made up of thin metal lines ($\sim 1 \mu\text{m}$) which act as the front contacts in inorganic solar cells (Yu et al. 2013). Metal meshes are thin-film electrodes comprised of networked structured metal lines. Metal meshes or grids possess defined and organized geometry forms that can be accurately controlled via the fabrication process. Metal meshes can be created by photolithography, nanoimprint

lithography, thermal evaporation, electroplating, inkjet printing and spin coating.

9.5.2 Transparent Conducting Oxide

TCO is the most common material for flexible solar cells electrodes. Tin-doped indium oxide (ITO) is the most utilized electrode material for solar cells (Xue and Forrest 2004). Several studies have been facilitated to alter the surfaces of ITO via UV ozone, and chemical and oxygen plasma (Li et al. 2005). There are several factors that inhibit the popularity of the ITO electrode (Sandström et al. 2012). These factors include the restricted global supply of indium and the high utilization of ITO (Gupta et al. 2013). However, new alternatives for ITO have been found, such as ZnO-based compounds (Liu et al. 2013; Park et al. 2011).

9.5.3 Metal Nanowires

Various structures of metal nanowires including gold, silver, copper and nickel have been presented as transparent electrodes for flexible solar cells. Until recently, silver nanowires are the most popular metal nanowire because of its positive optoelectronic characteristics and its low costs. Moreover, silver nanowires possess high thermal resistance and significantly high aspect ratio that is much higher than 10,000 (Huo et al. 2008). Copper nanowires are associated with lower costs than silver nanowires; however, they bear low thermal stability and resistance (Bobinger et al. 2017). The synthesis process of metal nanowires is facilitated in a wet-chemical solution process. For instance, the polyol process is the most widely utilized synthesis process of metal nanowires (Chen et al. 2006). While for copper nanowires, the hydrothermal process is preferable to carry out the metal synthesis.

The aspect ratio of metal nanowires, which represents the length to diameter ratio of the nanowire, has displayed positive impact on the conductivity and transparency of the nanowire (Kim and Tatsuma 2017; Lee et al. 2021). Metal nanowires come in various sizes with different dimensions. For example, the average length of a silver nanowire is between 0.5 and 220 μm , and the average diameter is between 13 and 150 nm (Sannicolo et al. 2016). Due to the small diameter of metal nanowires, the electrodes' chemical, thermal and electrical stability is negatively impacted (Lu et al. 2015). To overcome this challenge, it is necessary to integrate these metallic nanowires with other nanomaterials including conductive polymers, polystyrene sulfonate, metal oxides, graphene, carbon nanotubes, graphene oxide and metals. This integration presents several other improvements in the performance of the electrode (Kim et al. 2020).

9.5.4 Nanocarbons

Carbon nanotubes and graphene have received the attention of many researchers over the years because of their enhanced

electrical, optical and mechanical characteristics. Hence, these novel carbon materials can be applied as flexible electrodes in flexible solar cells (Zhang et al. 2005). Carbon nanotubes are classified based on their structure either into single-wall nanotubes or into multi-wall nanotubes based on the number of layers. Both of these categories have been integrated in optoelectronics posing as transparent electrodes. Single-wall nanotubes are much more transparent and conductive than multi-wall nanotubes due to the variances in the optical transmittance based on identical current density (Biris et al. 2008). Consequently, single-wall nanotubes are more preferable as electrodes for substituting the ITO transparent electrodes. Graphene produces high conductivity and utilizes organic polymers and metal oxides for altering its interface. Single-wall nanotubes and graphene electrodes can be synthesized and deposited by the means of chemical vapor deposition techniques (de Arco et al. 2010).

9.5.5 Conducting Polymers

Conducting polymers such as PEDOT:PSS are presented as an interlayer in organic optoelectronics. The presence of such polymers aids in smoothing the surfaces roughness of conductive layer and improving the hole interactions rates between the transport material and the hole (Po et al. 2011). PEDOT:PSS polymer electrodes are widely known for their cost-effectiveness and their enhanced optical characteristics. Polymer electrodes are associated with low electrical conductivities; however, these electrical conductivities can be enhanced through chemical doping (Hsiao et al. 2009). Additionally, high boiling point temperature solvents can improve the electrical conductivity of polymers (Nickel et al. 2010).

References

- Agrophotovoltaics for Mali and The Gambia: Sustainable Electricity Production by Integrated Food, Energy and Water Systems (APV-MaGa). In: United Nations University. Retrieved from <https://unu.edu/projects/agrophotovoltaics-for-mali-and-the-gambia-sustainable-electricity-production-by-integrated-food-energy-and-water-systems-apv-maga.html#outline>. Accessed on 11 Jul 2022
- Afroz MA et al (2020) Thermal stability and performance enhancement of perovskite solar cells through oxalic acid-induced perovskite formation. *ACS Appl Energy Mater* 3(3):2432–2439. <https://doi.org/10.1021/acsaem.9B02111>
- Akhil S et al (2021) Review on perovskite silicon tandem solar cells: status and prospects 2T, 3T and 4T for real world conditions. *Mater Des* 211:110138. <https://doi.org/10.1016/j.matdes.2021.110138>
- Al-Ashouri A et al (2020) Monolithic perovskite/silicon tandem solar cell with >29% efficiency by enhanced hole extraction. *Science* 370(6522):1300–1309. <https://doi.org/10.1126/science.abd4016>
- Babayigit A, Ethirajan A, Muller M, Conings B (2016) Toxicity of organometal halide perovskite solar cells. *Nat Mater* 15(3):247–251. <https://doi.org/10.1038/nmat4572>
- Balasundaraprabhu R, Monakhov EV, Muthukumarasamy N, Nilsen O, Svensson BG (2009) Effect of heat treatment on ITO film properties and ITO/p-Si interface. *Mater Chem Phys* 114(1):425–429. <https://doi.org/10.1016/j.matchemphys.2008.09.053>
- Benefits of Agrivoltaics and 5 real-life examples of successful implementations. In: RatedPower. Retrieved from <https://ratedpower.com/blog/benefits-agrivoltaics-examples/>. Accessed on 28 Jul 2022
- Best Research-Cell Efficiency Chart. In: Photovoltaic Research: NREL. Retrieved from <https://www.nrel.gov/pv/cell-efficiency.html>. Accessed on 28 Jul 2022
- Bifacial solar cells. In: Wikipedia. Retrieved from https://en.wikipedia.org/wiki/Bifacial_solar_cells. Accessed on 7 Aug 2022
- Biris AR et al (2008) High-quality double-walled carbon nanotubes grown by a cold-walled radio frequency chemical vapor deposition process. *Chem Mater* 20(10):3466–3472
- Bobinger M, Mock J, La Torraca P, Becherer M, Lugli P, Larcher L (2017) Tailoring the aqueous synthesis and deposition of copper nanowires for transparent electrodes and heaters. *Adv Mater Interfaces* 4(20):1700568
- Çetinkaya Ç et al (2021) Design and fabrication of a semi-transparent solar cell considering the effect of the layer thickness of MoO₃/Ag/MoO₃ transparent top contact on optical and electrical properties. *Sci Rep* 11:13079. <https://doi.org/10.1038/s41598-021-92539-8>
- Chel A, Kaushik G (2011) Renewable energy for sustainable agriculture. *Agron Sustain Dev* 31:91–118. <https://doi.org/10.1051/agro/2010029>
- Chen C et al (2006) Study on the synthesis of silver nanowires with adjustable diameters through the polyol process. *Nanotechnology* 17(15):3933
- Chen K-S, Salinas J-F, Yip H-L, Huo L, Hou J, Jen AK-Y (2012) Semi-transparent polymer solar cells with 6% PCE, 25% average visible transmittance and a color rendering index close to 100 for power generating window applications. *Energy Environ Sci* 5(11):9551–9557
- Chen B et al (2020) Blade-coated perovskites on textured silicon for 26%-efficient monolithic perovskite/silicon tandem solar cells. *Joule* 4(4):850–864. <https://doi.org/10.1016/j.joule.2020.01.008>
- Chen B, Fei C, Chen S, Gu H, Xiao X, Huang J (2021) Recycling lead and transparent conductors from perovskite solar modules. *Nat Commun* 12:5859. <https://doi.org/10.1038/s41467-021-26121-1>
- Cheo AE, Adelhardt N, Krieger T, et al (2022) Agrivoltaics across the water-energy-food-nexus in Africa: opportunities and challenges for rural communities in Mali. Discussion Paper Series, University of Freiburg, Wilfried Guth Endowed Chair for Constitutional Political Economy and Competition Policy
- Deline C, Peláez AS, Marion WF, Sekulic WR, Woodhouse MA, Stein J (2019) Bifacial PV system performance: separating fact from fiction.
- Deng Y, van Brackle CH, Dai X, Zhao J, Chen B, Huang J (2019) Tailoring solvent coordination for high-speed, room-temperature blading of perovskite photovoltaic films. *SciAdv* 5(12):1–8. <https://doi.org/10.1126/sciadv.aax7537>
- Dinesh H, Pearce JM (2021) The potential of agrivoltaic systems. *Renew Sustain Energy Rev* 54:299–308. <https://doi.org/10.1016/j.rser.2015.10.024>
- Dou B et al (2017) High-performance flexible perovskite solar cells on ultrathin glass: implications of the TCO. *J Phys Chem Lett* 8(19):4960–4966
- Dullweber T, Schmidt J (2016) Industrial silicon solar cells applying the passivated emitter and rear cell (PERC) concept—A Review. *IEEE J Photovoltaics* 6(5):1366–1381. <https://doi.org/10.1109/JPHOTOV.2016.2571627>

- Edmond C (2022) Combining crops and solar panels is allowing Kenya to 'harvest the sun twice'. In: World Economic Forum. Retrieved from <https://www.weforum.org/agenda/2022/03/solar-energy-security-farm-africa/>. Accessed 11 Jul 2022
- Eperon GE, Stranks SD, Menelaou C, Johnston MB, Herz LM, Snaith HJ (2014) Formamidinium lead trihalide: a broadly tunable perovskite for efficient planar heterojunction solar cells. *Energy Environ Sci* 7(3):982–988. <https://doi.org/10.1039/C3EE43822H>
- Fu F et al (2015) Low-temperature-processed efficient semi-transparent planar perovskite solar cells for bifacial and tandem applications. *Nat Commun* 6:8932. <https://doi.org/10.1038/ncomms9932>
- Gao Y et al (2017) Performance optimization of semi-transparent thin-film amorphous silicon solar cells. In: 2017 IEEE 44th photovoltaic specialist conference (PVSC). IEEE, pp 2605–2609. <https://doi.org/10.1109/PVSC.2017.8366241>
- Giuliano G et al (2019) Nonprecious copper-based transparent top electrode via seed layer-assisted thermal evaporation for high-performance semitransparent n-i-p perovskite solar cells. *Adv Mater Technol* 4(5):1800688. <https://doi.org/10.1002/ADMT.201800688>
- Gomez De Arco L, Zhang Y, Schlenker CW, Ryu K, Thompson ME, Zhou C (2010) Continuous, highly flexible, and transparent graphene films by chemical vapor deposition for organic photovoltaics. *ACS Nano* 4(5):2865–2873
- Greece launches the largest bifacial solar farm in Europe. In: Electrek. Retrieved from <https://electrek.co/2022/04/08/greece-launches-the-largest-bifacial-solar-farm-in-europe/>. Accessed on 28 Jul 2022
- Gu W, Ma T, Ahmed S, Zhang Y, Peng J (2020) A comprehensive review and outlook of bifacial photovoltaic (bPV) technology. *Energy Convers Manage* 223:113283. <https://doi.org/10.1016/j.enconman.2020.113283>
- Gupta D, Wienk MM, Janssen RAJ (2013) Efficient polymer solar cells on opaque substrates with a laminated PEDOT: PSS top electrode. *Adv Energy Mater* 3(6):782–787
- Gupta U (2021) "The case for agrivoltaics in India. Retrieved from <https://www.pv-magazine.com/2021/12/08/the-case-for-agrivoltaics-in-india/#:~:text=Agrivoltaics%20refers%20to%20the%20combination,than%20in%20most%20other%20countries.> Accessed 12 Jul 2022
- Hsiao Y-S, Chen C-P, Chao C-H, Whang W-T (2009) All-solution-processed inverted polymer solar cells on granular surface-nickelized polyimide. *Org Electron* 10(4):551–561
- Huo Z, Tsung C-k, Huang W, Zhang X, Yang P (2008) Sub-two nanometer single crystal Au nanowires. *Nano Lett* 8(7):2041–2044
- HZB sets new 29.8% efficiency record for perovskite-silicon tandem solar cells. In: Perovskite-Info. Retrieved from <https://www.perovskite-info.com/hzb-sets-new-298-efficiency-record-perovskite-silicon-tandem-solar-cells>. Accessed on 28 Jul 2022
- Ishizuka S, Yamada A, Matsubara K, Fons P, Sakurai K, Niki S (2010) Development of high-efficiency flexible Cu(In, Ga)Se₂ solar cells: a study of alkali doping effects on CIS, CIGS, and CGS using alkali-silicate glass thin layers. *Curr Appl Phys* 10(2 Supplement): S154–S156
- Jiang BH et al (2020) High-performance semitransparent organic photovoltaics featuring a surface phase-matched transmission-enhancing Ag/ITO electrode. *ACS Appl Mater Interfaces* 12(35): 39496–39504. <https://doi.org/10.1021/acsami.0c10906>
- Jošt M et al (2019) 21.6%-efficient monolithic perovskite/Cu(In, Ga)Se₂ tandem solar cells with thin conformal hole transport layers for integration on rough bottom cell surfaces. *ACS Energy Lett* 4(2):583–590. <https://doi.org/10.1021/acsenenergylett.9b00135>
- Jošt M, Kegelmann L, Korte L, Albrecht S (2020) Monolithic perovskite tandem solar cells: a review of the present status and advanced characterization methods toward 30% efficiency. *Adv Energy Mater* 10(26):1904102. <https://doi.org/10.1002/aenm.201904102>
- Jung HS, Han GS, Park N-G, Ko MJ (2019) Flexible perovskite solar cells. *Joule* 3(8):1850–1880
- Jung J, Guo R (2012) Optimized sputtering parameters for ITO thin films of high conductivity and transparency. In: *Advances and applications in electroceramics II: ceramic transactions*, vol 235, pp 43–53. <https://doi.org/10.1002/9781118511350.CH5>
- Kanna RR, Baranidharan M, Singh RR, Indragandhi V (2020) Solar energy application in Indian irrigation system. *IOP Conf Ser Mater Sci Eng* 937:12016. <https://doi.org/10.1088/1757-899X/937/1/012016>
- Kim M et al (2015) Promising efficiency enhancement in cobalt redox couple-based back-illuminated dye-sensitized solar cells with titanium foil substrate. *J Power Sources* 278:32–37
- Kim H, Kim H-S, Ha J, Park N-G, Yoo S (2016) Empowering semi-transparent solar cells with thermal-mirror functionality. *Adv Energy Mater* 6(14):1502466. <https://doi.org/10.1002/aenm.201502466>
- Kim GM, Tatsuma T (2017) Semi-transparent perovskite solar cells developed by considering human luminosity function. *Sci Rep* 7:10699. <https://doi.org/10.1038/s41598-017-11193-1>
- Kopecek R, Libal J (2018) Towards large-scale deployment of bifacial photovoltaics. *Nat Energy* 3:443–446. <https://doi.org/10.1038/s41560-018-0178-0>
- Kim J et al (2020) High performance flexible transparent electrode via one-step multifunctional treatment for Ag nanonetwork composites semi-embedded in low-temperature-processed substrate for highly performed organic photovoltaics. *Adv Energy Mater* 10(15): 1903919
- Lee D-G, Yoon S, Lee HW, Choi H, Kim J, Kang D-W (2021) Semitransparent perovskite solar cells with exceptional efficiency and transmittance. *Appl Phys Express* 14(12):126504. <https://doi.org/10.35848/1882-0786/ac3803>
- Leijtens T, Bush KA, Prasanna R, McGehee MD (2018) Opportunities and challenges for tandem solar cells using metal halide perovskite semiconductors. *Nat Energy* 3(10):828–838. <https://doi.org/10.1038/s41560-018-0190-4>
- Li CN et al (2005) Improved performance of OLEDs with ITO surface treatments. *Thin Solid Films* 477(1–2):57–62
- Li M et al (2020) Embedded nickel-mesh transparent electrodes for highly efficient and mechanically stable flexible perovskite photovoltaics: toward a portable mobile energy source. *Adv Mater* 32(38):2003422
- Li X, Li P, Wu Z, Luo D, Yu H-Y, Lu Z-H (2021) Review and perspective of materials for flexible solar cells. *Mater Rep Energy* 1(1):100001. <https://doi.org/10.1016/j.matre.2020.09.001>
- Liang F et al (2020) High-performance semitransparent and bifacial perovskite solar cells with MoO_x/Ag/WO_x as the rear transparent electrode. *Adv Mater Interfaces* 7(20):2000591. <https://doi.org/10.1002/admi.202000591>
- Liu et al (2013) Efficient and ultraviolet durable inverted organic solar cells based on an aluminum-doped zinc oxide transparent cathode. *Appl Phys Lett* 103(4):43309
- Liu Q et al (2020) 18% efficiency organic solar cells. *Sci Bull* 65(4):272–275. <https://doi.org/10.1016/j.scib.2020.01.001>
- LONGi and Enel to Build Mexico's Largest Bifacial Photovoltaic Power Plant. In: PV-Tech Daily Photovoltaic News. Retrieved from http://www.pv-tech.cn/news/Longi_and_Enel_build_Mexicos_largest_double-sided_photovoltaic_power_stat. Accessed on 28 Jul 2022
- LONGi will supply 224MW of bifacial PERC modules for the largest 'bifacial + tracking' project in the United States. In: PV-Tech Daily Photovoltaic News. Retrieved from <http://www.pv-tech.cn/news/>

- Longji_will_supply_224MW_double-sided_PERC_components_for_the_largest_doub. Accessed on 28 Jul 2022
- Lu H, Zhang D, Cheng J, Liu J, Mao J, Choy WCH (2015) Locally welded silver nano-network transparent electrodes with high operational stability by a simple alcohol-based chemical approach. *Adv Func Mater* 25(27):4211–4218
- Mahto R, Sharma D, John R, Putcha C (2021) Agrivoltaics: a climate-smart agriculture approach for Indian farmers. *Land* 10(11):1277. <https://doi.org/10.3390/land10111277>
- Mamun MAA, Dargusch P, Wadley D, Zulkarnain NA, Aziz AA (2022) A review of research on agrivoltaic systems. *Renew Sustain Energy Rev* 161:112351. <https://doi.org/10.1016/j.rser.2022.112351>
- New manufacturing technique for 26%-efficient tandem perovskite solar cell. Retrieved from <https://www.pv-magazine.com/2020/04/20/new-manufacturing-technique-for-26-efficient-tandem-perovskite-solar-cell/>. Accessed on 28 Jul 2022
- Nickel F et al (2010) Cathodes comprising highly conductive poly(3, 4-ethylenedioxythiophene): poly(styrenesulfonate) for semi-transparent polymer solar cells. *Org Electron* 11(4):535–538
- Noel NK et al (2014) Lead-free organic-inorganic tin halide perovskites for photovoltaic applications. *Energy Environ Sci* 7(9):3061–3068. <https://doi.org/10.1039/C4EE01076K>
- Park J-H, Ahn K-J, Na S-I, Kim H-K (2011) Effects of deposition temperature on characteristics of Ga-doped ZnO film prepared by highly efficient cylindrical rotating magnetron sputtering for organic solar cells. *Sol Energy Mater Sol Cells* 95(2):657–663
- Photovoltaic Equipment International Technology Roadmap for Photovoltaic (ITRPV) 2019 Results. Retrieved from <https://www.coursehero.com/file/70882591/ITRPV-2020pdf/>
- Po R, Carbonera C, Bernardi A, Camaioni N (2011) The role of buffer layers in polymer solar cells. *Energy Environ Sci* 4(2):285–310
- Pulipaka S, Peparthy M (2021) Agrivoltaics in India overview of operational projects and relevant policies. In: National Solar Energy Federation of India (NSEFI), New Delhi, India. New Delhi, India: Indo-German Energy Forum Support Office (IGEF-SO). Retrieved from <http://www.nsefi.in/>
- Rahmany S, Etgar L (2020) Semitransparent perovskite solar cells. *ACS Energy Lett* 5(5):1519–1531. <https://doi.org/10.1021/acsenergylett.0c00417>
- Randle-Boggis RJ, Lara E, Onyango J, Temu EJ, Hartley SE (2021) Agrivoltaics in East Africa: opportunities and challenges. *AIP Conf Proc* 2361:90001. <https://doi.org/10.1063/5.0055470>
- Ravishankar E, Booth RE, Saravitz C, Sederoff H, Ade HW, O'Connor BT (2020) Achieving net zero energy greenhouses by integrating semitransparent organic solar cells. *Joule* 4(2):490–506. <https://doi.org/10.1016/j.joule.2019.12.018>
- Ravishankar E et al (2021) Balancing crop production and energy harvesting in organic solar-powered greenhouses. *Cell Rep Phys Sci* 2(3):100381. <https://doi.org/10.1016/j.xcrp.2021.100381>
- Robins Air Force Base Solar 170MW. In: E Light Electric. Retrieved from <https://elightelectric.com/portfolio/robins-air-force-base-solar-170mw/>. Accessed on 28 Jul 2022
- Sandström A, Dam HF, Krebs FC, Edman L (2012) Ambient fabrication of flexible and large-area organic light-emitting devices using slot-die coating. *Nat Commun* 3(1):1–5
- Sannicola T, Lagrange M, Cabos A, Celle C, Simonato J-P, Bellet D (2016) Metallic nanowire-based transparent electrodes for next generation flexible devices: a review. *Small* 12(44):6052–6075
- Stein J et al (2021) Bifacial photovoltaic modules and systems: experience and results from international research and pilot applications. <https://doi.org/10.2172/1779379>
- Sun X, Khan MR, Deline C, Alam MA (2018) Optimization and performance of bifacial solar modules: a global perspective. *Appl Energy* 212:1601–1610. <https://doi.org/10.1016/j.apenergy.2017.12.041>
- Tandem Cells. In: PVEducation. Retrieved from <https://www.pveducation.org/pvcdrom/tandem-cells>. Accessed on 28 Jul 2022
- Taygete I Energy Project. In: 7X Energy. Retrieved from <https://7x.energy/taygete/>. Accessed on 28 Jul 2022
- Taygete II Energy Project. In: 7X Energy. Retrieved from <https://7x.energy/taygete-ii-energy-project/>. Accessed on 28 Jul 2022
- Tin and inorganic tin compounds. Retrieved from <https://apps.who.int/iris/handle/10665/43223>. Accessed on 28 Jul 2022
- The place where bees, crops and photovoltaic panels coexist. Retrieved from <https://www.endesa.com/en/projects/all-projects/circular-economy/agrivoltaica-generation-solar-energy-agriculture-beekeeping>. Accessed on 28 Jul 2022
- Trina Solar ships 600W+ series Vertex modules for a 850 MWp PV project, one of the largest in Brazil. In: Trina Solar. Retrieved from <https://www.trinasolar.com/en-glb/resources/newsroom/matrina-solar-ships-600w-series-vertex-modules-850-mwp-pv-project-one-largest>. Accessed on 28 Jul 2022
- Trommsdorff M (2021) Agrivoltaics for arid and semi-arid climatic zones: technology transfer and lessons learned from Japan and Germany. In: International webinar series on agrivoltaics in Africa. Retrieved from <https://www.ise.fraunhofer.de/>
- “Viticulture results—Sun’Agri. Retrieved from <https://sunagri.fr/resultats-viticulture/>. Accessed on 28 Jul 2022
- Wang X et al (2015) TiO₂ nanotube arrays based flexible perovskite solar cells with transparent carbon nanotube electrode. *Nano Energy* 11:728–735
- Wang ZB, Helander MG, Lu ZH (2013) 2–Transparent conducting thin films for OLEDs. In: Organic light-emitting diodes (OLEDs): materials, devices and applications. Woodhead publishing series in electronic and optical materials. Elsevier, pp 49–76
- Weselek A, Ehmman A, Zikeli S, Lewandowski I, Schindele S, Högy P (2019) Agrophotovoltaic systems: applications, challenges, and opportunities. A review. *Agron Sustain Dev* 39(35):1–20. <https://doi.org/10.1007/s13593-019-0581-3>
- What are tandem cells? Introduction to solar technology. Part 3. In: Metsolar. Retrieved from <https://metsolar.eu/blog/what-are-tandem-cells-introduction-to-solar-technology-part-3/>. Accessed on 28 Jul 2022
- Williams EW et al (1980) The electrophoresis of thin Film CdS/Cu₂S solar cells. *Solar Cells* 1(4):357–366
- Wong WS, Salleo A (2009) Flexible electronics: materials and applications, vol 11. Springer Science & Business Media
- Woodhouse MA, Smith B, Ramdas A, Margolis RM (2019) Crystalline silicon photovoltaic module manufacturing costs and sustainable pricing: 1h 2018 benchmark and cost reduction road map. <https://doi.org/10.2172/1495719>
- Xiao Y, Han G, Zhou H, Wu J (2016) An efficient titanium foil based perovskite solar cell: using a titanium dioxide nanowire array anode and transparent poly(3, 4-ethylenedioxythiophene) electrode. *RSC Adv* 6(4):2778–2784
- Xue J, Forrest SR (2004) Carrier transport in multilayer organic photodetectors: II. Effects of anode preparation. *J Appl Phys* 95(4):1869–1877
- Yan J, Saunders BR (2014) Third-generation solar cells: a review and comparison of polymer:fullerene, hybrid polymer and perovskite solar cells. *RSC Adv* 4(82):43286–43314. <https://doi.org/10.1039/C4RA07064J>
- Yi C et al (2020) High-temperature-resistant and colorless polyimide: preparations, properties, and applications. *Sol Energy* 195:340–354
- Ying Z et al (2019) Supersmooth Ta₂O₅/Ag/Polyetherimide film as the rear transparent electrode for high performance semitransparent perovskite solar cells. *Adv Opt Mater* 7(4):1801409. <https://doi.org/10.1002/adom.201801409>
- Yoon H, Kang SM, Lee J-K, Choi M (2016) Hysteresis-free low-temperature-processed planar perovskite solar cells with 19.1% efficiency. *Energy Environ Sci* 9(7):2262–2266

- Yu J-S et al (2013) Transparent conductive film with printable embedded patterns for organic solar cells. *Sol Energy Mater Sol Cells* 109:142–147
- Yun J (2017) Ultrathin metal films for transparent electrodes of flexible optoelectronic devices. *Adv Func Mater* 27(18):1606641
- Zardetto V, Brown TM, Reale A, Di Carlo A (2011) Substrates for flexible electronics: a practical investigation on the electrical, film flexibility, optical, temperature, and solvent resistance properties. *J Polym Sci Part B Polym Phys* 49(9):638–648
- Zhang M et al (2005) Strong, transparent, multifunctional, carbon nanotube sheets. *Science* 309(5738):1215–1219
- Zhang J, Zhang W, Cheng H-M, Silva SRP (2020) Critical review of recent progress of flexible perovskite solar cells. *Mater Today* 39:66–88
- Zhang D, Alami AH, Choy WCH (2022) Recent progress on emerging transparent metallic electrodes for flexible organic and perovskite photovoltaics. *Solar RRL* 6(1):2100830
- Zhao J et al (2017) Self-encapsulating thermostable and air-resilient semitransparent perovskite solar cells. *Adv Energy Mater* 7(14):1602599. <https://doi.org/10.1002/aenm.201602599>



Characterization Techniques for Photovoltaics Manufacturing

Abdul Hai Alami[✉], Shamma Alasad[✉], Haya Aljaghoub[✉],
Mohamad Ayoub[✉], Adnan Alashkar[✉], Ayman Mdallal[✉],
and Ranem Hasan[✉]

Abstract

Although most relevant characterization techniques were mentioned throughout the previous chapters of the book, this chapter is a standalone reference on such techniques that will be important for any PV fabrication process.

1 Introduction

Thin-film cells and the induction of third-generation solar cells into the solar photovoltaic technology scene created the need for researchers on both sides to optimize their performance. The performance of cells belonging to either of these technologies depends on many factors relating to the metallurgical aspects and resulting physical, optical, and electrical properties of the substrates. For example, the purity of deposited layers/films, their morphology, light sensitivity, diffusion length of electrons (and their lifetime), and other parameters are key factors in deciding how the assembled device would perform. It would be extremely convenient to be able to see electrons and holes as they generate from a photon that has just landed on the photoanode material, then

usher each of them toward their destination. Unfortunately, such scenario is not achievable in reality, but any step that brings us closer to it would be rewarded greatly. This is the reason why the creation and harnessing of a femtolaser has won the late Ahmed Zewail a Nobel Prize.

In the world of perovskite solar cells, which is a rising third-generation solar photovoltaic technology, their composition can be fine-tuned via optimizing the halide component in the perovskite layer in terms of bandgap and absorbance, which will directly affect their interaction with incident radiation. Moreover, passivating the perovskite layer, in particularly bulk passivation, enhances the lifetime of the electrons and their diffusion length within the perovskite layer. Surface passivation can reduce the number of pinholes that can be lethal to perovskite solar cells that causes the subsequent layer after the perovskite layer to leak into the layer preceding it. Based on the limited scope of the previously mentioned parameters and characteristics that can be optimized, it is imperative that proper and strong characterization techniques are used in order to define and optimize each respective aspect of a thin-film or third-generation solar cells. Sometimes the characterization step has to be repeated many times until the desired results in the form of peaks, curve attenuation or certain impedance response is altered in a favorable way. X-ray diffraction, for instance, can be used to ensure the existence of a specific crystal structure within a crystalline film. Scanning electron microscopy can be used to study the morphology of a given film and determine the number of pinholes or the size of grains within it. Atomic force microscopy (AFM) can be used to obtain the breadth of a thin film relative to a known substrate or determine the RMS roughness which can be important to control the crystallization of layers that may follow. UV–Vis is a spectroscopy test that is mainly used to determine the intensity of the absorbance, transmittance, or reflectance of a thin-film layer within the ultra-violet/visible light spectrum and through calculations obtain the corresponding bandgap. These characterization techniques can

A. H. Alami (✉) · H. Aljaghoub · M. Ayoub · A. Mdallal ·
R. Hasan
University of Sharjah, Sharjah, United Arab Emirates
e-mail: aalalami@sharjah.ac.ae

H. Aljaghoub
e-mail: haljaghoub@sharjah.ac.ae

M. Ayoub
e-mail: mohamad.ayoub@sharjah.ac.ae

A. Mdallal
e-mail: ayman.mdallal@sharjah.ac.ae

S. Alasad · A. Alashkar
American University of Sharjah, Sharjah, United Arab Emirates
e-mail: g00070854@aus.edu

A. Alashkar
e-mail: b00028197@alumni.aus.edu

help to understand the deposited layers on a microscopic scale and to know the flaws that need to be overcome in order to achieve better output whether it is efficiency, lifetime, or film surface.

2 X-Ray Diffraction

X-ray diffraction (XRD) is a technique that is used to characterize solar cells to identify and confirm the existence of desired materials within different films such as perovskite active layers and electron and hole transport layers. It is considered as a non-destructive measurement contrary to some characterization techniques that are used which will be discussed later on in this chapter. An X-ray diffractor is shown in Fig. 1.

In XRD, the point of focus is crystalline materials, which are materials comprising of atoms of regular order. These atoms are capable of scattering incident X-ray waves through their electrons. The process of generating the X-ray radiation and interacting with the tested material is as follows (Nasrollahzadeh et al. 2019)

1. The X-ray radiation is generated through a cathode ray tube.
2. The X-ray radiation is filtered to obtain a monochromatic radiation (of single frequency).
3. The X-ray radiation is concentrated and subsequently directed toward the measured sample.

When the X-ray radiation interacts with the crystal structure of a given film, it is diffracted at a certain angle unique to the material that makes up the crystalline film. Which means that based on the angle of the diffracted X-ray

radiation, further analysis can be carried out in order to identify a given material. The diffraction follows Bragg's law shown in Eq. (1), which relates the spacing between the atomic planes in a crystal structure and the angles of incident radiation that cause reflections of highest intensities, also known as X-ray diffraction peaks.

$$n\lambda[\text{nm}] = 2d[\text{nm}] \sin \theta [^\circ] \quad (1)$$

where n is a constant (1 or 2) depending on the order of refraction, λ is the wavelength of the X-ray radiation beam, d is the distance between the atoms of a crystal structure, and θ is the angle of the reflected radiation beam (<https://www.britannica.com/science/Bragg-law>).

After the substrate containing the targeted film is subject to X-ray diffraction and the data is extracted, a plot between the reflected radiation intensity and 2θ where θ is the reflected angle can be used to determine the identity of the material and the planes that make up its crystal structure.

XRD is essential when it comes to third-generation solar cells' fabrication. As in third-generation solar cells, the layers that make up the cell stack usually consist of a mixture of different materials dissolved in organic solvents in most cases to create a unique crystal structure. In perovskite solar cells for instance, the perovskite layer consists of an organic cation such as methylammonium iodide mixed with an inorganic cation usually lead and a halide anion (I, Cl, Br) to make up the perovskite crystal structure ABX_3 . However, in some cases, the formed layer does not consist purely of the desired perovskite crystal structure, where residues of the 3 separate components can still be embedded within the end film and decrease light absorption properties as well as the overall performance of the full cell stack. With the aid of XRD, the intensity of this residue can be accurately determined by correlating the diffraction peaks to these sole elements/compounds, then post-treatment methods and conditions can be optimized in order to decrease their inclusion within the film.

Figure 2 shows the XRD results for a perovskite film where peaks corresponding to 2θ 13.9° , 28.2° , and 31.6° represent perovskite peaks with crystal planes of (110), (220), and (310), respectively. However, there are peaks in the XRD plot that have a relatively high intensity that are considered irrelevant to the perovskite crystal structure which can be traced back to residue from the source materials. For instance, the peak at $2\theta \sim 19.8^\circ$ corresponds to methylammonium iodide, and the peak at around 25.18° corresponds to lead iodide (Stamplecoskie et al. 2015). Organic to inorganic compounds mixing ratio during precursor preparation, annealing temperatures, and deposition parameters can be optimized in this case to eliminate these foreign peaks.

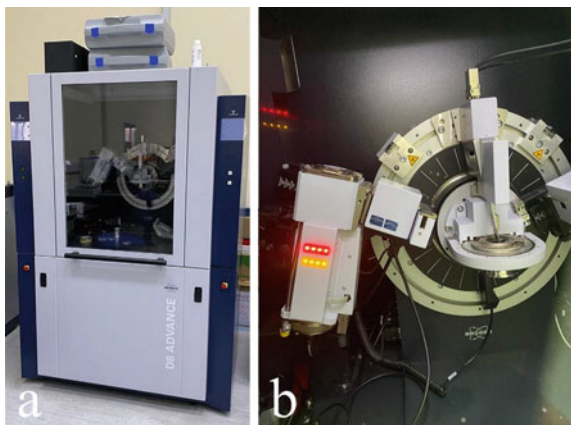


Fig. 1 a X-ray diffractor apparatus and b X-ray beam generator and detector (based on reflected radiation)

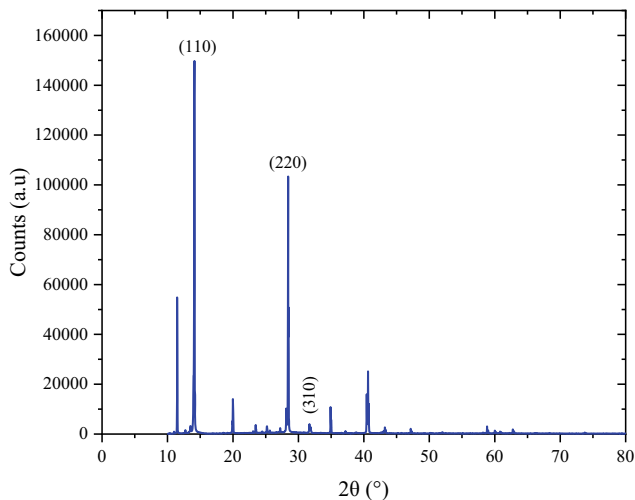


Fig. 2 XRD perovskite film ($\text{CH}_3\text{NH}_3\text{PbI}_3$)

3 Scanning Electron Microscopy

Scanning electron microscopy (SEM) is a technique used to determine the morphology, uniformity, and defects within the structure of a third-generation solar cells films. It produces high-quality pictures of the examined films that help in the optimization of coating techniques, post-treatment methods, or determine the effectiveness of passivating agents against pinholes. There are 4 main components of a scanning electron microscope.

1. Electron beam generation column
2. Specimen chamber
3. Vacuum-pump system
4. Track ball.

The vacuum-pump system allows for venting of the specimen chamber, where the samples are secured and reside, during the preparation of an SEM session. It also generates and ensures a high-quality vacuum during the SEM session to remove gas molecules that could affect the electrons' movement through the electron beam generation column up until it reaches the desired specimen.

The track ball is used to manipulate the specimen chamber holder and move it in specific directions to choose all the to-be-tested samples, and it allows for an easy operation of the scanning electron microscope through precise movements.

The electron beam generator column contains a thermionic cathode (tungsten wire) which is continuously being heated using an electric current from a high voltage source (up to 20 kV), thus releasing what are known as primary electrons, and an anode which is a hollowed-out metallic disk.

Due to the high voltage between the anode and the cathode, an electric field is generated between the two which accelerates the primary electrons from the tungsten wire. An electromagnetic lens is used to focus and direct the accelerated electron beam onto the specimen which knocks out secondary electrons from its surface.

A secondary electron detector attracts the knocked electrons from the specimen and records their amount. With the aid of a raster scan generator, the beam can be focused on a very small portion of the sample, continuously directs it to cover a rectangular area, and counts the number of electrons that are knocked out from each region.

A high flux of electrons makes up a very bright pixel in the rectangular picture, whereas an intermediate and low flux correspond to gray and black pixels, respectively. At the end of the scanning process, a picture very close to the reality of the examined specimen, or film in third-generation solar cells, can be obtained and analyzed.

The analysis in third-generation solar cells films is mainly concerned with the uniformity of the film, pinholes and obtaining the grain size and density of the multi-crystalline film. Figure 3 shows an SEM result for a perovskite film. The result indicates that the film is not uniform, where bumps and valleys can be found throughout the whole image, which could lead to worse contact resistance with other layers contrary to uniform films. The result also shines the light on the existence of pinholes in the film. Pinholes are regions where there is lack of the coated film, this could lead

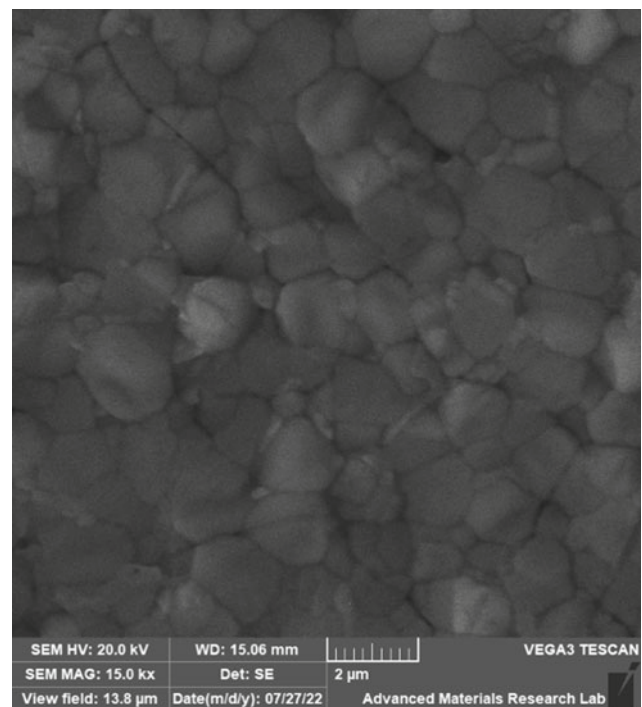


Fig. 3 SEM result for a perovskite film

to leakage from other materials in subsequently coated layers to previously coated layers through the perovskite layer which would short circuit the whole cell stack.

Based on the analyzed results, coating parameters can be adjusted to achieve better uniformity of the film, and pin-holes can be overcome by implementing a passivating-agent treatment.

Moreover, determining the grain size of the multi-crystalline film can be approximated based on SEM results. Using the SEM image from Fig. 4 and the reference ruler of 2 μm , a line with its length to scale can be drawn on the image. Then, the intersection between grain boundaries and the line is counted. The grain size is an average of the direct results of the division between the line length and number of intersections, such as shown in Eq. (2). Software such as Gwyddion (<http://gwyddion.net/>) can be used to carry out the analysis, such as shown in Fig. 5.

$$\text{Grain Size} = \frac{\sum_0^n \frac{\text{Line Length}_n}{\#\text{Intersections}_n}}{n} \quad (2)$$

where the Line Length_n is the length of the obtained line for a single trial, $\#\text{Intersections}_n$ is the number of intersections for a single trial, and n is the number of trials.

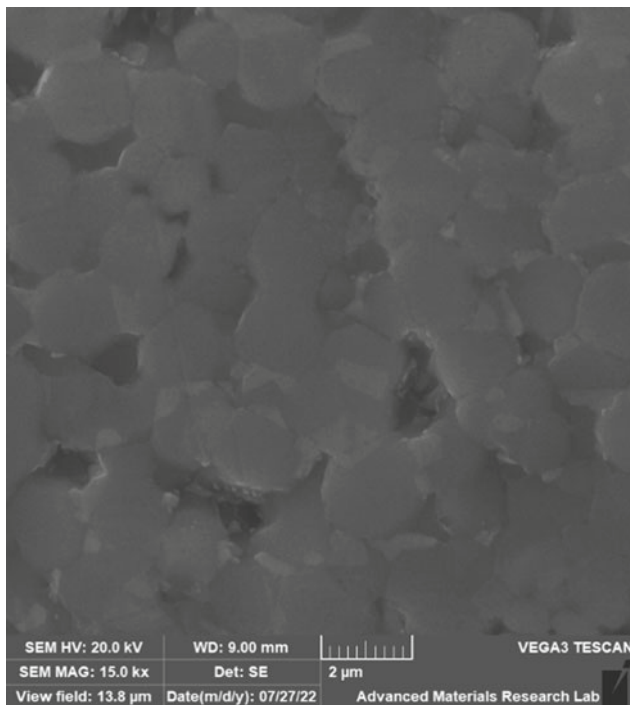


Fig. 4 SEM result of perovskite film (large grain size)

4 Atomic Force Microscopy

Atomic force microscopy (AFM) is a surface examination method that is used to characterize the topography of thin films at a nanoscale. In third-generation solar cells, AFM can be used to determine the thickness of opaque films deposited on TCO-coated and/or glass substrates, as well as the root mean square roughness of almost all films.

AFM consists of a probe that is connected to a highly reflective cantilever, and a laser beam source and detector pointing toward it. A thin-film coated substrate is placed under the microscope, which usually implements a shock/vibration-damping filter and is lifted to a point where Van der Waals forces between the thin-film atoms, and the highly sensitive probe is sufficient to cause it to move slightly. A schematic of an AFM is shown in Fig. 6.

As the AFM probe is scanning the surface of the film, the respective magnitude of the Van der Waals forces essentially represents the closeness or farness of the surface to the probe. Given that the probe is directly connected to a cantilever, it directly changes its elevation as well. This causes the reflected laser beam by the cantilever to be recorded at different locations on the laser detector.

The substrate moves in a lateral direction beneath the probe, and by the subsequent change in the elevation of the cantilever and the recording of the laser beam by the laser detector across different regions, an image representing the topography of the surface can be obtained at a nanometer scale.

In third-generation cells, it is very imperative to identify the thickness of the coated films, whether they are active layers such as (perovskite, P3HT:PCBM, etc.), transparent conductive oxides, or contacts. Given that the thickness of the film directly affects the contact resistance and the overall impedance of the cell. Moreover, optically, materials require a certain thickness with respect to their absorption coefficient in order to classify them as feasible for a solar cell operation and not to waste photon energies across the light spectrum.

AFM can be used to measure the thickness of some layers in third-generation solar cells by taking advantage of the difference between opaque films and transparent substrates such as glass, and by using analysis software that is set to scale, the thickness of the opaque film can be approximated. Unfortunately, thickness measurements using AFM are limited to films that are opaque. If the substrate is transparent, it hinders its use with transparent conductive oxides given that visibly there will not be a difference between the film and the substrate.

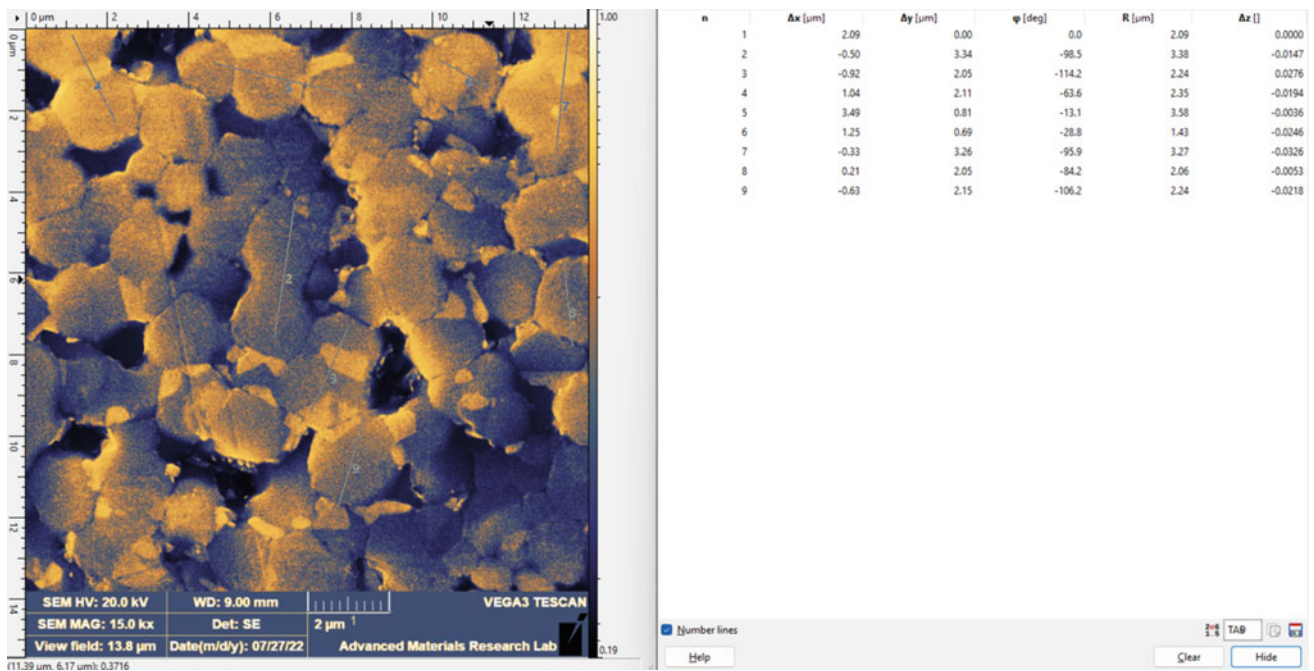


Fig. 5 Analyzed SEM result

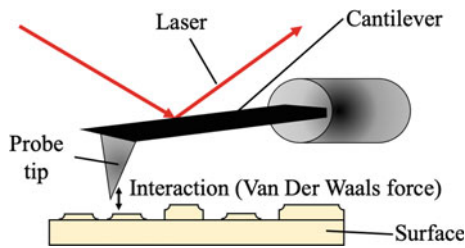


Fig. 6 Atomic force microscope

An AFM result of a passive layer deposited on a stainless-steel substrate is shown in Fig. 7. And by using an AFM analysis tool such as Gwyddion (<http://gwyddion.net/>), the difference between the stainless-steel substrate and the passive layer can be approximated by taking the difference of the average of the two regions in the horizontal profiles. In this case, the thickness is calculated by using this formula

$$\text{Top Peak} - \text{Bottom Peak} \tag{3}$$

AFM can also be used to approximate the root mean square (RMS) value of the roughness of the film. The RMS roughness should not be relatively high in a third-generation solar cell stack as it can influence a high contact resistance between the different layers. However, it should not be diminished completely. Having some roughness to the film, especially in films that precede the perovskite active layer in

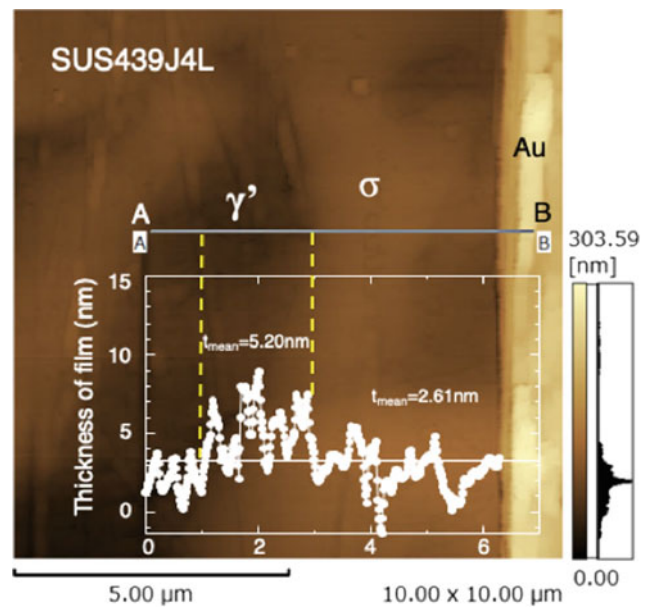


Fig. 7 AFM result of passive film on stainless-steel substrate for thickness measurement (Wang et al. 2019)

perovskite solar cells, is essential to allow for a good nucleation of the perovskite film as it is deposited. An AFM result and its plot are shown in Fig. 8. and Fig. 9, respectively.

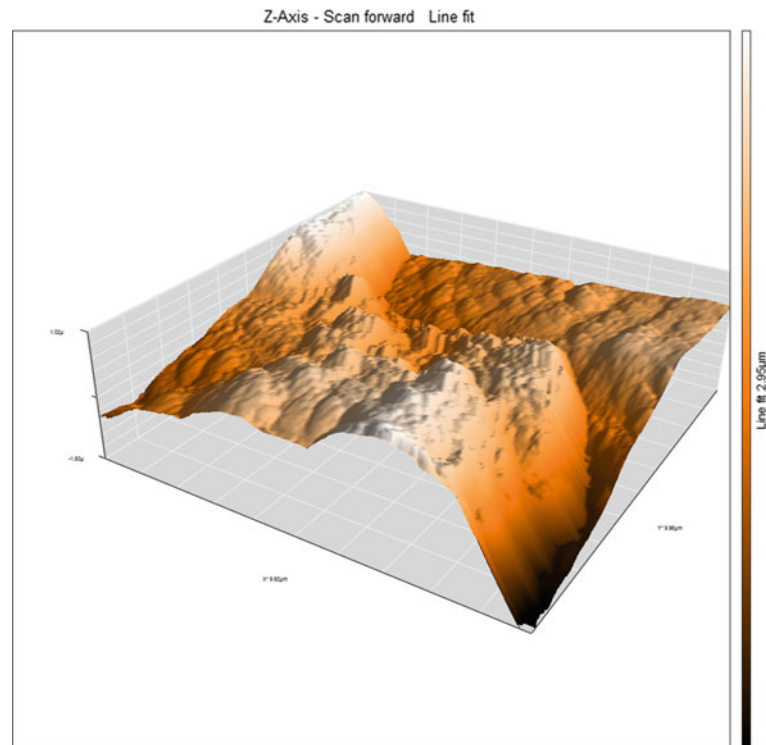


Fig. 8 AFM result

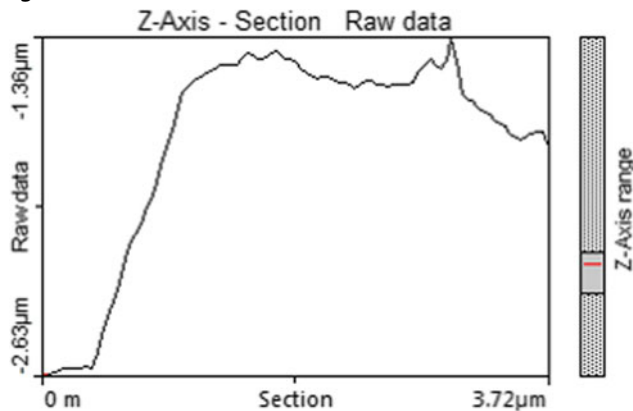


Fig. 9 Plotted AFM result

5 UV-Visible Spectrophotometry

UV-visible spectrophotometry, also known as UV-Vis Spectrophotometry, is a technique that is used to get transmittance and absorbance profiles of materials or coated thin films in third-generation solar cells, with respect to a baseline or reference substrate.

A UV-Vis spectrophotometer consists of a source lamp (usually xenon), a monochromator, sample holders, and detectors. The xenon source lamp provides a continuous white light feed throughout the process. The monochromator consists of gratings that isolate single wavelengths of

photons. When white light is incident on the grating, it is diffracted into the whole range of ultra-violet and visible light spectrum wavelengths, producing a rainbow of colors. As the light is reflected off the grating, light of a single wavelength is allowed to pass through the slit as it leaves the monochromator. During a UV-Vis measurement, the grating is moved slightly to allow for all wavelengths to pass through the slit. Similarly, a prism can be used to convert the white light into single wavelengths of the whole range of the UV-Vis spectrum.

A sample holder is where the sample of the preceding baseline is placed upon, it secures the samples in place and exposes them to the photons leaving the monochromator. The detectors are placed behind the sample holders; based on a reference or baseline sample, the detector measures the attenuation of the intensity of the detected photons and creates a profile of the transmittance based on the concentration of the thin film and the length the light travels through it before being detected such as shown in Eq. (4).

$$\text{Transmittance} = 10^{-\text{constant}(\text{concentration} \times \text{length})} \quad (4)$$

The absorbance of the material can be calculated using the following formula

$$\text{Absorbance} = \log\left(\frac{1}{\%T}\right) \quad (5)$$

Following Tauc equation, shown in Eq. (6), the bandgap of the semi-conducting material can be approximated by extrapolating the x-axis intersection from a linear region in the Tauc plot.

$$(\alpha h\nu)^\gamma = \text{Constant}(h\nu - E_g) \quad (6)$$

where α is the absorption coefficient, $h\nu$ is the photon energy, γ is either 1 or 2 depending on whether it is an indirect or a direct bandgap material, respectively, and E_g is the bandgap of the semi-conducting material.

Figure 10 shows the absorbance profile for a perovskite coated glass substrate, which is essentially the absorbance plotted against the respective wavelength. The data that the plot represents can be used, after some modifications, to obtain the Tauc plot, and the bandgap of the material can then be approximated.

Based on Fig. 11 and extrapolating the Tauc plot to the zero-x-axis point (black line), the bandgap of the perovskite material was approximated to be 1.96 eV which falls in the range for the bandgaps of perovskite materials ~ 1.5 – 2.2 eV.

6 Solar Simulator (Power Conversion Efficiency Measurement)

Power conversion efficiency (PCE) measurement is an end-phase test that determines the performance of the full solar cell stack. Characteristics such as power conversion efficiency, open-circuit voltage, short-circuit current density, fill factor, maximum power point parameters, and shunt and series resistances can be extracted.

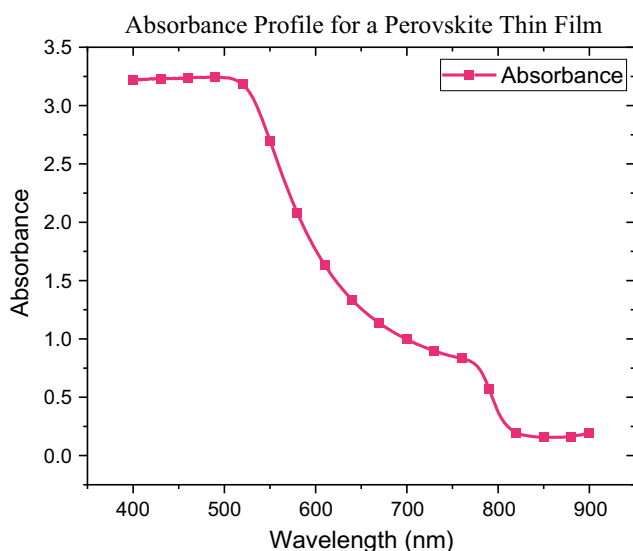


Fig. 10 Absorbance profile for a perovskite thin-film coated on a glass substrate

The power conversion efficiency measurement is done with the aid of what is known as a solar simulator. A solar simulator can provide STC conditions for testing a solar cell, such as an irradiance equal to 1 sun (STC) ($1000 \frac{W}{m^2}$) or even higher magnitudes reaching up to 5 suns. The spectrum that is simulated by the solar simulator must also match the STC spectrum shown in Fig. 12 (AM1.5G), where AM is the air mass representing the magnitude of the thickness of the atmosphere that the light travels through.

A solar simulator consists of a xenon lamp providing white light, mirrors in order to direct the light up until it exits the lens of the solar simulator, collimating lenses that ensures the uniformity of the light flux that reaches the tested sample and a stage where the sample is placed upon. A certified reference cell is used to ensure that the STC conditions are met. Usually, a bracket that has electrical contacts connected to the terminals of the cell is used to connect to a computer-based interface in order to control the measurement.

The data acquired from the solar simulator requires the least amount of analysis given that it is direct data and indications of performance. A J-V curve obtained from a perovskite solar cell stack is shown in Fig. 13. The direct data for the PCE measurement is also summarized in Table 1.

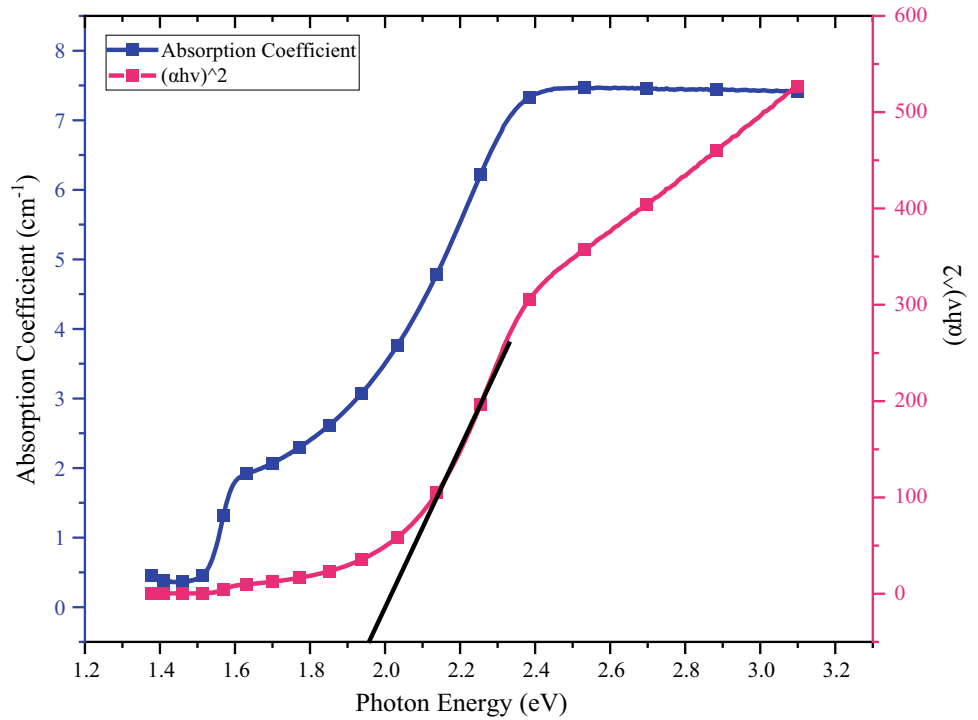
7 Quantum Efficiency

The quantum efficiency (QE) is the ratio between the number of incident photons to the number of electron/hole pairs generated within a solar cell. Quantum efficiency, commonly known as external quantum efficiency (EQE), is calculated using Eq. (7). If a solar cell can convert all incident light (photons) into electron hole pairs, the external quantum efficiency for photons above the bandgap is unity, whereas for photons with energy below the bandgap is zero. Recombination effects, for instance, hinder the collection of electron/hole pairs from an incident photon with their different types (surface, radiative, auger, traps “bulk”). High-energy blue light is absorbed near the front surface of a solar cell, which is subject to intense surface recombination that results in a reduction of the EQE. In the mid-range of the solar spectrum (green-yellow), the photons are absorbed in the bulk of the solar cell, where electron/hole pairs are required to diffuse within the material to get separated which is not always guaranteed to occur due to material defects that cause trapping of electrons and an overall low diffusion length.

$$EQE(\lambda) = \frac{N_{EH}(\lambda)}{N_{Photons}(\lambda)} \quad (7)$$

where EQE is the external quantum efficiency, N_{EH} is the number of electrons, $N_{photons}$ is the number of photons.

Fig. 11 Absorption coefficient profile versus energy blue and Tauc plot pink



In the red portion of the solar spectrum, low-energy photons penetrate deep into the bulk of the solar cell, where back surface recombination is prominent and can cause severe electron/hole recombination reducing the EQE in that region. Photons with energy below the bandgap of a solar cell result in no absorption events and thus no generation of

electron/hole pairs, where the EQE curve immediately terminates and goes to zero. An ideal EQE curve is shown in Fig. 14 where the value of EQE is constant at a unity for wavelengths with energies above the bandgap of silicon solar cells.

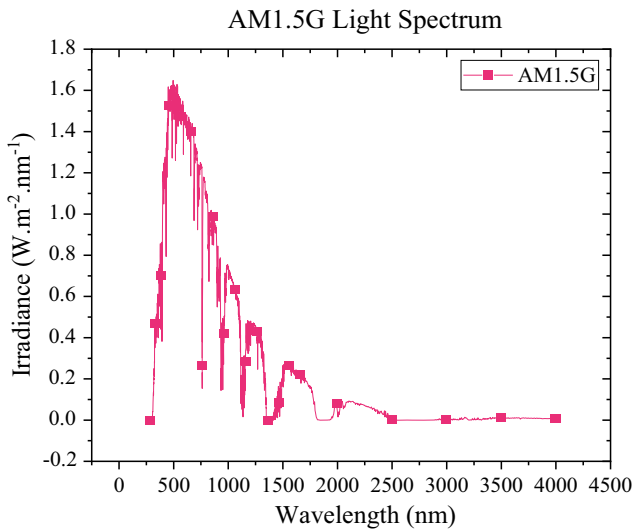


Fig. 12 STC light spectrum (AM1.5G)

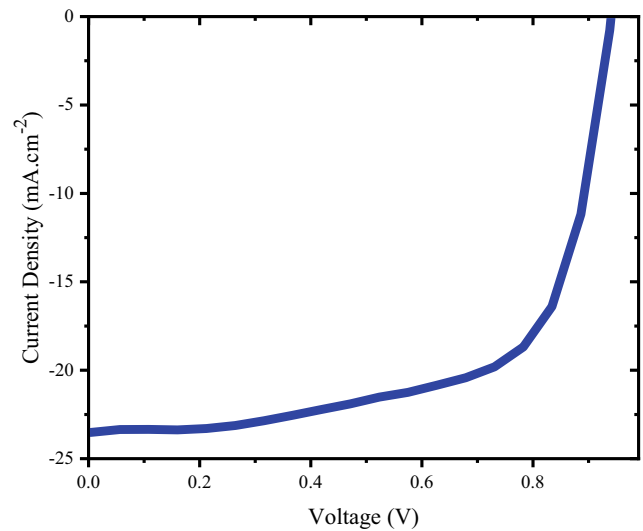
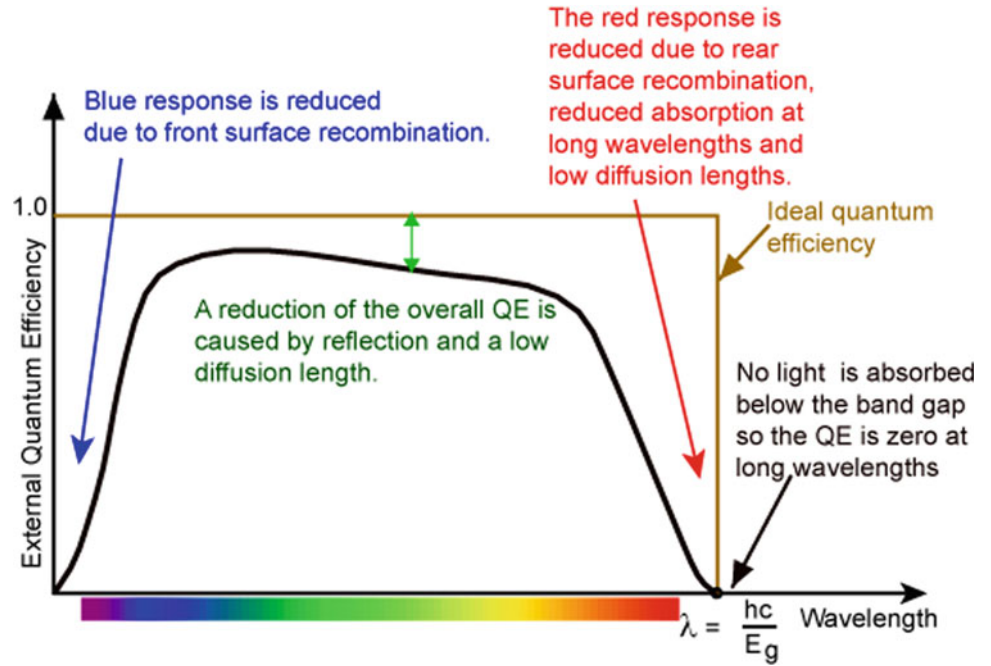


Fig. 13 J-V curve for a perovskite solar cell

Table 1 Perovskite solar cell performance parameters

PCE (%)	V _{OC} (V)	J _{SC} (mA·cm ⁻²)	FF (%)	MP (mW)	R _{Series} (Ω·cm ⁻²)	R _{Shunt} (Ω·cm ⁻²)
14.619	0.940	-23.478	66.204	-14.6193	3.906	1119.05

Fig. 14 External quantum efficiency (<https://www.pveducation.org/pvcdrom/solar-cell-operation/quantum-efficiency>)



Although it is important to study all types of losses and aspects to the operation of solar cells, sometimes, the quantum efficiency taken into account omits the transmission and reflection losses, considering a pure electrical performance of solar cells with a parameter known as the internal quantum efficiency (IQE). It indicates the effect of photons after they have been absorbed, and the electron/hole pair collection events that are subject to electrical losses such as diffusion and separation. The IQE can be obtained by measuring the EQE and measuring the absorption spectrum of a solar cell using UV–Vis spectroscopy, and it is calculated using Eq. (8).

$$IQE(\lambda) = \frac{EQE(\lambda)}{\%A(\lambda)} \tag{8}$$

A QE device, such as shown in Fig. 15, consists of a light source, light chopper, a prism/slit/gratings, lock-in amplifier, reference cell, and a computer interface software. The light source provides a continuous feed of a light that is incident on a grating mechanism that splits the light into photons of different wavelengths (monochromator) and directs to a focused output lens. The chopper acts as a shutter that creates a frequency of the source light (AC), and while the surrounding light noise is constant (DC), a lock-in amplifier

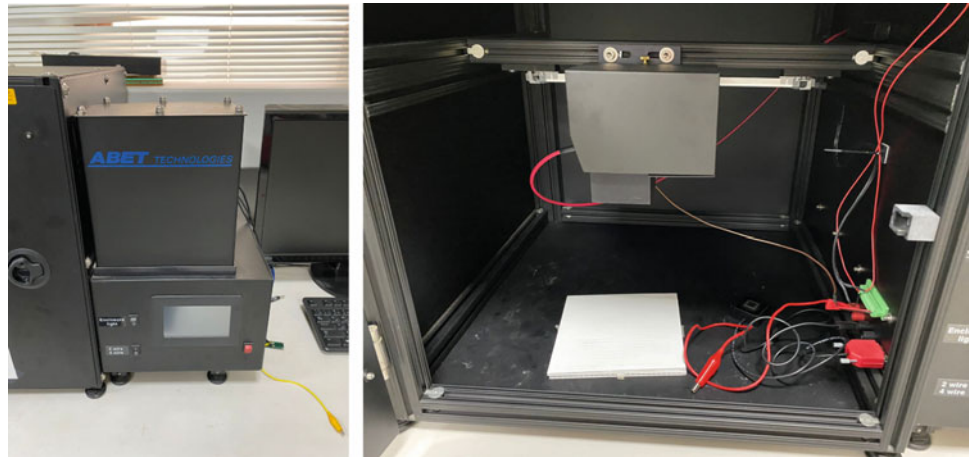
can be used to detect the known frequency of the chopper and filters out the DC output that is resultant from the DC surrounding light noise, thus leaving an output of the measured cell from the known light source.

QE measurements are also utilized to calculate the short-circuit current density for solar cells. A reference cell from the provider of a QE apparatus with a known and certified EQE plot is used. Then, the EQE of the targeted cell is measured with the same wavelength range of the reference cell (reference cells with different cut-off wavelengths can be used for better accuracy depending on the type of solar cell measured). The short-circuit current density can be related to the reference cell and calculated using the following equations.

$$EQE_{Reference}(\lambda) = \frac{N_{EH}(\lambda)}{N_{Photons}(\lambda)} = \frac{J_{sc}(\lambda) [mA \cdot cm^{-2}]}{q [C]} = \frac{\text{Intensity of light Source } (W(\lambda))}{\frac{h [J \cdot s] [C [m \cdot s^{-1}]]}{\lambda [nm]}} \tag{9}$$

And given that the light source is constant for both the reference cell and the targeted cell, the following relation can be obtained.

Fig. 15 Quantum efficiency apparatus



$$\frac{EQE_{\text{Reference}}(\lambda)}{EQE_{\text{Cell}}(\lambda)} = \frac{J_{\text{SC Cell}}(\lambda)}{J_{\text{SC Reference}}(\lambda)} \quad (10)$$

The area of the spotlight of the output of the QE device is constant as well, which transforms the current (density) into pure current, such as shown in Eq. (11).

$$\frac{EQE_{\text{Reference}}(\lambda)}{EQE_{\text{Cell}}(\lambda)} = \frac{I_{\text{SC Cell}}(\lambda)[\text{A}]}{I_{\text{SC Reference}}(\lambda)[\text{A}]} \quad (11)$$

With the $EQE(\lambda)$ and $I_{\text{SC}}(\lambda)$ of the reference cell obtained, and the EQE of the targeted cell is measured, the $I_{\text{SC}}(\lambda)$ of the target cell can be calculated and plotted, where the I_{SC} of the target cell can be calculated by integrating the $I_{\text{SC}}(\lambda)$ across the full wavelength range, such as shown in Eq. (12).

$$I_{\text{SC}} = \int_{\lambda_0}^{\lambda_{\text{cut-off}}} I_{\text{SC}}(\lambda)[\text{A}]d\lambda \quad (12)$$

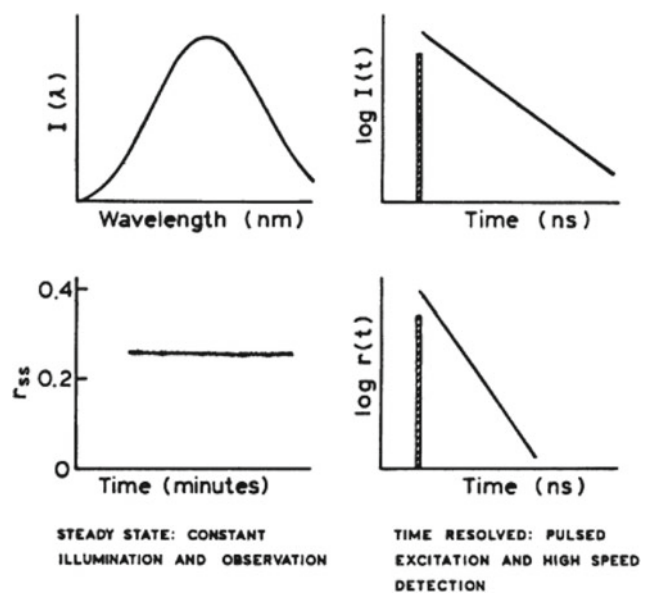


Fig. 16 Comparison between steady-state and time-resolved photoluminescence spectroscopy (Dave et al. 2021)

8 Time-Resolved Photo Luminescence

Spectroscopy can be defined as the study of atoms, molecules, and ions, by examining the interaction between these matter particles and electromagnetic radiation. The interaction in question can manifest itself in various forms, such as absorption, emission, and scattering. In absorption spectroscopy, the studied atoms transcend from lower to higher energy state due to the absorption of incident radiation, if the radiation's energy matches the difference between the two energy states. Similarly, emission spectroscopy relies on the difference between two energy states; however contrary to absorption spectroscopy, it detects the radiation emitted by particles while descending from higher to lower energy states. Finally, scattering spectroscopy measures the amount of light a substance scatters at various

wavelengths, to get an indication of its physical properties. Recently, photoluminescence spectroscopy has been gaining traction for investigating the rapid electron deactivation processes that lead to photon emission, or fluorescence. Fluorescence is mainly used to determine the material quality, identify spectral emissions with specific emissive states, or investigate energy transfer between components in mixed systems such as thin films or solar cells. Photoluminescence can be classified by two types of measurements: steady-state and time-resolved (Lakowicz 2006). Since the fluorescence time scale is in nanoseconds the steady-state is reached immediately. On the other hand, time-resolved measurements use a light pulse shorter than the decay time of the measured sample, and a high-speed detector measures the decay intensity of the sample.

Figure 16 compares steady-state and time-resolved photoluminescence spectroscopy.

Time-resolved photoluminescence spectroscopy (TRPL) can be carried out using several methods. Time-correlated single photon counting (TCSPC) is the most commonly used method to carry out TRPL measurements (Tesa et al. 2018). In TCSPC, the time between a laser pulse exciting the sample and the detection of a resultant photon due to the subsequent emission event is measured. A start-stop signal is compared between pulse release and photon detection, respectively. The process is repeated several times. Conventional luminescence lifetime of TCSPC typically ranges from 5 ps to 50 μ s.

A typical setup for TRPL measurements consists of an excitation source, a monochromator, and a detector. Photoluminescence spectroscopy usually deploys higher energy photons for sample excitation, allowing the emittance of lower energy photons. Figure 17 shows a simplified photoluminescence spectroscopy process.

The excitation source usually consists of a pulsed source that sends photons through a channel of monochromators and filters, and these components form the fluorescence spectrometer. Tungsten lamp is the most common light source used in spectrophotometers. The lamp has a wavelength of 330–900 nm, which can be used in the visible region, with a lifetime of 1200 h. Other frequently used lamps are the hydrogen/deuterium lamps. They are mainly employed in UV range at wavelengths of 200–450 nm. These lamps are known for their stability and long lifetime of 500 h. Xenon flash lamps are widely used in instruments. Xenon flash lamps work in UV–Vis range with wavelengths between 190 and 1000 nm. The lamps are known for long life and smooth operation as they do not heat up the instrument, therefore requiring less warm up time. All the detectors have the ability to operate using the TCSPC and MCS techniques. The detector is responsible for capturing the low-energy photons, after passing through a series of filters and monochromators. The most common type of

Fig. 17 Simplified fluorescence spectroscopy process

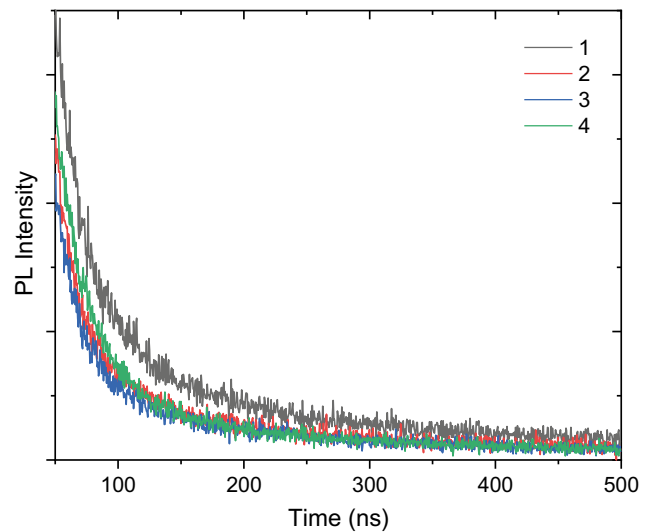
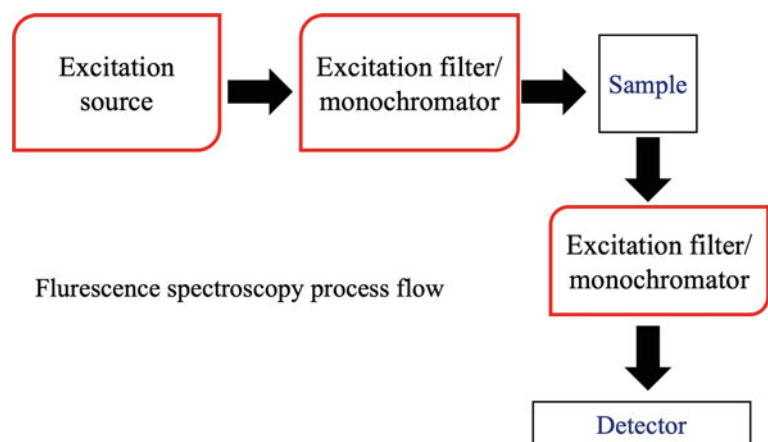


Fig. 18 TRPL decay of perovskite solar cells

detectors used is the photomultiplier tubes (PMT) that are ultra-sensitive to light in UV–Vis–NIR ranges of the spectrum.

TRPL is excessively used in perovskite solar cells to study the electron lifetime and electron decay inside the perovskite thin film. Figure 18 shows the TRPL decays curves of perovskite solar cells.

The TRPL results show the variation of the decay times of various perovskite solar cells. Sample 1 shows the slowest decay time as compared to the other samples. This indicates that the average lifetime of the electrons inside the perovskite film of samples is greater than the other samples.

9 Raman Spectroscopy

Raman spectroscopy is another form of spectroscopy that is utilized to study the chemical structure, crystallinity, and molecular interactions of a material. Raman is a non-destructive

chemical analysis technique based on light scattering from a high intensity laser. Raman spectroscopy is named after sir Chandrasekhara Venkata Raman who laid down the theory leading to the invention of the spectroscopy technique (Raman and Krishnan 1928). The first Raman experiment was conducted by utilizing a monochromatic light that penetrated a transparent material and fell on a spectrograph that allowed the recording of its spectrum (Raman and Krishnan 1928). Nowadays, Raman is widely used in research and industry as it provides information about the chemical structure and identity of atoms, phase and polymorphism, the intrinsic stress and strain, and any contamination or impurities present. Moreover, Raman spectroscopy is employed to analyze many samples such as solids, powders, liquids, slurries, and gasses. Raman can detect organic, inorganic, and biological materials. In addition, it is valid for pure chemicals, mixtures, solutions, and metallic oxides. The only limitation is metals and their alloys.

Raman spectroscopy is based on an interaction between light and molecules. When light is incident on a molecule and subsequently scattered by it, the electromagnetic field of the photon causes a polarization of the molecular electron, which increases the energy state of the molecule (Edwards 2005). This creates a short-lived and an unstable complex between the molecule and the photon, known as the virtual state of the complex. However, the photon is directly re-emitted due to the instability of this induced state. Typically, when a molecule interacts with a photon and scatters it, it retains its energy and wavelength in comparison with the initial incident photon, in a process called Rayleigh scattering. However, this is not always the case, where in some instances, an energy exchange takes place between the molecule and the incident photon, causing an inelastic scattering, where the scattered photon bears different energy and wavelength than the incident photon (Edwards 2005). Figure 19 shows the types of scattering process resulting from light-molecule interactions.

There are various excitation sources used for Raman spectroscopy. To compare Raman spectra that are obtained

from different excitation sources, the Raman scattered photon's wavelength is converted into Raman shift relative to the excitation wavelength (away from it) (Raman and Krishnan 1928) using the following equation:

$$\Delta\bar{\nu}(\text{cm}^{-1}) = \left(\frac{1}{\lambda_0(\text{nm})} - \frac{1}{\lambda_1(\text{nm})} \right) \times \frac{(10^7 \text{cm})}{(\text{nm})} \quad (13)$$

where λ_0 is the wavelength of the excitation laser and λ_1 is the wavelength of the Raman scatter.

Figure 20 shows the Jablonski diagram and energy levels of the various Raman scattering (<https://www.edinst.com/us/blog/what-is-raman-spectroscopy/>).

A Raman spectrometer has three primary components: an excitation source, a sampling device, and a detector. The excitation source has to be monochromatic; hence, lasers serve as the best source for excitation. Typical Raman devices contain various lasers with various wavelength to control the power of the Raman signal. Lasers with a shorter wavelength generate higher power that may cause fluorescence in organic molecules overwhelming the signal in the Raman spectrum. Raman scattering is usually weak and therefore requires a substantial time to collect photons to measure an apparent signal. Consequently, an extremely light sensitive device such as a silicon charged coupled device (CCD) is utilized as a photon detector in UV–Vis–NIR. Fiber optic probes used to direct laser light to the sample and then to the spectrometer. Since the Raman signal is quite weak, the signal is always collected at 0° angle normal to the sample, causing an interference from Rayleigh scattering. Figure 21 shows a Raman spectrometer and its components.

Raman spectroscopy can be used to study the chemical composition of thin film. For instance, Fig. 22 shows the Raman spectra of CuO thin films. The three peaks shown at 295 cm^{-1} , 344 cm^{-1} , and 295 cm^{-1} display the attributes of CuO with a single crystal structure (Fang and Xuan 2017).

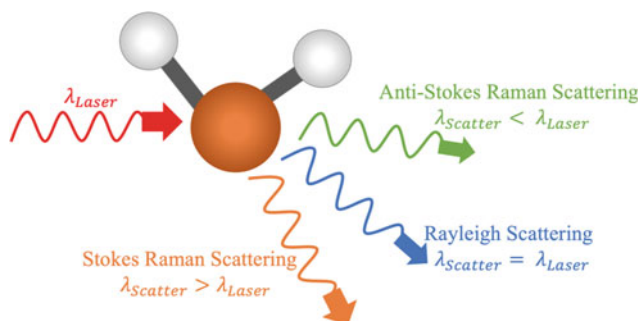


Fig. 19 Scattering modes taking place when light interacts with a molecule

10 Electrochemical Impedance Spectroscopy

Electrochemical impedance spectroscopy (EIS) is a technique that is used to study the behavior of an electrochemical system and to expose the factors that affect the electron/charge transfer which happen at a vast range of frequencies. All third-generation photovoltaic devices are electrochemical in essence. Thus, performing EIS on them allows pinpointing materials or interfaces with highest impedance. Higher impedance is expected at interfaces of different layers or whenever the work function of a material mismatches the one in an adjacent layer, making the motion of charged species more difficult. The reason why the term

Fig. 20 Jablonski diagram for the origin of the scattered light (<https://www.edinst.com/us/blog/what-is-raman-spectroscopy/>)

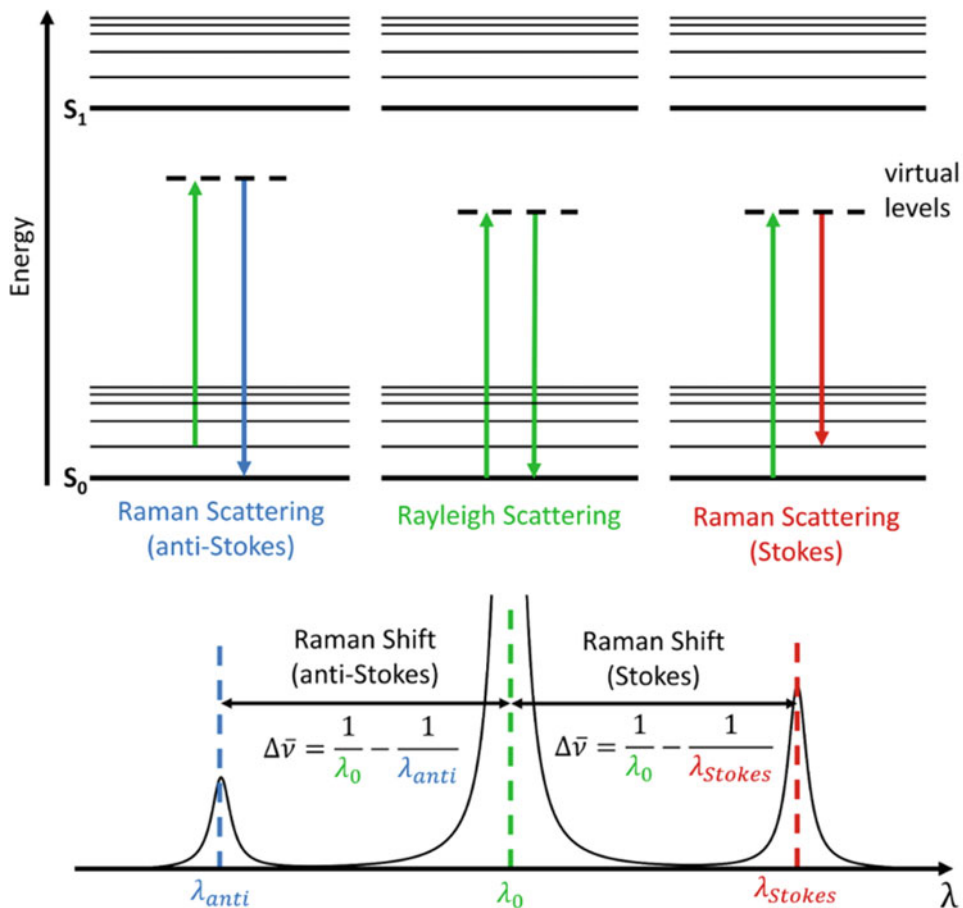


Fig. 21 Raman spectrometer

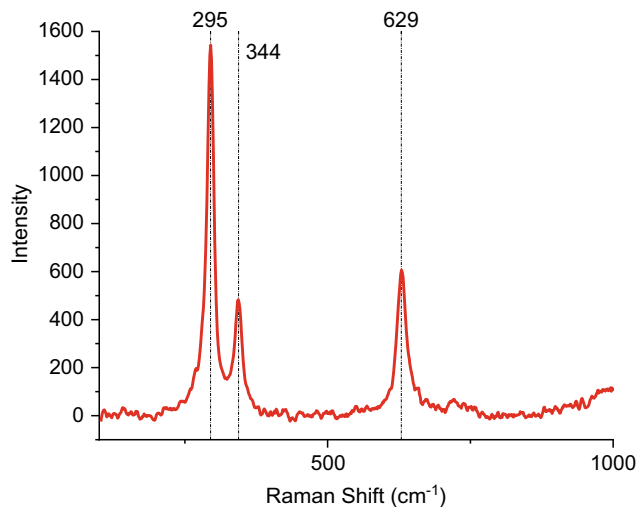


Fig. 22 Raman spectra of CuO thin films

(impedance) is used rather than (resistance) is obvious. While resistance usually shows a linear relationship between the applied voltage and resulting current, impedance describes a more general phenomenon, where the I-V

relationship would be nonlinear. And while a resistive circuit can be represented with a resultant resistance, an impedance circuit consists of a resistance (R), inductance (L), and a

capacitance (C). The impedance then depends on the value and interaction of this LCR equivalent circuit.

A piece of equipment that is used to test and display the impedance in an electrochemical system is called a potentiostat. While most electrical measurement devices can either measure current or voltage at one time, a potentiostat can do both tasks at the same time. Sometimes, current is applied and kept constant, and voltage changes are measured with respect to time (chronopotentiometry) or the voltage is applied, and kept constant and current changes are measured and recorded with respect to time (chronoamperometry). Since time is the common denominator in such measurements, a more informative test involves recording current changes with respect to voltage, which is known as cyclic voltammetry (CV).

In the case of EIS, the circuit is connected with clear definition of which part is the anode and cathode, or working electrode and counter electrode. Then voltage or current is applied, with a time dependent amplitude and angular frequency changes, while measuring an output current or voltage, respectively, of the same nature from the electrochemical system. A useful thing to note is a phase shift from the output relative to the input signal (Hauff 2019), thus indicating a delayed reaction of the system that should have a physical explanation. The idea of EIS comes from the simple definition of electrical resistance, where the ability of a circuit element to resist the electrical current flow is given by Ohm's law:

$$R = \frac{E}{I} \quad (14)$$

The limitation of the Ohm's law is the fact is that it is limited to only ideal resistors, neglecting the impedance resulting from capacitive and inductive effects, hence necessitating an alternative measurement protocol.

EIS procedure usually applies an AC potential to an electrochemical cell while measuring the generated current. The input signal will be a sinusoidal excitation, while the response to this potential is an AC current given as follows:

$$E_t = E_0 \sin(\omega t) \quad (15)$$

$$I_t = I_0 \sin(\omega t + \phi) \quad (16)$$

Hence, an expression for the impedance can be calculated using Ohm's law:

$$Z = \frac{E_t}{I_t} = \frac{E_0 \sin(\omega t)}{I_0 \sin(\omega t + \phi)} = Z_0 \frac{\sin(\omega t)}{\sin(\omega t + \phi)} \quad (17)$$

Note that the impedance is represented in term of the magnitude Z_0 and phase shift ϕ .

Using complex functions, the potential and current can be expressed as follows:

$$E_t = E_0 \exp(j\omega t) \quad (18)$$

$$I_t = I_0 \exp(j\omega t - \phi) \quad (19)$$

The impedance can now be represented as a complex number as follows:

$$Z(\omega) = \frac{E_t}{I_t} = Z_0 \exp(j\phi) = Z_0(\cos \phi + j \sin \phi) \quad (20)$$

Once the parameters are measured and transformed into frequency domain (using Fourier transformation), the impedance of the system can be obtained from a Nyquist plot. A Nyquist plot in this case has a negative imaginary component of the impedance on the Y-axis and the positive real impedance on its X-axis. Based on the electrochemical system's (such as DSSCs) equivalent circuit and the characteristics of the Nyquist plot, the resistances of the interfaces that impede the charge transfer can be obtained, which helps in understanding the electron mechanisms and their behavior inside electrochemical devices (Frank et al. 2004).

Conventionally, a Nyquist plot of a DSSC consists of 4 regions, such as shown in Fig. 23. The first region, that is defined by the open-circuit voltage exposes the series resistance, which is the intersect of the Nyquist plot and the real-x-axis. The three following regions are well defined semi-circles. Based on the frequency range that is used for the EIS measurement and by applying a decreasing frequency from left to right, the first semi-circle which corresponds to high frequency is directly related to the counter electrode parameters and interactions with an electrolyte and a hole transport material, for example. The second semi-circle is related to the electrolyte- semi-conductor material interface, such as the titanium dioxide interaction with dye and electrolyte. The last semi-circle is related to the diffusion of the ionic species through the electrolyte, and these parameters can depend on physical attributes of

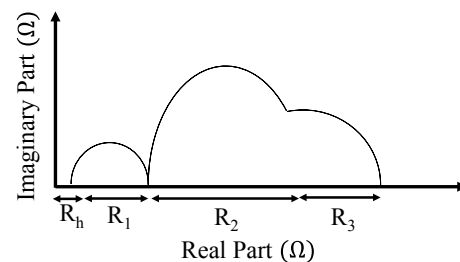


Fig. 23 Typical EIS Nyquist plot

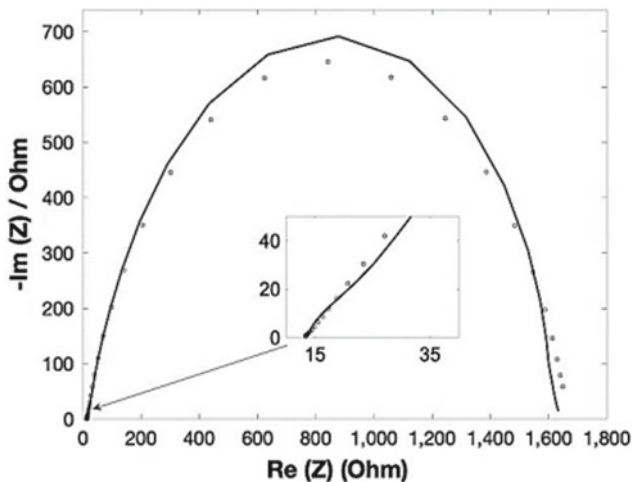


Fig. 24 Impedance (Nyquist) spectra for DSSC with Calotropis dye (Alami et al. 2021)

the electrolyte such as its concentration and viscosity (Becker et al. 2020). Generally speaking, the smaller the semi-circles, the better the performance of the cell. Plus, the Nyquist plot allows a systematic and quantitative revision of the solar cell build in order to reduce the impedance and consequently have positive impact on cell efficiency and power output.








Figure 24 shows the impedance results for a DSSC with natural dye sensitized from Calotropis Procera leaves (Alami et al. 2021). The shape of the spectrum is in line with the conventional shape response found in a typical cell. The behavior at high frequency (to the left) indicates impedance at the interface of the electrode and electrolyte. Intermediate frequencies have a peak due to electron diffusion in the photoanode semi-conducting material (ZnO , TiO_2) as well electron transfer processes at the interface between the active material and the electrolyte. The tail shown at the low frequencies is due to the diffusion process of the redox agent in the electrolyte.

References

- Alami A, Alachkar A, Alasad S, Alawadhi M, Zhang D (2021) Investigating Calotropis Procera natural dye extracts and PEDOT : PSS hole transport material for dye-sensitized solar cells. *Agron Res* 19(2):333–343. <https://doi.org/10.15159/AR.21.064>
- Becker M, Bertrams M-S, Constable EC, Housecroft CE (2020) How reproducible are electrochemical impedance spectroscopic data for dye-sensitized solar cells? *Mat (Basel)* 13(7):1547. <https://doi.org/10.3390/ma13071547>
- Britannica, Bragg's Law. <https://www.britannica.com/science/Bragg-law>
- Dave PY, Rajani AHA (eds) (2021) The perceive of fluorescent materials. Integrated Publications
- Education P, Quantum efficiency. <https://www.pveducation.org/pvc/drom/solar-cell-operation/quantum-efficiency>
- Edwards HGM (2005) Modern Raman spectroscopy—a practical approach, vol. 36, no. 8, Smith E, Dent G (eds). Wiley, Chichester, pp 210. ISBN 0 471496685 (cloth, hb); 0471497940 (pbk)
- Fang J, Xuan Y (2017) Investigation of optical absorption and photothermal conversion characteristics of binary CuO/ZnO nanofluids. *RSC Adv* 7(88):56023–56033. <https://doi.org/10.1039/C7RA12022B>
- Frank AJ, Kopidakis N, van de Lagemaat J (2004) Electrons in nanostructured TiO_2 solar cells: transport, recombination and photovoltaic properties. *Coord Chem Rev* 248(13–14):1165–1179. <https://doi.org/10.1016/j.ccr.2004.03.015>
- Gwyddion. <http://gwyddion.net/>
- Instruments E, What is Raman Spectroscopy? *Raman Spectroscopy*. <https://www.edinst.com/us/blog/what-is-raman-spectroscopy/>
- Lakowicz JR (2006) General features of protein fluorescence
- Nasrollahzadeh M, Atarod M, Sajjadi M, Sajadi SM, Issaabadi Z (2019) Plant-mediated green synthesis of nanostructures: mechanisms, characterization, and applications, pp 199–322
- Raman CV, Krishnan KS (1928) A new type of secondary radiation. *Nature* 121(3048):501–502. <https://doi.org/10.1038/121501c0>
- Stamplecoskie KG, Manser JS, Kamat PV (2015) Dual nature of the excited state in organic–inorganic lead halide perovskites. *Energy Environ Sci* 8(1):208–215. <https://doi.org/10.1039/C4EE02988G>
- Tesa M, Gakamsky A, Thomson S (2018) Measurement of photoluminescence lifetimes in the μs range. *Tech Note*, May, 48–51
- von Hauff E (2019) Impedance spectroscopy for emerging photovoltaics. *J Phys Chem C* 123(18):11329–11346. <https://doi.org/10.1021/acs.jpcc.9b00892>
- Wang R et al (2019) Using atomic force microscopy to measure thickness of passive film on stainless steel immersed in aqueous solution. *Sci Rep* 9(1):13094. <https://doi.org/10.1038/s41598-019-49747-0>



Third-Generation Photovoltaic Cell Manufacturing Processes

Abdul Hai Alami , Shamma Alasad , Haya Aljaghoub ,
Mohamad Ayoub , Adnan Alashkar , Ayman Mdallal ,
and Ranem Hasan 

Abstract

Most of the manufacturing techniques mentioned in this chapter have been visited in the previous chapters of this book. However, they are presented here in more details and comprehensive description, making this chapter a self-contained reference.

1 Introduction

The conventional silicon manufacturing processes for photovoltaic wafer production are steeped in history. There is a limited margin for substantial improvement or enhancement that would either dramatically increase the yield or significantly reduce the production costs. On the other hand, thin-film and third-generation photovoltaics still have no standard, unanimously adopted manufacturing techniques. This leaves wide room for examining the best techniques that would maximize a figure-of-merit (FOM) that usually is the ratio between the produced power (or efficiency) and production cost of each cell. Another important aspect for second and third-generation PV is the amenability to

automation, or what is usually known roll-to-roll (R2R) production. The speed of which the PV cells are made, stitched together and prepared for dispatch largely and directly affect the FOM. And thus, the amenability of many of the available manufacturing processes discussed in this chapter to R2R manufacturing will be highlighted. The ease of use as well as capital investment are also important aspects to consider. This chapter will focus on technologies such as photolithography, spin coating, slot-die, and thermal evaporation as the most facile manufacturing technologies available on the market. Mastering these techniques requires time and experience to set all competing process parameters to values that produce the required response from the manufactured solar cells. The user should be prepared for a lot of material and consumable waste before the process could produce the desired outcomes.

2 Photolithography

Photolithography is a technique that is predominantly used to print surface contacts on silicon solar cells. The process is similar to ink-jet printing, where the ink sticks only to a predetermined design that is printed onto a substrate. In the case of semiconductor and solar cell device fabrication, the silicon wafer acts as the substrate, while the deposition, lithography, and etching process create the desired features (the ink). Given the optical exposure requirement to generate the pattern in semiconductor lithography, the process is referred to as “photolithography”. This process is extremely interesting as there exists a better access to 3D printers as well as cheap and advanced software to superpose the desired structure (e.g., front emitter contacts) on the silicon substrate. Figure 1 provides a schematic representation of the process steps.

To achieve a successful photolithographic feature, a series of steps need to be followed (Newport 2022). The process commences with substrate cleaning and preparation.

A. H. Alami (✉) · H. Aljaghoub · M. Ayoub · A. Mdallal ·
R. Hasan
University of Sharjah, Sharjah, United Arab Emirates
e-mail: aalalami@sharjah.ac.ae

H. Aljaghoub
e-mail: haljaghoub@sharjah.ac.ae

M. Ayoub
e-mail: mohamad.ayoub@sharjah.ac.ae

A. Mdallal
e-mail: ayman.mdallal@sharjah.ac.ae

S. Alasad · A. Alashkar
American University of Sharjah, Sharjah, United Arab Emirates
e-mail: g00070854@aus.edu

A. Alashkar
e-mail: b00028197@alumni.aus.edu

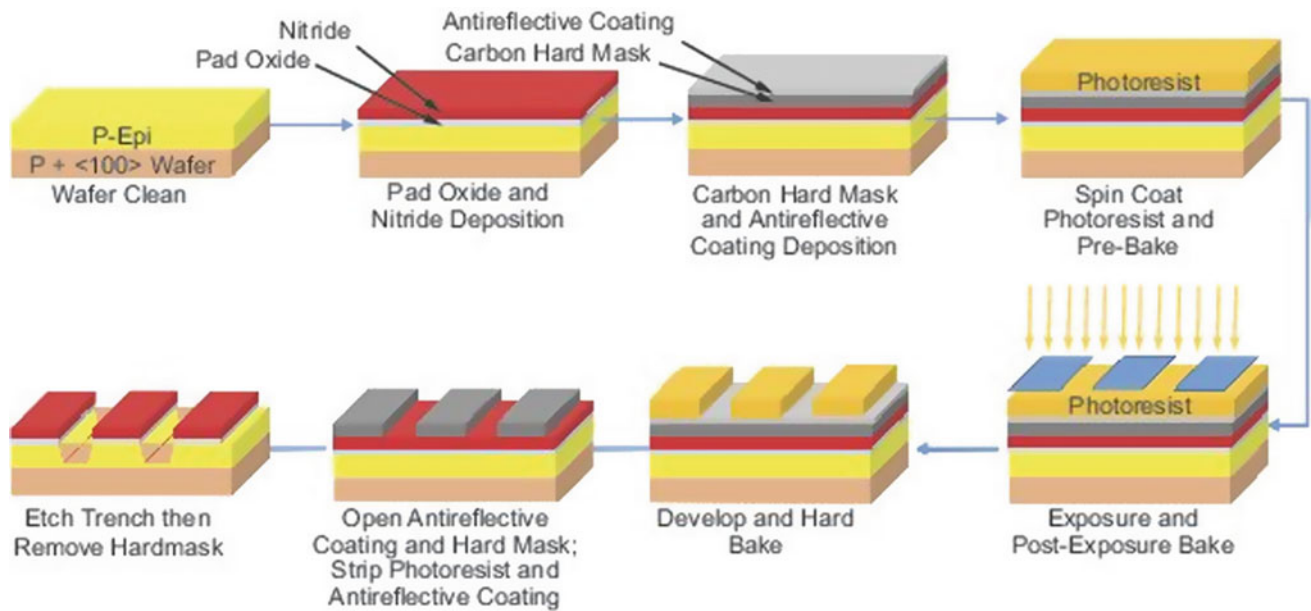


Fig. 1 Schematic representation of a semiconductor device patterning process (Newport 2022)

Next, layers of thermal oxide and silicon nitride are deposited on the substrate. This is followed by the inclusion of a carbon hard mask and an anti-reflective material. Subsequently, a layer of photoresist is then deposited, pre-baked, and aligned with the substrate, followed by an exposition to UV radiation and 4x 5x imaging. Post-exposure bake is then carried out to develop the pattern in the photoresist followed by a hard bake to remove any residue solvent. The dielectric anti-reflective coating (DARC) and hard mask pattern are opened through etching, and the photoresist as well as the DARC are removed. Trenches are then opened in the substrate through another separate etching process, and the hard mask is removed in the process. Finally, the surface is cleaned.

3 Screen Printing

Screen printing is a bulk coating process that is used in thin-film solar cells such as Cadmium-Telluride (CdTe), third-generation solar cells such as dye-sensitized solar cells and contact depositions in silicon based solar cells. Screen printing mainly consists of a frame around a silk-based screen and an either a metallic or a wooden squeegee. Figure 2 shows a depiction of the process, while Fig. 3 is an example of the process.

Other essential parts include a dye printed on a transparent sheet that is used to expose the desired coating shape on a UV-curable emulsion (a mold for the ink to follow while passing on the screen). The plastic-sheet-dye is placed beneath the uncured emulsion and above a UV-light source

for a substantial amount of time > 10 h. This step is crucial to ensure that the coated ink follows the targeted design.

1. Once the screen with a cured emulsion is prepared, it is placed on top of the to be coated substrate.
2. Then, the ink (deposited material) is placed on one end of the silk screen.
3. The screen is lifted at an angle with respect to the substrate.
4. Using the squeegee, the ink is spread to the other end of the silk screen to ensure that the entire emulsion is covered with ink.
5. The screen is placed back on top of the substrate.
6. Using the squeegee, and by applying sufficient pressure, the ink is pressed on the silk screen and passed onto the substrate.

Parameters that are important in the process of screen printing are the force applied by the squeegee (F), the speed of the squeegee (V_{sq}), the viscosity of the paste (η), the angle of the squeegee (α), and the print factor ($f(Q)$) shown in Eq. 1 (Hussain et al. 2022).

$$F[N] = \eta [N.s/m^2] V_{sq} [m/s] \frac{2\alpha [^\circ] \sin \alpha}{\alpha^2 - \sin^2 \alpha} f(Q) \quad (1)$$

3.1 Screen Printing—CdTe Thin-Film Solar Cells

In terms of thin-film CdTe solar cells, screen printing is mainly used to deposit the CdTe p type layer and the n-type

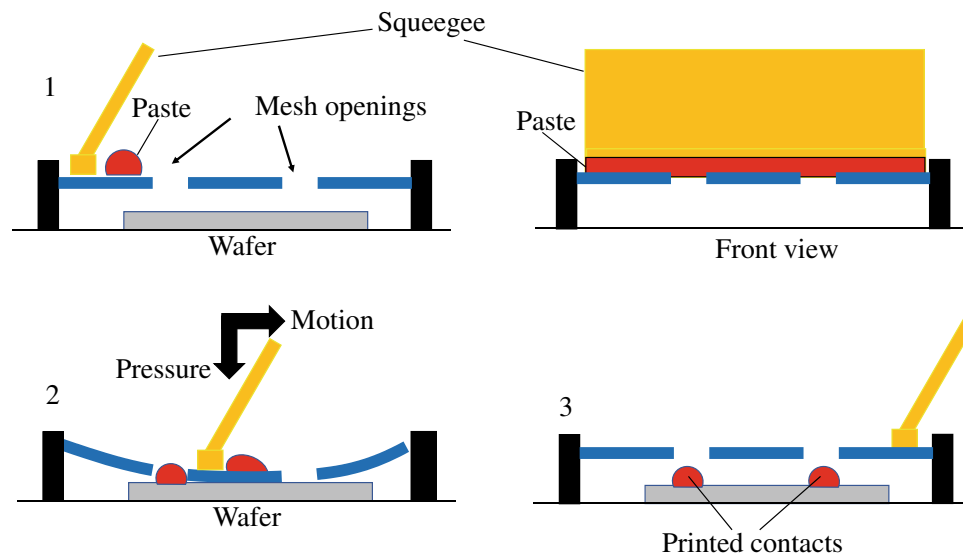


Fig. 2 Depiction of the screen-printing process steps

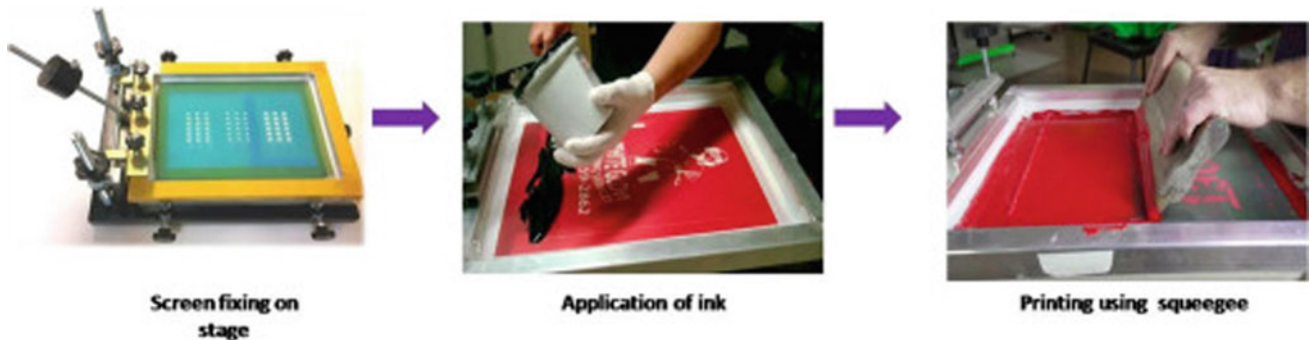


Fig. 3 Example of the screen-printing process (Hussain et al. 2022) (with permission 5273590576001)

CdS layer. However, the grain size based totally on these two materials through screen printing is very limited. Which is why the principle of sinters was introduced to these materials which consists of Cadmium chloride ($\text{CdCl}_2 \sim 1$ wt%) with an essential function that will help with the properties of the end film.

The sinter flux sticks to the host material (CdTe (5N) or CdS) in solid form. When the film is printed and goes through a heating post-treatment, the sinter flux melts and joins together the rather spread host materials grains and forms a film with larger grain size (up to $10 \mu\text{m}$ (<https://www.semanticscholar.org/paper/Thin-film-solar-cells-by-screen-printing-technology-Burgelman/f7a356e1c66f443a5604c07d69dbfc0de714cc77>) relative to the initial formation of it.

These screen-printing-inks are a combination of CdTe/CdS along with the previously mentioned sinters and a propanediol-based binder.

1. Respective inks are placed on the silk screen in the form of either CdTe or CdS particles along with CdCl_2 sinter flux.
 - a. The CdCl_2 sinter flux is chosen based on the solubility of both CdTe and CdS in it at moderate temperatures ($500\text{--}600^\circ\text{C}$), such as shown in Fig. 4.
2. The ink is printed on the screen and forms a film with small but dense grains.
3. The film is then heated to 600°C which melts the sinter flux and “sinters” the grains together forming large-grain-films of CdTe and CdS.
4. At 600°C , the vapor pressure reached by the CdCl_2 is sufficient to evaporate this volatile component leaving behind the desired materials on the substrate.

The process for screen-printing and sintering the CdTe/ CdCl_2 -based ink is showcased in Fig. 5.

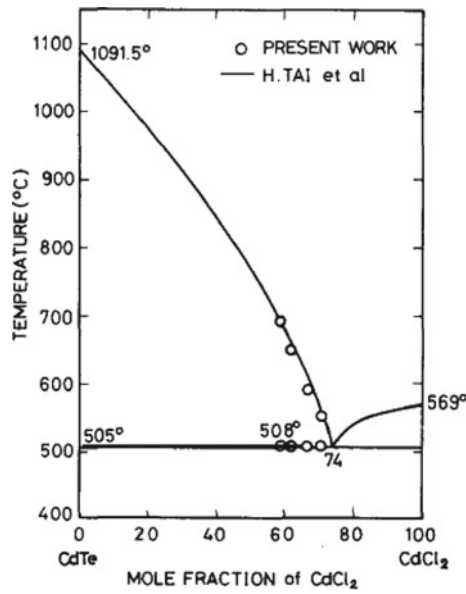
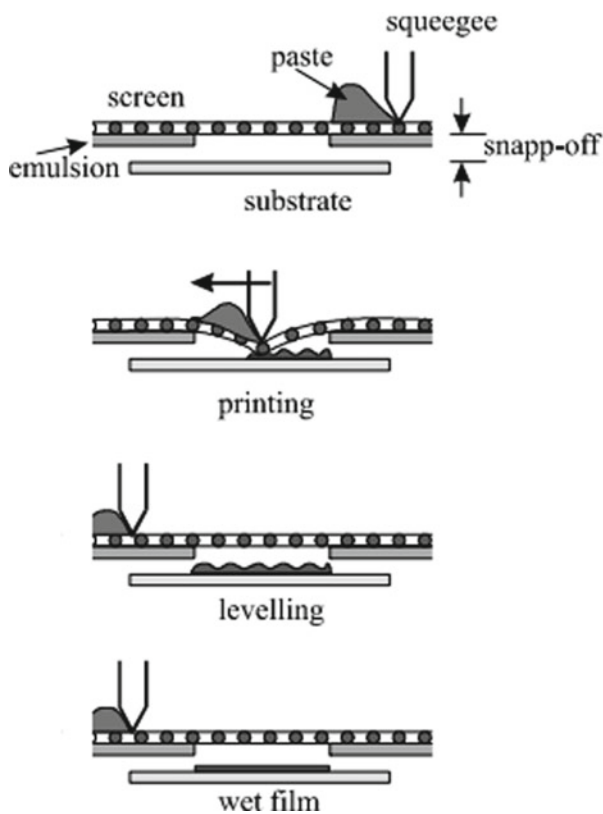


Fig. 4 CdTe–CdCl₂ phase diagram (Saraie et al. 1978)

3.2 Screen Printing—Silicon Solar Cells Contacts

Screen printing is used to achieve low-cost deposition of electrical contacts on silicon based solar cells. The material



of choice is silver paste due to its excellent electrical properties. The silver paste is a mixture of silver powder (providing conductive electrical properties) and glass frits (lead borosilicate-based) (Guo et al. 2011), which scratch the silicon cell's surface and allow the silver powder to segregate at a desired depth in the silicon substrate. Organic solvents are also used to provide fluidity to the paste for the ease of screen printing.

- Following the standard procedure for screen printing, shown in Fig. 2, the silver paste is printed using a cured emulsion that is based on the design and shape of the contact fingers. With some conditions that define the design of the emulsion such as
 - The opening of the reticule must be larger than the largest particle contained in the paste.
 - To form the front contact, the emulsion is formed in a mesh shape with typically 325 wires per inch and a wire diameter of 30 μm .
- After the printing is done, the cells are dried at a temperature using an IR furnace that would allow the evaporation of the organic solvent component in the silver paste.
- A firing step is carried using a time varying temperature profile (500–900 °C) to form the front contacts in their final form.

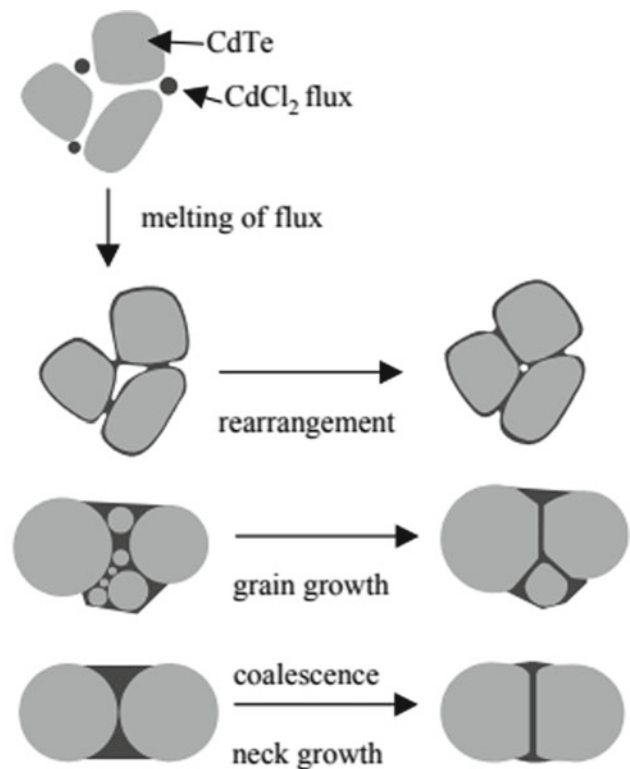


Fig. 5 Screen printing with subsequent sintering process (Burgelman 1998)

4. During the firing step, the glass frits act as a sinter that allows a larger growth of the silver contacts. Achieving the same purpose as that by CdC_2 in CdTe-based thin-film cells.
5. The glass frit is also able to etch through deposited layers on the silicon substrate such as anti-reflective coating and passivating layers.

3.3 Screen Printing—Dye-Sensitized Solar Cells

Screen printing can be used to deposit essential layers in dye-sensitized solar cells such as a silver grid, for parallel type metal grid embedded DSSCs which is the closest we got in scaling up this type of solar cells as shown in Fig. 6, and the TiO_2 active layer.

1. A silver grid is deposited on an FTO surface and then dried at around $200\text{ }^\circ\text{C}$.
 - a. This layer enhances the conductivity of the cell by decreasing the sheet resistance to about $0.2\ \Omega/\text{cm}$.
2. The TiO_2 active material is screen printed using the previously mentioned screen-printing procedure.
 - a. The printed film is then dried and heated up to $500\text{ }^\circ\text{C}$ to activate the sintering process.
 - b. The dried TiO_2 film is then immersed in a dye solution ruthenium (II) in absolute ethanol ($\sim 70\%$) for $>$ day (Ramasamy et al. 2007).
 - c. The counter electrode which consists of platinum and an acidic solvent is screen printed and then sintered accordingly at $400\text{ }^\circ\text{C}$.

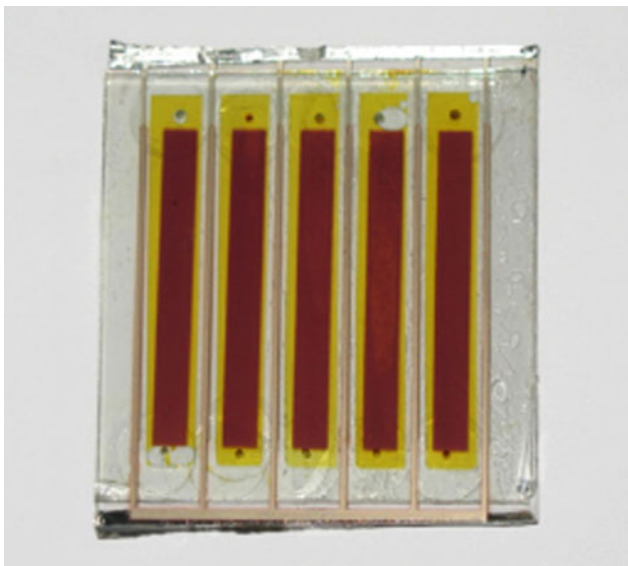


Fig. 6 Screen printed metal-grid embedded DSSC (Ramasamy et al. 2007) (With permission 5274140611103)

4 Spin Coating

Spin coating is a technique used to uniformly spread thin films of polymers, organic materials (Orava et al. 2014), or metal oxide inks (Solution Processed Metal Oxide Thin Films and for Electronic Applications 2020), on substrates such as glass, FTO, and flexible plastics. It utilizes the centrifugal force applied on a solution to spread it homogeneously over the selected substrate. Spin coating is also used in the microelectronics industry (Summers 2013), and it is at the forefront of the third-generation solar cells scene. In this section, the general spin coating system components, coating steps and principles, the advantages and disadvantages, as well as the application of spin coating in perovskite solar cells will be discussed.

4.1 System Components

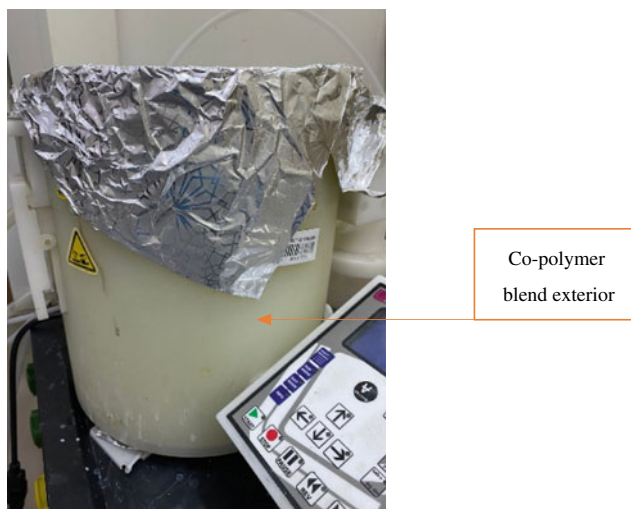
The heart of the spin coating machine is the rotating platform, the size (diameter), and rotational velocity of which determines the system capability. The motor selection is also important as it determines the torque applied on the platform and hence the ultimate rotational speeds. Although the process is extremely easy to use and many people have chosen to make the device themselves (check youtube.com for many examples), it is considered one of the most material intensive processes as the splash from the rotational motion of the solution before it solidifies is significant.

4.1.1 Device Hub

A specifically designed sturdy exterior is used to harbor the electrical and mechanical components that allow a spin coater to operate steadily under high rotational speed conditions, and it should also be of high tolerance toward solvents that are used in thin-film precursors. The exterior can be made of steel (<https://www.ossila.com/products/spin-coater>), natural polypropylene, which is a thermoplastic that offers good physical and chemical properties (<https://www.boedeker.com/Product/Polypropylene-Natural>), high chemical resistant PTFE that is stable in corrosive media (<http://www.standard-ptfe.com/chemical-resistance-guide-of-ptfe-and-filled-ptfe.php>, <https://www.spincoating.com/en/spin-coater-models/spincoater-polos300-advanced-spin-coating-machine/28/>), or solid co-polymer blends that achieve desired physical, mechanical, and chemical properties (<http://www.laurell.com/spin-coater/?model=WS-650-23B&s=2>), such as shown in Fig. 7, etc.

4.1.2 Motor

A spin coater motor provides the required torque to indirectly rotate the substrate, usually glass or FTO, along with



Co-polymer
blend exterior

Fig. 7 Spin coater exterior

the solution/precursor dispensed on it at desired speeds, reaching up to 12,000 rpm in some models (<https://www.spincoating.com/en/spin-coater-models/spincoater-polos300-advanced-spin-coating-machine/28/>, <http://www.laurell.com/spin-coater/?model=WS-650-23B&s=2>). In a DIY project, according to Teixeira et al. (2020), something as simple as the motor that is used to lift up or lower down windows of a car has sufficient torque (~ 12 N.m) to achieve speeds of 5000 rpm, which is suitable for some applications such as the coating of electron/hole transport layers used in third-generation solar cells.

Fig. 8 Vacuum-assisted substrate holder—side and top view



4.1.3 Substrate Holder

The substrate holder is the component that is directly being rotated by the motor of the spin coater. There are two main designs that are used in today's market:

- Vacuum-assisted circular turntable: Where the substrate is placed on a hollowed circular surface with an O-ring gasket, such as shown in Fig. 8, that aids with holding down the sample using the vacuum achieved between this surface and the substrate via an external vacuum-pumping system connected to the spin coater, such as shown in Fig. 9.
- Cavity Chuck: Alternatively, in some spin coater designs, the substrate is placed in a cut out cavity, also known as a chuck. The chuck boundaries are used to hold down the substrate in place without the need of a vacuum-pumping system, such as shown in Fig. 10.

4.1.4 Cover

Spin coaters utilize covers made of tempered glass or the same material as the device hub/interior, such as shown in Fig. 11. The cover is used to prevent the flinging of the precursor outside the spin coater boundaries while coating at high speeds, which is used as a safety measure and to avoid contamination of adjacent lab equipment.

4.1.5 Interface

Spin coaters are equipped with an integrated operating system that is accessible through an attached interface, shown in



Fig. 9 Spin coater vacuum system-nitrogen tank—compressor



Fig. 10 Chuck substrate holder

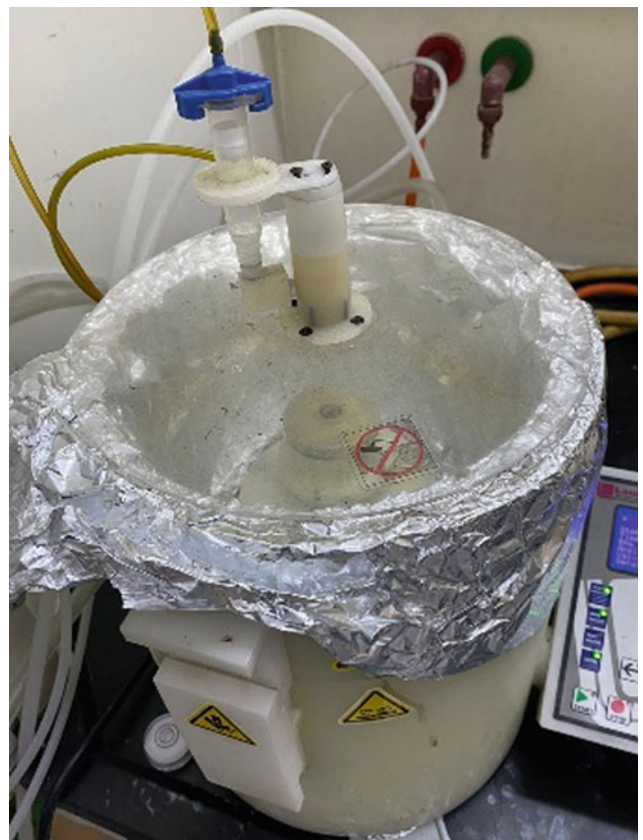


Fig. 11 Spin coater cover



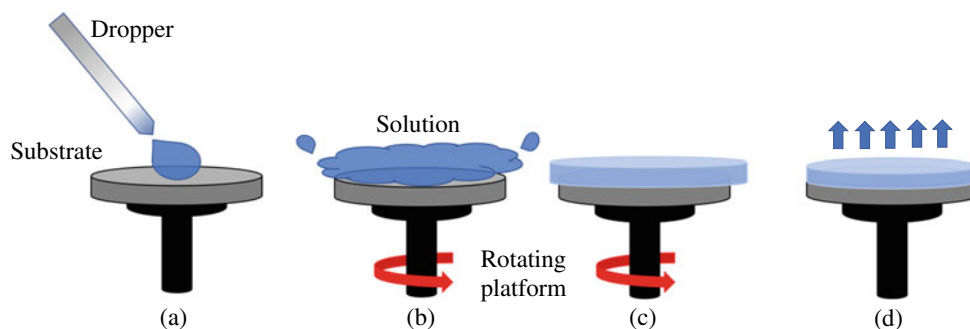
Fig. 12 Spin coater interface

Fig. 12. Through this interface, parameters such as rotational speed, time, stepping up speed, as well as multi-step programs can be input by the user according to their experiment's requirements.

4.2 Coating Steps and Principle

A spin coating process can be subdivided into 5 steps, which are pre-deposition, deposition, spinning up, spinning off, and evaporation (<https://www.ossila.com/pages/spin-coating>) such as shown in Fig. 13.

Fig. 13 Spin coating process steps **a** deposition, **b** spin up, **c** spin off, and **d** evaporation (Yilbas et al. 2019) (with permission: 5260980863854)



1. Pre-deposition

In some cases, substrates need to be UV treated to increase the wettability of the surface. Otherwise, the precursor would not stick to it and consequently ruin the end-film result.

2. Deposition

The precursor is dispensed onto the substrate using a pipette, and this can be done while the substrate is stationary (static spin coating), or it can be done while the substrate is rotating (dynamic spin coating) (<https://www.ossila.com/pages/spin-coating>). Dynamic spin coating is preferred over static spin coating in situations where the solvent's evaporation temperature is very low. Going through the dynamic route gives the solvent less time to evaporate uncontrollably in comparison with static spin coating, which leads to more reproducible results.

3. Spinning up

Centrifugal force spreads the dispensed precursor radially outwards, which results in covering the whole surface of the substrate (Mishra et al. 2019).

4. Spinning off

At this stage, the viscous force along with surface tension is dominating. This causes the excess precursor to be flung off the substrate, resulting in an even and level film across it (Mishra et al. 2019).

5. Evaporation

High volatile components (components that can evaporate at room temperature) are spontaneously evaporated at this stage, leaving behind the dry desired film. In some cases, such as the coating of the perovskite active layer in third-generation perovskite solar cells, the evaporation

process is aided with anti-solvents, such as chlorobenzene. Anti-solvents are dispensed during the coating process, and they result in better thin-film results by increasing the solvents evaporation rate (Yilbas et al. 2019).

The end-film thickness of a spin coating process can be estimated by Eq. (2), that is, based on the Emslie, Bonner and Peck model (Eq. 3).

$$h = \frac{h_0}{\sqrt{\left(1 + \frac{4\rho\omega^2 h_0^2 t}{3\eta}\right)}} \quad (2)$$

where

h_0 : thickness of the film at $t = 0$ (beginning of the coating process).

ρ : density of the fluid layer.

ω : rotational speed.

η : viscosity of the fluid layer.

t : time.

Similarly, the Emslie, Bonner, and Peck Model can be shown as follows:

$$\frac{\delta h}{\delta t} + \frac{\rho\omega^2 r}{\eta} h^2 \frac{\delta h}{\delta r} = -\frac{2\rho\omega^2 h^3}{3\eta} \quad (3)$$

where

$\frac{\delta h}{\delta t}$: rate of change in thickness.

$\frac{\delta h}{\delta r}$: rate of spreading.

However, with no regard to the evaporation of the solvents, the thickness obtained from this equation/model is not accurate.

a. Advantages and Disadvantages of Spin Coating

Advantages

- (i) Has the ability to achieve uniform thin films on desired substrates at ease.
- (ii) Thickness of the desired thin film can be controlled to an acceptable extent.
- (iii) Evaporation of solvents is aided with airflow due to the rotation of the turntable/substrate.

Disadvantages

- (iv) High material wastage—up to 98% of the deposited precursor is flung off during the coating process, and only 2% is left on the substrate (Sahu et al. 2009). This makes spin coating relatively more expensive than other coating techniques where there is less material wastage.
- (v) Spin coating is not compatible with roll-to-roll production lines. This limits its use to lab-scale

experiments and prevents spin coating from making the transition into commercial applications. Substrate size is also limited to a small area, depending on the substrate holder.

b. Spin Coating in Perovskite Solar Cells.

Spin coating is widely used in perovskite solar cells' fabrication. It is used to deposit the electron transport layer (e.g., TiO₂) on FTO substrates, as well as the perovskite active layer and the hole transport layer (e.g., Spiro-OMeTAD) accordingly. The coating procedure is standard for all the layers with the addition of anti-solvent treatment for the perovskite active layer as discussed earlier.

5 Slot-Die Coating

Slot-die coating was invented by Beguin in 1954. The system comprised of a coating-die-head that passed a ribbon of the coating-material onto an adjacent strip-material (<https://patents.google.com/patent/US2681294A/en>). It is currently being used in various fields, such as batteries, for depositing the electrolyte slurry, optical coating, for anti-reflective coatings applied on windows and most recently, slot-die coating has been portrayed as the gateway between third-generation solar cells and commercialization (<https://www.ossila.com/pages/slot-die-coating-theory>). A modern lab-scale slot-die coater is shown in Fig. 14.

Slot-die coating has a great potential for the application in third-generation solar cells given that it is a pre-metered technique, where the thin-film thickness is dependent on the precursor/solution flow rate, it is also dependent on the slot-die-head's distance relative to the to be coated substrate, coating speed, heating temperature, which allows for a lot of room for optimization. Furthermore, slot-die coating is compatible with roll-to-roll (R2R) and sheet to sheet (S2S) production lines, where third-generation solar cells' precursors that make up electron transport materials (ETMs), hole transport materials (HTMs), and perovskite active layers, in liquid form, can be deposited on rolled or sheet flexible substrates making scaling up third-generation solar cells achievable in the near future.

5.1 Device Components

There are 3 main parts that a conventional slot-die coater consists of.

1. The slot-die-head, which is responsible for the direct precursor distribution upon substrates, has various design



Fig. 14 Slot-die coater

parameters that can be optimized according to the coating application.

2. The pumping (metering) system, which is responsible for the transfer of precursors to the head and supplies a constant or a varying flow rate.
3. The coating stage, which is where substrates are placed, determines the coating speed by how fast the stage is moving, using stepper motors, relative to the head or vice versa in some designs. A slot-die coater's stage can also utilize an integrated heater that meets the requirements of some applications.

5.2 Slot-Die-Head

A conventional slot-die-head, shown in Fig. 15, consists of an inlet, manifold, lands, and lips. Moreover, accessories such as shims and meniscus guides can be utilized to optimize and adjust the overall coating process.

1. When the precursor enters the slot-die-head through a metering system (e.g., a syringe pump), the first thing it faces is the inlet hole.
2. Then, the precursor starts to fill the manifold that is usually placed directly beneath the inlet, which then spills the precursor out to the land and slot of the

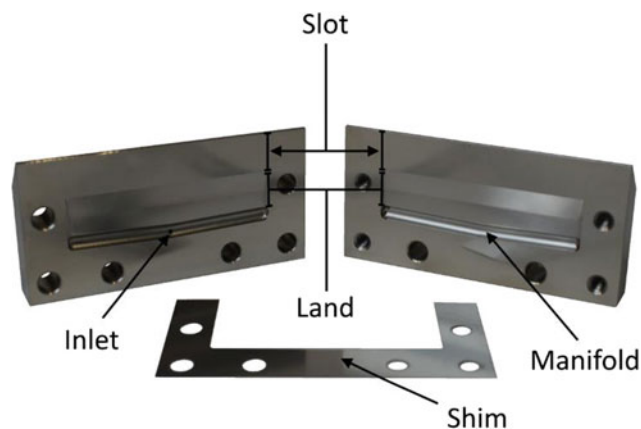


Fig. 15 Slot-die coating head (<https://www.ossila.com/pages/slot-die-coating-theory>)

die-head subsequently in order to start the coating process.

There are various designs of a slot-die-head's manifold that heavily influence the coating process. These designs are totally dependent on the difference in distances between the inlet and the exit of the die-head, and the manifold's lowest point and the exit of the die-head, such as shown in Fig. 16.

1. The T shaped manifold, shown in Fig. 16, presents an equal distance from the inlet and the edge of the manifold to the die-head exit. This results in a pressure difference moving away from the inlet and a variable (lower) flow rate near the edge of the manifold, as well as an uneven spread of the solution across the die-head and consequently the substrate (<https://www.ossila.com/pages/slot-die-coating-theory>).
2. Overcoming the issue of uniformity of the flow across the die-head exit, a coathanger manifold, shown in Fig. 16, can be utilized. The coathanger manifold reduces the distance from the manifold edge to the die-head exit while moving away from the inlet, which results in a uniform flow of the precursor across the width of the die-head exit. However, this design is dependent on the viscosity of the precursor that is being coated, and must be optimized accordingly, e.g., using shims to increase the width of the die-head channel (<https://www.ossila.com/pages/slot-die-coating-theory>).
3. To operate independently from the viscosity of the precursor, a constant shear manifold shown in Fig. 16 can be used. It varies the distance from the manifold edge to the exit of the die-head in a non-linear fashion, which in turn ensures a constant flow from the manifold edge to the die-head exit (<https://www.ossila.com/pages/slot-die-coating-theory>).

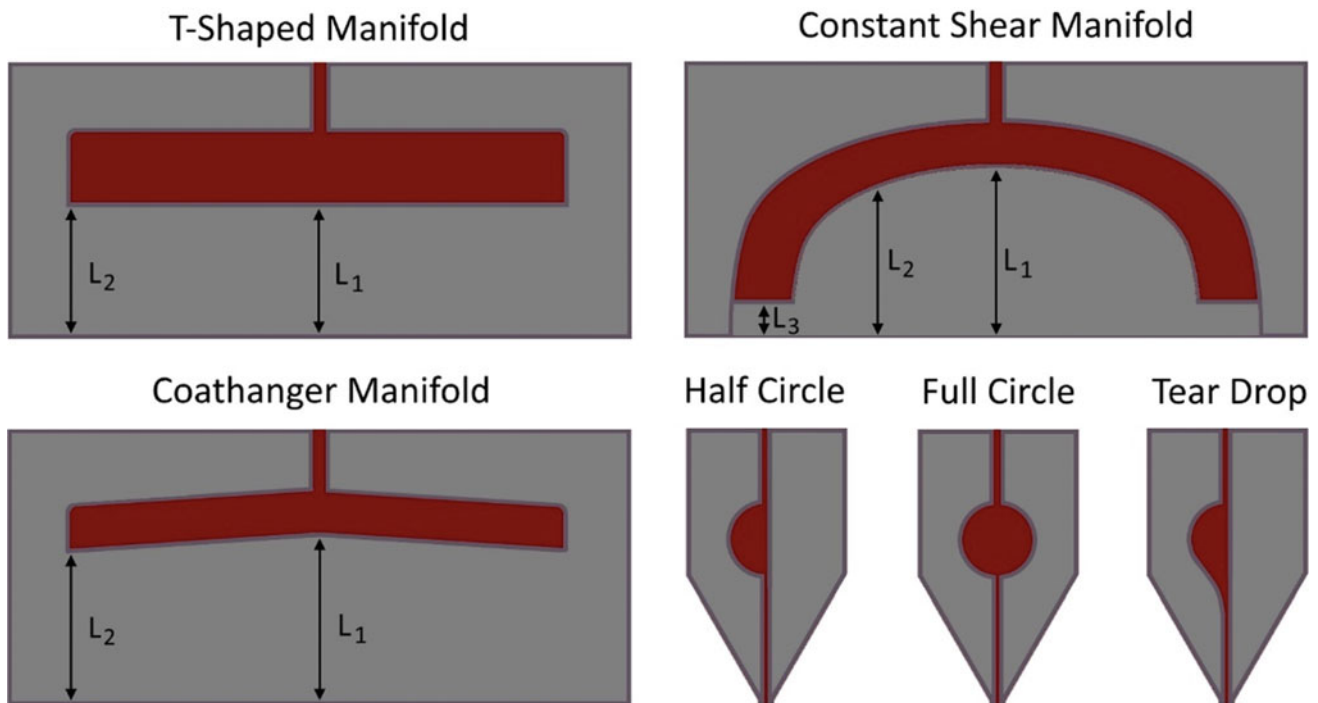
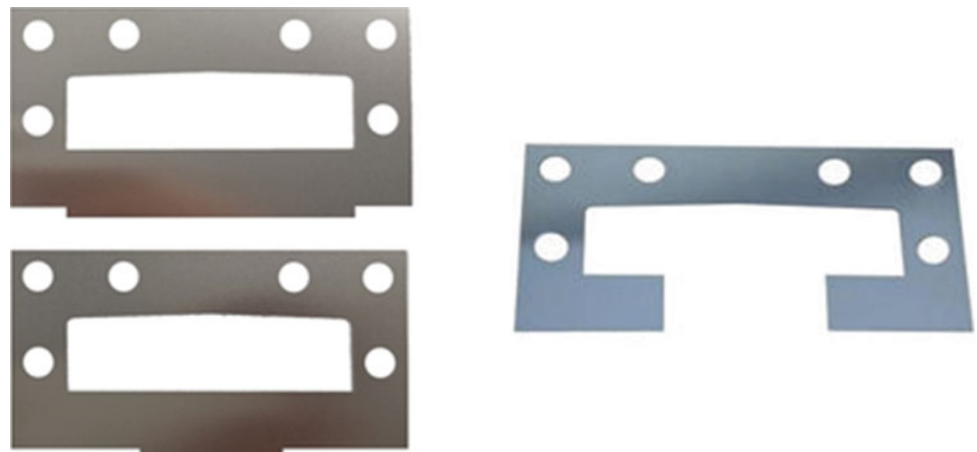


Fig. 16 Various manifold designs (<https://www.ossila.com/pages/slot-die-coating-theory>)

Fig. 17 Meniscus guide shim (https://www.ossila.com/products/slot-die-head?_pos=1&_sid=bc1331a13&_ss=r&variant=41159008878755)



For more info on head designs, the reader is encouraged to visit Ossila Website at: <https://www.ossila.com/pages/slot-die-coating-theory>.

Shims and meniscus guides can be used to have better control over the coating process in a slot-die coater as shown in Fig. 17. Depending on the design and number of shims used to adjust the width of the die-head channel, the die-outlet velocity can be directly controlled (Shin et al. 2020; Han et al. 2014).

Meniscus guides can also be implemented in order to control and direct the meniscus (point of contact between the die-head and the substrate) formation outside the die-head

and to adjust the relative distance from the die-head to the substrate (Krebs 2009), given that it extends out of the die-head lip.

5.3 Metering System

5.3.1 Syringe Pump

A syringe pump, shown in Fig. 18, is a lab-scale metering subsystem in slot-die coaters. It consists of a motor, pushing block, and a syringe. A precise motor moves the pushing block across a railway against the plunger flange of a syringe



Fig. 18 Syringe pump (<https://www.ossila.com/products/syringe-pump>)

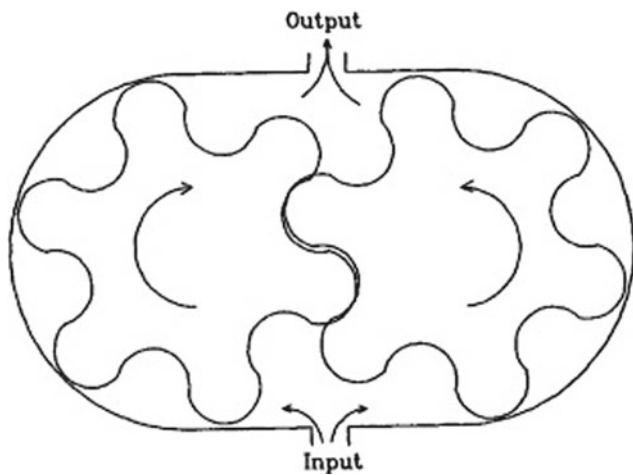


Fig. 19 Rotary pump with a gear and lobe design (Bajpai 2018) (with permission 5262570110935)

that can displace tiny volumes of the precursor into the slot-die-head with flow rates in the range of micro-liters per second. Lab-syringe pumps provide the option for complex programs of stepping up/down dispense rates depending on the application/experiment.

5.3.2 Rotary Pumps

A rotary pump (design shown in Fig. 19) is used for large-scale applications in slot-die coating. A liquid/precursor enters the rotary pump from one side and fills the passages of the gears, thus displacing them. As the gears are rotating, they pump the fluid/precursor away in the direction of the output of the pump. They are suited for viscous fluids, however, highly-viscous fluids require bigger pumps with low rotating speeds (Bajpai 2018).

5.4 Coating Principle

Slot-die coating is based on the delivery of liquids through the slot of the die-head and the deposition onto moving substrates by filling the gap between them. The boundaries of the die-head-substrate-gap are defined by upstream and downstream menisci that form what is known as the coating bead (Ding et al. 2016), such as shown in Fig. 20. The operation of slot-die coating is limited by the coating speed, liquid dispense rate, die-head-substrate gap, and liquid viscosity. There are three models that define the operating limits of slot-die coating, which are competing forces that influence the coating bead (<https://www.thefreelibrary.com/Comparison+of+vertical+and+horizontal+slot+die+coatings-a0171141698>; Romero et al. 2006).

1. Capillary model
2. Viscous model
3. Viscocapillary model

These models define what is known as the stable coating window, where any deviation away from it will cause defects in coated film. Defects such as chatter and ribbing, where the thickness of the coated film varies along the substrate with visible lines, uncontrollable dripping of the liquid, etc. (<https://www.ossila.com/pages/slot-die-coating-theory>).

5.4.1 Capillary Model

The coating stability in slot-die coating is totally dependent on the stability of the coating bead mentioned earlier. To ensure the stability of the coating bead, Beguin suggested the use of a vacuum box on the upstream meniscus (<https://patents.google.com/patent/US2681294A/en>). Ruschak (1976) set a model that defines limits for the vacuum pressure applied on the upstream meniscus based on capillary pressure on the coating bead with little regard to viscous effects, by using the inequalities shown in Eqs. (4) and (5).

$$-\frac{\sigma_u(1 + \cos \theta)}{h_u} + 1.34Ca^{\frac{2}{3}}\frac{\sigma_d}{t} \leq \Delta p \leq \frac{\sigma_u(1 - \cos \theta)}{h_u} + 1.34Ca^{\frac{2}{3}}\frac{\sigma_d}{t} \quad (4)$$

$$0 \leq \frac{1}{t} \leq \frac{1.49}{h_d} Ca^{-\frac{2}{3}} \quad (5)$$

where

σ : surface tension (upstream and downstream) of the menisci.

σ_d : represents the surface tension under atmospheric pressure.

Δp : vacuum pressure difference between the upstream and downstream menisci.

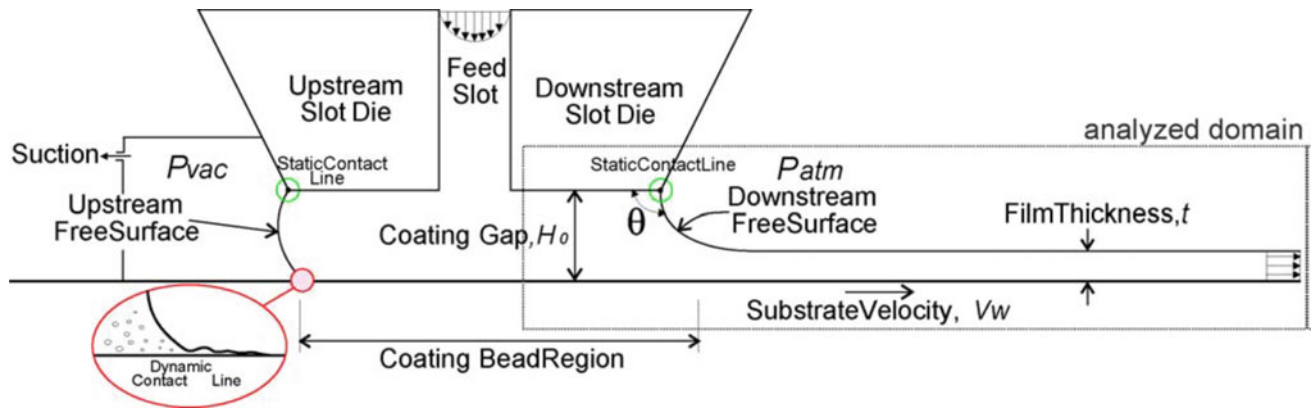


Fig. 20 Coating bead (Romero et al. 2006) (with permission 5262941365999)

Ca: capillary number (effect of viscous forces versus surface tension forces on the interface between a liquid and a gas).

h : coating gap.

θ : dynamic contact angle.

The upper and lower limits of the inequality shown in Eq. (4) represent the upper and lower limits of the vacuum pressure shown in Fig. 21. However, the line defining the upper limit does not cross the axis represented by $\frac{1}{l}$, which means that the thickness is infinitely large, making this model valid for thin coated films only (Ruschak 1976). The thin-film thickness when the pressure difference is zero is represented in Eq. (6).

$$t_0 = \frac{1.34\sigma_d}{\sigma_u} \text{Ca}^{\frac{2}{3}} \frac{h_u}{(1 + \cos \theta)} \quad (6)$$

As per Fig. 21, going below the coating window results in the upstream meniscus moving toward the exit of the die-head, leading to air entrapments and the formation of vortices this causes defects such as the ribbing and chattering

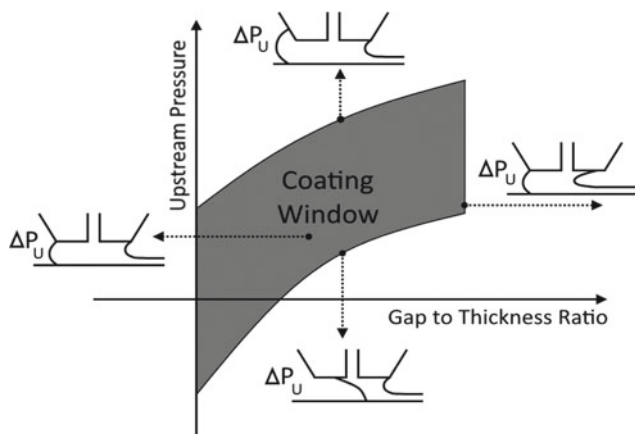


Fig. 21 Illustration of coating window with meniscus (<https://www.ossila.com/pages/slot-die-coating-theory>)

effects mentioned earlier (<https://www.ossila.com/pages/slot-die-coating-theory>).

Moving above and toward the upper limit of the coating window (usually due to the use of a vacuum box) causes the upstream meniscus to move past the upstream lip and to swell. This causes dripping and an uncontrollable variation in the thickness of the meniscus (<https://www.ossila.com/pages/slot-die-coating-theory>).

To the right of the coating window, the downstream meniscus starts to recede moving from left to right across the die-head, which causes air entrapments and the formation of bubbles that affect the end film (<https://www.ossila.com/pages/slot-die-coating-theory>).

5.4.2 Viscous Model

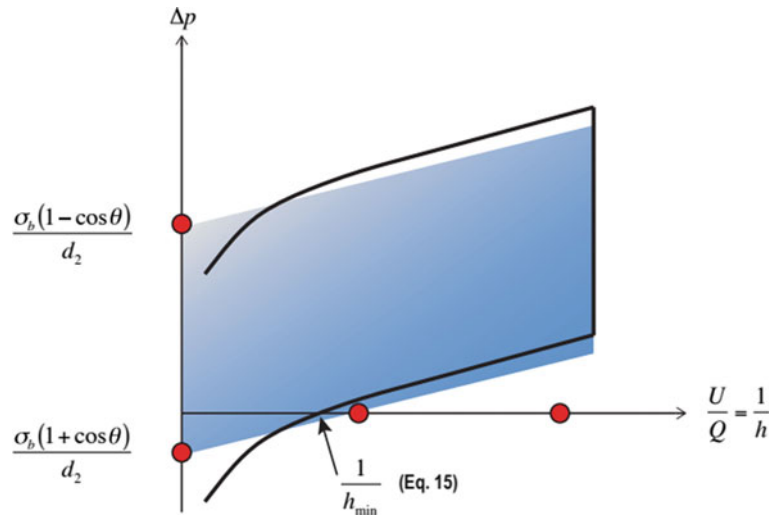
The operation in this model ignores capillary effects and takes into account viscous effects only on the coating bead (Higgins and Scriven 1980). In this model, the upstream meniscus is allowed to move across the upstream lip of the die-head, up until the downstream edge of the upstream lip, and variations in the coating speed or the vacuum pressure can lead to defects in the coated film (Ding et al. 2016). The stable coating window with respect to the vacuum pressure is defined in following inequality from Eq. (7). Where U is the coating speed and l is the lip length.

$$\frac{6\mu Ul_d}{h_d^2} \left[1 - \frac{2t}{h_d} \right] \leq \Delta p \leq \frac{6\mu Ul_d}{h_d^2} \left[1 + \frac{l_u h_d^2}{l_d h_u^2} - \frac{2t}{h_d} \right] \quad (7)$$

5.4.3 Viscocapillary Model

In the viscocapillary model, both capillary and viscous models are taken into account. Contrary to the viscous model, the upstream meniscus is not treated as pinned to the upstream edge of the die-head lip; however, it is treated as if it is free to move, which results in the following operating limits for the vacuum pressure provided in Eqs. (8) and (9) and illustrated in Fig. 22.

Fig. 22 Viscocapillary model stable coating window (Higgins 2011)



$$\Delta p \geq \frac{6\mu U l_d}{h_d^2} \left[1 - \frac{2t}{h_d} \right] - \frac{\sigma_u (\cos \theta_s + \cos \theta)}{h_u} + 1.34 \text{Ca}^{\frac{2}{3}} \frac{\sigma_d}{t} \quad (8)$$

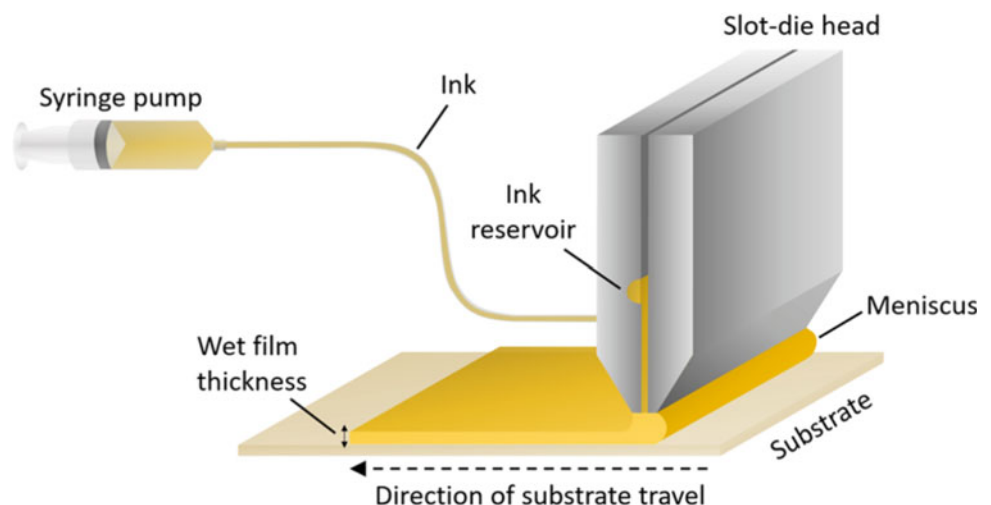
$$\Delta p \leq \frac{6\mu U l_d}{h_d^2} \left[1 + \frac{l_u h_d^2}{l_d h_u^2} - \frac{2t}{h_d} \right] - \frac{\sigma_u (\cos \theta_s + \cos \theta)}{h_u} + 1.34 \text{Ca}^{\frac{2}{3}} \frac{\sigma_d}{t} \quad (9)$$

5.5 Slot-Die Coating in Third-Generation Solar Cells

Slot-die coating is currently one of the most attractive techniques to fabricate third-generation solar cells (dye-sensitized solar cells and perovskite solar cells). This is

due to its capability to uniformly coat thin films across large areas, with throughput speeds reaching 600 m/min (Patidar et al. 2020) as well as the high compatibility with R2R (roll-to-roll) and S2S (sheet-to-sheet) production lines, such as shown in Fig. 23. Unlike spin coated perovskite/third-generation solar cells, the use of an anti-solvent is not an option. Post-treatments such as vacuum or nitrogen quenching are used to extract/remove the solvents from the wet film before it dries and crystalizes. For vacuum quenching, a coated perovskite sample is subject to a low level of vacuum pressure in vacuum chamber in order to extract away the solvents, most commonly dimethylformamide (DMF) and dimethyl sulfoxide (DMSO). Nitrogen quenching is used to assist with the evaporation of the previously mentioned solvents and to aid with the crystallization of the film (Du et al. 2020).

Fig. 23 Slot-die coating process (Patidar et al. 2020) (with permission 5263681213473)



6 Thermal Evaporation

Thermal evaporation is a physical vapor deposition technique that is used regularly in third-generation solar cells for depositing thin films that take on the transport of generated electron/hole pairs toward the solar cells' contacts, also known as electron/hole transport layers as well as gold/silver contacts. It uses resistive heating (joule heating) to evaporate a solid material, in powder or pallet form, onto a desired substrate in a vacuum environment. Thermal evaporation is suited for high rates of deposition, simple and considered to be of low cost. In this section, thermal evaporation device components and coating principle will be discussed.

6.1 Device Components

A thermal evaporator, such as shown in Fig. 24, consists of a



Fig. 24 Thermal evaporator

Fig. 25 Thermal evaporator glass chamber with protective mesh around it **a** open and **b** closeup



(a)

(b)

1. A glass chamber, such as shown in Fig. 25, which comes in a bell shape and ensures an isolated environment within it with the aid of rubber sealant gaskets.
2. A chamber elevator, highlighted in Fig. 24, is responsible for lifting and lowering the glass chamber during the beginning and the end of a coating process.
3. Resistive heaters/boat holder, such as shown in Fig. 26, which takes upon the task of raising the temperature of the boat that harbors the target/source material by passing an electrical current through it.
4. A substrate(s) holder, shown in Fig. 27, which is usually right above the boat/resistive heaters, is where the substrates are placed. A substrate holder is fixed on a rotating platform to ensure that all the substrates are equally exposed to the evaporated material. Substrates are secured onto the substrate holder using a heat resistant double tape.
5. Vacuum pump/nitrogen system is connected to the thermal evaporator chamber in order to achieve the desired vacuum environment required for a smooth evaporation/deposition process. See Fig. 25a for the vacuum pump in the lower left of Figure.
6. A control interface is used to lift or lower the glass chamber, trigger the rotation of the substrate holder, start the vacuum/vent process, and control the current flowing through the resistive heaters.

6.2 Thermal Evaporation Coating Steps

1. A source material is usually placed in a tungsten crucible (boat), and tungsten is most commonly used due to its high melting temperature of 3410 °C (<https://www.britannica.com/science/tungsten-chemical-element>).

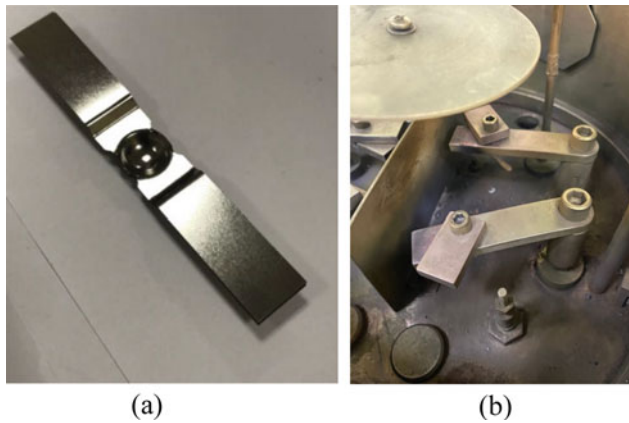


Fig. 26 a Boat/ resistive heaters, b location in thermal evaporator

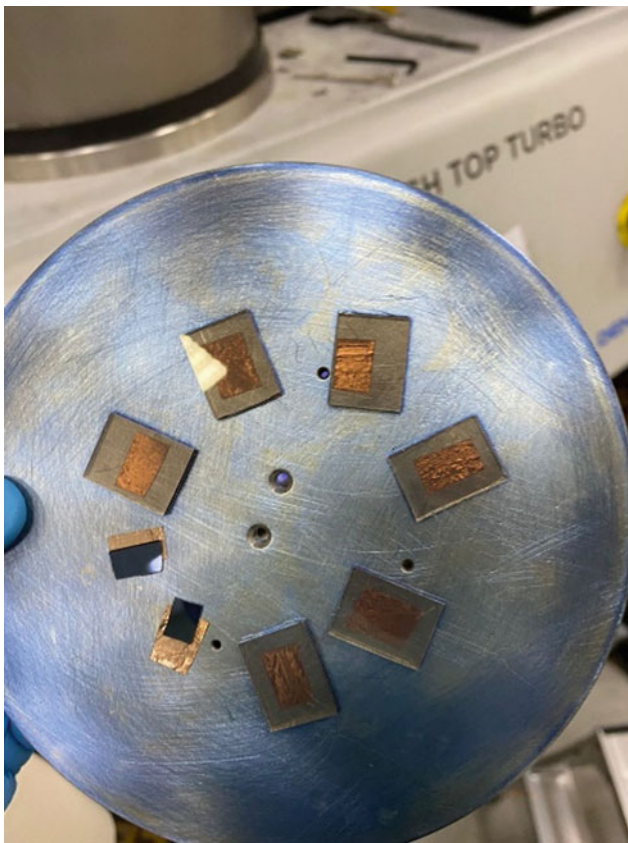


Fig. 27 Substrate holder

2. The targeted substrate, usually glass/conductive oxide coated glass or metal, is secured on a substrate holder above the boat.
3. A vacuum pump creates an inert environment for the evaporation to take place in, this step is crucial not to cause unnecessary oxidation of the deposited thin film (Lévy 2016).

4. After reaching a low enough vacuum pressure, around 10^{-2} Pa (Lévy 2016), the coating process can start.
5. Through a control interface, the current passing through the boat which results in heating it is stepped-up gradually up until the source material starts vaporizing—evaporation temperature is reached.
6. As the material is evaporating, it leaves the boat and ascends toward the substrate, and the inert condition removes the air-drag factor allowing for a smooth transition of the vapor from the boat to the desired substrate.
7. When the vapor reaches the relatively colder substrate, a phase change process takes place leading to a solidified thin film on the substrate.
8. Through the interface of the thermal evaporator, the evaporation rate can be always obtained. When a desired evaporation rate is reached, the current passing can be held constant unless there is a variation in the evaporation rate due to the lack of leftover source material.
9. When the thin film reaches a desired thickness, the current is stepped down gradually to protect the source material and the boat from fracture, and the thermal evaporator chamber is vented.
10. The substrate is then removed from the thermal evaporation chamber, and it can undergo any desired post-deposition treatment (i.e., annealing).

The overall coating process is shown in the schematic presented in Fig. 28.

7 Doctor Blade Coating

Doctor blade coating is a technique that has been utilized in the deposition of the perovskite active layer in perovskite solar cells and third-generation solar cells in general, such as shown in Fig. 29. The solution to be coated is placed in front of the blade, which is held at a set distance from the targeted substrate. The blade is then moved across the substrate, spreading the solution and resulting in a wet film with a desired thickness. The base operation of doctor blade coating deems it to be roll-to-roll compatible, allowing for its implementation in high throughput applications.

In terms of material wastage, doctor blade coating is said to have a solution loss of about 5% (Mishra et al. 2019) after an optimization process has taken place. In comparison with slot-die coating which is a similar roll-to-roll printing technique, doctor blade coating requires way less precursor solution to operate (Yilbas et al. 2019). Doctor blade-coated films' thicknesses are controlled by optimizing the concentration of the perovskite precursor (by adjusting the ratio and volume of the organic solvents that are used), blade speed, and the blade-substrate distance.

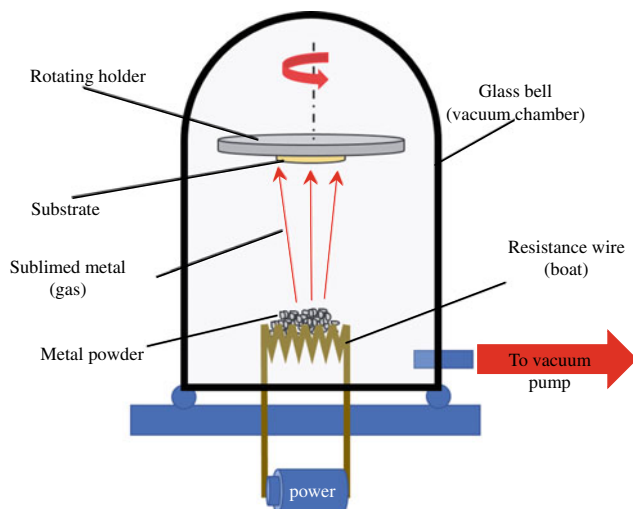


Fig. 28 Thermal evaporation coating process (with permission 5273140799497)

For a precursor to be compatible with doctor blade coating, it has to contain a relatively higher amount of binders and thickeners, in comparison with other roll-to-roll coating techniques, resulting in high viscosities ranging from 1000 to 10,000 mPa.s (Shin et al. 2020).

Perovskite solar cells were prepared by Wang et al. (Han et al. 2014), using doctor blade coating for the perovskite active layer and nickel oxide (NiO) as a hole transporting material instead of the conventional organic PEDOT:PSS. They achieved a 200 μm crystal domain for the perovskite active layer and a power conversion efficiency of 15.34%.

8 Curtain Coating

Curtain coating is a pre-metered coating technique that creates a continuous curtain of a flowing fluid which falls onto a moving substrate. This technique utilizes a tank that harbors the ink/precursor to be coated, with a slit or a slot-die-head to facilitate the fluid delivery, and a conveyer

belt to move the substrate across the curtain of fluid (<https://www.ossila.com/pages/slot-die-coating-theory>), a conventional curtain coating process is shown in Fig. 30.

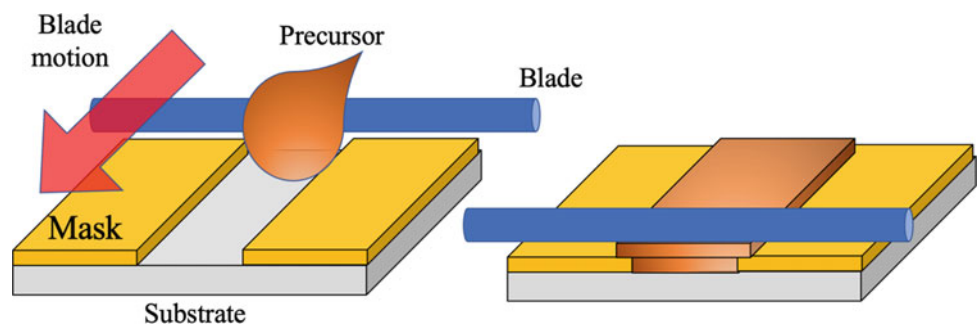
Third-generation solar cell precursors can be prepared and fed into a tank suited for curtain coating, with all the material property requirements taken into account, for direct roll-to-roll fabrication of these novel technologies. Precursor properties are essential to consider given that curtain coating operational variables depend on a base parameter known as the minimum flow rate for each liquid/precursor that can be used for a successful coating process. The minimum flow rate is a function of surface tension and the viscosity (in the range of 10–500 mPa.s (Ruschak 1976)) of the precursor used.

Curtain coating being a pre-metered techniques means that the amount of material that is used to achieve a certain thickness of the deposited material can be calculated beforehand. The flow rate of the fluid curtain is set with respect to the volume of the tank and the amount of material that is available, and the speed of the conveyer belt with respect to the width of the cell can be used to calculate exactly the amount of material that is deposited on the substrate within a single coating process. This allows for a moderately precise thickness control with little to no material waste (Higgins and Scriven 1980), and in case, there is excess material that was not utilized in the coating process, and a retrieving pan/bowl is placed beneath the conveyer belt as a collection station that pumps back the unused fluid into the holding tank (Krebs et al. 2009).

9 Pad Printing

Pad printing is a gravure offset printing technique that has a high throughput and a simple design. Pad printing consists of a flexible silicon rubber pad, a printing cliché (etched printing plate) that has the desired to be printed design engraved on it, and a doctor blade for spreading the ink across the cliché.

Fig. 29 Doctor blade coating process



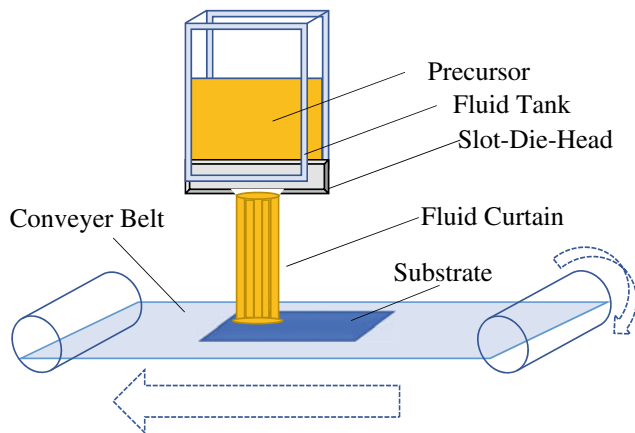


Fig. 30 Curtain coating process

The first step of pad printing is transferring the ink onto the cliché via a spatula and doctor blading the excess material away, while filling the engraved design with the desired ink. The volatile solvents start evaporating from the ink at this stage.

Then, the flexible silicon rubber pad is lowered to reach the cliché and picks up the ink as well as some of the leftover solvents. As the ink sticks onto the pad, the rest of the solvents still imbedded within the ink are evaporated. The pad is then lowered to come in contact with a non-planar solar cell surface (porous surface) and transfers the ink during the process. A conventional pad printing process is shown in Fig. 31.

To counter the issue of rapid evaporation of the conventional inks that are used in other techniques such as screen printing, an optimization of the ink precursors must take place by adjusting the type and ratio of the binders and solvents used.

The shape of the silicon pad also affects the overall printing process. Parameters that decide the curvature of the

pad are the shape and roughness of the substrate that the printing is set to take place onto.

Pad printing is compatible with roll-to-roll production lines to some extent and has a very high material utilization with little to no wastage and a moderate thickness control that is affected by the ink that is used and the solvents involved, as well as intermediate ink viscosity requirements of 10–200 mPa.s (Ruschak 1976).

10 Spray Coating

Spray coating is a primary process in surface engineering applications, such as wear and corrosion prevention. It is a cost-effective solution that has been implemented in a variety of industries given that it is compatible with roll-to-roll production lines.

The process of spray coating begins with the material feedstock which is molten or semi-molten powder. Through the spray coating-nozzle's barrel, the material is propelled onto the desired substrate through a stream of hot gas or plasma. Temperature control mechanisms are used to ensure that the targeted substrate is kept at a temperature that suits the coating material. Once the coating material reaches the cool surface of the substrate, it cools down and subsequently contracts forming a very strong bond with the substrate's surface. The coating is done layer by layer to reach a desired thickness. However, the thickness is not precisely controlled in this process in comparison with other roll-to-roll alternatives. Spray coating process is illustrated in Fig. 32.

Spray coating has an adverse high material wastage, given that the base of the coating process does not allow for a precise ejection of the source material. Spray coating requires a relatively low viscosity of the molten source material at 1–40 mPa.s (Ruschak 1976).

Fig. 31 Pad printing process

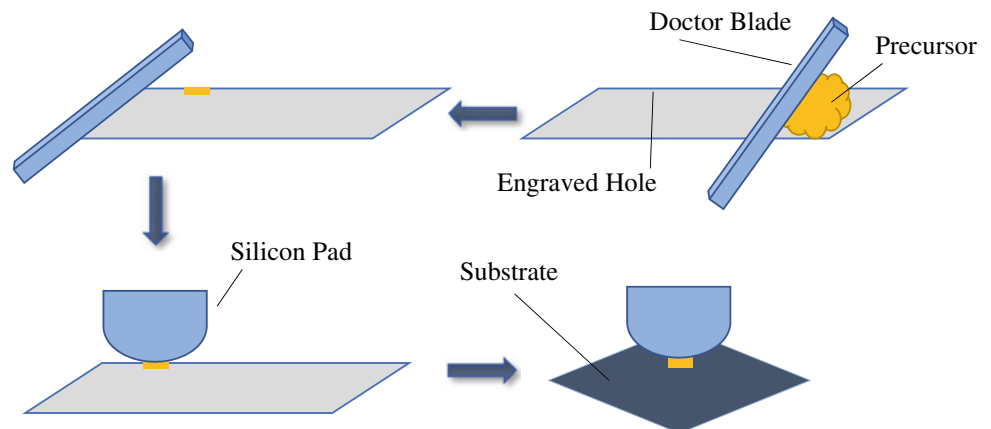
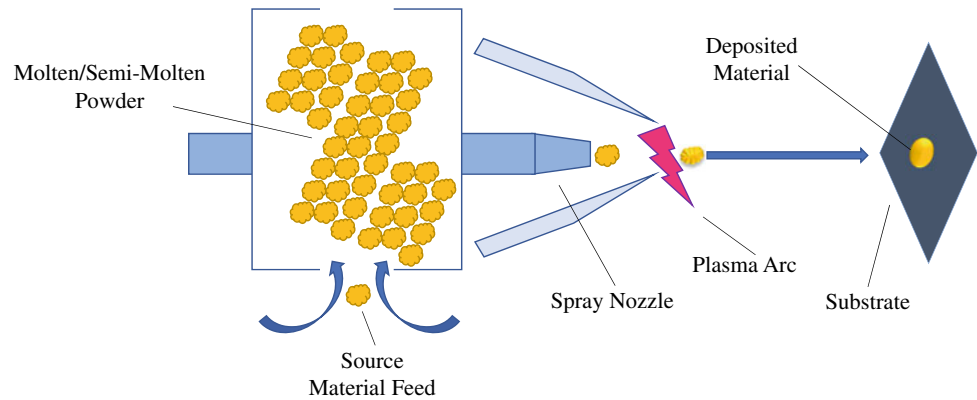
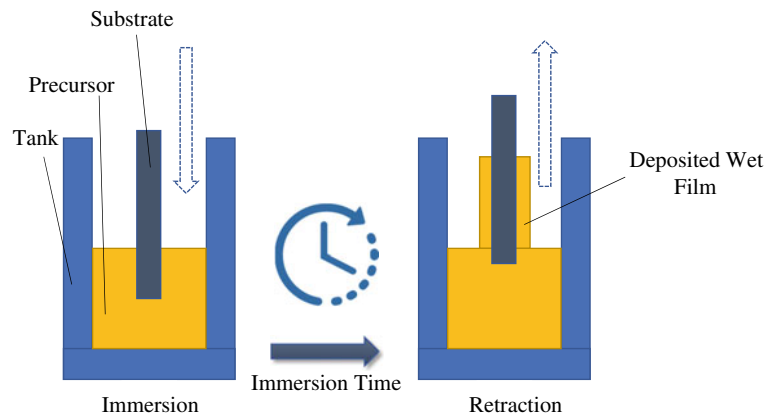


Fig. 32 Spray coating process**Fig. 33** Dip coating process

11 Dip Coating

Dip coating is an established industrial process that is compatible with various kinds of substrates, including those of conventional third-generation solar cells. Dip coating is relatively simpler than comparable roll-to-roll systems. It essentially consists of a precursor-containing tank, and a substrate that can be immersed into or rolled in and out of the tank. The layer that is deposited on the substrate depends on the immersion time, surface tension, and the viscosity (1–200 mPa.s (Ruschak 1976)) of the solution/precursor.

Dip coating is considered to be one of the most effective techniques of fabricating perovskite solar cells, with low cost and a precisely controllable layer thickness with few drawbacks such as a relatively slow production rate (Vak et al. 2015).

The dip coating process, such as shown in Fig. 33, consists of two steps. A targeted substrate is immersed into a precursor-containing tank with optimized precursor properties, and the immersion speed is controlled through an immersing hand. A sufficient immersion time is spent to allow the precursor to stick to the substrate resulting in a workable wet film. The second step is retracting the substrate

at a speed that suits the surface tension and the viscosity of the precursor and moving it along the production line for further processing.

References

- Bajpai P (2018) Hydraulics. In: Biermann's handbook of pulp and paper. Elsevier, pp 455–482. <https://doi.org/10.1016/B978-0-12-814238-7.00023-4>
- Burgelman M (1998) Thin film solar cells by screen printing technology
- Chemical Resistance Guide of PTFE and Filled PTFE [Online]. Available: <http://www.standard-ptfe.com/chemical-resistance-guide-of-ptfe-and-filled-ptfe.php>
- Coaters LS, Spin coaters from Laurell—WS-650–23B spin coater. Laurell Technologies Corporation [Online]. Available: <http://www.laurell.com/spin-coater/?model=WS-650-23B&s=2>
- Comparison of Vertical and Horizontal Slot Die Coatings. Free Online Library. <https://www.thefreelibrary.com/Comparison-of-vertical-and-horizontal-slot-die-coatings-a0171141698> (accessed Jul. 20, 2022)
- Ding X, Liu J, Harris TAL (2016) A review of the operating limits in slot die coating processes. *AIChE J* 62(7):2508–2524. <https://doi.org/10.1002/aic.15268>
- Du M et al (2020) High-pressure nitrogen-extraction and effective passivation to attain highest large-area perovskite solar module

- efficiency. *Adv Mater* 32(47):2004979. <https://doi.org/10.1002/adma.202004979>
- Guo G et al (2011) Effect of dispersibility of silver powders in conductive paste on microstructure of screen-printed front contacts and electrical performance of crystalline silicon solar cells. *J Mater Sci: Mater Electron* 22(5):527–530. <https://doi.org/10.1007/s10854-010-0172-1>
- Han GH, Lee SH, Ahn W-G, Nam J, Jung HW (2014) Effect of shim configuration on flow dynamics and operability windows in stripe slot coating process. *J Coat Technol Res* 11(1):19–29. <https://doi.org/10.1007/s11998-013-9485-3>
- Higgins B (2011) Slot die coating: the physics of the viscocapillary coating bead. https://www.researchgate.net/publication/245320474_Slot_Die_Coating_The_Physics_of_the_Viscocapillary_Coating_Bead (accessed Jul. 24, 2022)
- Higgins BG, Scriven LE (1980) Capillary pressure and viscous pressure drop set bounds on coating bead operability. *Chem Eng Sci* 35(3):673–682. [https://doi.org/10.1016/0009-2509\(80\)80018-2](https://doi.org/10.1016/0009-2509(80)80018-2)
- Hussain W, Rashid B, Sridewi N, Ahmed W, Ahmad MS (2022) Development of dye-sensitized solar cell module and its optimization. In: *Dye-sensitized solar cells*. Elsevier, pp 137–157. <https://doi.org/10.1016/B978-0-12-818206-2.00009-8>
- Krebs FC (2009) Polymer solar cell modules prepared using roll-to-roll methods: knife-over-edge coating, slot-die coating and screen printing. *Sol Energy Mater Sol Cells* 93(4):465–475. <https://doi.org/10.1016/j.solmat.2008.12.012>
- Krebs FC, Gevorgyan SA, Alstrup J (2009) A roll-to-roll process to flexible polymer solar cells: model studies, manufacture and operational stability studies. *J Mater Chem* 19(30):5442. <https://doi.org/10.1039/b823001c>
- Lévy F (2016) Film growth and epitaxy: methods. In: *Reference module in materials science and materials engineering*. Elsevier, B9780128035818010000. <https://doi.org/10.1016/B978-0-12-803581-8.01012-2>
- Mishra A, Bhatt N, Bajpai AK (2019) Chapter 12—Nanostructured superhydrophobic coatings for solar panel applications. In: Nguyen Tri P, Rtimi S, Plamondon CMO (eds) *Nanomaterials-based coatings*. Elsevier, pp 397–424. <https://doi.org/10.1016/B978-0-12-815884-5.00012-0>
- Newport M (2022) Semiconductor lithography. <https://www.newport.com/n/photolithography-overview>
- Orava J, Kohoutek T, Wagner T (2014) Deposition techniques for chalcogenide thin films. In: *Chalcogenide glasses*. Elsevier, pp 265–309. <https://doi.org/10.1533/9780857093561.1.265>
- Patidar R, Burkitt D, Hooper K, Richards D, Watson T (2020) Slot-die coating of perovskite solar cells: an overview. *Mater Today Commun* 22:100808. <https://doi.org/10.1016/j.mtcomm.2019.100808>
- PP Polypropylene Natural Specifications Boedeker [Online]. Available: <https://www.boedeker.com/Product/Polypropylene-Natural>
- Ramasamy E, Lee WJ, Lee DY, Song JS (2007) Portable, parallel grid dye-sensitized solar cell module prepared by screen printing. *J Power Sources* 165(1):446–449. <https://doi.org/10.1016/j.jpowsour.2006.11.057>
- Romero OJ, Scriven LE, Carvalho MS (2006) Slot coating of mildly viscoelastic liquids. *J Nonnewton Fluid Mech* 138(2–3):63–75. <https://doi.org/10.1016/j.jnnfm.2005.11.010>
- Ruschak KJ (1976) Limiting flow in a pre-metered coating device. *Chem Eng Sci* 31(11):1057–1060. [https://doi.org/10.1016/0009-2509\(76\)87026-1](https://doi.org/10.1016/0009-2509(76)87026-1)
- Sahu N, Parija B, Panigrahi S (2009) Fundamental understanding and modeling of spin coating process: a review. *Indian J Phys* 83(4):493–502. <https://doi.org/10.1007/s12648-009-0009-z>
- Saraie J, Kitagawa M, Ishida M, Tanaka T (1978) Liquid phase epitaxial growth of CdTe in the CdTe–CdCl₂ system
- Shin D, Lee J, Park J (2020) Effect of slit channel width of a Shim embedded in slot-die-head on high-density stripe coating for OLEDs. *Coatings* 10(8):772. <https://doi.org/10.3390/coatings10080772>
- Solution Processed Metal Oxide Thin Films for Electronic Applications (2020) Elsevier. <https://doi.org/10.1016/C2017-0-02104-3>
- Slot-Die Coating Theory, Design & Applications | Ossila. <https://www.ossila.com/pages/slot-die-coating-theory> (accessed Jul. 20, 2022)
- Slot-Die Coating Theory, Design & Applications | Ossila. <https://www.ossila.com/pages/slot-die-coating-theory> (accessed Feb. 15, 2023)
- Slot-Die Head, Shims & Meniscus Guides | Coater Accessories | Ossila. https://www.ossila.com/products/slot-die-head?_pos=1&_sid=bc1331a13&_ss=r&variant=41159008878755 (accessed Jul. 24, 2022)
- Spin Coater Low Price Compact Spin Coating System. *Ossila* [Online]. Available: <https://www.ossila.com/products/spin-coater>
- Spin Coating: Complete Guide to Theory and Techniques. *Ossila* [Online]. Available: <https://www.ossila.com/pages/spin-coating>
- Spincoating SPSE, POLOS300 advanced. www.spincoating.com [Online]. Available: <https://www.spincoating.com/en/spin-coater-models/spincoater-polos300-advanced-spin-coating-machine/28/>
- Syringe Pump | Low Price Single/Dual Laboratory Device | Ossila. <https://www.ossila.com/products/syringe-pump> (accessed Jul. 24, 2022)
- Summers H (ed) (2013) vol 5. Elsevier, Amsterdam; Boston
- Teixeira ES et al (2020) Building and testing a spin coater for the deposition of thin films on DSSCs. *Mat Res* 23(6):e20200214. <https://doi.org/10.1590/1980-5373-mr-2020-0214>
- Thin Film Solar Cells by Screen Printing Technology | Semantic Scholar. <https://www.semanticscholar.org/paper/Thin-film-solar-cells-by-screen-printing-technology-Burgelman/f7a356e1c66f443a5604c07d69dbfc0de714cc77> (accessed Jul. 20, 2022)
- tungsten Uses, Properties, & Facts Britannica [Online]. Available: <https://www.britannica.com/science/tungsten-chemical-element>
- US2681294A—Method of Coating Strip Material—Google Patents. <https://patents.google.com/patent/US2681294A/en> (accessed Jul. 20, 2022)
- Vak D et al (2015) 3D printer based slot-die coater as a lab-to-fab translation tool for solution-processed solar cells. *Adv Energy Mater* 5(4):1401539. <https://doi.org/10.1002/aenm.201401539>
- Yilbas BS, Al-Sharafi A, Ali H (2019) Chapter 3—Surfaces for self-cleaning. In: Yilbas BS, Al-Sharafi A, Ali H (eds) *Self-cleaning of surfaces and water droplet mobility*. Elsevier, pp 45–98. <https://doi.org/10.1016/B978-0-12-814776-4.00003-3>